PIEZOELECTRIC KINETIC ENERGY-HARVESTING ICS

A Dissertation
Presented to
The Academic Faculty

by

Dongwon Kwon

In Partial Fulfillment
of the Requirements for the Degree
Doctor of Philosophy in the
School of Electrical and Computer Engineering

Georgia Institute of Technology
May 2013

PIEZOELECTRIC KINETIC ENERGY-HARVESTING ICS

Approved by:

Dr. Gabriel A. Rincón-Mora, Advisor
School of Electrical and Computer Engineering
Georgia Institute of Technology

Dr. David G. Taylor
School of Electrical and Computer Engineering
Georgia Institute of Technology

Dr. Thomas G. Habetler
School of Electrical and Computer Engineering
Georgia Institute of Technology

Dr. Jun Ueda
School of Mechanical Engineering
Georgia Institute of Technology

Dr. John D. Cressler
School of Electrical and Computer Engineering
Georgia Institute of Technology

Date Approved: March 04, 2013

To my wife Hayang

ACKNOWLEDGEMENTS

First of all, I would like to thank my advisor, Dr. Gabriel Alfonso Rincón-Mora, for his passionate and insightful guidance throughout my Ph.D. program. None of this research could have been possible without his vision and advice.

I also thank my dissertation and proposal committee members, Dr. John D. Cressler, Dr. Thomas G. Habetler, Dr. David G. Taylor, Dr. Jun Ueda, and Dr. Deepakraj Divan, for their priceless technical recommendations and support for my research.

I sincerely thank Bryan Legates, Josh Caldwell, and Linear Technology Corporation for their technical, financial, and logistical support throughout the research program.

I extend my thanks to my colleagues at the Georgia Institute of Technology, Luke Milner, Suhwan Kim, Erick Torres, Amit Patel, Justin Vogt, JinJyh Su, Rajiv Damodaran Prahba, Orlando Lazaro, Karl Peterson, Carlos Solis, and Andres Blanco, for their invaluable discussions about circuits and life as a graduate student.

I am extremely grateful to my loving wife, Hayang Kim, who has supported me and my life as a Ph.D. student with unending love, trust, understanding, and sacrifice.

I express my deepest appreciation and respect to my father Yongwoo Kwon and mother Kisook Hong, who raised me with endless love, encouragement, and support.

I would like to thank my father- and mother-in-law, Hyuncheol Kim and Eunhee Park, for their immense support for my family and program.

Finally, I thank God for all the blessings I hold today. A seed of faith He planted in my mind made all these possible.

TABLE OF CONTENTS

LIST OF TABLES

LIST OF FIGURES

SUMMARY

Wireless micro-sensors can enjoy popularity in biomedical drug-delivery treatments and tire-pressure monitoring systems because they offer in-situ, real-time, non-intrusive processing capabilities. However, miniaturized platforms severely limit the energy of onboard batteries and shorten the lifespan of electronic systems. Ambient energy is an attractive alternative because the energy from light, heat, radio-frequency (RF) radiation, and motion can potentially be used to continuously replenish an exhaustible reservoir. Of these sources, solar light produces the highest power density, except when supplied from indoor lighting, under which conditions the available power decreases drastically. Harnessing thermal energy is viable, but micro-scale dimensions severely limit temperature gradients, the fundamental mechanism from which thermo piles draw power. Mobile electronic devices today radiate plenty of RF energy, but still, the available power rapidly drops with distance. Harvesting kinetic energy may not compete with solar power, but in contrast to indoor lighting, thermal, and RF sources, moderate and consistent vibration power across a vast range of applications is typical. Although operating conditions ultimately determine which kinetic energy-harvesting method is optimal, piezoelectric transducers are relatively mature and produce comparatively more power than their counterparts such as electrostatic and electromagnetic kinetic energy transducers.

The presented research objective is to develop, design, simulate, fabricate, prototype, test, and evaluate CMOS ICs that harvest ambient kinetic energy in periodic

and non-periodic vibrations using a small piezoelectric transducer to continually replenish an energy-storage device like a capacitor or a rechargeable battery. Although vibrations in surrounding environment produce abundant energy over time, tiny transducers can harness only limited power from the energy sources, especially when mechanical stimulation is weak. To overcome this challenge, the presented piezoelectric harvesters eliminate the need for a rectifier which necessarily imposes threshold limits and additional losses in the system. More fundamentally, the presented harvesting circuits condition the transducer to convert more electrical energy for a given mechanical input by increasing the electromechanical damping force of the piezoelectric transducer. The overall aim is to acquire more power by widening the input range and improving the efficiency of the IC as well as the transducer. The presented technique in essence augments the energy density of micro-scale electronic systems by scavenging the ambient kinetic energy and extends their operational lifetime.

This dissertation reports the findings acquired throughout the investigation. The first chapter introduces the applications and challenges of micro-scale energy harvesting and also reviews the fundamental mechanisms and recent developments of various energy-converting transducers that can harness ambient energy in light, heat, RF radiation, and vibrations. Chapter 2 examines various existing piezoelectric harvesting circuits, which mostly adopt bridge rectifiers as their core. Chapter 3 then introduces a bridge-free piezoelectric harvester circuit that employs a switched-inductor power stage to eliminate the need for a bridge rectifier and its drawbacks. More importantly, the harvester strengthens the electrical damping force of the piezoelectric device and increases the output power of the harvester. The chapter also presents the details of the

integrated-circuit (IC) implementation and the experimental results of the prototyped harvester to corroborate and clarify the bridge-free harvester operation.

One of the major discoveries from the first harvester prototype is the fact that the harvester circuit can condition the piezoelectric transducer to strengthen its electrical damping force and increase the output power of the harvester. As such, Chapter 4 discusses various energy-investment strategies that increase the electrical damping force of the transducer. The chapter presents, evaluates, and compares several switched-inductor harvester circuits against each other. Based on the investigation in Chapter 4, an energy-investing piezoelectric harvester was designed and experimentally evaluated to confirm the effectiveness of the investing scheme. Chapter 5 explains the details of the IC design and the measurement results of the prototyped energy-investing piezoelectric harvester. Finally, Chapter 6 concludes the dissertation by revisiting the challenges of miniaturized piezoelectric energy harvesters and by summarizing the fundamental contributions of the research. With the same importance as with the achievements of the investigation, the last chapter lists the technological limits that bound the performance of the proposed harvesters and briefly presents perspectives from the other side of the research boundary for future investigations of micro-scale piezoelectric energy harvesting.

CHAPTER 1

HARVESTING ENERGY IN MICROSYSTEMS

1.1. Miniaturized Applications

Miniaturized electronic systems, such as wireless micro-sensors and biomedical implants, can provide monitoring and processing capabilities in diverse areas ranging from health and lifestyle to automotive, industrial, and military applications [1]–[17]. As shown in Figure 1.1(a), biomedical applications include wearable electrocardiogram (ECG) sensors that monitor of cardiac activity [4]–[5] and pacemakers that sense the heart rate and provide electrical stimulation when the rate falls below a certain threshold [6]. Smaller-scale drug-delivery implants that exploit micro-electro-mechanical-system (MEMS) technology can also monitor one's health status and provide preventive or therapeutic treatment *in situ,* as shown in Figure 1.1(b) [7]–[10]. In addition, as shown in Figure 1.1(c), the automotive industry extensively uses tiny acceleration and pressure sensors for safety and control functions in airbag-triggering and tire-pressure-monitoring systems [2]–[3], [11]–[13]. Industrial applications also employ acceleration and pressure sensors in addition to temperature and humidity sensors for the maintenance of machinery in large factories and power plants [1]–[2]. In particular, the wireless feature of these small sensors can substantially reduce the cost of cable installations and the risk in hazardous areas [13]. Dynamic microelectronic systems, such as micro-aerial vehicles (MAVs) [14], biomimetic micro-robots [15], and hybrid insects, illustrated in Figure 1.1(d) [16] can perform military surveillance and reconnaissance missions in critical situations or over dangerous terrain.

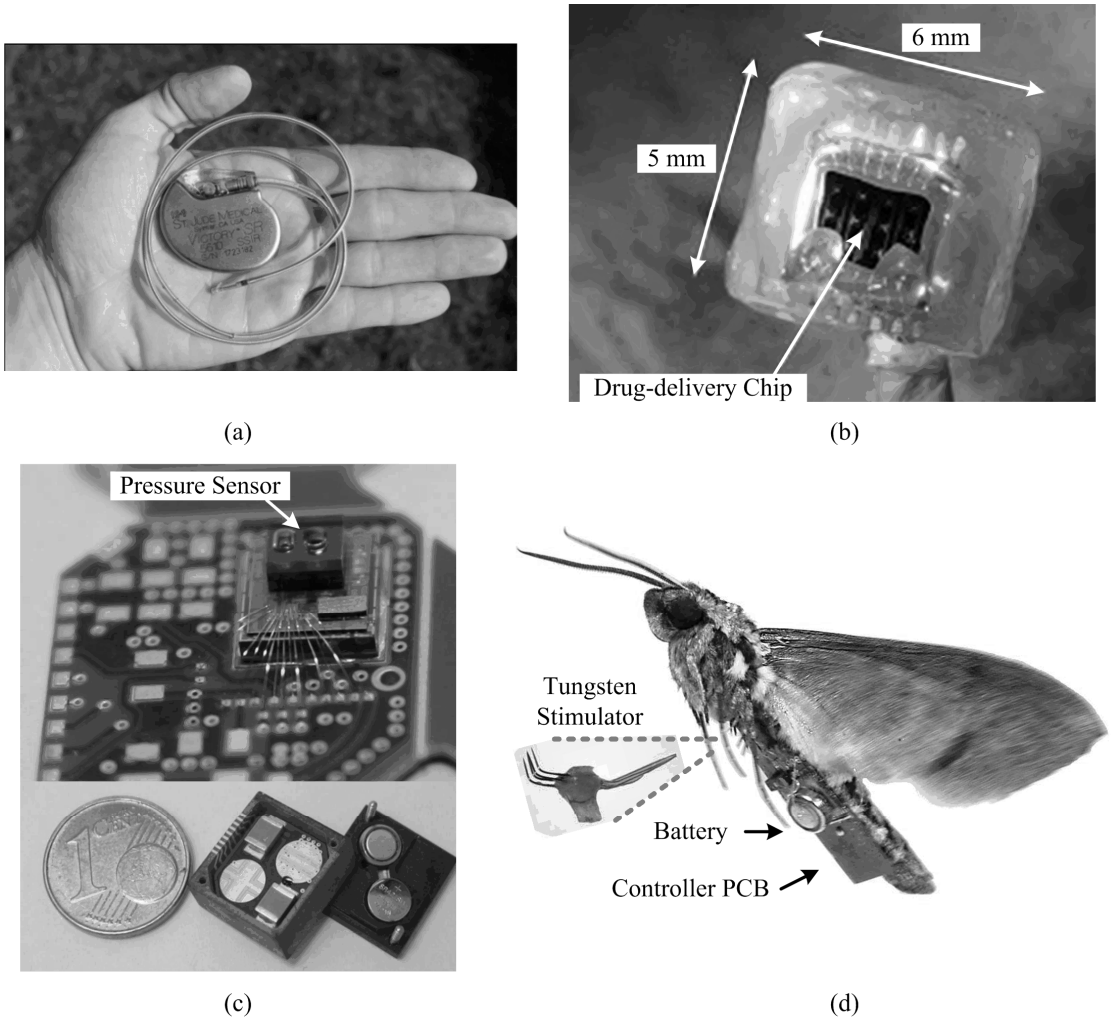

Figure 1.1. Miniaturized electronic systems: (a) pacemaker [6], (b) drug-delivery implant [7], (c) tire-pressure sensor [12], and (d) cyborg moths [16].

Small electronic systems are versatile because they are capable of providing valuable information about typically inaccessible sites, while occupying little-to-negligible space. However, the micro-scale platform that offers unobtrusiveness inherently limits the size of on-board energy/power storage and constrains the operational lifetime and functionality of the system. Furthermore, replacing easily exhaustible on-board batteries can be prohibitively risky and expensive. These tiny systems often are installed in unreachable places, such as inside the human body, and they operate in

concert with numerous other small devices [1]. Therefore, one of the main technological challenges in implementing microsystems is how to power them.

1.2. Technological Challenges

Miniaturized systems demand high-energy-density sources to sustain a long operational lifetime within a limited space. The small devices also require high-power-density sources that can rapidly meet the demands of the power-hungry functions of wireless communication and signal processing. Currently, electrochemical batteries such as the li-ion battery (Li-ion) serve as the predominant power sources for small electronics as they exhibit a good compromise of energy and power performance [18]–[22]. However, despite improvements in their storage densities, electrochemical batteries tend to occupy the bulkiest portion of small electronic systems. For example, mobile-phone batteries account for up to 36% of the mass of the entire phone, and the percentage tends to increase for smaller devices such as wireless micro-sensors [18]. Possible solutions to reduce the size of batteries include employing energy supplies with higher capacities than electrochemical batteries and harvesting ambient energy from the surrounding environment.

Reported various state-of-the-art sources such as micro-turbines [23]–[24] and micro-heat engines [25]–[26] exhibit high-energy densities. Of these, micro-fuel cell (μFC) technology can offer five to ten times as much energy density as rechargeable electrochemical batteries such as Li-ions [27]–[36]. Direct-methanol fuel cells (DMFCs) feature the pertinent characteristics of a low operating temperature, amenability to miniaturization, and low cost [32]. As revealed in Figure 1.2(a), DMFCs feed the fuel (i.e., methanol CH_3OH) into an anode that produces protons (H^+), electrons (e^-), and carbon-dioxides (CO_2) on electrode surfaces covered with catalysts [27]. The proton-exchange membrane (PEM) in the middle allows the protons, but not the electrons, to conduct; therefore, electrons flow through an external circuit and drive an electrical load.

In a cathode, protons and electrons react to form water (H_2O) in the presence of oxygen (O_2) and catalysts.

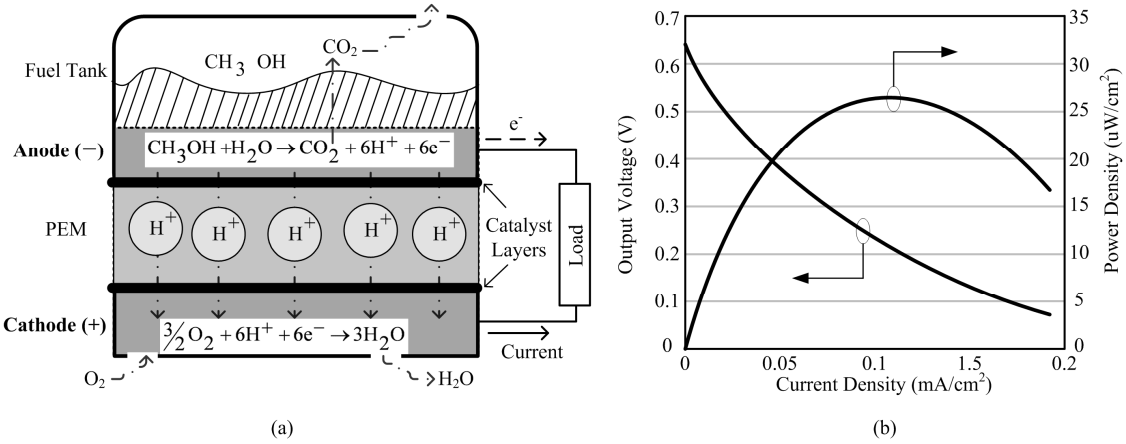

Figure 1.2. (a) Direct-methanol fuel cell (DMFC) structure and (b) output voltage and power density profiles [29].

DMFCs implemented with existing silicon-processing technologies have boosted the feasibility of co-fabricating μFCs that can secure high-energy-density sources in small form factors at a low cost [32]. However, as illustrated in Figure 1.2(b), the main drawbacks of μFCs are their low voltage and power. Moreover, since the output voltage rapidly decreases with any load-current increase, the output power peaks under certain output current and voltage conditions even though the μFC uses the same amount of fuel to generate electricity. Hence, μFCs requires a power-management circuit to extract the largest-possible amount of electrical energy from a given quantity of fuels. The power-management circuit should control the μFCs to supply a low and slowly varying load power and regulate the cell voltage around its maximum power point (MPP) [35]–[36].

Another device that can supply more than ten times as much energy density as μFCs is the nuclear battery [37]–[43]. Nuclear batteries exploit radioisotope decay to produce electrical energy. Beta particles originating from radioisotope materials, such as the ^3H [37] and ^{63}Ni [39] bombard PN junctions, shown in Figure 1.3(a), to generate electron-hole pairs (EHPs). The electric field of the depletion region then sweeps the

EHPs, producing a drift current from an N- to a P-type semiconductor. This procedure is similar to the photovoltaic effect in solar cells except that the beta particles trigger EHP generations instead of photons. The equivalent circuit model of nuclear batteries presented in Figure 1.3(b) resembles that of a solar cell [37], [39]. The current source I_{EHP} models the current generated by beta particles, and the diode D_{PN} represents the PN junction where internal electron-hole recombination and EHP generation occur.

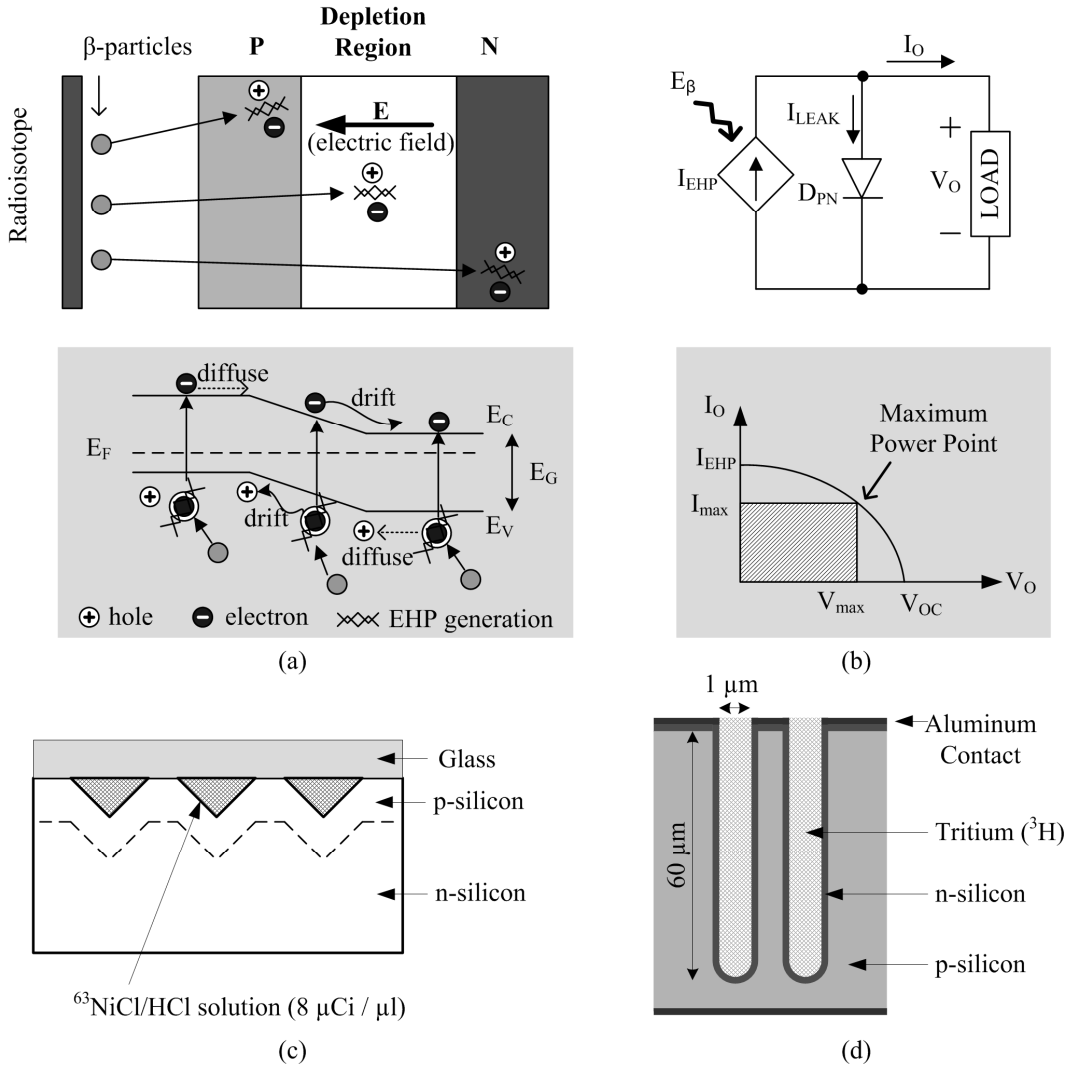

Figure 1.3. Beta-voltaic effect: (a) a PN junction with an energy band diagram, (b) an equivalent circuit model with output characteristics. Battery implementation: surface areas increased by using (c) an inverted pyramid array [39], and (d) a porous silicon diode [37].

The cross sections of beta-voltaic batteries that enlarge surface areas to increase the levels of current and efficiency are illustrated in Figures 1.3(c) and (d). The current generated by radioisotopes is governed by several factors, such as the type and the amount of the radioisotope material, the depth and doping densities of the PN junction, the minority-carrier diffusion length, and the amount of leakage current [39]. Of these, as shown in Figure 1.3 (b), the leakage current flowing through the diode is a function of the battery voltage. Hence, any power-management system that interfaces with these nuclear batteries, like solar-cell applications, must consider maximum-power-point tracking (MPPT) control. In addition, because the output power of these nuclear batteries is very low [37], the power-management system needs to include power caches such as capacitors that can handle instantaneous loads.

These novel battery solutions (i.e., μFCs and nuclear batteries) can significantly promote the energy capacities of small-scale systems. Nevertheless, integration challenges remain because these systems run on fuel that requires practical and safe packaging. Furthermore, even though the operational lifetime of μFCs and nuclear batteries may be considerably longer than that of electrochemical batteries such as the Li-ions, fuel-based energy sources inherently cannot eliminate the need for manual recharging. One way to eliminate the need for manual recharging is to harvest energy from ambient sources such as light, heat, radio-frequency (RF) radiation, and motion. Harvesting ambient energy to replenish the on-board batteries can augment the energy density of microsystems and prolong their operational lifetime [18], [44]–[49]. However, ambient sources can supply a finite amount of energy in sporadic fashion within a certain period, and a miniaturized platform limits the performance of energy transducers. Therefore, for any target application, it is crucial to judiciously select the appropriate energy sources and harvesting schemes.

1.3. Ambient Energy Sources

For centuries, the idea of harvesting electrical energy from the environment has been put into practice in the form of windmills, watermills, and solar-power systems. However, harvesting energy under small-scale constraints is an emerging topic of research that has been the focus of considerable interest in both academia and industry [46]. Although the fundamental concept may vary only slightly with scale, most practical features such as available power levels, manufacturability, and costs vary significantly according to scale and provide challenges for realization [18], [45]–[46]. Fortunately, advancements in low-power electronics and MEMS technology synergistically promote the development of energy-harvesting techniques for miniaturized platforms that scavenge energy from ambient sources such as light, heat, RF-electromagnetic waves, and kinetic motion.

1.3.1. Light Energy

Light-energy harvesting, which uses the photovoltaic effect in the PN junction of semiconductors, has been heavily investigated and commercially developed in various applications [50]–[65]. Photovoltaic cells generate electricity much the same way as beta-voltaic nuclear batteries, introduced in the previous section. Instead of the beta particles in nuclear batteries, photons with energy greater than the bandgap energy of the semiconductor promote electrons from a valance band to a conduction band and leave a corresponding number of holes in the valence band. The electric field of space charges in the depletion region sweeps the generated electron-hole pairs (EHPs) within the depletion region of the PN junction (or within a minority-carrier diffusion length from the edges of the depletion region) and drives the pairs through an external load. This EHP generation procedure in a widely used silicon solar-cell structure is illustrated in Figure 1.4 [50].

Note that the textured surface reduces reflection and refracts light so that photons can travel a long path within the silicon. Aluminum paste covering the entire bottom surface enlarges the contact area and therefore decreases the contact resistance.

Moreover, an annealing process during fabrication introduces a P^+-doped region above the bottom electrode that also reduces resistance. Minimizing the series resistance of a solar cell is important because 5-Ω series resistance may decrease the efficiency of the device to less than 30% of what it would be with zero-Ω series resistance [50].

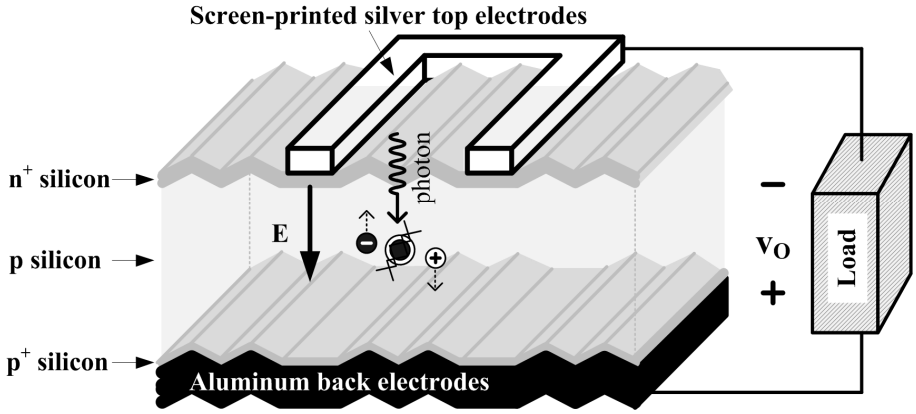

Figure 1.4. A silicon solar-cell structure with screen-printed electrodes.

Because of the similarity between this solar cell and the beta-voltaic cell during physical operation, the equivalent circuit model of a solar cell also resembles the counterpart of a beta-voltaic cell, shown in Figure 1.3(b). Thus, to obtain the maximum output under a given temperature and irradiance, solar cells require MPPT control to automatically find the optimal voltage or current at which a device should operate [61]–[65]. The literature presents a great number of MPPT concepts realized in various implementations. Generally, high-power (e.g., above 1 W) applications tend to employ current sensors and digital-signal processors to compute the optimal operating point, while low-power applications are used to develop low-power analog circuits for the same purpose.

One advantage of photovoltaic cells for micro-scale systems is that they can be integrated using current semiconductor technologies. Through post-processing, various thin-film photovoltaic cells can be integrated using amorphous silicon (a-Si:H) and copper indium gallium (di)selenide (CIGS) on CMOS chips [56]–[57]. PN-junction diode

solar cells implemented on standard CMOS processes can harvest up to 22.5 mW/cm^2 from white light intensity of 20 kLUX, which emulates sunny outdoor conditions [54]–[55]. However, the output power drastically declines as the light intensity decreases, which is the case in typical indoor applications [64]. Therefore, for light energy harvesting applications, it is critical to examine whether the device can receive enough light from the right direction for enough time [66].

1.3.2. Heat Energy

Harnessing heat energy through thermoelectric (TE) devices has attracted a great deal of interest because of its potential to generate electrical power and to cool down the hot electronic systems such as the central-processing units (CPUs) in laptops [67]–[68]. As shown in Figure 1.5(a), TE devices employ many TE couples that consist of P- and N-type TE materials connected electrically in series and thermally in parallel. This series/parallel configuration simultaneously maximizes the output voltage and the total thermal gradient of a TE device. Under temperature difference ΔT across the device, the holes in P-type material and the electrons in N-type columns diffuse from a hot side to a cold side. As a result, a net charge builds up at the cold end, producing voltage across a thermocouple. This phenomenon, referred to as the Seebeck effect, predicts that the output voltage of a TE device will be proportional to the ΔT across the surfaces [69]–[70].

A good TE material should exhibit a large Seebeck coefficient to generate a high voltage for a given ΔT, low thermal conductivity to maintain the temperature difference, and high electrical conductivity to minimize Joule heating, which can interrupt carrier (i.e., holes and electrons) diffusion [69]. However, since, generally speaking, a good electric conductor is also a good thermal conductor and vice versa, traditional TE materials cannot meet the conflicting requirements of electrical and thermal conductivities. Since glass provides low thermal conductivity, the best materials reported

are crystalline semiconductors [70]. As a result, the most popular TE materials are alloys of bismuth telluride (Bi_2Te_3) and antimony telluride (Sb_2Te_3) [70]. While the reported power densities of TE devices generally range from 4 to 15 $\mu W/cm^2$ per degree Celsius (ºC) [71]–[77], some commercial products, on their datasheets, claim more than 100 $\mu W/cm^2$ per ºC [78]–[79]. Even higher performance TE device is presented in [80] at 543 $\mu W/cm^2$ per ºC, and the device uses Bi_2Te_3-based super-lattice materials to promote its power level. CMOS-compatible materials such as poly-Si and poly-SiGe can also produce electrical power from thermal gradients [81]–[82], but the high series resistances in the MΩ-range severely limit the power density to lower than 1 $\mu W/cm^2$ per ºC.

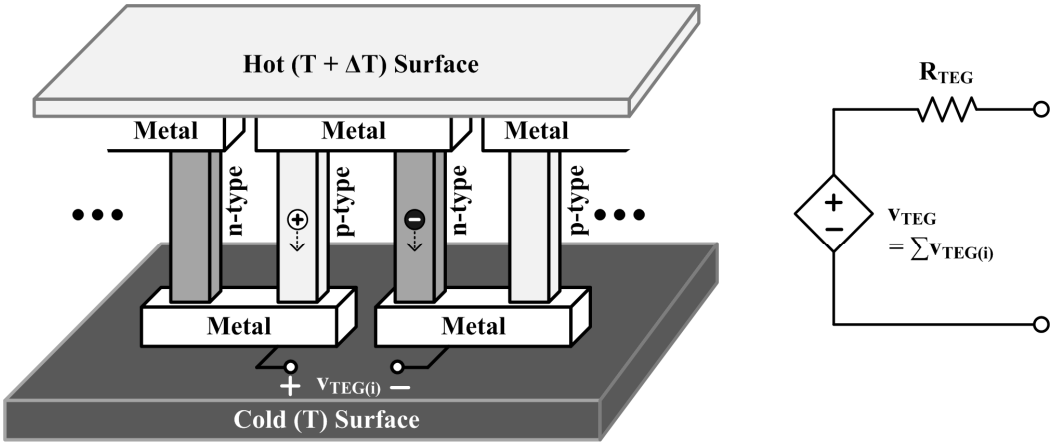

Figure 1.5. (a) Thermoelectric device structure and (b) its equivalent circuit model.

The equivalent circuit model of the TE device illustrated in Figure 1.5(b) consists of a direct-current (DC) thermal-gradient-dependent voltage source v_{TEG} and a series resistance R_{TEG}. v_{TEG} is the sum of each TE-couple voltage $v_{TEG(i)}$, which is proportional to ΔT and the Seebeck coefficient of the material. R_{TEG} depends on the characteristics of the material and the geometry of the device. Some commercial products feature resistances as low as 5.2 Ω [76]–[77] while silicon-based counterparts report 10 MΩ [82]. The existence of these series source resistances prevents TE-harvesting circuits from drawing indefinitely large current and power from TE devices. Hence, to extract as much

power as possible from these devices, TE harvesters attempt to match their input impedance to the source counterpart. If the source resistance is a known constant, a harvester can employ a fixed duty-cycle DC–DC converter that matches the impedance [73]. When the source impedance is unknown or a time-varying variable, a system can adaptively regulate the terminal voltage at half of the open-circuit voltage of the TE device [74], but it does so at the expense of extra power consumption.

Advancements in TE materials and harvesting circuits have been transforming TE harvesting into a viable energy solution for miniaturized applications. However, the available output voltage and power from micro-scale TE devices are still low, because the temperature difference ΔT of microsystems is severely limited. This small ΔT is a fundamental challenge of TE-energy harvesting, because even though it is relatively easy to find high-temperature environments, it is difficult to maintain a high ΔT across small systems.

1.3.3. Radio-frequency (RF) Electromagnetic Energy

One of the earliest electronic devices that harnessed energy from RF-electromagnetic waves to power a system was a crystal radio [48], [83]. Although many configurations are possible, an essential crystal radio requires only an antenna and a diode to rectify amplitude-modulated (AM) RF signals and drive the diaphragm of an earphone. Because of the limited usable distance from the broadcasting station, modern radios and wireless telecommunication devices utilize batteries or wall power to secure energy and use only the information associated with the RF signal. While this practice is still common for electronic systems, the recent proliferation of wireless networks has triggered the idea of harvesting ambient RF-electromagnetic energy [84]–[88]. Unfortunately, RF-radiation power drops at the rate of $1/d^2$, in which d is the distance from the radiating source, and it drops even faster if multi-path fading is taken into account [89]–[93]. Therefore, even if a broadcasting station transmits powerful RF signals, the amount of power that can be

scavenged is low unless a device is very close to the transmission source. Some measured RF signals in the literature are summarized in Table 1.1.

Table 1.1. Comparison of power densities for various ambient RF sources.

Energy Sources	Power Densities	Measurement Condition	Reference
AM Radio Broadcast	1.63 $\mu W/cm^2$	100 m distance (USA)	[48], [90]
FM Radio Broadcast	1.04 $\mu W/cm^2$	At ground level beneath FM towers (USA)	[48], [90]
TV (UHF) Broadcast	< 0.26 $\mu W/cm^2$	500 m from the TV tower (Japan)	[48], [84]
GSM	0.01 – 0.1 $\mu W/cm^2$	25 – 100 m distance (Europe)	[91], [92]
WLAN	0.001 – 0.01 $\mu W/cm^2$	25 – 100 m distance (Europe)	[91], [92]

Even though the power densities expected from ambient RF signals tend to be impractically low, the fact that power can be delivered wirelessly is still an attractive idea. Therefore, many researchers in academia and industry are investigating energy-transfer methods using dedicated RF sources for various applications such as RF identification [93]–[94] and wireless sensor networks [95]–[100].

1.3.4. Kinetic Energy

Kinetic energy in motion and vibrations is very common in our surroundings. For example, abundant ambient vibrations exist in tires, engines, and the seats of various types of vehicles [13], [44], [47], [101]. A human body also produces a considerable amount of kinetic energy that can generate 1 W of electrical power (from the heel strike of a shoe [102]) or 2.1 mW/cm^3 of power density (from a human walking motion [103]). In addition, a variety of ambient vibrations occur in household appliances, heating/venting/air-conditioning (HVAC) systems, industrial equipment, buildings, and bridges. A list of kinetic-energy sources with their acceleration magnitude and the frequency of fundamental vibration modes is presented in Table 1.2.

Table 1.2. Ambient kinetic-energy sources [44], [47], and [103].

Sources	Acceleration [m/s^2]	f_{FUND} [Hz]	Sources	Acceleration [m/s^2]	f_{FUND} [Hz]
Car Engine	12	200	Clothes Dryer	3.5	121
Tire	6.5	103	3-axis Machine Tool	10	70
Car Dashboard	3	13	Door Frame	3	125
Car Hood (3000 rpm)	0.26	147.5	HVAC Vents	0.9	60
Car Hood (750 rpm)	0.07	35.6	Windows	0.7	100
Knee (walking)	11	0.91	CD on Laptop	0.6	75
Heel Tapping	1	3	Busy Office Floor	0.2	100
Blender Casing	6.4	121	Office Desk	0.09	120
Microwave Oven Side	4.21	148.1	Computer Side Panel	0.04	276.3
Microwave Oven Top	1.11	120	Bridge	0.02	171.3

Ambient kinetic energy can be harvested into the electrical domain through three representative transduction mechanisms: electrostatic, electromagnetic, and piezoelectric mechanisms. Although each mechanism exhibits distinct physical properties, requirements, and conversion performance, they all exert an electrical damping force against an external movement to convert electrical energy. The electrical damping force functions similarly to a mechanical damping force (e.g., friction) except that for harvesting, the work done by the external movement against the electrical damping can be stored in the electrical domain rather than dissipated in the form of heat. Since this conversion process reduces the kinetic energy of the total system, which consists of a vibration source and a harvester, some technologies such as regenerative braking exploit a similar mechanism to decelerate the vehicle and collect the energy that would otherwise be lost as heat [104]. However, unlike regenerative braking, miniaturized kinetic-energy transducers can typically harvest only a tiny fraction of the source energy. Hence, the source motion and vibrations can continue without being affected by the scavenging action.

Reported implementations of kinetic-energy transducers show a wide range of power densities and physical dimensions [45]–[46]. However, all three transduction mechanisms have a common problem: as the size of the transducer decreases, the less

power it generates. The limited dimension restricts the displacement of the transducers as well as the capacitor size, the number of coil-turns, and the amount of available charge for electrostatic, electromagnetic, and piezoelectric approaches, respectively. Therefore, the amount of available power declines as the system size decreases [46]. Another repercussion of the micro-scale requirement is the high resonant frequency of the transducers. The resonant frequency of a mechanical system increases if the system is stiff (i.e., a high spring coefficient), short (i.e., a short length), or light (i.e., low mass). All of these parameters in most kinetic-energy transducers tend to increase the resonant frequency if they are to fit in micro-scale dimensions. The increased resonant frequency poses a problem, because ambient vibrations frequencies are usually low (e.g., < 200 Hz), and harvesting is most efficient when the resonant frequency of the transducers and the vibration frequency of the sources match.

Other issues of micro-scale transducers are their cost and reliability. Exotic materials can be expensive, and the moving parts of kinetic-energy transducers may cause mechanical problems over the long term [45]. However, meaningful progress has been made in miniaturized kinetic-energy transducers, which will be reviewed in detail in the following chapters. In addition, studies pertaining to practical MEMS devices with improved power levels are appearing in the literature. Hence, although challenges for micro-scale kinetic-energy harvesting remain, because of the wide availability of ambient motion and vibrations, kinetic energy is a very promising power source for small-scale electronic systems.

1.4. Kinetic-energy Transducers

Although a particular application ultimately determines what energy source is most appropriate, kinetic energy in the movements of people, vehicles, venting ducts, and industrial equipment can become a reliable source for a wide range of applications because it is abundant in our surroundings. Kinetic energy can be converted into the

electrical domain through three representative transduction mechanisms—electrostatic, electromagnetic, and piezoelectric—each with unique characteristics. This chapter will first outline the basic concepts and operating principles of these three kinetic-energy transduction mechanisms and then review the general trends and technical challenges in the development of miniature transducers reported in the literature.

1.4.1. Electrostatic Transducers

An electrostatic transducer harnesses electrical energy from the work that motion exerts against an electrostatic force between two oppositely charged plates of a mechanically variable capacitor. This transduction mechanism can be classified into two categories: charge- and voltage-constrained, shown in Figures 1.6(a) and (b), respectively. When the charge of the capacitor is constrained by leaving the capacitor open circuited, the external force pulls the plates of the capacitor to decrease the capacitance and increase the capacitor voltage, eventually augmenting the energy stored in the capacitor with the kinetic energy of the external force. On the other hand, when the capacitor voltage is clamped with a voltage source, as shown in Figure 1.6(b), the mechanical energy that separates the capacitor plates reduces the capacitance and the electric field between the plates. As a result, the charge departs from the plates and flows into the clamping voltage source that stores the converted electrical energy.

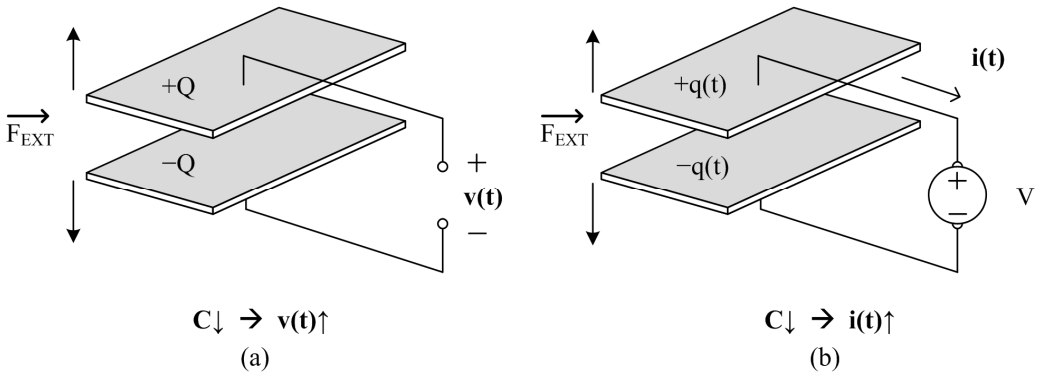

Figure 1.6. Electrostatic transduction: (a) charge- and (b) voltage-constrained approaches.

The realization of the electrostatic-harvesting scheme in micro-scale platforms requires a capacitor that can vary its capacitance in response to mechanical vibrations. The advancement of silicon-micromachining techniques such as deep reactive-ion etching (DRIE) [105] has enhanced a multitude of MEMS devices, including variable capacitors. The fact that these capacitors can be implemented by MEMS technology is a significant advantage over other kinetic-energy transducers such as electromagnetic and piezoelectric approaches because electrostatic transducers can be built using current semiconductor fabrication techniques [45]–[46]. Another critical building block toward the realization of the electrostatic scheme is a power-electronics circuit that can invest (i.e., pre-charge) energy into the variable capacitor before the separation of the capacitor plates and harvest the converted electrical energy from the variable capacitor [106]–[114]. Although various types of conditioning circuits are reported, because the amount of energy extracted from ambient motion is already small, all of them require very efficient operation to produce the energy gain in the harvesting cycle.

For both the charge- and voltage-constrained approaches, the amount of harvested energy depends on the dynamic range of a variable capacitor (i.e., $C_{MAX} - C_{MIN}$) and the maximum allowable voltage in the system [106]–[117]. Hence, electrostatic harvesters favor large capacitance variation and sometimes employ expensive and specialized technologies such as the silicon-on-insulator CMOS process, which can provide very high-voltage devices [115]–[116]. Nevertheless, because miniaturized dimensions severely limit the capacitance range, which is typically below 500 pF, reported output power levels tend to reside below the regime of a few microwatts [106]–[117].

1.4.2. Electromagnetic Transducers

Like conventional macro-scale electric generators, electromagnetic transducers exploit Faraday's Law of Induction to harness kinetic energy in motion into the electrical domain. An electromotive force (EMF) that produces an electric potential difference

across two open-circuited terminals is induced whenever a magnetic flux linkage changes in a coil or a conductor. The induced voltage can drive the current if the terminals are connected through an electrical load or a harvesting circuit.

An example of a moving magnet with a stationary coil is shown in Fig. 1.7. As the external force moves the magnet towards the coil, the magnetic flux linking through the coil increases, thereby inducing a current that opposes the relative motion of the magnet and the coil, as explained by Lenz's Law. Conversely, when the magnet moves away from the coil, the resulting voltage and the current change their polarity, which explains why the outputs of the electromagnetic transducers are alternative-current (AC) when vibrations are the energy source.

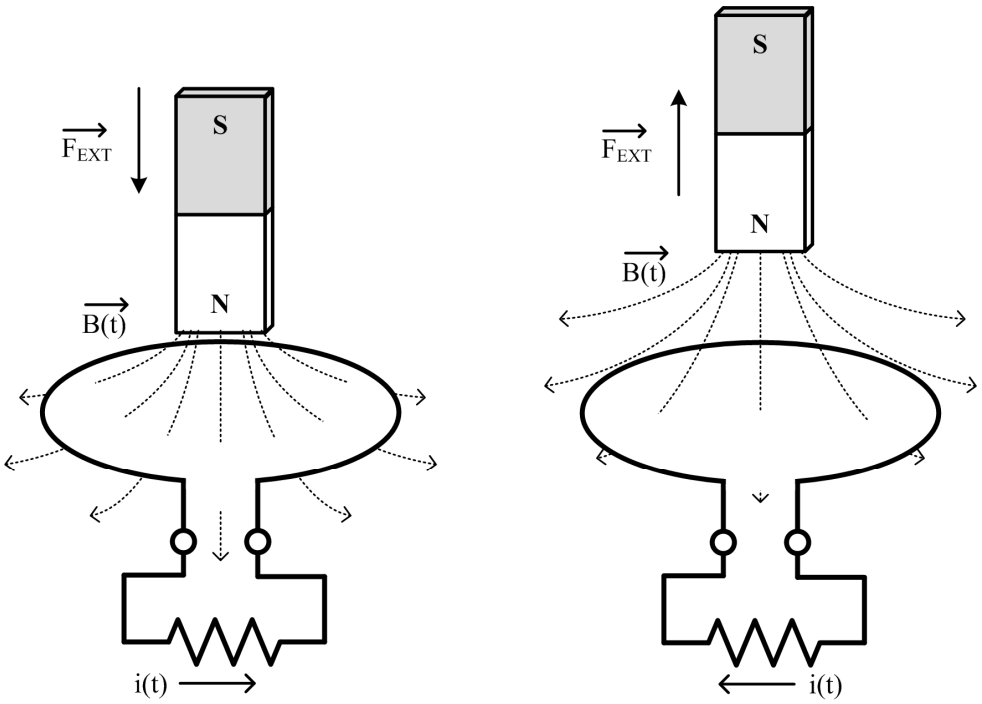

Figure 1.7. Electromagnetic transduction.

Commercial applications use this electromagnetic-conversion mechanism to supply energy for shake-driven flashlights and self-powered watches [48], [118]. Smaller transducers in the sub-cubic centimeter (cm^3) range exploit MEMS technology [119]–

[126]. The restricted dimensions, however, tend to limit the number of coil-turns and the relative velocity between the coil and the magnet, which in turn limit the voltage amplitudes, typically to several tens of millivolts. Because the circuit should be able to rectify the AC to DC and boost the rectified voltage to a higher DC voltage for the rest of the system, this low AC-voltage amplitude may create stringent requirements on the vibration strength and on the harvester circuit. Hence, some of the implemented prototypes have employed an excessive number of coil-turns, transformers, or charge-pump circuits to augment the voltage into a feasible range [123]. However, these additional elements increase the cost, the complexity, and the size of the system [119]. In addition, the limited space leads to major challenges to the integration of permanent magnets and ferromagnetic materials for flux paths [46], [123].

1.4.3. Piezoelectric Transducers

When an external force is applied to a piezoelectric material, mechanical energy is stored as elastic energy in the strained structure, and electrical energy is stored in the electric field of the polarized material induced by the rearranged lattice structure, which shifts the charge balance of the crystal [46], [127]. Piezoelectricity in an ionic non-centrosymmetric crystal, in this case, quartz is illustrated in Figure 1.8 [18], [128].

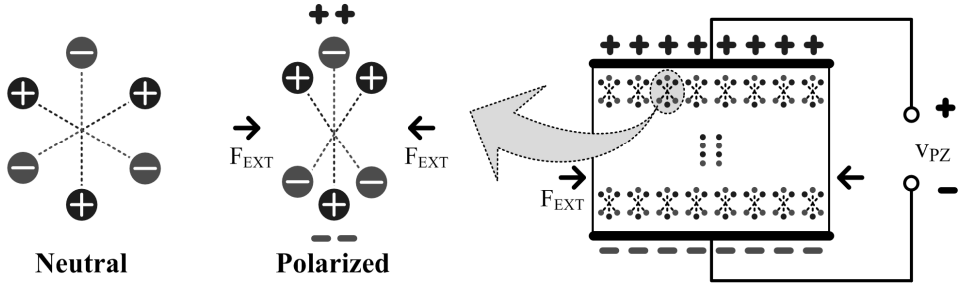

Figure 1.8. Piezoelectric transduction.

Piezoelectric molecules are electrically neutral when they are stress free. However, when an external force induces stress and strain on the material, the molecules

deform, as shown in Figure 1.8, and internal dielectric polarization occurs. Eventually, the polarized molecules induce surface charges that then appear as open-circuit voltage v_{PZ} across the material.

Most miniaturized piezoelectric transducers adopt a cantilever structure, shown in Figure 1.9(a). Piezoelectric materials are deposited on the top and the bottom of a mechanical shim that provides the structural strength of the transducer. As vibration swings the cantilever up and down, the piezoelectric materials experience compressive and tensile forces that generate voltage. The complex models in [129]–[131] can describe the transduction mechanism in detail. However, in essence, the piezoelectric material behaves like a vibration-dependent AC-current source (i_{PZ}) that charges the capacitance (C_{PZ}) across the surface of the material, where parasitic leakage (R_{LEAK}) represents only a slight drain as shown in Fig. 1.9(b) [131], [155]–[159].

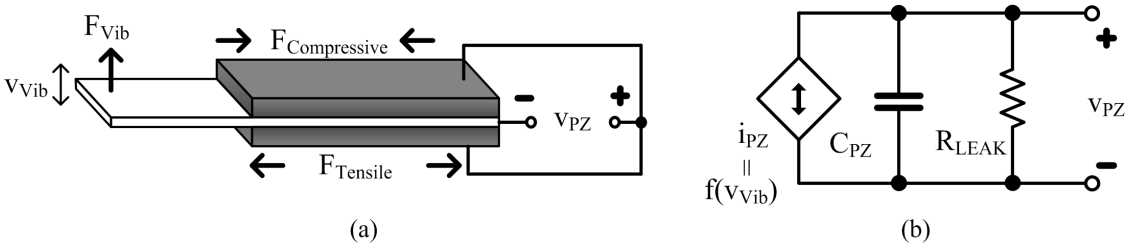

Figure 1.9. (a) A cantilever structure and (b) a simplified equivalent circuit model of piezoelectric transducers.

Because of their availability and simplicity, piezoelectric transducers are used in a variety of (non-harvesting) applications, including fire igniters [132], microphones [133], and vibration sensors [134]. They are widely available in many forms such as single crystals (e.g., quartz), piezoceramic (e.g., lead zirconate titanate, or PZT), thin film (e.g., sputtered zinc oxide), screen-printable thick films using piezoceramic powders, and polymeric materials (e.g., polyvinylidene fluoride, or PVDF) [45]. In addition, unlike other kinetic-energy transduction mechanisms that require special pre-charging circuits or complex structures to convert mechanical energy, the current and the voltage that the

external motion generates can be tapped simply by attaching electrodes to the surfaces. Naturally, these attractive features of piezoelectric materials have sparked life into a multitude of piezoelectric transducers that can harness energy from mechanical impact and vibration.

Impact-coupled piezoelectric transducers draw electrical energy from direct forces that can be readily found in crashing objects and various human motions such as walking [135]–[136]. These devices are typically larger than several cubic centimeters (cm^3) and have been reported to produce relatively large amounts of power, from a few milliwatts to watts [135]–[137]. However, the mechanical shocks may also be problematic for piezoelectric devices because of their brittle nature and the poor efficiency of the energy transfer between the impacting object and the transducer [45]. Hence, as harvesters shrink toward the micro-scale, on which transducers become vulnerable to mechanical shocks, piezoelectric transducers tend to exploit vibrations by matching the resonance frequency of a transducer to the vibration frequency. Many resonant-type piezoelectric transducers employ the cantilever configuration shown in Figure 1.9 (a). The cantilever allows low resonant frequencies, which are favorable for capitalizing on ambient vibrations by increasing the weight of the proof mass or the length of the cantilever through spiral structures [45].

Numerous piezoelectric transducers examined in the literature have taken advantage of MEMS technology to implement micrometer-scale prototypes. The reported power levels for these minuscule devices nominally range from a few microwatts to hundreds of microwatts, depending on their structure, material, and (sometimes unreported) mechanical inputs [44], [138]–[146]. As with the other transduction mechanisms, the performance of piezoelectric transducers degrades as their dimensions decrease because the amount of generated charge is proportional to the strain and surface area, which is severely limited in miniaturized platforms. In addition, the thin-film piezoelectric layers used in μm-scale devices typically suffer from greatly reduced

mechanical-to-electrical coupling efficiency, which directly deteriorates the amount of charge a transducer can produce [45]. The limited charge directly translates into the small amplitude of the AC-output voltage. This small voltage can create challenges on the harvester circuit that interfaces the piezoelectric source with the rest of the system.

1.5. Summary

Various forms of ambient energy can be incorporated into the electrical domain through appropriate transducers. The representative energy sources with their corresponding transduction mechanisms and their reported output power levels are summarized in Table 1.3. Note that despite the effort to narrow down the survey list to sub-cubic centimeter devices, the estimated output power of each harvesting approach exhibits huge variation. These reported power levels are generated often under very distinct experimental setups (even within the same transduction categories), and energy inputs are optimized for each given device configuration. Therefore, when the output power levels are compared with other results, the parameters and conditions under which the experiments were conducted should be carefully examined.

While the energy in ambient light, heat, and RF radiation could definitely contribute to extending the life of miniaturized electronic systems, the limited availability of these energy sources in the surroundings can easily restrict the amount of extractable energy. By contrast, kinetic energy from motion or vibrations is a more versatile and ubiquitous energy source. Although the determination of the optimal kinetic-energy transducer for general applications may be a source of debate, many researchers have been investigating piezoelectric transducers as a promising energy solution for small-scale electronic systems. The enthusiasm generated for such research stems, in part, from the simple mechanical requirements and the wide accessibility of the material. Perhaps more importantly, piezoelectric-energy harvesting, as several comparative research results corroborate, seems to outperform the other two mechanisms in power density

[45]–[47], [105], [147]. In fact, even though the piezoelectric-coupling factors are low and the displacement is restricted to micro-scale devices, the reported power densities of piezoelectric transducers are quite encouraging, as presented in Figure 1.10 and Table 1.4.

Table 1.3. Summary of ambient energy sources.

Energy Sources	Transduction Mechanism	Estimated Power [*1]	Remarks	Limitations
Light	Photovoltaic Effect	5μW/cm^2 – 20mW/cm^2	• High power density under direct lighting • DC-voltage generation	• Light availability for indoor and mobile applications
Heat	Seebeck Effect	5μW/cm^2/°C – 1mW/cm^2/°C	• Applicability as a thermal management device for portable electronics • DC-voltage generation	• Temperature gradients for small-scale applications
RF Radiation	Inductive /Capacitive Coupling	< 2 μW/cm^2	• High-frequency AC-voltage generation • AC–DC conversion required	• Availability of significant ambient RF power
Motion / Vibration	Electrostatic	4μW/cm^3 – 110μW/cm^3	• Pre-charging required	• Variable capacitance range • Maximum allowable voltage
	Electro-magnetic	5μW/cm^3 – 2208μW/cm^3	• Low-frequency AC-voltage generation • AC–DC conversion required	• Number of coil-turns • Reduced velocity between the coil and the magnet • Integration of ferromagnetic materials
	Piezoelectric	16μW/cm^3 – 3510μW/cm^3	• Low-frequency AC-voltage generation • AC–DC conversion required • Capacitive source	• Strain (deformation) range • Surface area of the piezoelectric material • Weak mechanical-to-electrical coupling

[*1] Surveyed from the measured data of sub-cubic centimeter devices in [44]–[49], [51], [53]–[54], [71]–[73], [80], [84], [90]–[92], [105]–[126], and [135]–[149]. For kinetic harvesters, devices with 500Hz or lower resonant frequency were considered in the list.

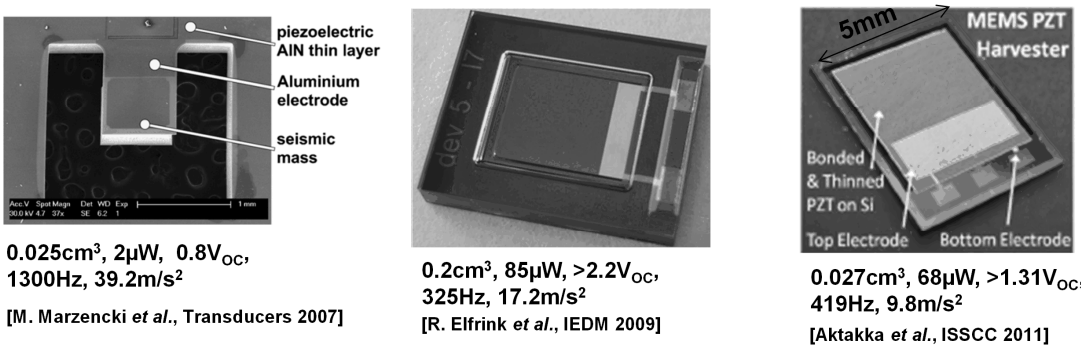

$0.025cm^3$, 2μW, $0.8V_{OC}$, 1300Hz, $39.2m/s^2$
[M. Marzencki *et al.*, Transducers 2007]

$0.2cm^3$, 85μW, $>2.2V_{OC}$, 325Hz, $17.2m/s^2$
[R. Elfrink *et al.*, IEDM 2009]

$0.027cm^3$, 68μW, $>1.31V_{OC}$, 419Hz, $9.8m/s^2$
[Aktakka *et al.*, ISSCC 2011]

Figure 1.10. Representative MEMS piezoelectric transducers in the literature.

Table 1.4. State-of-the-art MEMS piezoelectric transducers.

Year	$P_{OUT(MAX)}$ [μW]	Acceleration [m/s^2]	f_{VIB} [Hz]	Reference
2001	2	9.8	80	[139]
2005	1	107	13900	[146]
2006	2.16	9.8	608	[141]
2007	40	23	1800	[145]
2007	2	39.2	1300	[142]
2008	1.29	19.6	214	[144]
2008	60	19.6	572	[150]
2009	17	6.3	353	[151]
	85	17.15	325	
2010	0.15	0.98	263	[152]
	10.2	19.6	252	
2011	1.8	0.98	429	[153]
	68	9.8	419	

Nevertheless, to produce meaningful output power levels, the micro-scale transducers tend to demand stronger (i.e., higher acceleration rate) and faster (i.e., higher vibration frequency) vibrations than the ambient sources typically provide. This trend is revealed in Figure 1.11 by overlaying the data from Tables 1.2 and 1.4. Therefore, despite the abundance of ambient vibrations and numerous advancements in the technology of these devices, the power and the voltage that small-scale transducers produce under ambient vibrations may not be very high. Thus, research groups worldwide are investigating not only to improve the performance of micro-scale

transducers but also to overcome the limitations of small transducers through innovative circuit and system design.

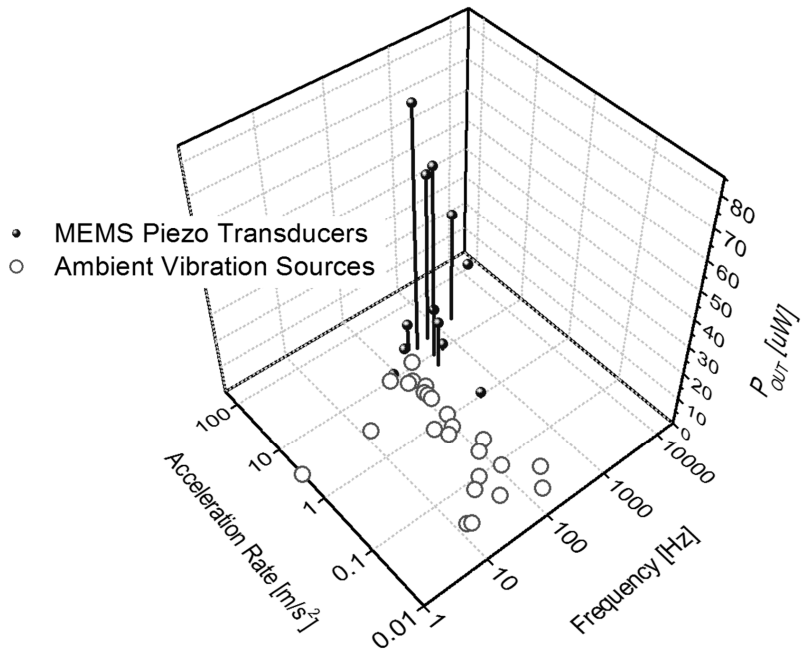

Figure 1.11. Acceleration rates and frequencies of ambient vibration versus the testing conditions of MEMS piezoelectric transducers.

CHAPTER 2

BRIDGE-BASED PIEZOELECTRIC HARVESTERS

Piezoelectric transducers harvest ambient kinetic-energy by converting mechanical energy in motion into the electrical domain. The internal charge configuration of piezoelectric transducers changes in response to the mechanical stimulations and generates AC voltage across the capacitance that their opposing surfaces constitute. Figure 2.1 shows a general architecture for piezoelectric-energy harvesting systems. The harvester circuit must extract energy from the changing voltage of the piezoelectric capacitor and deposit the charge into an intermediate energy reservoir that can supply DC power to electrical loads or ensuing DC-DC converters and linear low-dropout (LDO) regulators on demand. Intermediate energy storage devices such as rechargeable batteries or large capacitors are unfavorable in terms of system size, but necessary because they enable accumulation of the sporadic and low energy in the ambient movements and allow burst energy transfer (i.e., high power) to the subsequent stages of the system [154].

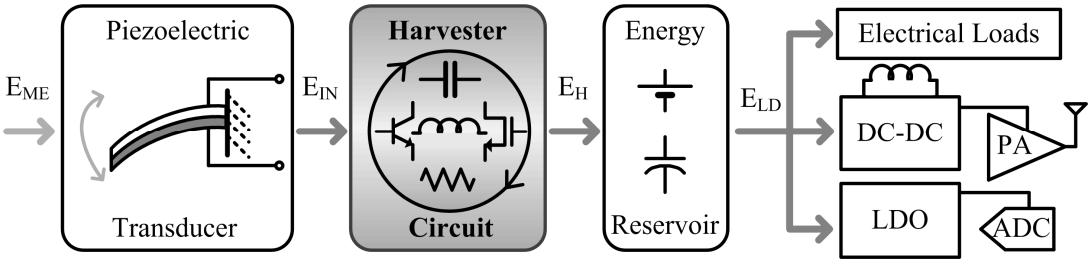

Figure 2.1. General system architecture of piezoelectric-energy harvesters.

While the piezoelectric transducers produce AC current and voltage from vibrations, the electrical loads typically require DC voltage at their power supply terminals. Hence, conventional piezoelectric harvesters usually employ AC-DC converting bridge rectifiers in the system. As the dimensions of piezoelectric transducers shrink, however, bridge-based rectifiers face challenges regarding input voltage amplitudes and the net energy

gain from harvesting. Therefore, research has been carried out to alleviate the fundamental limitations associated with bridge rectifiers and to enhance the harvesting performance by improving the rectifier itself along with its conditioning circuits. This chapter will review the operation of the reported bridge-rectifier piezoelectric harvester systems and discuss their effectiveness and challenges.

2.1. Diode-bridge Rectifiers

When an external force F_{EXT} moves a piezoelectric cantilever, as shown in Figure 2.2(a), the mechanical energy of the system consists of a kinetic portion in the movement and an elastic portion in the displacement as in a spring-mass system. One simplified approach to model this system is to employ a series inductance L_m, capacitance $C_{1/k}$, and resistance R_d to embody the lumped mass, stiffness, and mechanical damping, respectively. In addition to these circuit elements, the equivalent circuit in Figure 2.2(b) includes a voltage source (v_{F_EXT}), which results in a current (i_{VEL}) proportional to the velocity of the vibrating cantilever to represent the external force that drives the cantilever to vibrate [131], [145]. An ideal transformer whose turns-ratio is $1/\Gamma$ can symbolize the piezoelectric effect that outputs the current i_{PZ} proportional to the velocity of the cantilever.

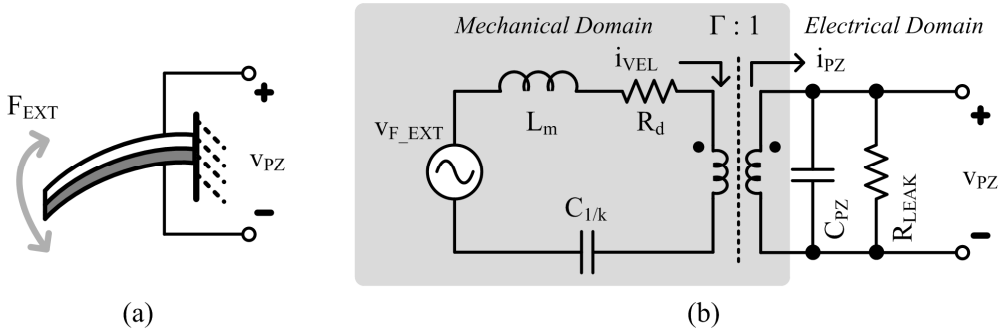

Figure 2.2. (a) A piezoelectric cantilever and (b) its equivalent circuit model.

To further simplify, the mechanical and the piezoelectric transformation parts can be modeled as a dependent current source, as in Figure 1.9, whose output value is set

primarily by the velocity of the transducer [155]–[159]. Electrical loading of the transducer can affect the value of i_{PZ} if the loading becomes significant enough to slow down the cantilever movement considerably. However, for most miniaturized piezoelectric transducers, the electromechanical coupling is not strong enough to allow the electrical loading to substantially change the mechanical movement.

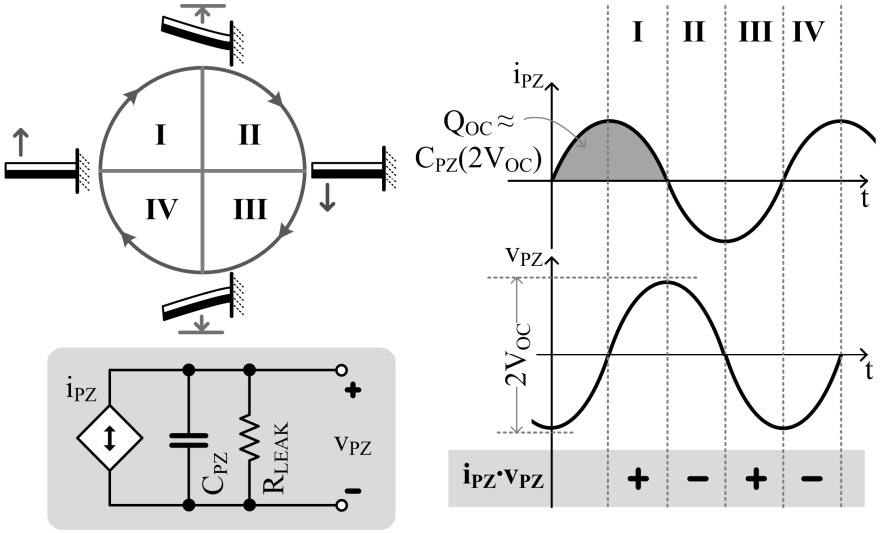

Figure 2.3. Open-circuited piezoelectric transducer operations.

Since the leakage resistance R_{LEAK} is typically very large, the input impedance of a piezoelectric transducer alone is practically reactive. Therefore, when the transducer is open circuited, the device does not produce any net electrical energy from vibrations except for the negligible losses in R_{LEAK}. Figure 2.3 demonstrates the energy flow of an open-circuited piezoelectric transducer in vibrations. For instance, when the device is moving upward in the Phase I of the vibration cycle, the product of i_{PZ} and v_{PZ} is positive. This means that the transducer is generating electrical energy that is accumulated in the capacitor voltage v_{PZ}. However, after the positive peak, when the transducer starts to move downward in Phase II, v_{PZ} is still positive but i_{PZ} is not. In other words, the vibration is discharging C_{PZ}, and the electrical energy is now going back to the

mechanical domain. Similarly, the vibration produces and withdraws electrical energy in Phase III and IV, respectively, leaving no net energy generated from the vibration.

To extract and channel the net power that a piezoelectric transducer generates into an intermediate DC storage device, harvesters often employ full-wave diode-bridge rectifiers [155]–[159]. These full-wave rectifier circuits, as exemplified in Figure 2.4, steer charge to the output only when i_{PZ} charges C_{PZ} above the barrier voltage that two conducting diodes ($2V_D$) and the output capacitor C_{RECT} (V_{RECT}) produce. Acquiring the maximum charge during the conduction phase T_{COND} typically requires choosing C_{RECT} that is much larger than C_{PZ}. As a result, V_{RECT} remains virtually unchanged within a vibration cycle T_{VIB}, and the input voltage v_{PZ} is practically clamped to the aggregate sum of the two diode voltage drop $2V_D$ and the rectifier output voltage V_{RECT} as the diode is conducting current.

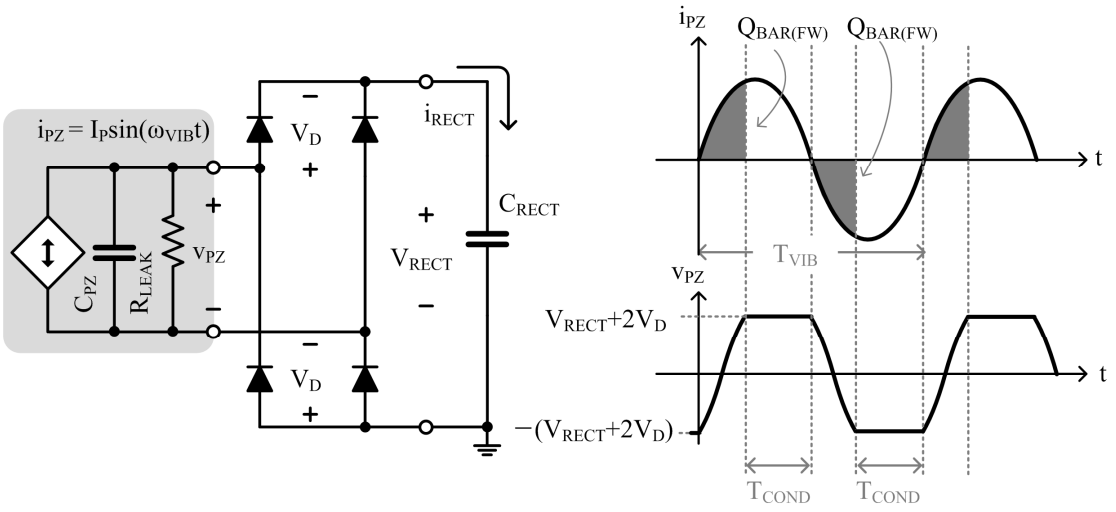

Figure 2.4. A full-wave diode-bridge rectifier.

Note that after each positive and negative-conduction phase (T_{COND}), the vibration has to bring down or up the piezoelectric voltage to overcome the barrier voltage. The amount of charge $Q_{BAR(FW)}$ used in this process is

$$Q_{BAR(FW)} = C_{PZ}\left[\left(V_{RECT} + 2V_D\right) + \left(V_{RECT} + 2V_D\right)\right] = 2C_{PZ}\left(V_{RECT} + 2V_D\right). \qquad (2.1)$$

Since this charge does not flow to the output of the rectifier, the amount of charge conduct to C_{RECT} per every half cycle is

$$Q_{RECT(FW)} = Q_{OC} - Q_{BAR(FW)} = 2C_{PZ}\left[V_{OC} - \left(V_{RECT} + 2V_D\right)\right], \tag{2.2}$$

where Q_{OC} represents the amount of charge that the piezoelectric transducer generates from the vibration, which swings v_{PZ} from $-V_{OC}$ to $+V_{OC}$ under an open-circuited condition (Figure 2.3). Therefore, assuming that C_{RECT} maintains almost constant voltage at V_{RECT}, the amount of energy a full-wave diode-bridge rectifier can harness per cycle is

$$E_{RECT(FW)} = 2Q_{RECT(FW)}V_{RECT} = 4C_{PZ}\left[V_{OC} - 2V_D - V_{RECT}\right]V_{RECT}, \tag{2.3}$$

which peaks at $C_{PZ}(V_{OC} - 2V_D)^2$ when V_{RECT} is $0.5(V_{OC} - 2V_D)$.

Because the leakage in piezoelectric transducers is typically negligible (i.e., R_{LEAK} is large) and C_{PZ} is a reactive component (which does not consume power), most of the energy i_{PZ} carries through the diodes reaches the output, except for the portion the diodes dissipate. Thus, the full-wave diode-bridge rectifier efficiency $\eta_{RECT(FW)}$, the ratio of the rectified output energy per cycle $E_{RECT(FW)}$ to the input energy per cycle $E_{IN(FW)}$, is determined by the diode voltage drop V_D, as the following equation illustrates.

$$\eta_{RECT(FW)} = \frac{E_{RECT(FW)}}{E_{IN(FW)}} = \frac{2\int_{T_{COND}} i_{RECT}(t)V_{RECT}\,dt}{2\int_{T_{COND}} i_{PZ}(t)\left(V_{RECT} + 2V_D\right)dt} \approx \frac{V_{RECT}}{V_{RECT} + 2V_D}. \tag{2.4}$$

On the other hand, the half-wave diode-bridge rectifier with a diode clamp in Figure 2.5 can also harness the energy piezoelectric devices produce [160]–[165]. The circuit is also known as a voltage doubler, which can readily be recognized if the piezoelectric transducer circuit model is presented in a Thévenin equivalent circuit (i.e., an AC voltage source with a series C_{PZ}). The generated energy flows to the output when i_{PZ} charges C_{PZ} above $V_{RECT}+V_D$, the barrier voltage that the output and the diode D_{RECT} establish. After the positive conduction phase T_{COND}, the vibration brings down the

piezoelectric voltage, resembling the full-wave diode-bridge operation. However, instead of going all the way down to $-(V_{RECT}+2V_D)$, v_{PZ} is clamped by the diode D_{CLP} at $-V_D$ until i_{PZ} becomes positive. After that T_{CLAMP} duration, the vibration charges C_{PZ} from $-V_D$ to $V_{RECT}+V_D$ to start driving the generated current to the output.

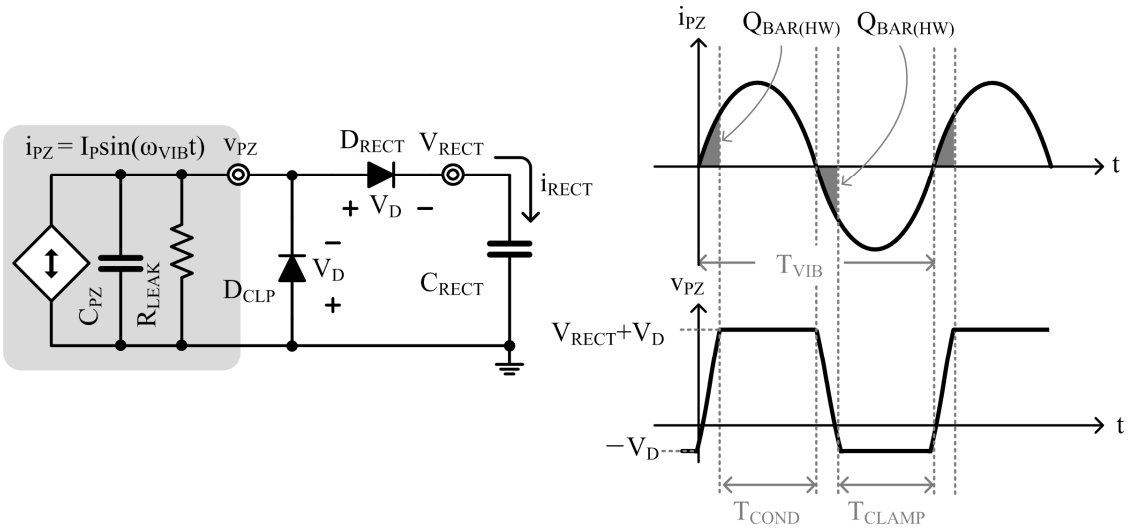

Figure 2.5. A half-wave diode-bridge rectifier with a diode clamp.

The amount of charge used to overcome the barrier voltage for this half-wave case is

$$Q_{BAR(HW)} = C_{PZ}\left[\left(V_{RECT}+V_D\right)-\left(-V_D\right)\right] = C_{PZ}\left(V_{RECT}+2V_D\right), \tag{2.5}$$

as v_{PZ} changes from $-V_D$ to $V_{RECT}+V_D$. Hence, the output receives

$$Q_{RECT(HW)} = Q_{OC} - Q_{BAR(HW)} = C_{PZ}\left[2V_{OC}-\left(V_{RECT}+2V_D\right)\right] \tag{2.6}$$

per vibration cycle. Because only the charge generated during the half cycle contributes to the harvested energy, the half-wave diode-bridge rectifier with a diode clamp outputs

$$E_{RECT(HW)} = Q_{RECT(HW)}V_{RECT} = C_{PZ}\left[2V_{OC}-2V_D-V_{RECT}\right]V_{RECT}, \tag{2.7}$$

assuming that C_{RECT} holds the output voltage at V_{RECT} during the conduction phase. Note that the peak value of this half-wave rectifier output energy is higher at $C_{PZ}(V_{OC}-V_D)^2$

than it is at the full-wave counterpart. This is because, although this rectifier utilizes only half of the total cycle, D_{CLP} prevents v_{PZ} from dipping too much toward the negative voltage, and consequently saves the charge and time wasted in overcoming the barrier voltage.

Analogous to the full-wave case, the efficiency of this modified half-wave rectifier $\eta_{RECT(HW)}$ is the ratio of the rectified output energy per cycle $E_{RECT(HW)}$ to the input energy per cycle $E_{IN(HW)}$. While the output receives i_{RECT} only during T_{COND}, the input current i_{PZ} flows into and out of the v_{PZ} terminal during T_{COND} and T_{CLAMP}, respectively. Even though the current flows outward from the circuit during T_{CLAMP}, the energy consumed during the phase contributes to $E_{IN(HW)}$ because the potential is negative at $-V_D$. The efficiency expression reduces to a function of V_{RECT} and V_D as shown in (2.8) because i_{RECT} is the same as i_{PZ} in T_{COND}, and the total charges i_{PZ} carry during T_{COND} and T_{CLAMP} are the same except that they are the opposite polarity. Despite the differences in the operations, the efficiency of the modified half-wave case results in the same expression as the full-wave counterpart in (2.4).

$$\eta_{RECT(HW)} = \frac{E_{RECT(HW)}}{E_{IN(HW)}} = \frac{\int_{T_{COND}} i_{RECT}(t) V_{RECT} dt}{\int_{T_{COND}} i_{PZ}(t)(V_{RECT} + V_D) dt + \int_{T_{CLAMP}} i_{PZ}(t)(-V_D) dt} = \frac{V_{RECT} \int_{T_{COND}} i_{RECT}(t) dt}{(V_{RECT} + V_D) \int_{T_{COND}} i_{PZ}(t) dt + (-V_D) \int_{T_{CLAMP}} i_{PZ}(t) dt} \approx \frac{V_{RECT}}{V_{RECT} + 2V_D} \quad . (2.8)$$

For both of the diode-bridge rectifiers, the lower diode voltage V_D improves the rectifier performance by increasing the efficiency and the output energy as (2.3), (2.4), (2.7), and (2.8) corroborate. However, the diode voltage in integrated circuits (IC) can exhibit 0.5 – 1 V depending on the implementation, threshold voltage of transistors,

temperatures, and current flowing through the diode. Figure 2.6 tabulates some possible diode options for diode-bridge rectifiers.

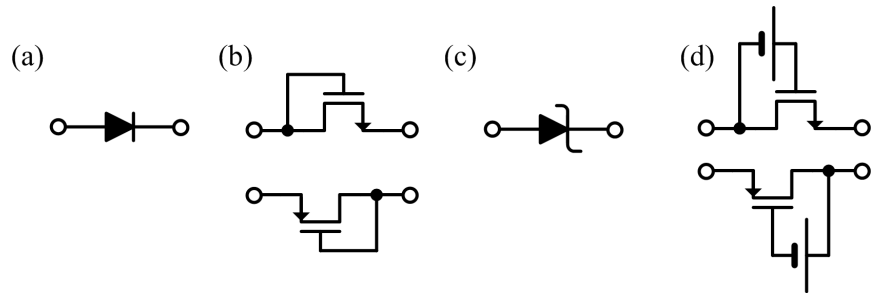

Figure 2.6. (a) PN-junction diode, (b) diode-connected transistors, (c) Schottky diode, and (d) threshold-canceled transistors.

Considering the low-voltage output of small-scale piezoelectric transducers, the diode voltage of the PN-junction diode, the diode-connected transistor, and the on-chip Schottky diode [166]–[167] in Figures 2.6(a), (b), and (c) can be problematically high because they would not only deteriorate the efficiency but also raise the barrier voltage, ultimately reducing the output energy. One way of reducing V_D, shown in Figure 2.6(d), is to superimpose a bias voltage V_B onto the gate of a transistor, which effectively cancels the threshold voltage of the transistor. Various techniques exploiting an external battery [168]–[169], an internal battery (i.e., current-conducting diode-connected transistor) [4], [170], and floating gates [93], [171] can reduce the V_D, but they demand extra power and circuits for V_B generation. More importantly, they may incur a high off-state leakage current since the transistors are on the verge of conduction in their off condition.

2.2. Switch-bridge Rectifiers

Diodes are the most convenient approach to establishing a unidirectional current flow because they do not require extra control signals. However, the voltage drop across the diode increases the losses and the barrier voltage, both of which would be detrimental for low-voltage and current applications. Bridge-rectifiers can employ transistors, not diodes, as switches to replace the diode voltage with its ohmic counterpart, which can exhibit on

the order of millivolts for low current applications. Because of the similar reasons for efficiency, switching converters generally use switches rather than diodes. The system, however, requires additional intelligence and control circuits to turn the switch on or off appropriately. It would be both convenient and efficient if the system could use already existing information to control the switches as happens with switching converters. Unfortunately, for energy harvesting applications that deal with unpredictable inputs, the switches often need dedicated control circuits to realize the ideal diode features. One widely adopted technique [158]–[163], [172]–[176] is to use a comparator to sense the voltage across a switch and control the state of the switch. Figure 2.7 presents this self-synchronizing switch (also known as active diode), which uses N-type metal-oxide-semiconductor (NMOS) and P-type MOS (PMOS) transistors.

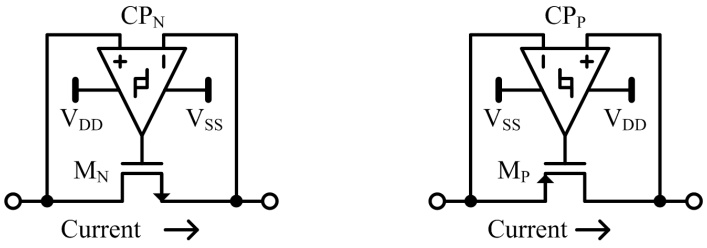

Figure 2.7. Self-synchronizing switches implementing diodes functionality.

The comparator CP_N monitors the drain and source voltages of M_N to apply V_{DD} or V_{SS} to turn M_N on or off when the drain voltage is higher or lower than the source counterpart, respectively. Likewise, CP_P observes the source and drain voltages of M_P and applies V_{SS} and V_{DD} to allow or block the current conduction when the source potential is higher or lower than that of the drain. Because these active diodes do not demand additional control signals from the system, they can easily replace the diodes in the full-wave and the modified half-wave diode-bridge rectifiers introduced in Figures 2.4 and 2.5 to lower the V_D and the barrier voltage [158–163], [172]–[176]. The conduction losses of the switch-bridge rectifier will, therefore, be less than those in the

diode-bridge case; nevertheless, because the MOS switches feature parasitic gate capacitance, which consumes energy, the switch sizes must be carefully designed to optimize the conduction and the gate-driving losses. The comparators also incur losses that did not exist in diode-bridge rectifiers. Hence, if power benefits are to be achieved, these additional power losses must be minimized to become lower than the savings in conduction losses.

The comparators in the active diodes need additional design considerations beyond just minimizing the quiescent power. For example, the comparators should be fast enough to engage and disengage the switches quickly. If the propagation delay before the switch turn-on is too long, the current may conduct through the body-diodes of the transistors and lose the conduction energy. On the other hand, if the delay for turning-off is too long, the current will flow in the opposite direction and deteriorate the energy transfer performance [172], [177]–[178]. Moreover, because the comparators need to be functional for the switch-bridge rectifiers to channel the energy to a storage element at its output, the headroom of the comparators often sets (or needs to be set at) the input threshold of a switch-bridge rectifier [175]–[176].

Some switch-bridge rectifiers employ an inverter as the comparator [164], [179]. Since the inverter would consume no static power without any complex control circuits, the efficiency of the rectifier can be very high, as high as 98% [164]. However, inverter-based switches do not function like a diode since the inverter compares the input voltage of the switch to the threshold of the inverter, not the output voltage of the switch. This means that when a PMOS switch is driven by an inverter as a diode in a rectifier, the switch will turn on when the input voltage surpasses the threshold of the inverter and charge the output capacitor. However, when the input voltage falls after its peak, the switch will allow the reverse current to discharge the output capacitor until the input voltage crosses the threshold of the inverter. Therefore, despite its high efficiency, the

inverter-based switch-bridge rectifier may not be optimal for piezoelectric-energy harvesting applications.

Another popular approach to implementing a switch-bridge rectifier is to cross-couple two MOS transistors so that the input voltage can drive the switches directly [158]–[159], [172]–[176], [180]–[181]. Figure 2.8 shows NMOS and PMOS cross-coupled transistors in parallel with their diode counterparts. When v_{PZ} is positive and higher than the threshold of the MOS transistors, M_{N2} will turn on (and M_{N1} will be off) and short v_{PZ}^- to V_{RECT}^-. On the other hand, if v_{PZ} is negative and its amplitude is higher than the threshold of the MOS transistors, M_{N1} will turn on to connect v_{PZ}^+ to V_{RECT}^-. This NMOS cross-coupled pair compares v_{PZ}^+ and v_{PZ}^- to output the lower one between two for V_{RECT}^- analogous to two parallel diodes sharing their anodes as the output. The PMOS cross-coupled pair selects the higher voltage terminal between v_{PZ}^+ and v_{PZ}^- for V_{RECT}^+, which is also similar to the two parallel diodes sharing their cathodes as the output. Furthermore, because the cross-coupled pairs are MOS transistors, the current flowing through the switches generates much lower voltage and therefore lower conduction losses than occur in the diode case.

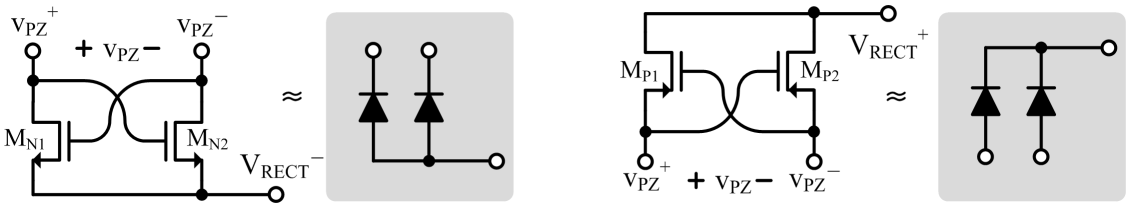

Figure 2.8. NMOS and PMOS cross-coupled transistors.

Cross-coupled MOS transistors are simple and efficient as they do not require comparators or other control circuits to implement a switch-bridge. Nonetheless, some limitations exist. First, the input voltage amplitude (i.e., $|v_{PZ}|$ in Figure 2.8) should be high enough to drive the MOS transistors in their triode region. In other words, an input threshold exists because of the threshold voltage in the MOS devices. Besides, since they

turn on and off by comparing the input voltage to their threshold voltage, not to the output counterpart, a reverse current will ensue after the input's peak, and the output voltage will fall with the input unlike the diodes, which hold the peak voltage. Therefore, in practice, the switch-bridge rectifiers employ cross-coupled MOS transistors in conjunction with diodes such as diode-connected transistors and active diodes [158]–[159], [172]–[176]. Figure 2.9 shows two representative examples of switch-bridge rectifiers in the literature.

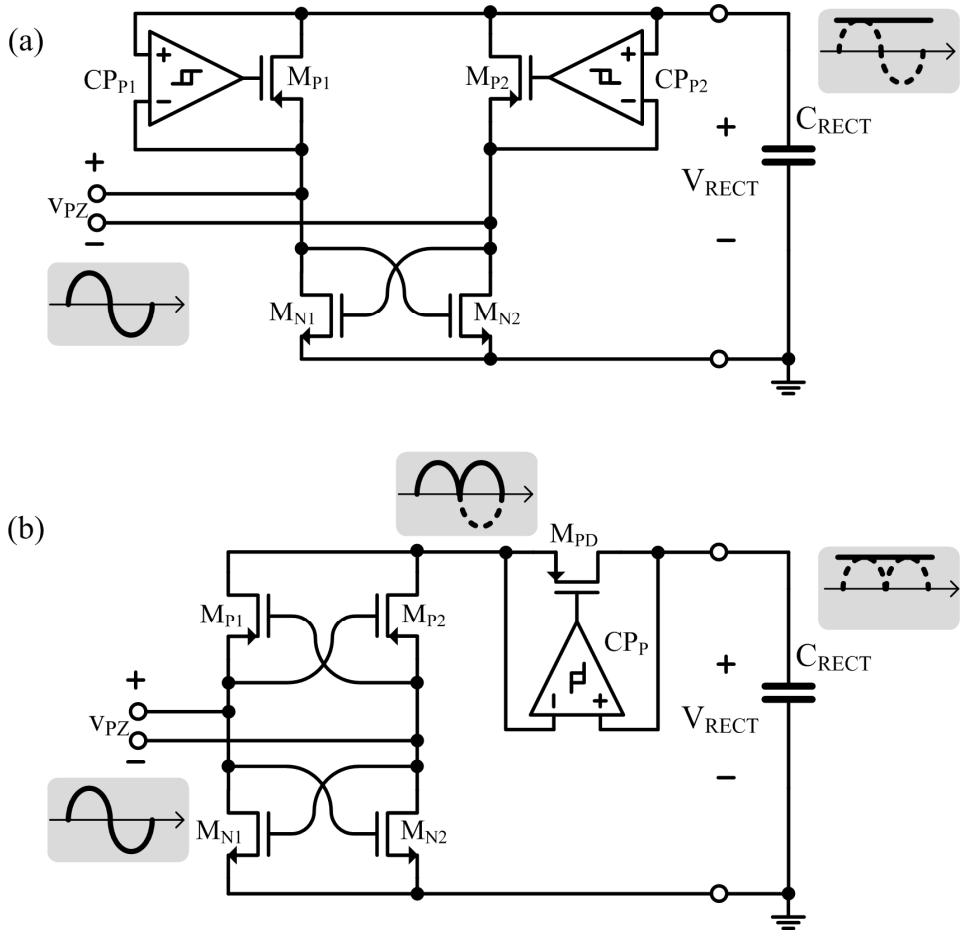

Figure 2.9. (a) Cross-coupled NMOS with two active diodes, (b) cross-coupled PMOS and NMOS with one active diode.

In Figure 2.9(a), when v_{PZ} rises above the threshold voltage of the NMOS transistor, M_{N2} engages to short the bottom terminal of v_{PZ} to the ground. The rectifier

then transfers the energy when CP_1 senses that v_{PZ} is higher than V_{RECT} and engages M_{P1}. The negative half cycle will resemble this positive half operation by turning M_{N1} when v_{PZ} falls below the threshold voltage of NMOS and by supplying current when CP_2 detects that $-v_{PZ}$ is higher than V_{RECT}. On the other hand, the cross-coupled PMOS and NMOS pairs in Figure 2.9(b) first convert the negative input voltage to a positive one. Then the active diode, consisting of M_{PD} and CP_P, conducts the current when the converted voltage is higher than the output voltage.

While various circuit techniques for improving the performance (e.g., speed, headroom, input common-mode range, etc.) of the active-diode comparators exist, usually the main objective of the implementations is to improve the overall power transfer efficiency. As a matter of fact, the reported efficiencies can approach near 100% when the amount of power delivered is much higher than the power consumed by the comparators and when the decreased V_D is negligibly lower than V_{RECT}. However, a fundamental limitation in the rectifiers is that v_{PZ} must exceed at least the rectifier output voltage to extract energy from the piezoelectric transducer. In other words, even if V_D is reduced to zero V and the active-diode comparators consume no power at all, the rectifiers will not be able to harvest any energy when v_{PZ}'s open-circuit peak voltage V_{OC}, as in Figure 2.3, is below V_{RECT}, which can easily happen under weak vibrations with small transducers that suffer from a low electromechanical-coupling factor.

2.3. Conditioning Rectified Outputs

As reviewed in previous chapters bridge rectifiers are simple and convenient, and therefore widely adopted for piezoelectric harvesting systems. The active diodes can raise the efficiency and lower the input barrier voltage by reducing the diode voltage V_D. However, because bridge rectifiers cannot eliminate the threshold originating from the output voltage V_{RECT}, piezoelectric transducers generating lower voltage than V_{RECT} will not be able to produce any real power from vibrations. A way to alleviate this input

threshold problem is to intentionally lower the rectifier output voltage than the v_{PZ} voltage so that the energy can flow through the diodes (including active ones). The lower V_{RECT} will result in a lower threshold and more charge flowing through the rectifier. However, this lower V_{RECT} does not guarantee more harvested energy because the amount of energy is the product of the charge and voltage. Likewise, V_{RECT} that is high, but slightly below the open-circuited voltage of the piezoelectric voltage $V_{OC,}$ will not provide the maximum power condition because the charge flowing through the rectifier will be (too) small. It should be noted that the efficiency of this high V_{RECT} condition can be high, as (2.4) and (2.8) corroborate, but the efficiency is not as important as the absolute amount of energy harnessed. Therefore, piezoelectric harvesters using bridge rectifiers need to condition the output of the rectifier to ensure that the maximum energy is harvested.

The energy flowing through a rectifier E_{RECT} is a parabolic function of V_{RECT} that exhibits one optimal point between zero V and the open-circuited voltage V_{OC} ($2V_{OC}$ for the modified half-wave rectifiers) of a piezoelectric transducer under a given vibration. This condition has been derived in (2.3) and (2.7) for full-wave and modified half-wave diode-bridge rectifiers, respectively, and Figure 2.10 shows the relations by assuming 10-nF C_{PZ}, 2-V V_{OC}, and 0.1-V V_D as an example. Hence, to output positive energy, V_{RECT} should remain under 1.8 V and 3.8 V, and to maximize the energy transfer, the harvesting system must regulate V_{RECT} at 0.9 V and 1.9 V, respectively, for full-wave and modified half-wave cases. Note that the modified half-wave rectifier exhibits a wider V_{RECT} range and a higher peak E_{RECT} value than the full-wave rectifier because of the clamping diode explained in section 2.1. Since the optimal output voltage of rectifiers change with V_{OC} and V_D (i.e., $0.5V_{OC}-V_D$ or $V_{OC}-V_D$), both of which vary with external vibrations, bridge-rectifier harvesters need to adjust V_{RECT} in real-time to collect as much energy as possible for a given mechanical input.

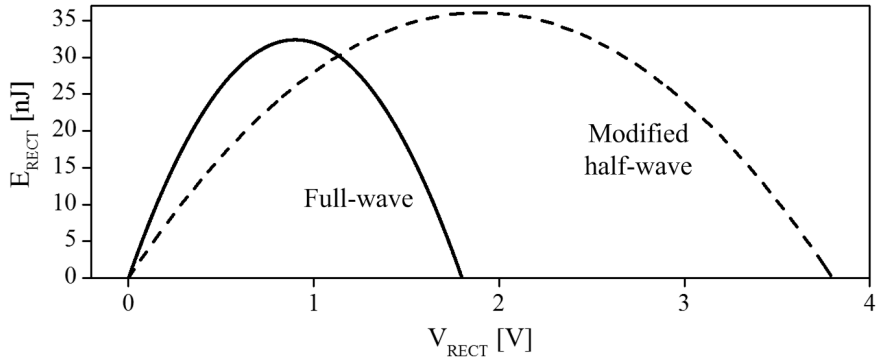

Figure 2.10. Theoretical output energy of bridge rectifiers.

Ottman *et al*. in [155] implemented the rectifier-output conditioning system by connecting the rectifier output to a DC-DC switching converter whose output is connected to a battery. Figure 2.11 illustrates the schematic of the approach. To find the optimal V_{RECT}, the system first senses the battery-charging current i_{CHARGE} for a given vibration input. Then, the controller, for example, increases the duty-cycle (d) of the switching DC-DC converter to see whether i_{CHARGE} has been increased or decreased. If the new current value is higher than the previous one, the controller keeps increasing d until i_{CHARGE} starts to decrease. This hill-climbing approach, which is also widely adopted in various maximum-power-point-tracking techniques (MPPT) for other types of energy harvesting, is a simple and effective way to find the optimal rectifier output voltage for a given vibration input. However, because it requires an iterative process that can be slow and power-consuming, the technique seems to be applicable only for slow, periodic, and strong vibration energy harvesting. In [156], the authors found an efficient approach that employs a fixed duty-cycle switching DC-DC converter operating in a discontinuous-conduction-mode (DCM). The new system eliminated the iterative procedure for MPPT of variable mechanical inputs, but needs a very high input voltage (e.g., 40-100 V) to satisfy the requirements of the harvester.

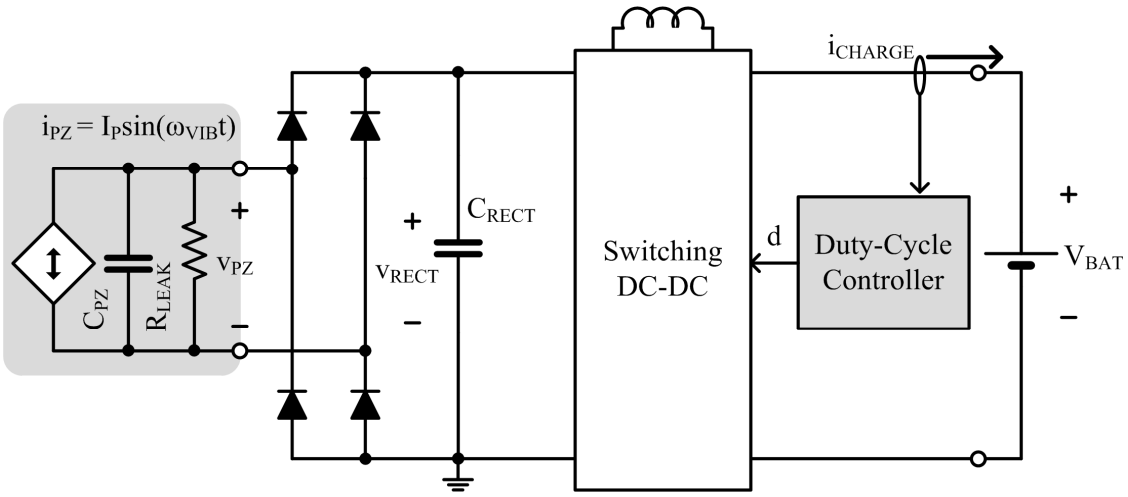

Figure 2.11. Maximum output power conditioning by sensing the charging current.

Another output conditioning technique to maximize the harvested power is presented in [157]–[158]. Figure 2.12 shows the proposed system. The technique also utilizes a switching DC-DC converter to regulate v_{RECT} around an optimal point, but this system directly senses the input voltage amplitude to find the optimal reference voltage for v_{RECT}. To do this, the vibration-tracking unit in Figure 2.12 needs the open-circuited voltage (V_{OC}) of the piezoelectric transducer for a given vibration. However, since v_{PZ} will be clamped to v_{RECT} when the rectifier and the ensuing DC-DC converter drive currents to a load, the system periodically opens the switch S_{DC} to disconnect the DC-DC converter and capture V_{OC} to establish the optimal reference voltage. Then, the tracking control monitors v_{RECT} with a hysteretic comparator to turn on or off S_{DC}, to start or stop draining the charge from C_{RECT}, when v_{RECT} either rises above or falls below the reference window. While the vibration tracking unit of this approach requires simpler circuits and lower power than does the hill-climbing approach in [155], the MPPT scheme will be effective only for periodic vibrations whose amplitude changes very slowly. In other words, the harvester will not be able to optimally extract energy from the practical ambient vibrations whose amplitude may change cycle by cycle. By design, the proposed system cannot harvest energy during the V_{OC}-sampling process; hence, the

duty-cycle of the tracking unit should be kept as low as possible to harvest as much portion of vibration energy as possible. However, because of this exclusive operation of the main harvesting block and the tracking unit, the system cannot update the reference every cycle.

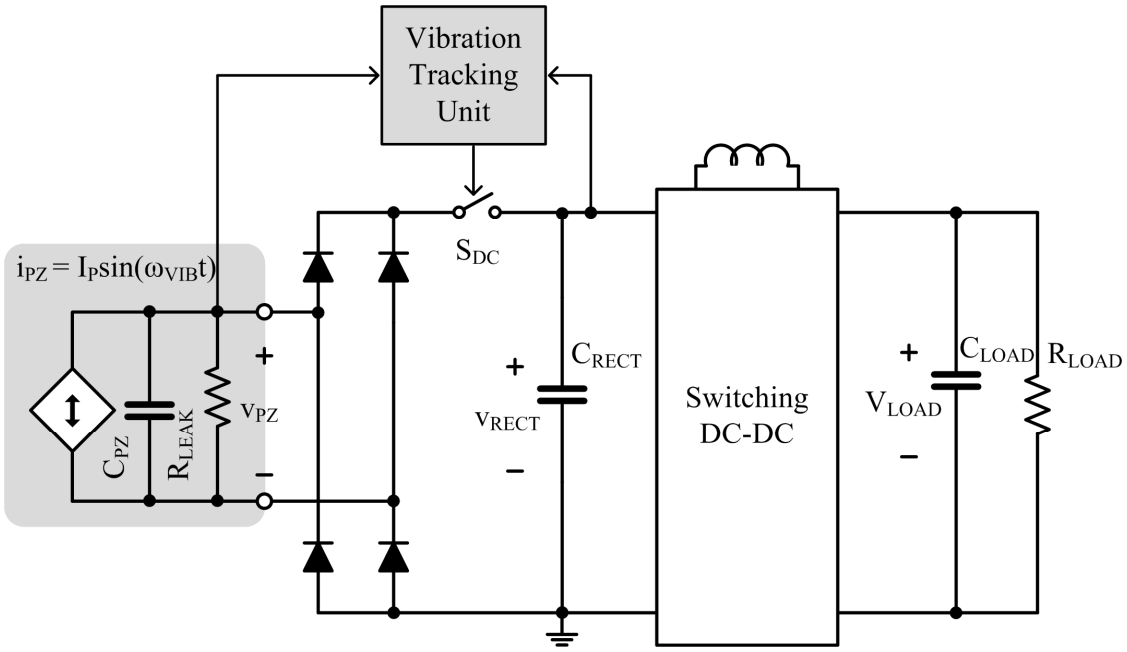

Figure 2.12. Maximum output power conditioning by periodically sensing the open-circuited voltage of the piezoelectric transducer.

Preparing the accurate optimal reference voltages for unknown vibrations is challenging for rectifier-based harvesters because the only way to know how much v_{PZ} will rise or fall requires waiting until it reaches the peak, which is already too late for the rectifier to optimally harness the generated energy. Therefore, the most practical approach to finding the optimal reference is perhaps to use a modified half-wave rectifier, using the negative half-cycle of the vibration to set the reference for the following positive half. Although this approach still assumes that the amplitude should vary only slightly in a half cycle, the previous half-cycle seems to be the best time frame to gather data to predict the current half. Authors in [165] implemented a modified half-wave diode-bridge rectifier with an analog controller that senses the conduction time T_{CLAMP} of

the clamping diode D_{CLP} to regulate v_{RECT} at the optimal point. As shown in Figure 2.13, the system employs a switching DC-DC converter after the rectifier to drain the charge of C_{RECT} and lower v_{RECT} as in the previous example of Figure 2.12. Note that despite the fact that D_{CLP} prevents v_{PZ} from falling to $-V_{OC}$, the value needed to find the optimal reference, the system can speculate the amplitude of the open-circuited voltage from the ratio of T_{CLAMP} to the total vibration period as the ratio will monotonically increase as V_{OC} magnitude increases.

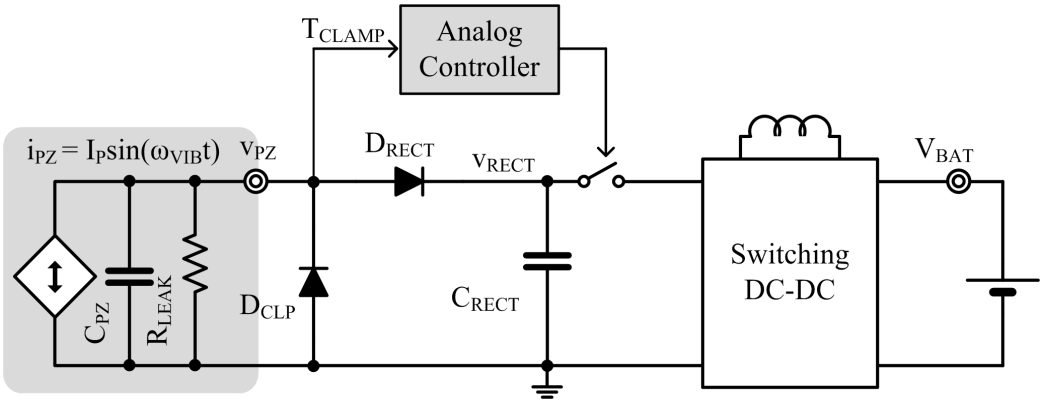

Figure 2.13. Maximum output power conditioning by sensing the conduction time (T_{CLAMP}) of the clamping diode D_{CLP}.

It is necessary for bridge-rectifier harvesters to condition the output voltage of the rectifier if the system is attempting to extract the most available energy from a given vibration. However, the challenge exists in finding the correct reference voltage because the rectifier can only guess the true target voltage from the previous vibrations. Moreover, the power that the control circuits and the additional stage (i.e., switching DC-DC converter) consume may easily exceed the power that a tiny transducer can harness under weak vibrations. Consequently, even if the diodes in bridge rectifiers exhibit zero V_D, the energy that the extra circuits and stages require will form a threshold on the piezoelectric transducer voltage below which the harvester cannot produce a net energy gain.

2.4. Summary

Bridge rectifiers have been a useful vehicle for converting AC input voltage into DC output voltage. For many medium-to-high voltage industrial applications, the standard full-wave diode-bridge rectifier is a simple, efficient, and reliable block that does not raise too many engineering issues. In contrast, for low-voltage, low-power applications such as miniaturized piezoelectric-energy harvesting, the diodes and the bridge structure can severely limit the performance because the losses and thresholds are not negligibly small anymore. Therefore, many researchers and engineers have been attempting to implement diodes better than just a PN junction or a diode-connected transistor.

One of the most promising solutions is to use a switch with a comparator that controls the state of the switch based on the voltage across it. Because the ohmic voltage drop across the on-resistance of the transistor is typically lower than the work-function induced voltage drop across the diodes for low currents, this active-diode approach can reduce conduction losses as well as losses in barrier voltage in bridge rectifiers that occur at the expense of comparator and switching losses. Another useful technique for switch-bridge rectifiers is to cross-couple MOS transistors in a way that not only controls the switches directly from the input voltage, but that also converts bipolar inputs to unipolar outputs. This approach eliminates the (need for) comparators and the associated losses and limitations, but it requires a high input voltage amplitude to drive the MOS transistors into their triode region. Moreover, since the cross-coupled MOS transistors cannot block the reverse current, the harvester system employing this cross-coupled pair needs at least one diode (including the active ones) in the harvesting current path.

While these circuit techniques can amend the local problems of the bridge rectifier, the fundamental limitation of bridge structures still exists. That is, the bridge rectifier will not be able to harness any energy if the output voltage of the rectifier is higher than the input voltage from the piezoelectric transducer under a given vibration. Hence, various strategies were proposed for conditioning the output of the bridge rectifier

to extract the most possible energy for a given mechanical input. The techniques can be effective in relatively slowly-varying periodic vibration energy harvesting; however, it seems to be challenging to accomplish the MPPT for practical vibrations because the target voltage for the rectifier output can be speculated on only from the previous vibration cycles, which can differ from the current one. In addition, the control circuits and the switching DC-DC converter that follows the rectifier spend an amount of power that can severely limit the net energy gain of a small-scale piezoelectric-energy harvester.

CHAPTER 3

BRIDGE-FREE PIEZOELECTRIC HARVESTER

Bridge rectifiers provide simple solutions to harness the electrical energy that piezoelectric transducers convert from surrounding vibrations. The circuit techniques introduced in the previous chapter, including active diodes and output conditioners, can improve the harvesting performance of bridge-based systems. However, the minimum input requirement imposed by the bridge rectifier and the extra conditioning circuits will ultimately limit the applicability of the harvester because the voltage generated by piezoelectric transducers decrease in amplitude as the physical dimensions of transducers shrink. Furthermore, even with centimeter-scale piezoelectric transducers, which typically are able to produce higher voltage than their micrometer-scale counterparts, weak vibrations prevalent in practical operating environments generate low voltage.

This chapter will introduce a bridge-free piezoelectric-energy harvester IC that aims to eliminate the input threshold problem of the rectifier. Another key advantage of the circuit is that it augments the electromechanical damping force of a transducer to extract energy from the vibrations. First, the bridge-free operation will be presented to describe how the system eliminates the threshold and induces the transducer to harness energy from the environment. Then, the design details of the prototype IC implementations will be introduced before the experimental results of the system are examined [182]–[184].

3.1. Bridge-free Operation

3.1.1. AC–DC Conversion

Fundamentally, the challenges in bridge-rectifier-based harvesters arise from the bridge rectifier. The problems associated with the bridge rectifier can be solved if a piezoelectric

harvester can convert the AC voltage of piezoelectric transducers to the DC output voltage of an energy storage element such as batteries or large capacitors [185]–[186]. One possible approach for the AC–DC conversion is to employ switched-inductor converters. Figure 3.1 illustrates examples of how switched-inductor converters can deliver energy from an AC input to a DC output.

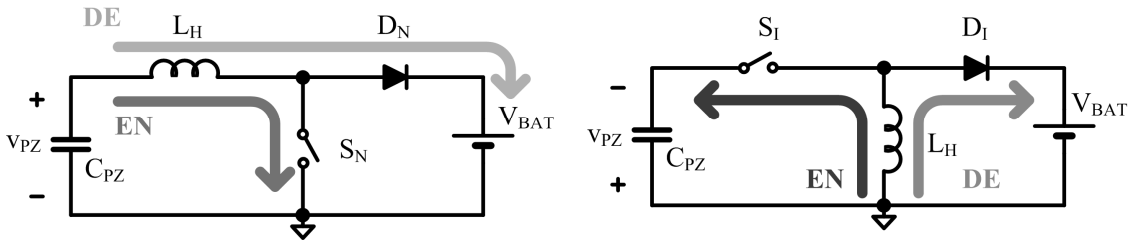

Figure 3.1. Boost and inverting buck–boost converters for AC–DC conversion.

When the input v_{PZ} and output V_{BAT} are both positive, a boost converter can first energize the inductor L_H from the capacitor C_{PZ} by turning on the switch S_N and then opening it to de-energize L_H to V_{BAT} through the diode D_N to transfer energy from the input to output. For the negative v_{PZ}, an inverting buck–boost converter can energize L_H from C_{PZ} by closing the switch S_I and then opening it to de-energize L_H to V_{BAT} through the diode D_I to deliver energy from the input to output. In this way, a system can harvest energy from the AC piezoelectric input and charge the DC output by exploiting switched-inductor converters.

3.1.2. Energy Flow

Figure 3.2 illustrates how a bridge-free harvester collects and transfers energy across a vibration cycle. When vibrations move the piezoelectric cantilever in the positive cycle, the system waits until the voltage across piezoelectric capacitance C_{PZ} peaks, which happens when the cantilever reaches its maximum displacement. At this point, the system energizes harvesting inductor L_H from C_{PZ} in energizing time τ_{LE}^{+} and then de-energizes L_H into the battery in de-energizing time τ_{LDE}^{+}. Transferring energy this way requires

only a few microseconds, which represents a negligible fraction of the milliseconds vibration period, so the position of the transducer is practically static during the transfer. Similarly, after depositing positive-cycle charge into the battery, the system waits until the piezoelectric device charges C_{PZ} in the negative direction to its negative peak. The switched-inductor circuit then quickly energizes and de-energizes L_H in τ_{LE}^- and τ_{DLE}^- from C_{PZ} to the battery, respectively. This negative-cycle transfer concludes the full cycle, and the sequence repeats as long as vibrations persist.

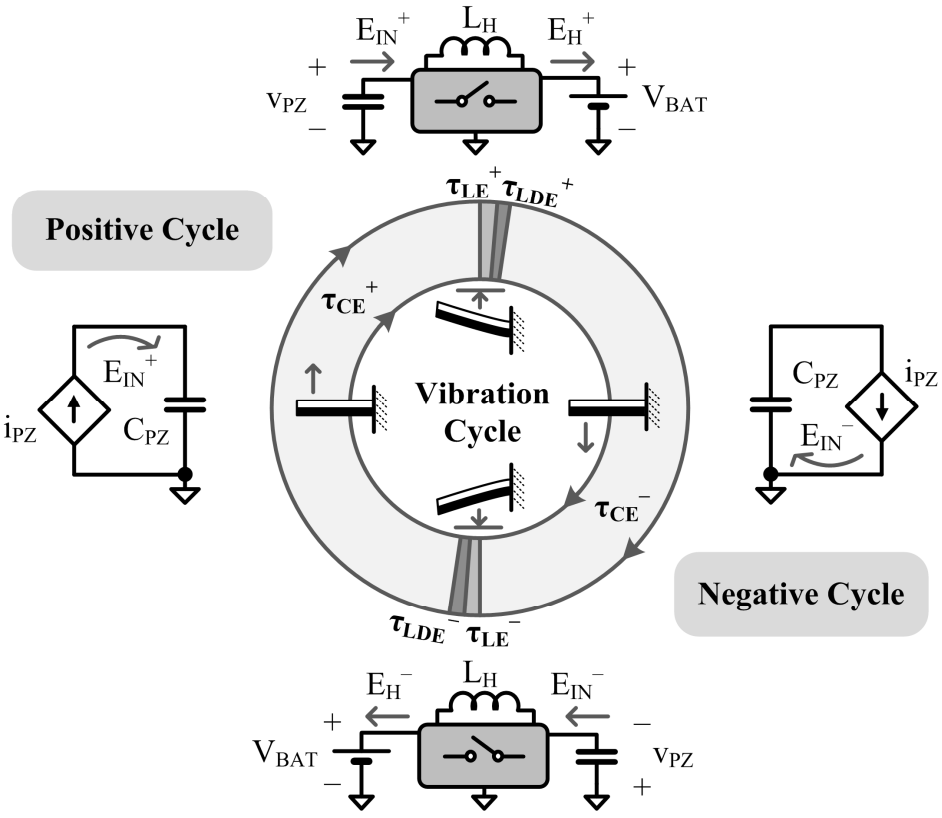

Figure 3.2. Full-cycle operation of the bridge-free piezoelectric harvester prototype.

C_{PZ} stores the energy that the piezoelectric material produces each half cycle (E_{IN}^+), and the switched-inductor converter extracts all E_{IN}^+ from C_{PZ}. Assuming piezoelectric current i_{PZ} is sinusoidal at $I_P\sin(\omega_{VIB}t)$, v_{PZ} during positive-cycle time τ_{CE}^+ is

$$v_{PZ}(t) = \frac{1}{C_{PZ}} \int_0^t i_{PZ}(\tau) d\tau = \left(\frac{I_P}{\omega_{VIB} C_{PZ}} \right) \left[1 - \cos(\omega_{VIB} t) \right]. \quad (3.1)$$

After τ_{CE}^{+}, C_{PZ} accumulates

$$E_{IN}^{+} \approx \int_0^{\tau_{CE}^{+} \approx T/2} i_{PZ}(t)\, v_{PZ}(t) dt = \frac{2I_P^2}{\omega_{VIB}^2 C_{PZ}}. \quad (3.2)$$

Since the negative cycle generates an equivalent amount (i.e., $E_{IN}^{+} \approx E_{IN}^{-}$), the net energy harvested (E_H) by the proposed system is

$$E_H = E_{IN}^{+} + E_{IN}^{-} - E_{LOSSES} = \frac{4I_P^2}{\omega_{VIB}^2 C_{PZ}} - E_{LOSSES}, \quad (3.3)$$

where E_{LOSSES} represent the sum of the energy lost in one cycle. This harvested energy can be compared to the maximum energy transfer capability of the bridge rectifiers derived in Chapter 2.1 by taking advantage of the fact that the open-circuit peak-to-peak voltage $2V_{OC}$ is equal to $v_{PZ}(t)$ of (3.1) at $t=T_{VIB}/2$ because the displacements of the piezoelectric transducer are the same in both cases. Therefore, the maximum output energy of the full-wave bridge-rectifier $E_{RECT(MAX)}$ can be expressed as

$$E_{RECT(MAX)} = C_{PZ} \left(V_{OC} - 2V_D \right)^2 = C_{PZ} \left(\frac{I_P^2}{\omega_{VIB}^2 C_{PZ}^2} - 2V_D \right)^2, \quad (3.4)$$

where V_D is the diode voltage drop. If the losses and the voltage drop across the diodes are ignored for the sake of comparison, the proposed bridge-free system can harvest four times (400%) more energy than a full-wave bridge-rectifier with ideal diodes can possibly acquire from the same mechanical input.

3.2. Switched-inductor Power Stage

The simplified schematic of the switched-inductor power stage is shown in Figure 3.3. In the positive cycle, with switch S_I open, the system waits for i_{PZ} to charge C_{PZ} to the

positive peak $V_{PZ(PK)}^{+}$, as the experimental waveforms of Figure 3.4 illustrate. However, $V_{PZ(PK)}^{+}$ is not the actual peak because the implemented peak-detection circuit includes delay and offset, the causes and implications of which subsequent subsections will address. The system then closes S_I and S_N to discharge C_{PZ} into L_H for energizing time τ_{LE}^{+}, allowing the inductor current i_L to reach positive peak current $I_{L(PK)}^{+}$. Because an inductor can fully discharge a capacitor in a quarter of their LC-resonance period, the system sets τ_{LE}^{+} to one-fourth of $2\pi\sqrt{(L_H C_{PZ})}$. After τ_{LE}^{+}, S_N opens and i_L charges the parasitic capacitance at node v_{SW}^{+} node until non-inverting diode D_N steers i_L into the battery. The positive cycle ends automatically once D_N completely drains L_H during de-energizing time τ_{LDE}^{+}.

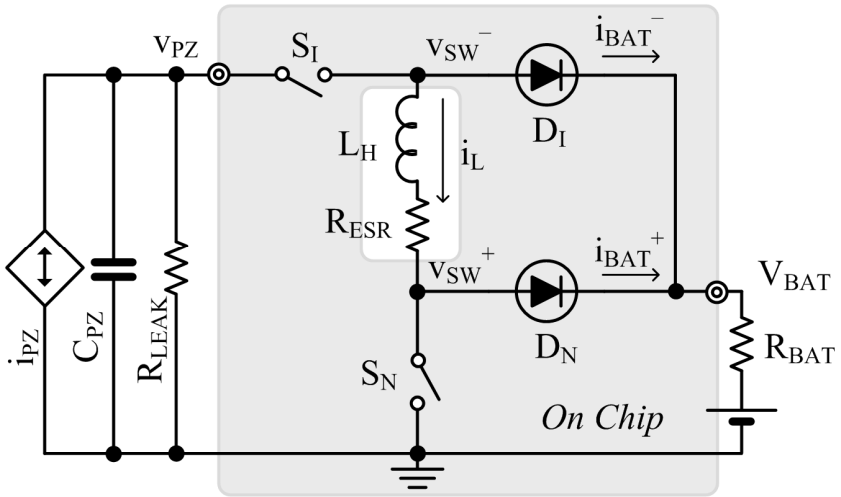

Figure 3.3. Switched-inductor power stage of a bridge-free harvester.

The negative cycle operates similarly except that the power stage inverts its functionality to create an inverting buck–boost operation. As such, the system waits for i_{PZ} to charge C_{PZ} in the negative direction until v_{PZ} reaches the negative peak $V_{PZ(PK)}^{-}$. S_I and S_N then drain C_{PZ} into L_H for one-fourth of the LC-resonance period, after which point S_I opens and i_L charges the parasitic capacitance at the v_{SW}^{-} node until inverting diode D_I conducts i_L into the battery.

Unlike bridge-based harvesters, a bridge-free switched-inductor circuit can extract all the piezoelectric energy in C_{PZ}, which is to say that the circuit does not suffer from a minimum input threshold. In addition, L_H automatically raises v_{SW}^+ and v_{SW}^- to whatever voltage the battery demands, which means the circuit does not require the additional DC-DC converter stage that bridge rectifiers must adopt to buffer the voltage gap between their output and the battery. Furthermore, unlike bridge-based harvesters with conditioning circuits, which typically include a lossy control loop to adjust the rectifier output voltage to draw the maximum power from C_{PZ}, the proposed harvester can ideally derive four times (4×) more energy than standard full-wave rectifier-based harvesters, which do not have correcting loop.

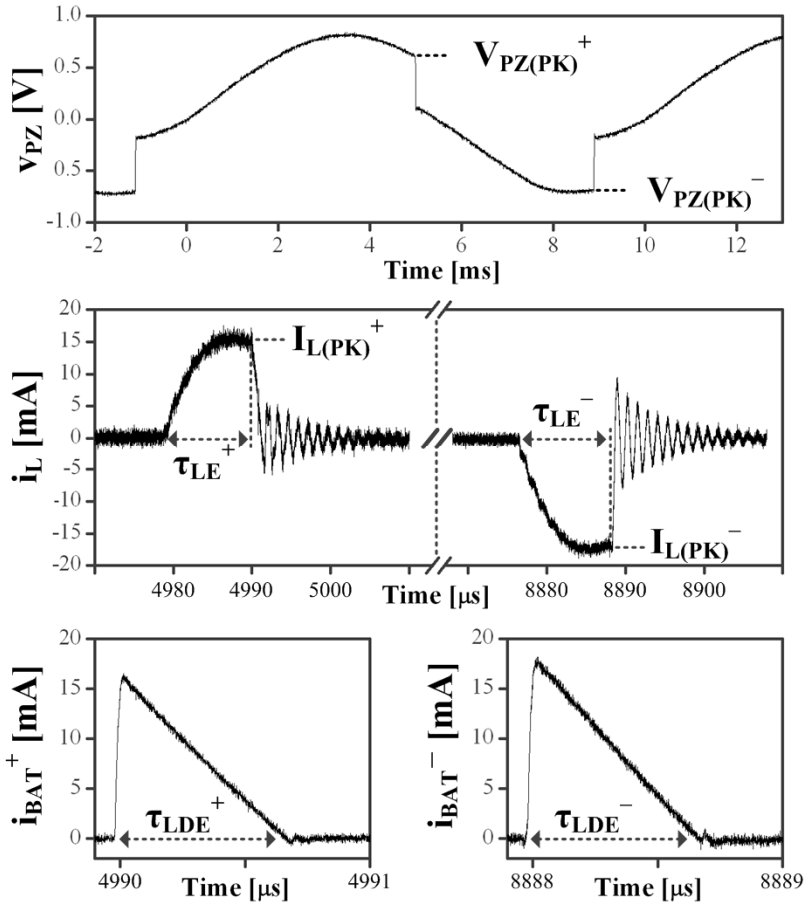

Figure 3.4. Experimental time-domain waveforms of piezoelectric voltage v_{PZ} and inductor current i_L's de-energizing (battery) currents i_{BAT}^+ and i_{BAT}^-.

3.3. IC Implementation

The prototyped harvester shown in Figure 3.5 integrates the switches, controller, and bias generator into a single 2-µm CMOS IC. Bias resistor R_{PTAT} and delay filter elements R_D and C_D are off chip for testing flexibility. For the same reasons, external voltages V_{ADJ}^{+} and V_{ADJ}^{-} set energizing durations τ_{LE}^{+} and τ_{LE}^{-} externally. The piezoelectric cantilever, the battery, and L_H are also off chip.

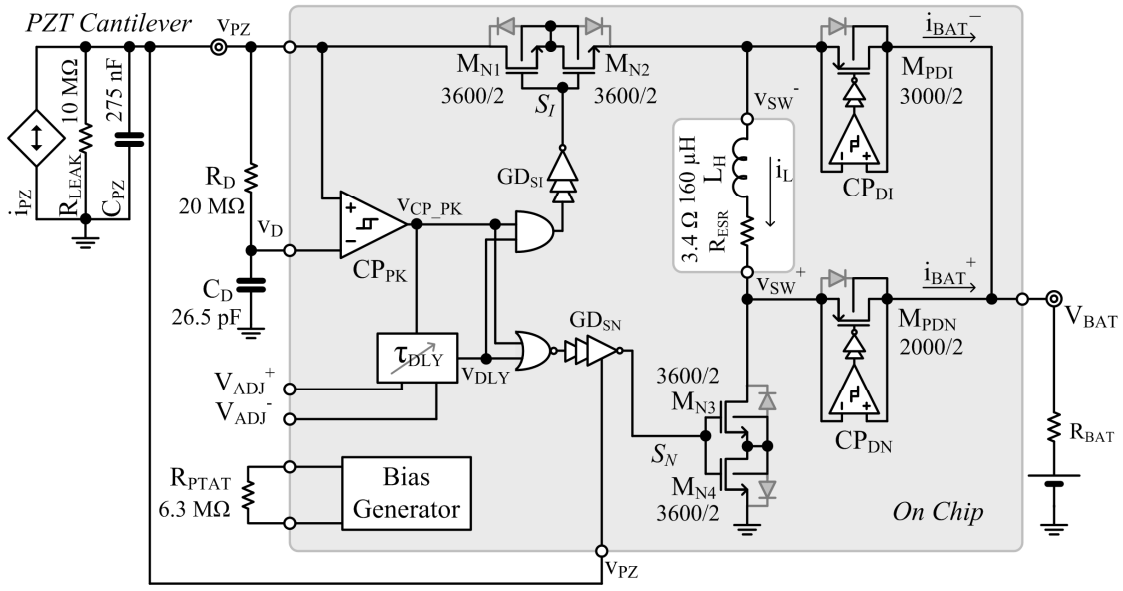

Figure 3.5. Prototyped bridge-free harvester IC and system (transistor dimensions are in µm).

3.3.1. Switches and Gate Drivers

A series combination of two NMOS transistors in an isolated p-well implements both S_I and S_N in Figure 3.5. The purpose of the back-to-back body diodes is to block the undesired diode current that would otherwise result through the body diode of a single transistor when v_{PZ} swings below ground (in the negative cycle) or above battery voltage V_{BAT} (in the positive cycle). Note that the series combination of two switches increases the channel resistance and gate capacitance, which raises conduction and switching losses, respectively, but not to the extent that body-diode conduction dissipates power.

Allowing v_{PZ} to swing below ground demands that gate driver GD_{SN} outputs a negative voltage. More specifically, while S_N is open during the negative cycle, when v_{PZ} falls below ground, switching node voltages v_{SW}^{+} and v_{SW}^{-} follow v_{PZ} below ground. During this time, driving the gate voltage of S_N to zero V does not sufficiently disengage S_N. This problem can be avoided if the last driver stage of GD_{SN} connects to v_{PZ} instead of ground, as Figure 5.6(a) shows. Accordingly, as the simulation results of Figure 5.6(b) illustrate, the output v_{GDSN_OUT} of GD_{SN} follows v_{PZ} during the negative cycle and nears V_{BAT} otherwise. Because the gate capacitance of S_N is orders of magnitude smaller than the C_{PZ} capacitance, GD_{SN} hardly drains C_{PZ}, that is, has negligible impact on v_{PZ}. However, when the system raises v_{GDSN_OUT} to V_{BAT} (to close S_N and energize L_H), inverter M_{PGD3}-M_{NGD3} conducts considerable shoot-through current (for about 50 ns) because the source voltage of M_{NGD3} (i.e., v_{PZ}) rises relatively slowly (in τ_{LE}^{-}) but the gate voltage of M_{NGD3} drops to zero V quickly (in a few ns). Minimizing this shoot-through loss requires that the width-to-length aspect ratio W/L of M_{NGD3} be designed to have relatively low value to increase resistance, yet maintained to be high enough to open S_N in time to drain L_H into the battery.

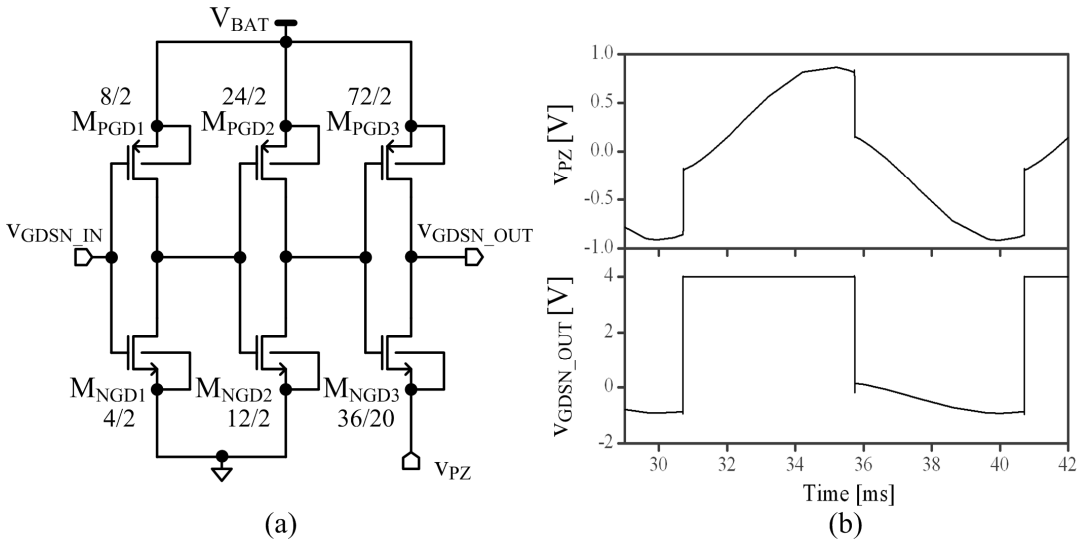

Figure 3.6. (a) Gate-driver circuit for S_N (transistor dimensions are in µm) and (b) the simulated waveforms of v_{PZ} and the gate voltage of S_N (i.e., v_{GDSN_OUT}).

3.3.2. Self-synchronizing Switches (active diodes)

As mentioned, there will be no v_{PZ} threshold below which the system cannot harness energy even if PN-junction diodes realize D_N and D_I, as in Figure 3.3, because they are placed after the inductor, which will raise their anode voltage to the value at which the diodes can conduct the current. Still, the PN-junction diodes dissipate significant power due to their considerable forward voltage drop. Replacing D_N and D_I with switches M_{PDN} and M_{PDI}, as in Figure 3.5, can effectively reduce this conduction loss.

It should be noted that synchronizing M_{PDN} and M_{PDI} demands precise timing control to minimize the overall power losses. For example, consider that if the gate-control signals of S_N and S_I overlap with those of M_{PDN} and M_{PDI}, S_N-M_{PDN} and S_I-M_{PDI} might initially short-circuit V_{BAT} to ground or to the input, which is why dead time between adjacent switches is imperative. Unfortunately, a fixed dead time in light of variable mechanical input strength, that is, an unpredictable peak-inductor current, also causes additional losses [177]–[178]. With a short dead time, M_{PDN} and M_{PDI} conduct before v_{SW}^+ and v_{SW}^- reach V_{BAT}, which causes the switches to dissipate power. On the other hand, a long dead time allows i_L to charge v_{SW}^+ and v_{SW}^- above V_{BAT}, increasing the time the body diodes conduct and dissipate power. In addition, turning M_{PDI} and M_{PDN} off after v_{SW}^- and v_{SW}^+ fall below V_{BAT} discharges the battery with reverse current.

Fundamentally, the above-mentioned losses result because M_{PDI} and M_{PDN} transition with non-zero voltage. The prototype reduces this loss by using comparators CP_{DI} and CP_{DN} to sense when v_{SW}^- and v_{SW}^+ reach V_{BAT}, thereby turning on and off M_{PDI} and M_{PDN} only when their terminals are close to 0 V. However, CP_{DI} and CP_{DN} require a finite time to respond, which, on one end, extends the time the lossy body-diodes conduct charging currents and, on the other, prompts M_{PDI} and M_{PDN} to drain the battery with reverse current.

A fast response often demands considerable quiescent current. The comparator implementation in Figure 3.7(a) minimizes this requirement by ensuring the circuit

operates only when needed, that is, only when L_H has sufficient energy to deliver to V_{BAT} and power the comparator. More explicitly, as L_H de-energizes into C_{PAR} to raise v_{SW}, some of i_L flows into the mirror M_{NB}-M_{NO} to activate the comparator, which then compares the currents that the source-gate voltages of M_{PB} and M_{PO} generate. Since M_{PB} and M_{PO} match, M_{PB} drives more current than M_{PO} does and engages M_P when v_{SW} is above V_{BAT}, and vice versa otherwise. Since L_H de-energizes only twice per cycle and since the required time is a small fraction of the cycle, the comparator energy losses are low (around 0.5 nJ per cycle in the prototyped case).

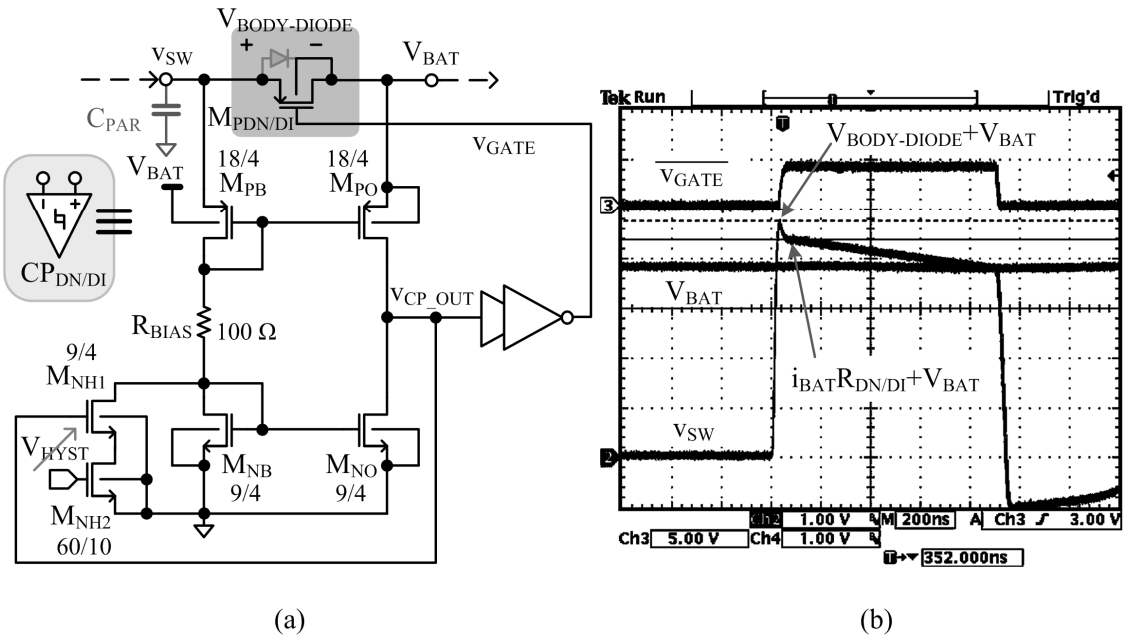

Figure 3.7. (a) Schematic (transistor dimensions are in µm) and (b) experimental waveforms of the self-synchronizing switch.

Because v_{SW} is 0 V initially, the gate voltage of M_{PO} is 0 V and v_{CP_OUT} is pulled up to V_{BAT} to ensure M_P is off while the comparator in Figure 3.7(a) is consuming no current. When L_H drives its current into C_{PAR} and through M_{PB}, v_{SW} increases rapidly, as Figure 3.7(b) illustrates, to produce strong overdrive input voltage, which in turn expedites the turn-on process. Once v_{SW} rises above V_{BAT} and M_{PB}-M_{NB}-M_{NO} lowers v_{CP_OUT}, M_P engages and v_{SW} remains above V_{BAT} from the ohmic voltage that i_L

produces across the series resistance of M_P. As a result, v_{SW} decreases with i_L as L_H de-energizes into V_{BAT}. When i_L reaches 0 A, which happens when the system depletes the inductor energy, v_{SW} drops to V_{BAT}, and the comparator transitions to turn M_P off. Because i_L no longer carries sufficient current to power the comparator, the circuit shuts off automatically.

During the turn-off process, the overdrive input voltage is small (because v_{SW} is near V_{BAT}), so the shut-off operation is relatively slow, which means M_P can momentarily conduct reverse current. To prevent this event, the comparator raises its shut-off trip-point by leaking current away from M_{NB} through M_{NH1} so that the circuit switches earlier, when v_{SW} is slightly above V_{BAT}. In addition to this offset for shut-off transition, the current of M_{NH2} establishes the turn-on hysteresis, which prevents inadvertent transitions of v_{CP_OUT} caused by the ringing events in v_{SW}. In the prototype system of Figure 3.7(a), V_{HYST} sets the hysteresis current.

3.3.3. Peak Detector

The proposed bridge-free piezoelectric harvester system starts energizing the inductors by detecting the positive and negative peaks of v_{PZ}. The comparator CP_{PK} in Figure 3.5 compares v_{PZ} with a delayed version of itself (v_D) to capture the moments when v_{PZ} stops leading v_D. As shown in Figure 3.8, v_{PZ} drops below v_D just when v_{PZ} begins falling from its positive peak, and v_{PZ} rises above v_D just when v_{PZ} begins increasing from its negative peak. CP_{PK} incorporates about ±10 mV of hysteresis to deglitch noise in v_{PZ} and v_D. To establish the hysteresis, the cross-coupled, positive-feedback P-type mirror unbalances the N-type differential pair in both directions. The circuit operates in subthreshold region to minimize power (with nanoamps), so its delay is in the microsecond range. Such a slow response is tolerable because microseconds constitute a negligible fraction of the milliseconds vibration period, meaning v_{PZ} does not change appreciably in microseconds. To mitigate risk in evaluating the power stage and its basic control scheme, external

negative source V_{SS} extends CP_{PK}'s input common-mode range (ICMR) below ground so that it can accommodate negative v_{PZ} voltage.

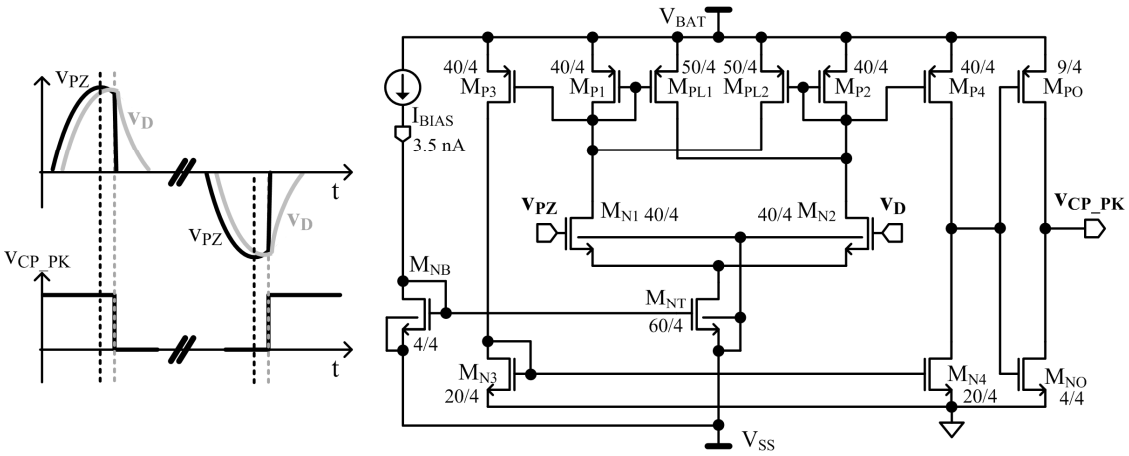

Figure 3.8. Peak-detecting comparator CP_{PK} (dimensions are in µm, and body terminals connect to their respective supplies, unless otherwise specified).

3.3.4. Adjustable Delay

The harvester stops energizing L_H after one-fourth of the resonance period set by L_H and C_{PZ}. Figure 3.9 shows that V_{ADJ}^{+}-R_{ADJ}^{+} and V_{ADJ}^{-}-R_{ADJ}^{-} in set the source and sink currents that charge and discharge C_{ADJ} so that the voltage across C_{ADJ} reaches the threshold of the ensuing inverter in $0.5\pi\sqrt{(L_H C_{PZ})}$. Since tolerance in R_{ADJ} and C_{ADJ} offset this time, and since other parasitic effects similarly shift how long C_{PZ} should discharge into L_H, V_{ADJ}^{+} and V_{ADJ}^{-} are adjustable. Note that M_{NSQ} and M_{PSQ} dissipate any shoot-through power because the voltage of C_{ADJ} rises and falls slowly. This loss is reduced by making their channel lengths relatively long at 10 µm. If tuning the effective R-C time constants externally becomes prohibitive, the inductor energizing intervals τ_{LE}^{+} and τ_{LE}^{-} can be alternately set by monitoring the inductor voltage v_L with a comparator so that it trips when v_L (which equals to $L_H di_L/dt$) crosses zero (when i_L peaks). However, note that the equivalent-series resistance (ESR) of L_H is parasitic and must therefore remain negligibly low to minimize any timing error and harvesting performance degradation.

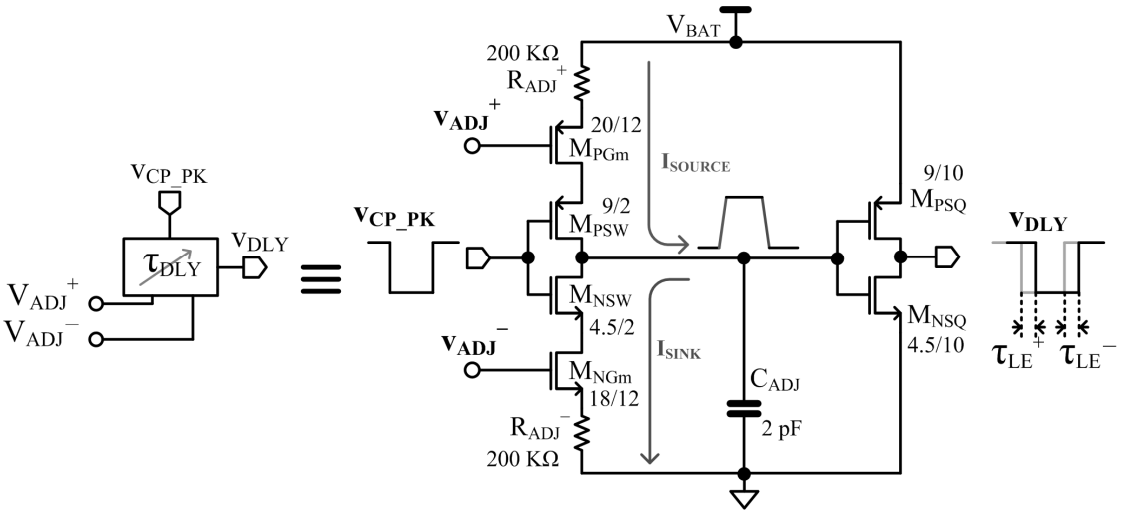

Figure 3.9. Adjustable delay τ_{DLY} (dimensions are in µm, and body terminals connect to their respective supplies, unless otherwise specified).

3.3.5. Bias Generator

The nA-bias generator shown in Figure 3.10 supplies bias currents for the peak-detecting comparator CP_{PK}. The one-to-one mirror M_{P1}-M_{P2} and gate-coupled pair M_{N1}-M_{N2} ensure that the M_{N1}-M_{N2} source voltages are equal. As a result, the area ratio between Q_{P2} and Q_{P1} establishes proportional-to-absolute-temperature (PTAT) diode-voltage difference ΔV_D across R_{PTAT} to set I_{BIAS} to

$$I_{BIAS} = \frac{\Delta V_D}{R_{PTAT}} = \frac{V_t \ln\left(\frac{I_{P1}A_2}{I_{P2}A_1}\right)}{R_{PTAT}} = \frac{V_t \ln 2}{R_{PTAT}}, \tag{3.5}$$

which is independent of supply voltage. Here, V_t is the thermal voltage, and I_{P1}-I_{P2} and A_1-A_2 are the currents and areas of Q_{P1} and Q_{P2}, respectively. The large off-chip resistance of R_{PTAT} (at 6.3 MΩ) ensures that I_{BIAS} is in the nA range. Note that I_{BIAS} is only P_{TAT} if R_{PTAT} has a low temperature coefficient, which is not a requirement for this circuit. Without the start-up transistor M_{NS1}, the circuit can be stable at either the above-defined I_{BIAS} or off state. M_{NS1} forces the circuit into its on state because the gate-source voltage of M_{NS1} would otherwise be high enough (as defined by M_{PS0}, M_{PS1}, M_{PS2}, M_{NS2},

and Q_{PS1}) to steer current from M_{P1} into M_{N1}. Diode-connected PMOS transistors M_{PD1} and M_{PD2} shift the voltage level of the current-bias terminal voltage of CP_{PK} (across M_{NB} in Figure 3.8) to alleviate channel-length modulation errors in M_{P3}.

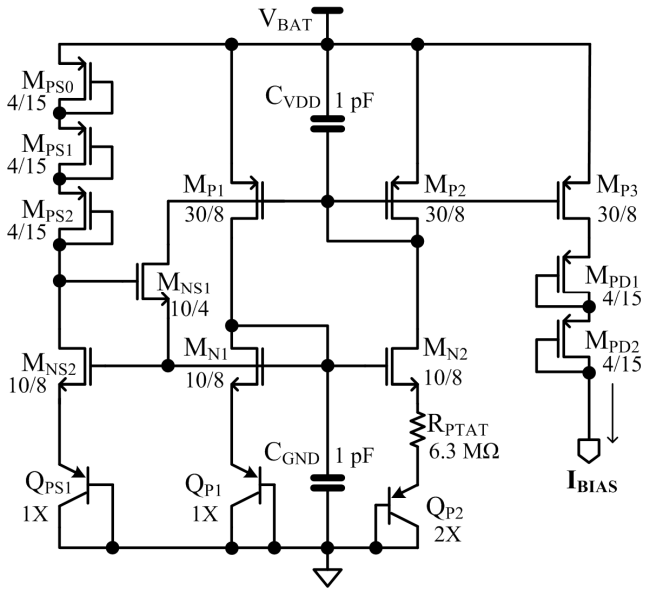

Figure 3.10. PTAT bias-current generator (dimensions are in µm and body terminals connect to their respective supplies, unless otherwise specified).

3.4. Harvesting Performance

Figure 3.11 illustrates the fabricated 940 µm × 960 µm 2-µm CMOS IC and its corresponding printed-circuit-board (PCB) prototype. The system used an off-chip 4.4 mm × 4.4 mm × 1.4 mm, 160-µH, 3.4-Ω inductor from Coilcraft. The Brüel & Kjær's Mini-shaker 4810 shown in Figure 3.12 generated the periodic vibrations that stimulated the 44 mm × 13 mm × 0.4 mm piezoelectric cantilever from PiezoSystems. A laser-displacement sensor measured the vertical position of the cantilever to study the relationship between mechanical and electrical parameters. The results show that the open-circuit voltage of the transducer V_{OC} and the acceleration rate of the cantilever rise almost linearly with vibration strength. For example, V_{OC} was 0.35, 0.5, 0.7, and 0.9 V when the acceleration rates at the base of the cantilever were 0.048, 0.069, 0.094, and 0.120 m/s^2, and at the tip of the cantilever, they were 3.05, 4.49, 6.44, and 8.34 m/s^2,

respectively. Note that typical HVAC systems in the typical office setting feature accelerations higher than 0.2 m/s^2 [105].

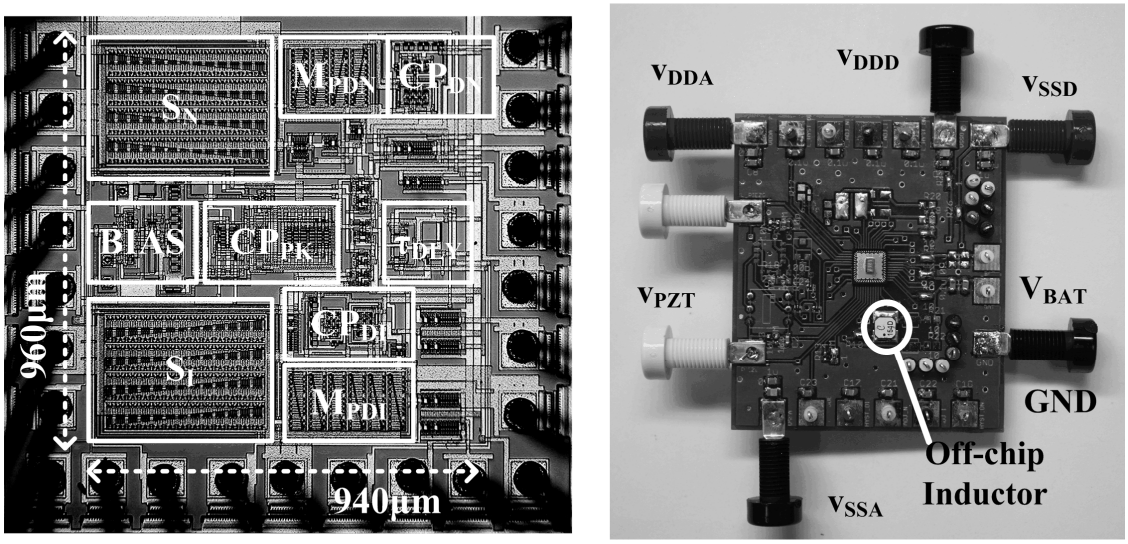

Figure 3.11. Prototyped die and PCB.

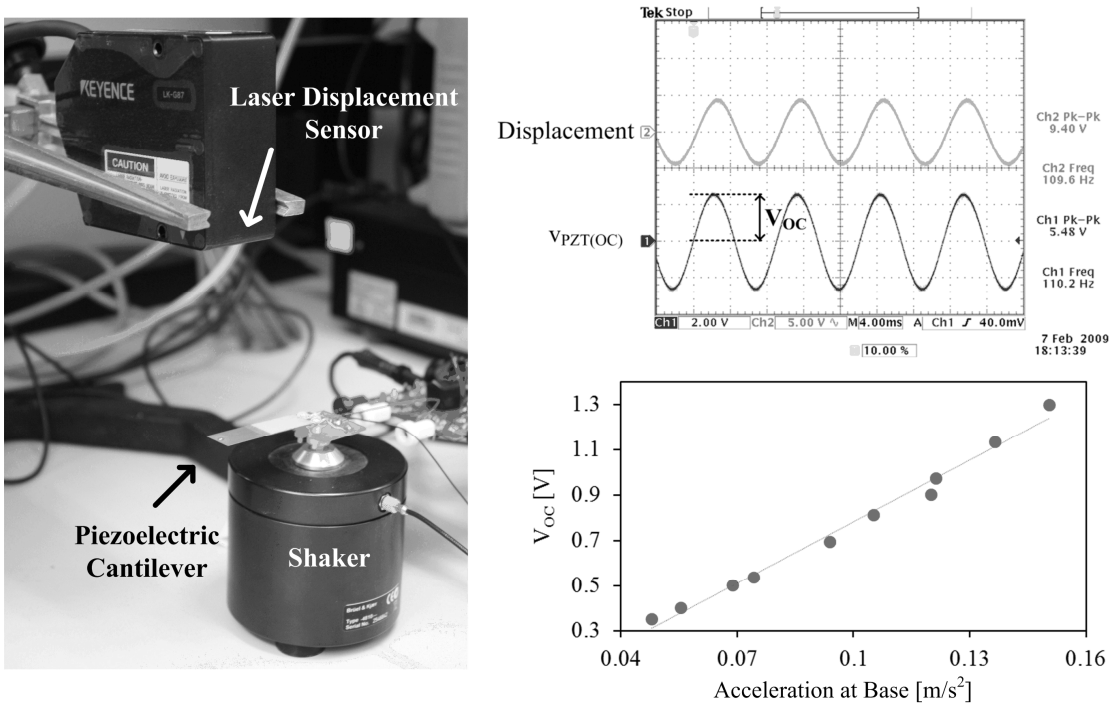

Figure 3.12. Test setup and the measured open-circuited voltage across acceleration rates.

3.4.1. Harvesting from Periodic Vibrations

The prototype successfully charged 160-nF ceramic surface-mount-device (SMD) and 23-µF electrolytic capacitors from vibrations that induced V_{OC} of 0.35, 0.5, 0.7, and 0.9 V. As Figure 3.13 indicates, the input voltage amplitudes were lower than that of the output capacitor (i.e., v_{BAT}), but the proposed bridge-free harvester was able to harvest energy from the small input voltage that a micro-scale transducer would generate and successfully charged the output energy storage. The output capacitor voltage increased in staircase fashion because the circuit deposited a packet of energy (from C_{PZ}) every half cycle as with a pulse charger [187]–[189]. As expected, the resulting step sizes increased with larger V_{OC} because stronger mechanical vibrations allowed the system to deposit more energy into C_{PZ}.

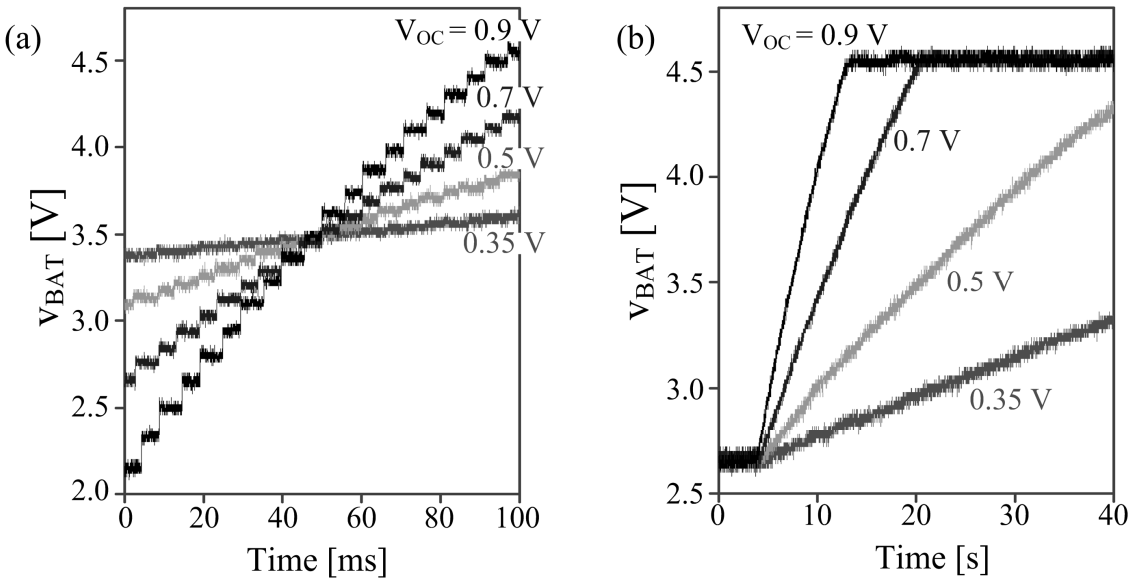

Figure 3.13. Experimental time-domain charging profiles for (a) 160-nF ceramic SMD and (b) 23-µF electrolytic capacitors.

Although energy per cycle was low and charging time was relatively long, the 1.2- and 1.5-mAh Li-Ion batteries in Figure 3.14 (i.e., Panasonic ML414 and VL621) were charged from 0.65- and 0.9-V V_{OC} to raise their corresponding voltages by 24 mV

and 39 mV in 300 minutes. For these capacitor and battery charging experiments, an external low-leakage operational amplifier in a unity-gain configuration monitored v_{BAT}, and a low-leakage off-chip diode connected to an external 4-V supply clamped v_{BAT} within the targeted range.

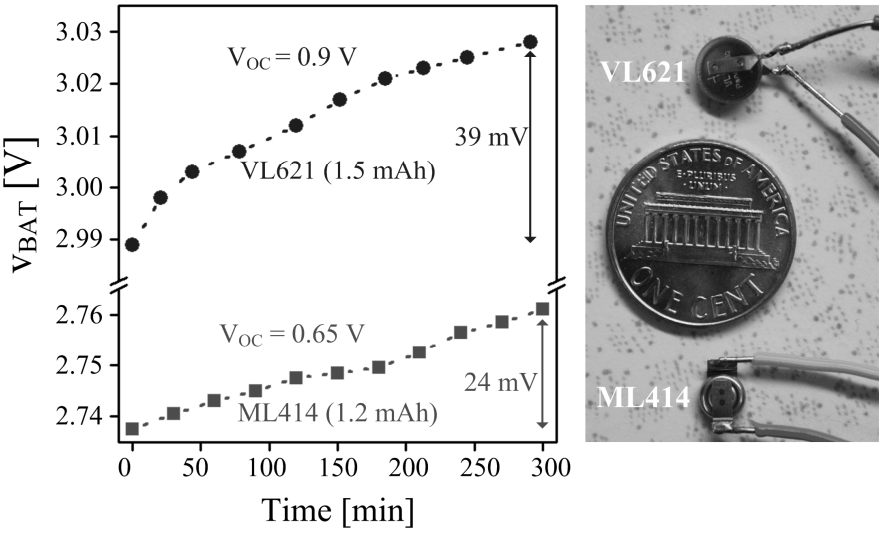

Figure 3.14. Experimental time-domain charging profiles for Li-Ion batteries ML414 and VL621.

With the losses taken into consideration, the system harnessed up to 30 µW (P_H in Figure 3.15) from 72 µW of transducer-generated power (P_{IN}). As Figure 3.15 depicts, under equal mechanical stimulations (i.e., same V_{OC}), the proposed harvester draws more power than an ideal bridge rectifier could have gleaned ($P_{BRIDGE(MAX)}$), an amount which is $C_{PZ}V_{OC}^2f_{VIB}$. In other words, the best possible bridge-rectifier-based system with perfect output conditioning circuits would draw roughly 56% of what the proposed harvester can (e.g., 40 of 72 µW). This improvement arises because the proposed harvester exhausts C_{PZ} close to 0 V every half cycle and because the effective peak voltage of C_{PZ} increases more than V_{OC}. Consequently, for the given mechanical input, this higher peak voltage increases the electromechanical damping force impressed upon the transducer and derives more energy from the vibration than the bridge-based systems can.

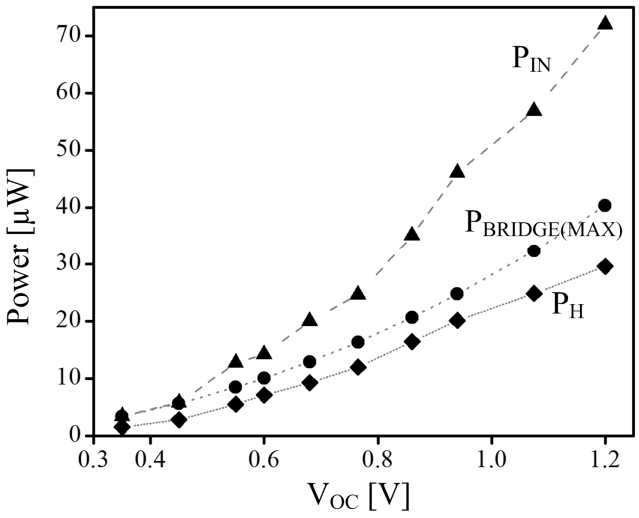

Figure 3.15. Measured harvester input power P_{IN}, output power P_H, and calculated maximum output power of bridge rectifiers $P_{BRIDGE(MAX)}$ across mechanical vibration strengths (i.e., across C_{PZ}'s V_{OC}).

Although the fact that the proposed harvester augmented the harvested power corroborates the theory, the increased rate of 178% (when V_{OC} is 1.2 V) did not correspond to 400% as (3.3) predicted. One reason for this discrepancy stems from the 36-mV input-referred offset of CP_{PK}, which caused the system to discharge C_{PZ} past the peak of v_{PZ} (i.e., after C_{PZ} lost some energy to vibrations), as already mentioned and shown in Figure 3.4. In addition, since the offset voltage did not scale with the input, the fraction of energy lost to vibrations was larger for smaller inputs. Another possible reason for the discrepancy originates from the parasitic resistances in switches S_N and S_I and across L_H in Figures 3.3 and 3.5. As Figure 3.4 demonstrates, the harvester pulled v_{PZ} to the voltage drop across the combined series resistance of S_N, L_H, and S_I (i.e., R_{SN} + R_{ESR} + R_{SI}) instead of fully draining C_{PZ} into L_H and lowering v_{PZ} to 0 V. This non-zero v_{PZ} at the end of each half harvesting cycle not only represented remnant energy that the system could not harvest but also lowered the peak v_{PZ} amplitude (i.e., electromechanical damping force) of the ensuing half cycle.

3.4.2. Power Losses and Conversion Efficiency

Despite the fact that the switched-inductor converter allows efficient energy delivery, power losses remain in the converter due to the parasitic resistances, capacitances, and the control circuits of the system. The harvester loses conduction power P_C to the finite resistances of switches and ESR of L_H when i_L flows through L_H during the positive- and negative-cycle, energizing and de-energizing intervals τ_{LE}^{+}, τ_{LDE}^{+}, τ_{LE}^{-}, and τ_{LDE}^{-}:

$$P_C \approx \left[\left(\frac{I_{L(PK)}^{+}}{\sqrt{3}} \right)^2 + \left(\frac{I_{L(PK)}^{-}}{\sqrt{3}} \right)^2 \right] (R_{SI} + R_{SN} + R_{ESR})(\tau_{LE} + \tau_{LDE}) f_{VIB}, \tag{3.6}$$

where f_{VIB} represents the vibration frequency. The energizing times τ_{LE}^{+} and τ_{LE}^{-} and the de-energizing counterparts τ_{LDE}^{+} and τ_{LDE}^{-} equal τ_{LE} and τ_{LDE}, respectively. $I_{L(PK)}^{+}/\sqrt{3}$ and $I_{L(PK)}^{-}/\sqrt{3}$ approximately estimate the root-mean-squared (RMS) currents flowing through the resistors across positive and negative cycles, respectively, as they exhibit triangular waveforms. P_C reduces as L_H values increase because, even though τ_{LE} increases with $L_H^{0.5}$ (from $0.5\pi\sqrt{(L_H C_{PZ})}$), $(I_{L(PK)}^{+})^2$ and $(I_{L(PK)}^{-})^2$ decreases with L_H^{1} for the given power flow. Wider MOS transistors (i.e., lower R_{SI} and R_{SN}) also decrease P_C, but at the expense of silicon real estate and higher switching gate-drive losses $P_{SW(GD)}$, as the following discussion will elucidate.

The system loses $P_{SW(GD)}$ in inverter drivers when they charge and discharge parasitic gate capacitances in S_I, S_N, and D_N and D_I (from Figure 3.5). Since all the switches in the proposed harvester turn on and off once per cycle, gate-drive losses amount to

$$P_{SW(GD)} \approx \left[(C_{SI} + C_{DI} + C_{DN}) {V_{DD}}^2 + C_{SN} \left(V_{DD} + \left| V_{PZ(PK)}^{-} \right| \right)^2 \right] f_{VIB}, \tag{3.7}$$

where C_{SI}, C_{DI}, C_{DN}, and C_{SN} refer to the parasitic capacitances that S_I, D_I, D_N, and S_N introduce, respectively. These capacitances scale with transistor channel widths. Note

that S_N causes more energy loss than other switches because its gate swings between V_{DD} and $V_{PZ(PK)}^{-}$.

The system also experiences overlap losses $P_{SW(IV)}$ when MOS drain currents and drain-source voltages briefly overlap every time they transition. In the prototype system, this overlap occurs when S_N and S_I turn off because v_{SW}^{+} and v_{SW}^{-} transition with a non-zero i_L:

$$P_{SW(IV)} \approx \left(0.5I_{L(PK)}^{+}\tau_{SN\_OFF} + 0.5I_{L(PK)}^{-}\tau_{SI\_OFF}\right)\left(V_{BAT} + V_D\right)f_{VIB}, \tag{3.8}$$

where V_D is the body-diode voltage of M_{PDN} and M_{PDI}. Here, because the switch current is assumed to decrease linearly from $I_{L(PK)}^{+}$ and $I_{L(PK)}^{-}$ to 0 A during the turn-off transition time τ_{SN_OFF} and τ_{SI_OFF}, respectively, $0.5I_{L(PK)}^{+}\tau_{SN\_OFF}$ and $0.5I_{L(PK)}^{-}\tau_{SI\_OFF}$ approximate the total conducted charge of S_N and S_I during the transitions.

Quiescent power (P_Q) is dissipated by peak-detecting comparator CP_{PK}, the bias generator, adjustable-delay block τ_{ADJ}, the logic gates, and the comparators CP_{DN} and CP_{DI} for D_N and D_I in Figure 3.5. However, P_Q tends to be dominated by the losses in CP_{PK} and the bias circuit because they operate through the entire vibration cycle, whereas the other circuits engage only for a substantially smaller fraction.

Because of these losses, the harvester prototype exhibited efficiencies below 50% in the tested power range, as Figure 3.16(a) reveals with the dissected loss profiles. Note that P_C overwhelms the losses from the other mechanisms and severely reduces the efficiency. This unbalanced loss profile, however, indicates the possibility of improving efficiency by balancing P_C and P_{SW}. In other words, the system can employ larger switches to reduce the conduction losses so that the increased switching losses do not deteriorate the overall efficiency. Efficiency can also be enhanced by adopting a physically larger inductor (with the same inductance value) which has lower ESR than that of a smaller inductor. Figure 3.16(b) depicts the simulated efficiency and loss profiles of a harvester employing 10× larger switches and a 0.84-Ω, 160-μH inductor that

occupied 5 mm × 5 mm × 3 mm in system volume. Of course, the tradeoff is space (i.e., cost) because both die size and board space increase. Nevertheless, with these values, P_C decreases more than P_{SW} increases, and efficiency, as a result, reaches 75%. However, the design is now optimum only for a higher power range, which means efficiency drops below 50% at lower power levels, when P_{SW} and P_Q dominate. The efficiency will eventually drop if the power flow through the converter increases to cause P_C to dominate, as Figure 3.16(a) illustrated.

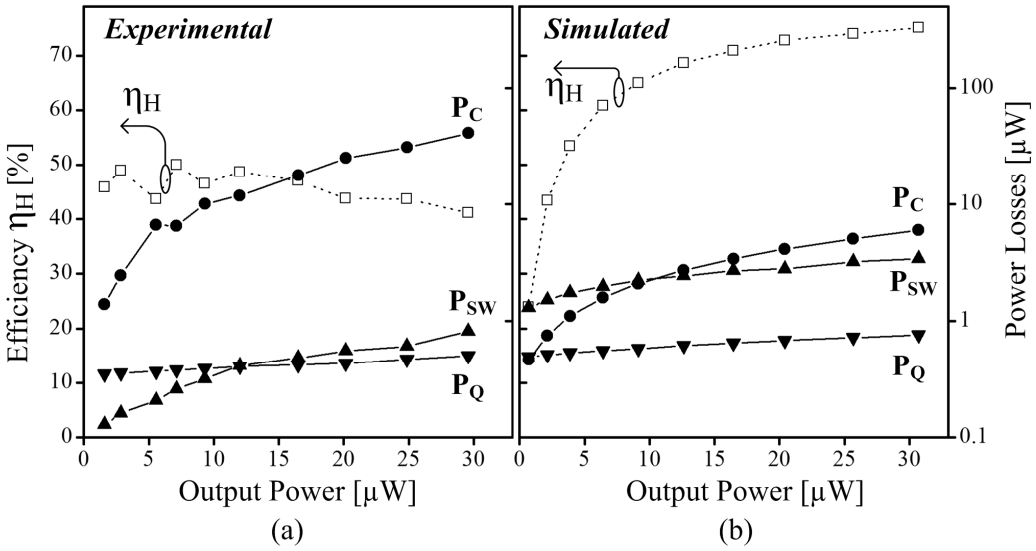

Figure 3.16. Efficiency and losses in the harvester with physically (a) smaller (experimental) and (b) larger (simulated) switches and inductors.

3.4.3. Harvesting under Practical (Aperiodic) Operating Conditions

Vibrations in practical operating environments occur, for the most part, at relatively low frequencies, between maybe 1 Hz for a person walking to 167 Hz for an engine cycling at 10,000 revolutions per minute. The rate is often inconsistent and maybe even non-recurring, as in the case of human motion, wind-propelled movements, and vibrations generated from some random impact. What all this means is that matching the narrow band of a transducer to vibrations, which is the recipe for high conversion efficiency, can limit the applicability of resonant-type vibration harvesters [190]. Although it may not be

optimal in terms of conversion efficiency, piezoelectric transducers can generate voltage from non-periodic stimuli. Therefore, the harvester circuit should also be able to glean the energy produced by the transducer from non-periodic mechanical inputs. Because the prototyped harvester automatically detects when to draw energy from C_{PZ}, the system is capable of harnessing energy from non-periodic stimuli.

When a 145-g official major-league baseball was dropped from 40 cm above the experimental setup table in Figure 3.17, for example, the impact of the ball bouncing once off the table indirectly induced the piezoelectric cantilever to vibrate and produce the pulse train in Figure 3.18. In this case, the prototype system charged 500 nF (from 3.04 V) from a single bounce for three separate trials by roughly 200 mV.

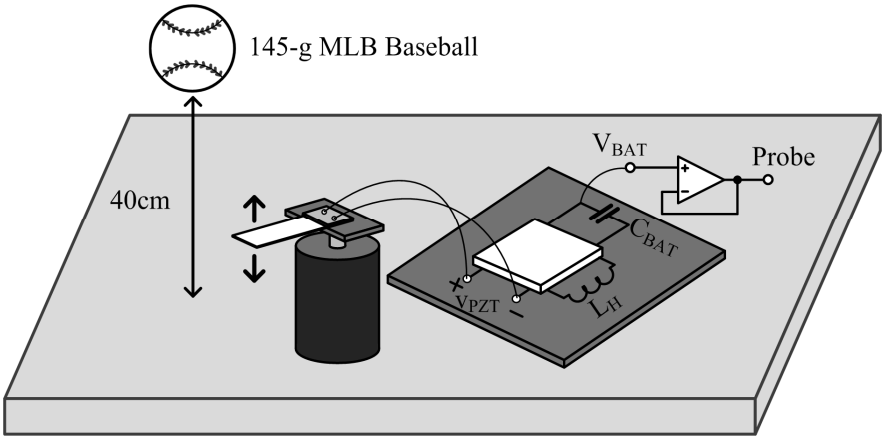

Figure 3.17. Test setup for harvesting aperiodic vibration energy.

Each drop produced the decaying vibrations as shown in Figure 3.18(b), and the system harvested energy by quickly draining C_{PZ} into L_H and then L_H into the 500-nF capacitor each time v_{PZ} peaked. However, as the peak amplitude of v_{PZ} (and mechanical strength) decreased, the offset of the peak-detecting comparator CP_{PK} exhibited a larger impact on how much input power P_{IN} the system harnessed, which means that output power P_H decreased more than basic theory predicted. In fact, under the weak vibrations, the delays in R_D-C_D and CP_{PK} increased the undesirable impact of the offset in CP_{PK} to

degrade the harvesting performance. In contrast, just as the offset added to the effects of the delay in CP_{PK} in the positive half-cycle, the offset cancelled the delay in the negative half-cycle, as Figures 3.4 and 18(b) illustrate, which means alternating the polarity of the offset can improve overall performance.

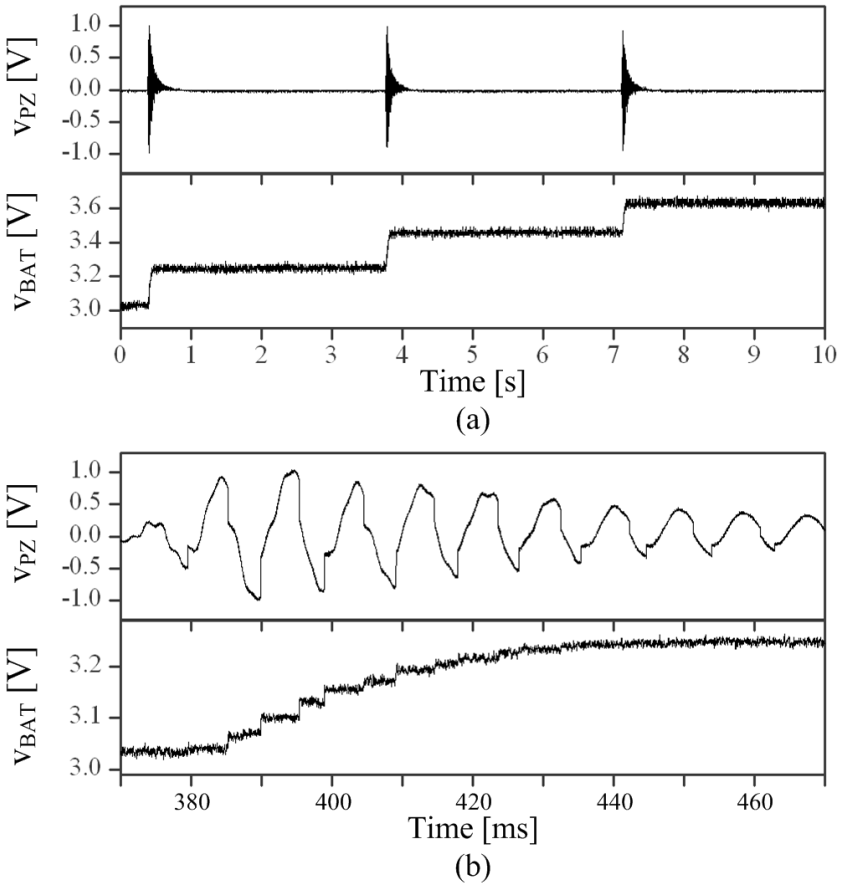

Figure 3.18. (a) Second and (b) millisecond (magnified) responses to the impact of a baseball bouncing off a table.

Although efficiency η_H is a metric for the harvester IC itself, it does not reveal how much mechanical energy E_{ME} reaches the output as harvested energy E_H. Figure 3.19 shows a test setup for measuring the energy transfer all the way from the mechanical input to the harvesting storage. A means of applying a known value for E_{ME} (and approximating the end-to-end conversion efficiency η_{TOTAL}) is to tie an object of known mass m_W to the tip of the piezoelectric cantilever with a light string and subsequently cut

the link. Since the elastic force F_C of the cantilever balances the gravitational pull F_G of the object, E_{ME} relates to F_G and the tip displacement distance d_C of the cantilever as follows:

$$E_{ME} = \frac{K_C d_C^2}{2} = \frac{(K_C d_C) d_C}{2} = \frac{F_C d_C}{2} = \frac{F_G d_C}{2} = \frac{(m_W g) d_C}{2}, \tag{3.9}$$

where K_C and g refer to the spring constant and gravitational acceleration, respectively.

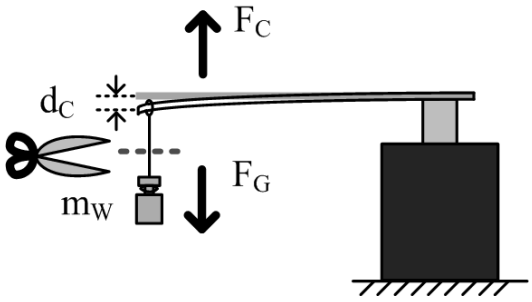

Figure 3.19. Test setup for measuring the total energy transfer.

In this way, if the parasitic weights are set aside and it is assumed that the string severs instantaneously, the prototyped harvester charged (experimentally) 500 nF by roughly 400 mV from a 3-g weight, as Figure 3.20 shows. As a result, subtracting the quiescent energy E_Q (to the chip for CP_{PK}, bias generator, adjustable delay, and logic gates) and gate-driving losses $E_{SW(GD)}$ from the energy deposited in the 500-nF capacitor reduces E_H to

$$E_H = 0.5 C_{BAT} \left({V_{BAT(F)}}^2 - {V_{BAT(I)}}^2 \right) - E_Q - E_{SW(GD)}, \tag{3.10}$$

which ranged between 100 and 660 nJ when stimulated with 1.2 to 10.8 μJ of E_{ME} from 1-, 2-, and 3-g weights to yield 6.1 ± 1.5% to 8.8 ± 6.9% of η_{TOTAL} or E_H/E_{ME}. Table 3.1 summarizes the statistical results (mean and standard deviation) for each weight across 20 trials. To minimize the mechanical disturbance that cutting the link creates, Table 3.1

considered only data whose initial peak voltage (v_{PZ}) was small (e.g., less than 100 mV), like v_{PZ} in Figure 3.20.

Table 3.1. Measured mechanical and net harvested energy, and end-to-end efficiencies.

Weight [g]	E_{ME} [nJ]	E_H [nJ]	η_{TOTAL} [%]
1	1198.0 ± 17.6	104.8 ± 82.3	8.76 ± 6.89
2	4797.0 ± 123.1	402.8 ± 173.3	8.39 ± 3.60
3	10792.8 ± 190.3	659.1 ± 171.2	6.10 ± 1.54

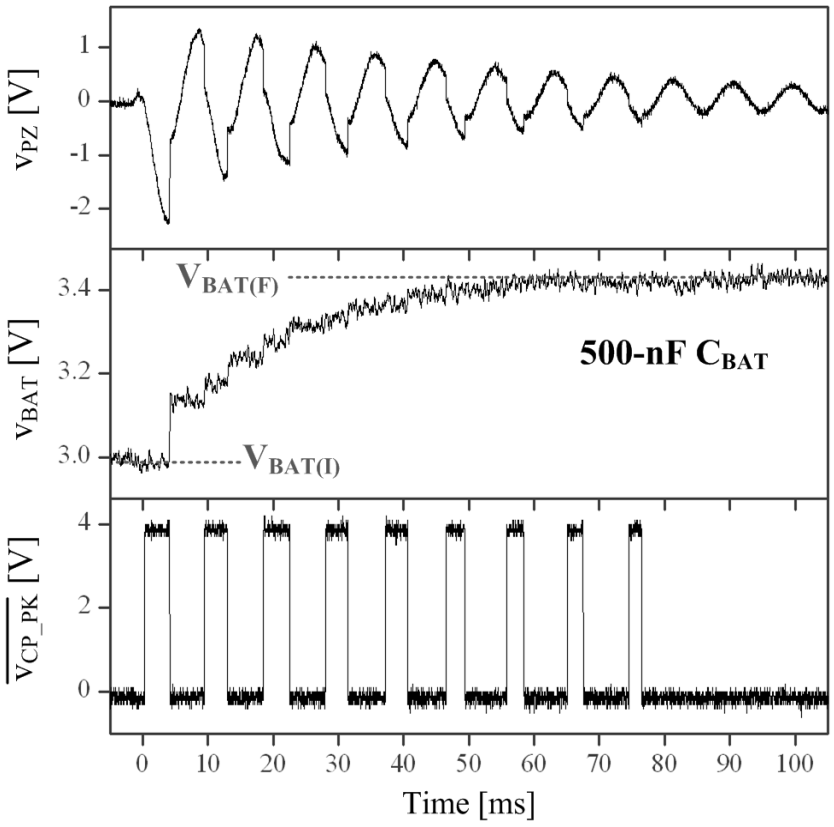

Figure 3.20. End-to-end harvesting waveforms for a 3-g weight.

η_{TOTAL} incorporates the collective performance of the transducer (η_{PZ}) and the harvester (η_H), which means η_{PZ} is η_{TOTAL}/η_H or roughly 14% – 20% when assuming (from Figure 3.16(a)) η_H is 45% on average. Although this simple analysis is by no means accurate or complete, it shows that mechanical losses are significant at around

80% and that conditioning the transducer to increase P_{IN} is as important as reducing the losses across the switched-inductor converter (i.e., increasing η_H).

3.5. Summary

The prototyped 2-µm CMOS switched-inductor piezoelectric harvester developed, experimentally evaluated, and presented in this chapter generated and steered up to 30 µW from a periodic 72-µW piezoelectric source directly into a capacitor or battery. In doing so, the harvester increased the electromechanical damping force of the piezoelectric cantilever to raise the mechanical-to-electrical conversion efficiency by up to 78%. The system also harnessed up to 659 nJ from non-periodic vibrations with 6.1 ± 1.5% to 8.8 ± 6.9% end-to-end mechanical-electrical efficiencies. One key feature of the presented harvester is that it eliminates the need for a bridge rectifier. As a result, the system no longer (*i*) places an input threshold imposed by diodes and/or the output voltage on mechanical vibrations, (*ii*) loses power across an otherwise additional stage (i.e., across a rectifier), or (*iii*) limits how much the circuit dampens the transducer. Conditioning the piezoelectric device to increase output power is an important attribute, as is the relatively simple, and low-power, control strategy the system adopts to energize and de-energize the inductor directly into the energy-storage device. The bridge-free prototype featured efficiency below 50% due to the dominant conduction losses for the tested power range. Nonetheless, as the simulation results corroborate, balancing the losses, for instance, by enlarging the switches can improve the efficiency. The harvester was also able to harness energy from short, aperiodic mechanical vibrations, which are more prevalent than the periodic counterparts in real-life applications, such as in human motion, wind-propelled movements, and vibrations produced by crashing objects.

CHAPTER 4

ENERGY-INVESTMENT STRATEGIES

Harvesting kinetic energy in motion and vibrations by employing piezoelectric transducers provides a viable alternative to tiny batteries because the transducers draw power from their surroundings, which serve as a vast energy tank. Because ambient vibrations generate AC piezoelectric voltage but most electronics need DC voltage for their operation, many harvesting systems utilize bridge-based full- or half-wave rectifiers to harness the power from the transducer. However, the inherent threshold and need for an output conditioning circuit of the bridge-based systems can limit the performance and applications of the piezoelectric-energy harvesters.

The bridge-free switched-inductor harvester introduced in Chapter 3 removes the bridge rectifier and its inherent threshold limitation coupled to the output battery voltage. More importantly, the switched-inductor converter allows the transducers to build up higher voltage than the output battery voltage so that the harvester can draw more energy than bridge rectifiers harness from the same vibrations. However, even with this switched-inductor circuit, the generated and conditioned voltage of the transducer is small in amplitude, and so is the output power, if the vibration is weak and/or the piezoelectric coupling factor is low. As a matter of fact, the versatility of switched-inductor converters allows a harvester to condition the transducer voltage to improve the energy conversion performance of the transducer and increase the output power. This chapter will introduce, review, and compare various switched-inductor circuits that can augment the output power of piezoelectric-energy harvesters.

4.1. Role of Investment

Fundamentally, when energy harvesters “harvest” the kinetic energy in vibrations, they

convert and remove some portion of the mechanical energy of a moving transducer into an electrical domain. In other words, harvesters dampen the movements of the transducer to supply electrical power to their outputs. Since micro-scale kinetic-energy transducers typically feature a low electromechanical-coupling factor and limited space for movements, they can capture only a fraction of the kinetic energy and produce only low electrical power [45], [141]–[147], [152]. This low conversion performance implies that the damping forces of the miniaturized transducers are weak [147], [191]. To increase the amount of converted electrical energy from a given mechanical input, harvesting circuits can condition the transducer to boost the damping force that loads the vibration, as long as this force is below a threshold beyond which vibrations cease to generate lesser energy than optimal. The optimal damping condition under which the transducer generates the maximum electrical power occurs when the electrical damping increases up to the mechanical damping of the transducer [191]–[192]. For tiny transducers, because the low electromechanical-coupling factor weakens the loading from the electrical side, the vibration amplitude of the device is set primarily by external mechanical stimulations and is virtually independent of the electrical loading. This means that increasing the electrical damping force in miniaturized harvesters will raise the output power in a monotonic fashion.

In piezoelectric transducers, the voltage across the piezoelectric capacitance C_{PZ} establishes the electrical damping force against which vibrations work to generate power [193]–[194]. This means that a harvester circuit can invest energy to C_{PZ} to strengthen the damping force and draw more power from vibrations compared to the output of a zero-investment case. Figure 4.1 illustrates two voltage waveforms of piezoelectric transducers without and with an initial investment. When there is no investment, during a half vibration cycle, v_{PZ} increases from 0 V to Δv_{PZ} and C_{PZ} accumulates the piezoelectrically generated energy as follows:

$$E_{PZ} = 0.5C_{PZ}\Delta v_{PZ}^2, \tag{4.1}$$

which is the amount which can be gleaned by a harvester circuit. On the other hand, if a system invests initial energy E_{PC} to pre-charge C_{PZ} to V_{PC} and then lets the vibration move the open-circuited piezoelectric device for the same half cycle, v_{PZ} will increase from V_{PC} to $(V_{PC} + \Delta v_{PZ})$ and C_{PZ} will accumulate

$$E_{PZ(INV)} = 0.5C_{PZ}\left(V_{PC} + \Delta v_{PZ}\right)^2. \tag{4.2}$$

Note that this derivation assumes that the electrical loading from the pre-charging is negligible as miniaturized piezoelectric transducers feature low electromechanical-coupling factors. That is, the displacement of the transducer and the amount of charge generated are the same in the two cases. The net energy harvested by the system, discounting the initial investment, is

$$\begin{aligned} E_H &= E_{PZ(INV)} - E_{PC} = 0.5C_{PZ}\left(V_{PC} + \Delta v_{PZ}\right)^2 - 0.5C_{PZ}V_{PC}^2 \\ &= 0.5C_{PZ}\left(\Delta v_{PZ}\right)^2 + C_{PZ}V_{PC}\Delta v_{PZ} \end{aligned}. \tag{4.3}$$

This equation reveals that investing E_{PC} results in the extra harvested energy of $C_{PZ}V_{PC}\Delta v_{PZ}$ compared to the zero-investment case as long as E_{PC} does not over-damp the transducer movements.

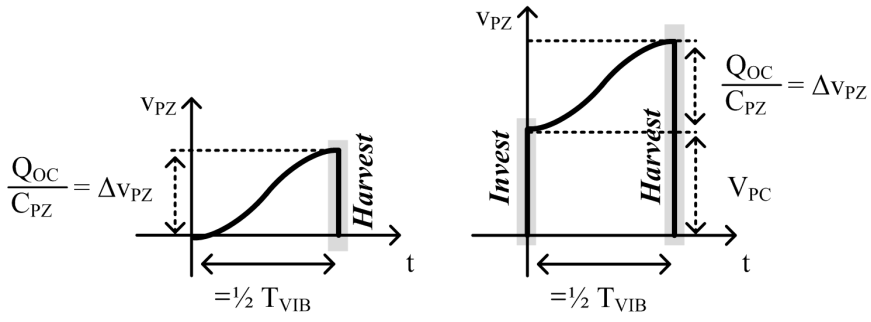

Figure 4.1. Piezoelectric voltage waveforms without and with an initial investment.

Unlike the previous piezoelectric-energy harvesters, energy-investing harvesters exhibit bi-directional energy flow. Figure 4.2, a modified version of Figure 2.1, illustrates the bi-directional energy flow of investing piezoelectric harvesters. As before, a piezoelectric transducer converts mechanical energy E_{ME} and stores E_{PZ} in its inherent capacitance C_{PZ}, but the investing harvester can now pre-charge the transducer with E_{PC} to induce the transducer to increase E_{PZ}. The system can harvest E_H from C_{PZ} and charge the output energy reservoir with E_{CHG}. Because practical circuits consume power, how the system transfers energy during investing and harvesting operations determines how much net energy the system can gain from vibrations. In particular, the energy-investing schemes and the circuit implementations can vary based on how the system procures E_{PC}. For instance, the harvester can pre-charge C_{PZ} by directly re-investing the harvested energy E_H from the input. On the other hand, the harvester can derive the investing energy E_I from its output energy reservoir to supply E_{PC}. The harvester can also combine the harvested energy from the input and the invested energy from the output to pre-charge the piezoelectric transducer. The following sub-chapters will review and present these possible investing harvester strategies and circuit designs.

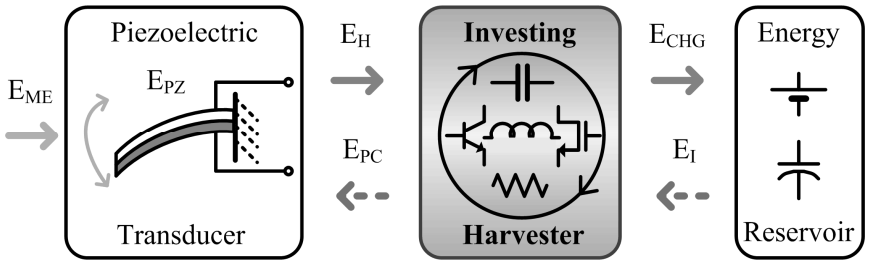

Figure 4.2. Energy-investing piezoelectric harvester architecture.

4.2. Re-invest Harvested Energy

One means of deriving pre-charge energy E_{PC} for C_{PZ} is to take it from harvested energy E_H directly. A system first harvests energy from its input piezoelectric transducer, and then, instead of transferring all the energy to its output, it invests some portion or all of

the harvested input energy back into the transducer. Re-investing input energy this way strengthens the damping force of the piezoelectric transducer for the ensuing vibration cycles and ultimately increases the harvested energy.

4.2.1. Prior Arts: Bridge-based Re-investing Harvesters

The authors of [195]–[201] applied the idea of using the input energy to improve harvesting performance by employing a parallel switched-inductor circuit between a transducer and a full-wave diode-bridge. Figure 4.3 demonstrates the system schematic and the waveforms of this parallel synchronized-switch-harvesting-on-inductor (SSHI) technique. This approach operates similar to that of the full-wave diode-bridge harvester explained in Chapter 2 except for the two short durations between the positive and negative conduction phases. That is, in a steady state, after the system transfers the input energy through the bridge during the positive conduction phase T_{COND}^{+}, the switch S_P turns on to harvest the remaining input energy in C_{PZ} and energize L_P for a quarter L_PC_{PZ}-resonance period $0.5\pi\sqrt{(L_PC_{PZ})}$. However, instead of sending the harvested energy to the output, the system re-invests the energy to charge C_{PZ} with negative polarity by keeping S_P engaged for another quarter L_PC_{PZ}-resonance period. Although the negative voltage after the re-investment will not reach the barrier voltage $-(V_{RECT}+2V_D)$ because of the losses in the current path, the amount of charge $Q_{BAR(P\text{-}SSHI)}$ required to overcome the barrier of the bridge rectifier can be much smaller than that of a conventional bridge rectifier as long as the switch losses are minimized. The negative half cycle operation is analogous to this positive operation.

By re-investing the input energy through the switched-inductor network S_P-L_P, this system can drive the following amount of charge through the bridge rectifier every half cycle.

$$Q_{RECT(P\text{-}SSHI)} = Q_{OC} - Q_{BAR(P\text{-}SSHI)}. \tag{4.4}$$

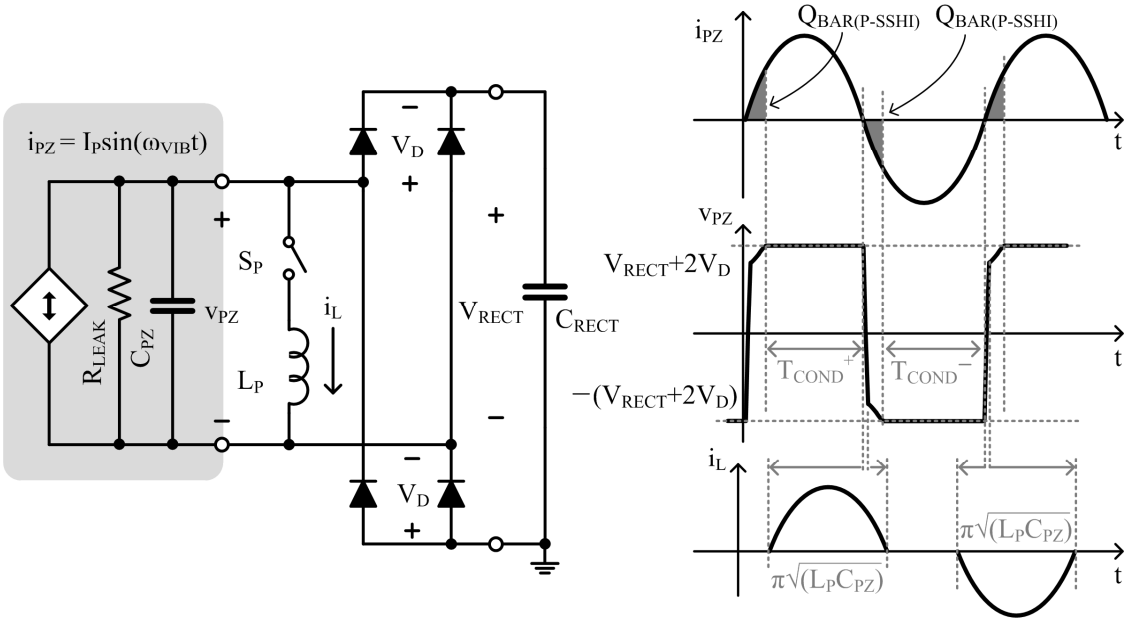

Figure 4.3. Re-investing input energy using the parallel synchronized-switch-harvesting-on-inductor (SSHI) technique.

Q_{OC} represents the total charge that the vibrating piezoelectric transducer can generate in the open-circuited condition during a half cycle as demonstrated in Figure 2.3. Since the bridge rectifier output receives this amount of charge twice in a cycle with V_{RECT} voltage, the output energy per cycle is

$$\begin{aligned} E_{RECT(P\text{-}SSHI)} &= 2Q_{RECT(P\text{-}SSHI)}V_{RECT} = 2Q_{OC}V_{RECT} - 2Q_{BAR(P\text{-}SSHI)}V_{RECT} \\ &= 4C_{PZ}V_{OC}V_{RECT} - E_{LOSS(P\text{-}SSHI)} \end{aligned}, \qquad (4.5)$$

where Q_{OC} is $2C_{PZ}V_{OC}$ as defined in Figure 2.3, and $E_{LOSS(P\text{-}SSHI)}$ reflects the energy losses occurred in this re-investing system. Comparing this performance to the best case (i.e., when $V_{RECT} = 0.5V_{OC}$) of a full-wave diode-bridge rectifier in (2.3) reveals that the parallel-SSHI approach can harness twice as much energy as the maximum of the bridge-rectifier under ideal conditions (i.e., no losses and zero V_D) for the sake of intuitive comparison. Note that, unlike (2.3), whose output is a parabolic function of V_{RECT} as

shown in Figure 2.10, (4.5) seems to imply that the harvested energy can indefinitely rise if V_{RECT} increases without limits. In practice, various parameters such as the breakdown voltage of a process, the efficiency of the switched-inductor circuit, and the over-damping of the transducer will limit the V_{RECT} amplitude. However, the specific penalty of high V_{RECT} for this parallel-SSHI strategy is the high input barrier formed by the bridge rectifier. This barrier can prohibit the harvesting of the ambient vibration-energy with miniaturized piezoelectric transducers.

Although it can draw more energy from vibrations than can occur with normal bridge rectifiers, the parallel-SSHI technique does not expose the transducer to a stronger damping force than that of standard bridge rectifiers. This is because the diode bridge clamps the piezoelectric voltage at the same amplitude (i.e., V_{RECT}) as in the standard cases. Nevertheless, because the switched-inductor circuit operation allows longer conduction time than that of the standard rectifier, which leads to higher average voltage amplitude, the average damping force can be stronger than that of conventional bridge-based harvesters.

The same research group that developed the parallel SSHI presented a different re-investing scheme by employing a switched-inductor circuit in a series with a piezoelectric transducer and a bridge rectifier [197]–[200], [202]–[205]. Figure 4.4 illustrates the proposed schematic, which is called the series-SSHI approach, and its waveforms. The system waits until maximum v_{PZ} and then harvests C_{PZ} energy to energize L_S and C_{RECT} simultaneously by closing switch S_S. C_{PZ} will quickly be discharged to 0 V, but by keeping S_S engaged until inductor current i_L depletes to 0 A, the circuit can re-invest some portion of the harvested input energy to pre-charge C_{PZ} at $-V_{PC}$. Because of this pre-charging, the ensuing negative half cycle can experience increased voltage and strengthened damping forces in the piezoelectric transducer. At the negative peak, the system again engages S_S to harvest energy in C_{PZ} to charge L_S and C_{RECT}, and re-invests some of the energy back into the input to pre-charge C_{PZ} to V_{PC}.

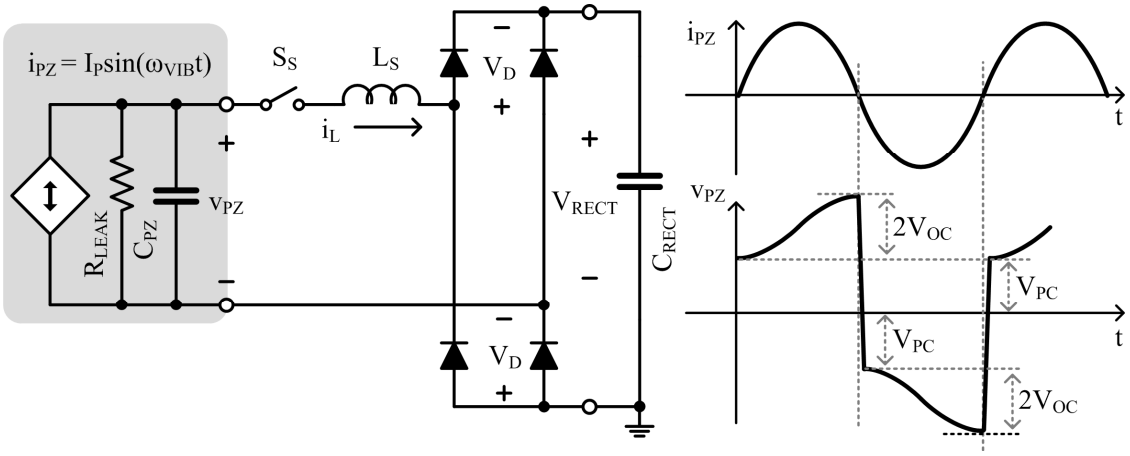

Figure 4.4. Re-investing input energy using the series synchronized-switch-harvesting-on-inductor (SSHI) technique.

In steady state, the system harvests input energy at the positive peak ($2V_{OC}+V_{PC}$) and immediately re-invests the harvested energy back into pre-charge C_{PZ} to $-V_{PC}$. Since this energy transaction occurs every half cycle, the amount of energy reached at the bridge rectifier output in a cycle is

$$\begin{aligned} E_{RECT(S\text{-}SSHI)} &= 2\left(0.5C_{PZ}\left[\left(2V_{OC}+V_{PC}\right)^2 - V_{PC}^2\right]\right) - E_{LOSS(S\text{-}SSHI)} \\ &= C_{PZ}\left(4V_{OC}^2 + 4V_{OC}V_{PC}\right) - E_{LOSS(S\text{-}SSHI)} \end{aligned}, \qquad (4.6)$$

where $E_{LOSS(S\text{-}SSHI)}$ represents the aggregated sum of the losses in the system. This result indicates that re-investing this way can harvest more energy than the best case of the standard bridge rectifier by a factor of $4(1+V_{PC}/V_{OC})$, assuming the losses in both circuits are similar. When compared to the parallel-SSHI strategy of (4.5), the harvested energy ratio without losses of series- to parallel-SSHI approaches is ($V_{OC}+V_{PC}$) to V_{RECT}. The harvesting performances will be determined by V_{PC} and V_{RECT} values, but if V_{RECT} is set to be lower than V_{OC} to allow single-cycle harvesting, the series approach will outperform the parallel approach. Unlike the parallel technique, this series-SSHI method augments the amount of the harvested power by strengthening the electrical damping force of the piezoelectric device. In other words, because the series S_S-L_S de-couple the

piezoelectric transducer from the bridge-rectifier output, the bridge rectifier no longer clamps the amplitude of the electrical damping force across the material.

These parallel- and series-SSHI approaches re-invest input energy to enhance the harvesting performance. However, because both systems employ bridge rectifiers to convert AC voltage into DC voltage, these re-investing systems retain some of the drawbacks of the bridge rectifiers. For example, the vibrations driving the piezoelectric transducers need to be strong enough to generate higher piezoelectric voltage amplitudes than the threshold voltage ($V_{RECT}+2V_D$) for bridge rectifiers to harness the input energy. If vibrations are reliable and consistent, the parallel switched-inductor circuit can build up the piezoelectric voltage v_{PZ} across multiple vibration cycles by re-investing all the harvested energy back to C_{PZ} until the voltage reaches the barrier [200]. Accumulating v_{PZ} this way would allow a parallel-SSHI system to use high V_{RECT} to increase the harvested power. Unfortunately, because ambient motion and vibrations are mostly inconsistent, and frequently, the result of irregular impact-induced motion, as when a falling object hits the ground, single-cycle harvesting is more practical than accumulating v_{PZ} across multiple cycles for harvesting. Another way to handle the threshold problem is to use an output conditioning circuit as discussed in Chapter 2.3. If the output of the rectifier can adaptively change according to the vibration strength, it would not only alleviate the threshold problem, but also increase the harvested power. However, the output conditioning circuits for these SSHI re-investing harvesters will face similar challenges as discussed in Chapter 2.3.

4.2.2. Bridge-free Re-investing Harvester

It has been shown in Chapter 3 that a switched-inductor converter can eliminate the bridge rectifiers and their disadvantages while offering improved piezoelectric-energy harvesting performance. Figure 4.5 shows a bridge-free switched-inductor strategy for re-investing piezoelectric-energy harvesters. When vibrations move the piezoelectric

cantilever into the positive half, the system waits until the voltage across piezoelectric capacitance C_{PZ} peaks, which represents that the energy E_{PZ}^{+} that C_{PZ} accumulated during the positive cycle has reached its maximum. At that peak, the system harvests the energy from C_{PZ} to energize inductor L_H, and after a quarter L_HC_{PZ}-resonance period, which is a negligible fraction of the milliseconds vibration cycle, L_H will possess all the harvested energy E_H^{+}. Instead of depositing this energy in the output, the harvester re-invests the energy back in pre-charge C_{PZ}, conditioning the piezoelectric device to harness the increased amount of kinetic energy into C_{PZ} during the negative half cycle. At the negative peak, the switched-inductor circuit then quickly harvests energy from C_{PZ} and charges the output battery V_{BAT} by energizing and de-energizing L_H, respectively. This negative-cycle transfer concludes a single cycle, and the sequence repeats as long as vibrations persist.

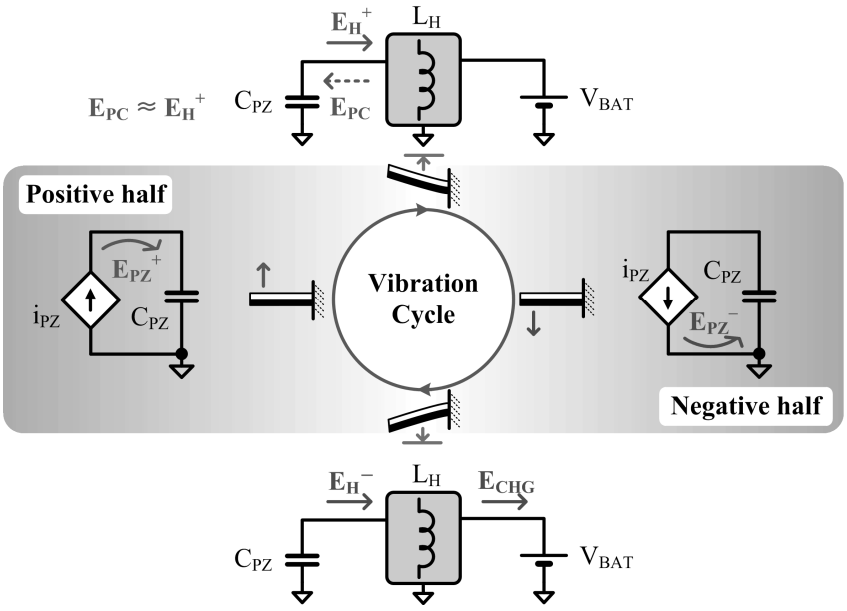

Figure 4.5. Re-investing input energy using a bridge-free switched-inductor converter.

The switched-inductor circuit proposed in Figure 4.6 implements the energy flow shown in Figure 4.5. Here, switch S_C opens to allow vibrations to charge C_{PZ} (with i_{PZ}) until v_{PZ} peaks at $2V_{OC}$, at which point S_C closes to discharge C_{PZ} into L_H for a quarter

L_HC_{PZ}-resonance period $0.25T_{LC}$. Note that $2V_{OC}$ is used instead of V_{OC} to be consistent with the previous discussion (e.g., Figure 2.3). To re-invest the input energy directly back into the transducer, S_C closes another $0.25T_{LC}$ to pre-charge C_{PZ}. The pre-charged voltage amplitude V_{PC} can closely approach $2V_{OC}$ if the losses in S_C are minimized. Then, S_C opens to allow the vibrations to charge C_{PZ} further in the negative direction until v_{PZ} reaches its negative peak. At this point, S_C closes again to harvest the energy in C_{PZ}, but only for $0.25T_{LC}$ to deplete C_{PZ}, and then opens to steer the inductor current i_L through diode D_B into V_{BAT} until i_L drops to zero, at which point one vibration cycle ends.

If the vibrations are reliable and steady, S_C can remain closed another $0.25T_{LC}$ to re-deposit the energy in L_H back into C_{PZ}, rather than to charge V_{BAT}. In other words, the circuit can re-invest all the energy it harvests across several cycles to continually raise the electrostatic force (i.e., v_{PZ}) against which motion works to generate power. In this way, the circuit may harvest an increasing amount of energy until either the voltage reach the breakdown limits of the switches, or the conduction losses, which increase with input power, overwhelm energy gains, or the force dampens the vibrations too much. However, as mentioned, since the ambient vibrations cannot guarantee such consistency, completing a harvesting operation within a single vibration-cycle is practical.

Since the circuit re-invests the energy required to charge C_{PZ} to $2V_{OC}$ in the positive half cycle back into C_{PZ}, C_{PZ} pre-charges to $-V_{PC}$, whose amplitude is approximately $2V_{OC,}$ when losses are small. The harvester then allows motion to charge C_{PZ} further, another $2V_{OC}$ from $-2V_{OC}$ to $-4V_{OC}$, before finally draining C_{PZ} fully into V_{BAT}. Hence, the net amount of energy that can charge V_{BAT} per cycle is

$$\begin{aligned} E_{CHG(RE)} &= E_H^+ - E_{PC} + E_H^- - E_{LOSS(RE)} \\ &\approx 0.5C_{PZ}\left[(2V_{OC})^2 - (2V_{OC})^2 + (4V_{OC})^2\right] - E_{LOSS(RE)}\,, \\ &= 8C_{PZ}V_{OC}^2 - E_{LOSS(RE)} \end{aligned} \tag{4.7}$$

which reveals that this re-investing bridge-free harvester can theoretically harness eight times more energy than the best of standard bridge rectifiers discussed in Chapter 2. In addition, because this system does not impose a threshold on the input vibration strengths, the harvester can collect the amount of energy that (4.7) predicts from both periodic and aperiodic mechanical stimulations, without the aid of extra output conditioning circuits.

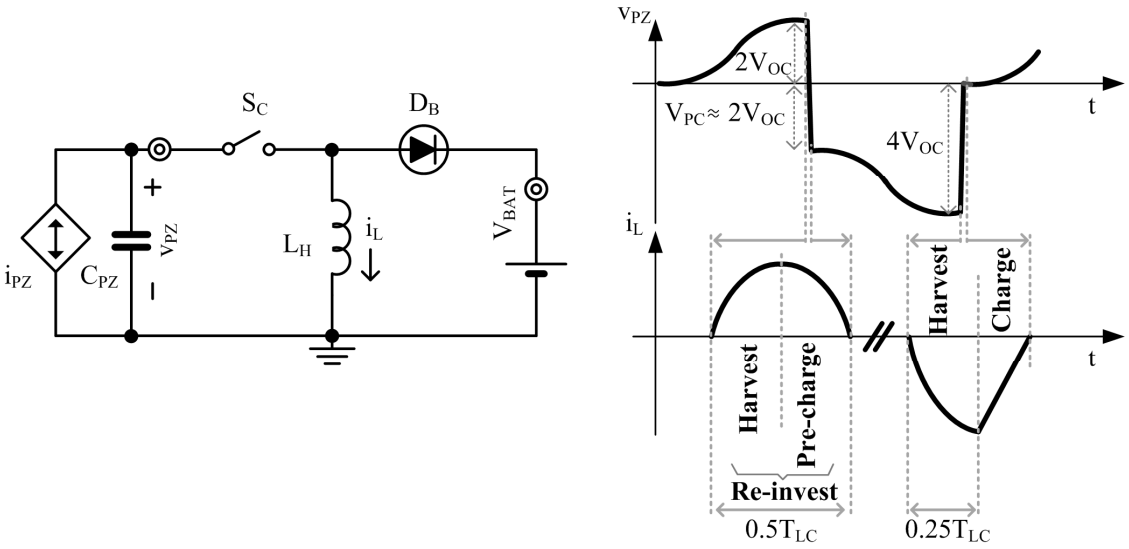

Figure 4.6. Schematic and waveforms for the proposed re-investing bridge-free harvester.

4.3. Invest Battery Energy

The re-investing approach is simple and efficient as it exploits the natural resonance of L_H and C_{PZ} by using only one switch. Nonetheless, one drawback of the re-investing method is that the harvested energy in a half vibration may not establish sufficient electrical damping force for miniaturized piezoelectric transducers. Deriving energy from a battery output, rather than from the harvested input, can raise the investment limit as the battery typically reserves much more energy than a piezoelectric device can generate within a half vibration cycle. A harvester circuit can invest the energy from the battery to pre-charge a piezoelectric transducer at the beginning of a vibration cycle. Vibrations

subsequently work against the increased electrical damping force during a half cycle and store the converted energy in the piezoelectric capacitance C_{PZ} until its voltage peaks, at which point the circuit collects the energy in C_{PZ} to charge the battery. Immediately after the battery charging event, the next half cycle operation can begin.

4.3.1. Prior Arts: Multiple-inductor Investing Harvesters

The authors of [194] implemented a harvester system that invests energy from a battery to pre-bias a piezoelectric transducer. Figure 4.7 shows the simplified schematic of the power stage and its operating waveforms. The circuit invests energy from the investing battery V_{BAT_I} to pre-bias C_{PZ} to $\pm V_{PB}$ by using one of the investing-buck switched-inductor circuits. When the system detects the peaks of the vibration, which can be spotted by monitoring the peaks of piezoelectric voltage v_{PZ}, it harvests the energy in C_{PZ} and charges the harvesting battery V_{BAT_H} through the harvesting-buck converter. Note that the speed of these energy transfers is typically much faster than the vibration; therefore, the position of the piezoelectric transducers during the energy transactions virtually remains the same.

To pre-bias C_{PZ} to V_{PB}, the system connects the negative terminal of v_{PZ} to ground by closing S_{G1}, then engages switch S_{I1} to energize investing inductor L_{I1} and C_{PZ} from V_{BAT_I}. The amount of investment, or the amplitude of V_{PB} which can ideally increase to $2V_{BAT\_I}$, can be controlled by the turn-on time of S_{I1}. When the system opens S_{I1}, diode D_{I1} will deplete the energy in L_{I1}, concluding the investing transaction. On the other hand, to harvest and charge, at the positive peak of v_{PZ}, switch S_{H1} turns on to energize harvesting inductor L_H and V_{BAT_H} from the input until C_{PZ} depletes. At that point, the system turns off S_{H1} to transfer all the remaining energy in L_H (i.e., inductor current i_L) into V_{BAT_H} until diode D_H stops i_L at 0 A. The negative half cycle operation is symmetrical to its positive counterpart.

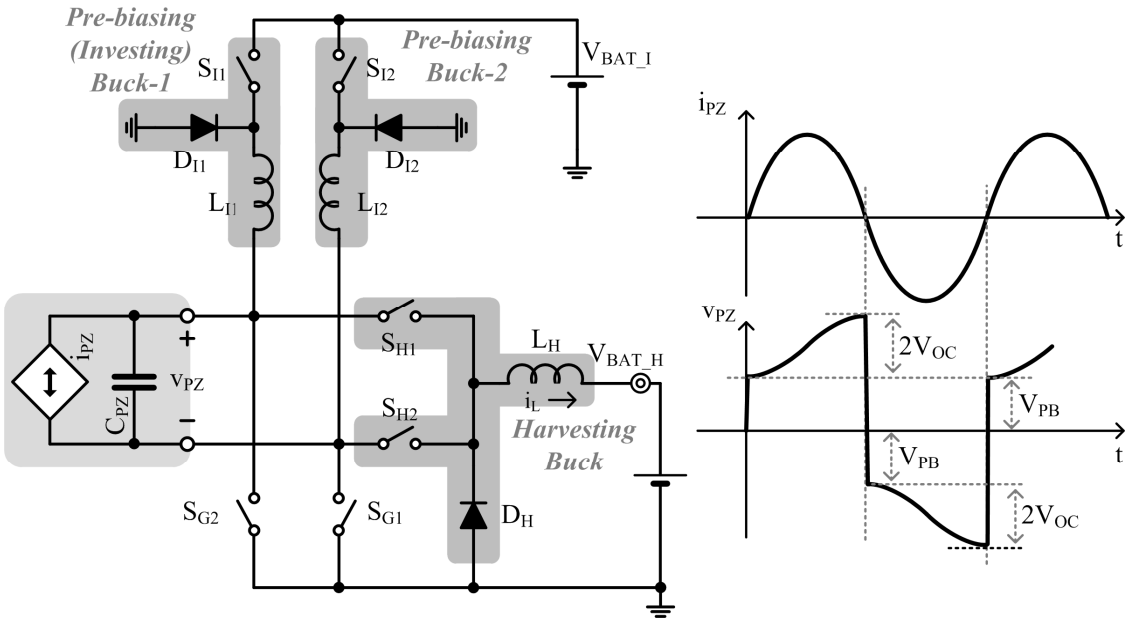

Figure 4.7. Investing battery energy using pre-biasing H-bridge circuit.

Every half cycle, the system invests battery energy to pre-bias the amplitude of v_{PZ} to V_{PB} and harvests C_{PZ} energy at $(2V_{OC}+V_{PB})$. Hence, the net amount of energy that this harvester can charge into a battery in one vibration cycle is

$$\begin{aligned} E_{CHG(PB)} &= 2\left(0.5C_{PZ}\left[-V_{PB}^2+\left(2V_{OC}+V_{PB}\right)^2\right]\right)-E_{LOSS(PB)} \\ &= C_{PZ}\left(4V_{OC}^2+4V_{OC}V_{PB}\right)-E_{LOSS(PB)} \end{aligned}, \tag{4.8}$$

where $E_{LOSS(PB)}$ is the sum of the losses of this pre-biasing approach. Note that this result appears to be the same as that expressed in (4.6) except that V_{PC} for the re-investing series-SSHI scheme is now replaced with V_{PB}. However, this difference can lead to a large difference in harvesting performance because the amplitude of V_{PC} for the re-investing approach is lower than $2V_{OC}$ while the amplitude of V_{PB} can rise up to $2V_{BAT\_I}$, which is a design parameter that the system can increase.

Another piezoelectric-energy harvester that invests battery energy to improve harvesting performance is reported in [206]. Figure 4.8 illustrates the schematic and the waveforms of the energy-injecting piezoelectric harvester. The main idea and the

operation sequences are similar to those in the previous example as the waveforms evidence. However, this system uses one less inductor and battery, which can be a considerable improvement for small-scale piezoelectric harvester systems.

At the beginning of a new vibration cycle (or the end of the previous cycle), the system invests energy from battery V_{BAT} to C_{PZ} through the energy-injecting path shown in the gray area of Figure 4.8. More specifically, to pre-charge C_{PZ} to $+V_{INJ}$, the system turns on switches S_{I1} and S_{G1} to energize L_I and C_{PZ} from V_{BAT}. Because this circuit configuration connects V_{BAT} to the discharged C_{PZ} and L_I in a series, the voltage across C_{PZ}, which can be controlled by the turn-on time of S_{I1} and S_{G1}, is ideally able to rise to $2V_{BAT}$ when diode D_{I1} stops the current flow at 0 A. After this investment, the vibration raises the piezoelectric voltage by $2V_{OC}$ until the system starts harvesting at the peak of v_{PZ}. The harvesting for the positive half starts by closing the switch S_{H1} to energize L_H from C_{PZ}. When C_{PZ} fully discharges in about a quarter the L_HC_{PZ}-resonance period, the system opens S_{H1} to charge V_{BAT} from L_H. Note that this L_H-de-energizing process will not charge C_{PZ} in the other direction (which was also the case in the series-SSHI example in Chapter 4.2.1) because the clamping diode D_{CLP} will conduct the inductor current when v_{PZ} falls below the ground. The positive cycle operation ends when L_H is depleted, and the system immediately injects energy into C_{PZ} to pre-charge C_{PZ} to $-V_{INJ}$ by closing switches S_{I2} and S_{G2}. After the vibrations work against the strengthened electrical damping force during the negative half, the system harvests the energy in C_{PZ} and charges V_{BAT} through the switched-inductor operation of S_{H2}-L_H.

Both of the investing approaches effectively increase the electrical damping force for piezoelectric transducers to augment the amount of power extracted from a given vibration. Because these systems use switched-inductor circuits for harvesting, they are able to harvest low voltage regardless of the output battery voltage. The switched-inductor circuits are adopted in these investing harvesters to achieve high efficiency energy transfer between two capacitive energy storage elements (i.e., C_{PZ} and V_{BAT}). As

will be discussed in later sections, the efficiency of the system is crucial because the investing (as well as re-investing) harvesters will be meaningless if the losses occurring during the investment become larger than the gains from the investments. However, since the power inductors are bulky and expensive components, these investing approaches may burden the space and cost budgets of miniaturized piezoelectric harvesting applications. Furthermore, the switched-inductor circuits in these systems are limited to pre-charge C_{PZ} up to twice the battery voltage at best. Because the electrical damping force is determined by the voltage across C_{PZ}, to build up strong electrical damping forces, these harvesters will require high voltage batteries which may be another challenging requirement for small-scale harvesting systems.

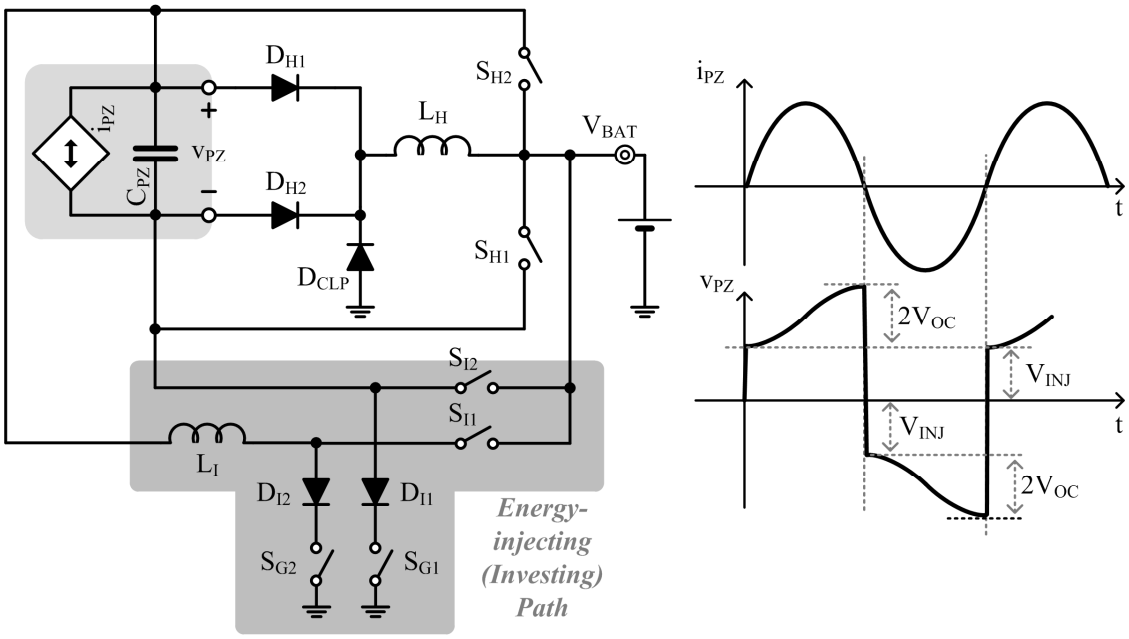

Figure 4.8. Investing battery energy using an energy-injection circuit.

4.3.2. Single-inductor Investing Harvester

Figure 4.9 shows a full-cycle operation of a single-inductor piezoelectric-energy harvester that invests battery energy to increase the electrical damping force of a piezoelectric transducer. When vibrations move the piezoelectric device to energize C_{PZ}

with E_{PZ}^{+} in the positive half, the single-inductor converter quickly harvests energy E_H^{+} to charge the battery V_{BAT} with E_{CHG}^{+}. Then the system immediately invests battery energy E_I^{+} to pre-charge the transducer with E_{PC}^{+} for the following negative half-cycle. The vibration works against the increased electrical damping force until the negative peak position of the cantilever and charges C_{PZ} with E_{PZ}^{-}. The single-inductor harvester again quickly harvests E_H^{-} from C_{PZ} and charges E_{CHG}^{-} to V_{BAT}, then invests E_I^{-} from V_{BAT} and pre-charges E_{PC}^{-} to C_{PZ} for the ensuing positive half cycle.

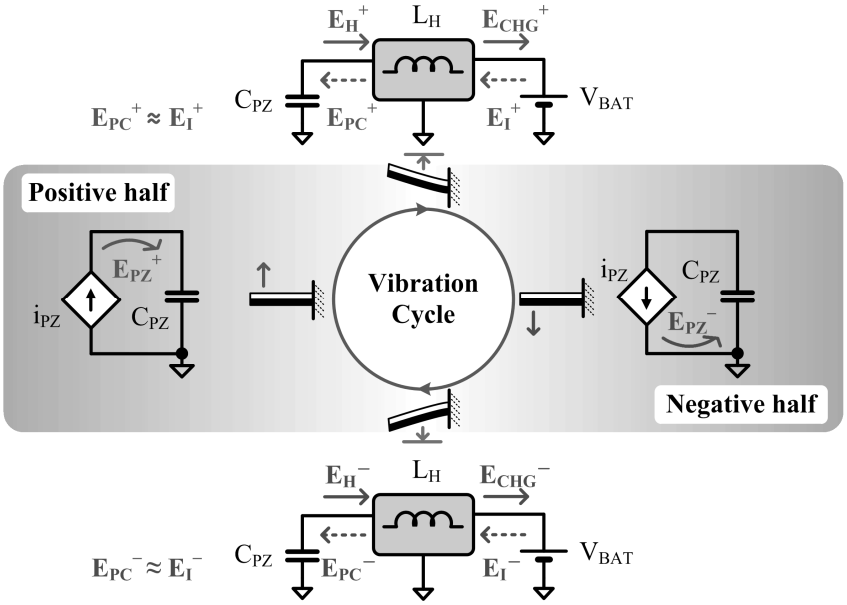

Figure 4.9. Investing battery energy using a single-inductor switching converter.

The energy-flow sequence and the fundamental rationale for investing battery energy are the same as for the previous approaches. The important and different part of the proposed harvester is the single-inductor switching converter, which invests battery energy and harnesses piezoelectric energy. This circuit should exhibit no pre-charging voltage limitation caused by the battery voltage. The circuit proposed in Figure 4.10 can meet these requirements by multiplexing the inductor in time and by adopting buck–boost switching converter architectures. At the positive peak of the piezoelectric voltage v_{PZ}, the system harvests the input energy to charge battery V_{BAT} by energizing inductor L_H

through switches S_C and S_{X2} and de-energizing L_H through the switches S_{X1} and S_{B1}. Immediately after this, the circuit derives energy from V_{BAT} to pre-charge C_{PZ} by energizing and de-energizing L_H through S_{B2}-S_{X2} and S_C-S_{X2}, respectively. The harvester then follows a similar sequence at the negative peak of v_{PZ}. To harvest and charge, S_C-S_{X2} drain C_{PZ} into L_H, and S_{B2}-S_{X2} empty L_H into V_{BAT}. Then to invest and pre-charge, S_{B1}-S_{X1} invest V_{BAT} energy into L_H, and S_{X2}-S_C drain L_H into C_{PZ}.

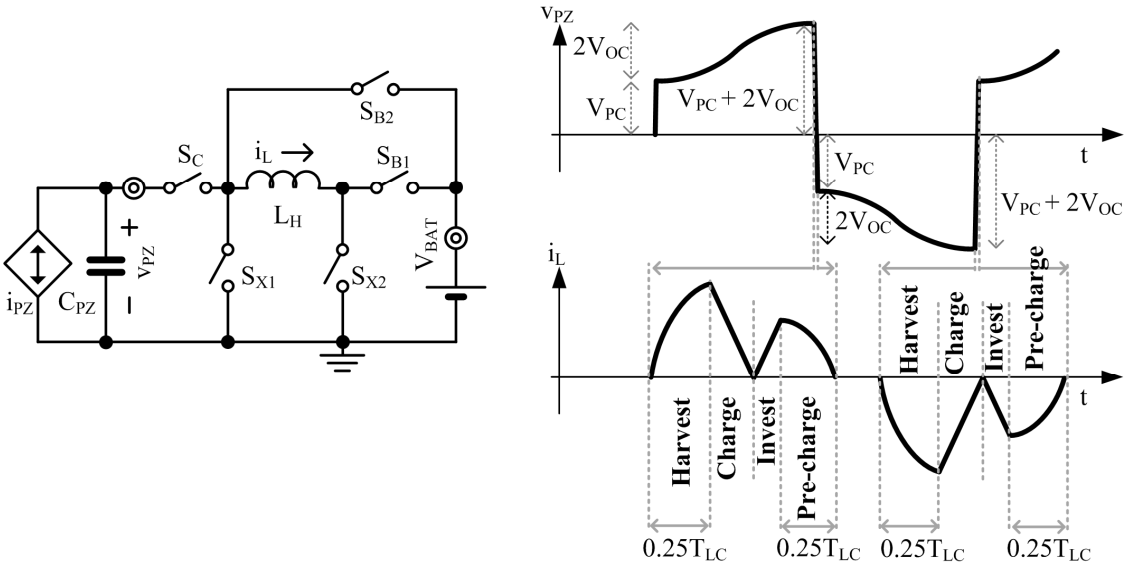

Figure 4.10. Schematic and waveforms for the proposed single-inductor investing harvester.

Analogous to the previous investing harvesters, this single-inductor system invests battery energy to pre-charge the amplitude of v_{PZ} to V_{PB} and harvests C_{PZ} energy at (V_{PC}+2V_{OC}). Hence, the net amount of energy that this harvester can charge into a battery in one vibration cycle is

$$\begin{aligned} E_{CHG(I\_L)} &= 2\left(0.5C_{PZ}\left[-V_{PC}^2+\left(V_{PC}+2V_{OC}\right)^2\right]\right)-E_{LOSS(I\_L)} \\ &= C_{PZ}\left(4V_{OC}^2+4V_{OC}V_{PC}\right)-E_{LOSS(I\_L)} \end{aligned}, \tag{4.9}$$

where $E_{LOSS(I\_L)}$ is the sum of the losses of this single-inductor battery-energy investing harvester system. As expected, this expression is the same as that for the previous

investing approaches. However, with the new system, the pre-charging voltage V_{PC} is not limited by the battery voltage. This is because the single-inductor converter in Figure 4.10 functions as a bi-directional non-inverting and inverting buck–boost converter operating in discontinuous-conduction mode (DCM) for the positive and negative half cycles, respectively. Therefore, as long as the battery energy is sufficient, the electrical damping force for the transducer can be strengthened regardless of the battery voltage amplitude.

4.4. Invest and Re-invest Energy

Investing battery energy can remove the limitation of the re-investing approach introduced in Chapter 4.2. When harvested energy from input alone is insufficient, another way to supply enough pre-charging energy is supplement (not replace) the harvested input energy with battery-derived energy. Figure 4.11 presents an energy-flow diagram of a hybrid investing strategy that invests the battery energy and re-invests the harvested input energy to C_{PZ} together. When vibrations charge C_{PZ} to its peak, the system first invests E_I from battery V_{BAT} to energize inductor L_H, which is then further energized with harvested energy E_H^+. The harvester now re-invests all the combined energy in L_H back into the input to pre-charge C_{PZ} for the next half cycle. Subsequently, C_{PZ} accrues the converted energy until the next peak of the C_{PZ} voltage. Then, the circuit harvests all the energy in C_{PZ} to charge the battery through the inductor.

It is possible to change the sequence of investing and re-investing. That is, at the positive peak, the system can first re-invest the harvested input energy back into C_{PZ} and then invest the V_{BAT} energy to C_{PZ} by energizing and de-energizing L_H twice. Nevertheless, since combining energy at L_H and de-energizing L_H at once allows one less de-energizing transaction, the proposed sequence can save the power lost in switches.

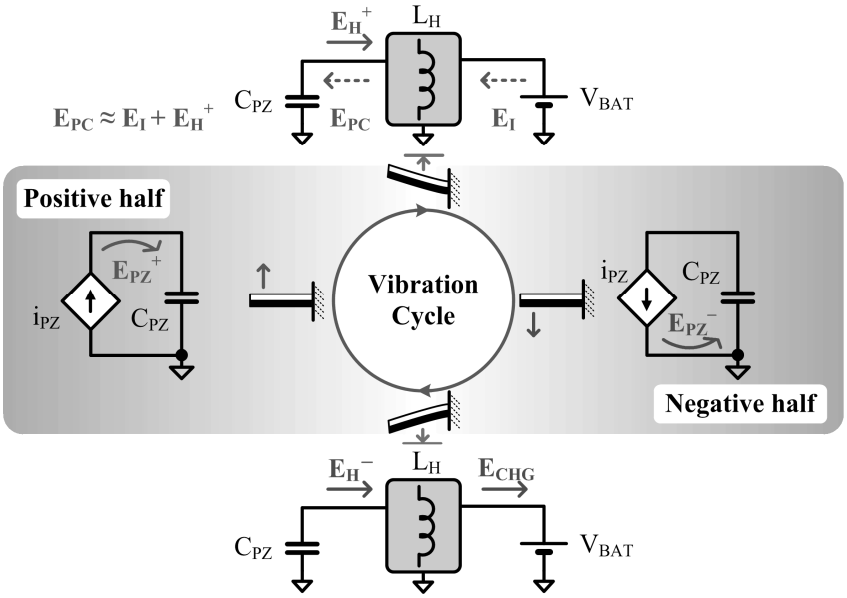

Figure 4.11. Investing and re-investing energy using a switched-inductor harvester.

The proposed switched-inductor circuit and the operating waveforms for the hybrid investing strategy are shown in Figure 4.12. The converter resembles the circuit in Figure 4.6 except that switch S_B here replaces active-diode D_B in Figure 4.6 to enable a bi-directional energy flow for the investment from V_{BAT}. The operation is also similar to the re-investing scheme, except that this system invests energy from V_{BAT} in advance to the re-investment by engaging S_B for investment time τ_{INV} to energize L_H as soon as v_{PZ} peaks in the positive vibration cycle. Next, the circuit executes the re-investment by first harvesting the energy in C_{PZ} to further energize L_H and then pre-charging C_{PZ} from L_H by turning on switch S_C until L_H exhausts its current i_L (i.e., energy). After that, motion charges C_{PZ} across the negative half cycle to its peak, which is when the harvester closes S_C for a quarter-L_HC_{PZ} resonance period to transfer all the harvested and invested energy in C_{PZ} to L_H and ultimately charge V_{BAT} by prompting S_B until i_L stops at 0 A.

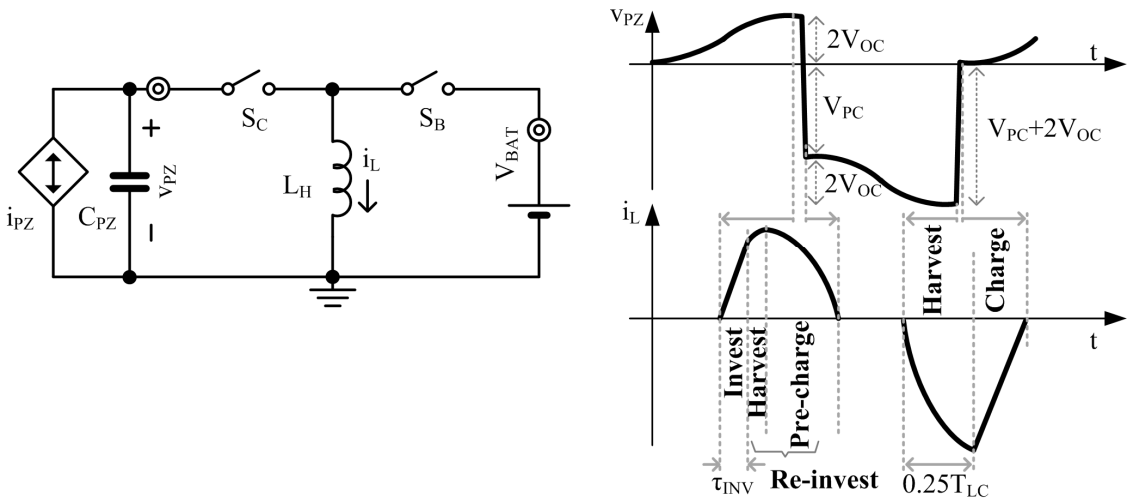

Figure 4.12. Schematic and waveforms for the proposed invest and re-invest harvester.

The harvesting occurs twice at $2V_{OC}$ and $-(V_{PC}+2V_{OC})$, and the combined investing occurs once to pre-charge C_{PZ} to $-V_{PC}$ as the waveform in Figure 4.12 depicts. Therefore, the net amount of energy that this technique can charge a battery in one vibration cycle is

$$\begin{aligned} E_{CHG(I\_RE)} &= 0.5C_{PZ}\left[(2V_{OC})^2 - V_{PC}^2 + (V_{PC}+2V_{OC})^2\right] - E_{LOSS(I\_RE)} \\ &= C_{PZ}\left(4V_{OC}^2 + 2V_{OC}V_{PC}\right) - E_{LOSS(I\_RE)} \end{aligned}, \tag{4.10}$$

where $E_{LOSS(I\_RE)}$ represents all the losses of this combined investing approach. Note that the system can control the amplitude of V_{PC} by controlling τ_{INV}. Thus, the proposed single-inductor switching converter can raise the electrical damping force to draw the increased amount of energy from vibrations without the limitations from both the input energy and output voltage.

4.5. Evaluation and Comparison

All three investing strategies presented in this chapter are capable of increasing the output power of a piezoelectric transducer. However, irrespective of the electronics used and the investment scheme adopted, there is an optimal electrical damping force with which to

draw the most power from the piezoelectric device [192]. The optimal point occurs when the electrical damping force set by the piezoelectric voltage equals the mechanical damping of the transducer. For small-scale energy transducers whose electromechanical-coupling factors are low, harvesting circuits often use high voltage to dampen the transducer [207]–[208]. However, because the breakdown voltage limits of conventional CMOS processes are usually lower than those with such high voltage levels, the breakdown voltage of semiconductor devices in harvester circuits often limits the electrical damping for the transducers before it reaches the optimal point defined by the mechanical parameters. Figure 4.13 shows two sets of graphs for ideal charging performances of the three investing strategies limited by the breakdown voltage of a CMOS process.

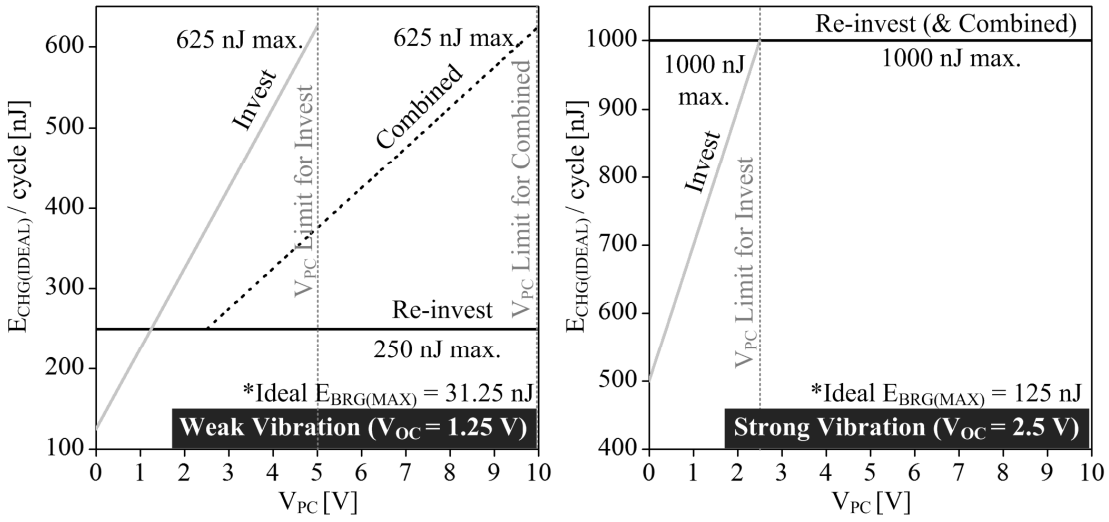

Figure 4.13. Charging performances of three investing strategies under weak and strong vibrations.

The examples are divided into weak and strong vibrations, because the combined investing technique becomes the same as that of the re-investing case if the vibration is strong enough for the harvester to pre-charge C_{PZ} (which is set to 20 nF for these illustrations) to the breakdown voltage without demanding any battery energy. Under weak vibrations, the re-investing technique can ideally harvest 250 nJ per cycle

regardless of pre-charging voltage V_{PC}. Assuming a 15-V breakdown voltage process, the investing technique can pre-charge C_{PZ} to ±5 V and harvest up to 625 nJ per cycle. The combined approach can also maximally harness 625 nJ per cycle even though the harvesting happens only once at the negative peak. This is because V_{PC} for the combined approach can reach –10 V, whereas the investing approach can use only ±5 V maximum. In contrast, under strong vibrations, the re-investing approach can ideally collect 1000 nJ per cycle, which coincides with the maximum harvesting performance of the investing strategy. Note that an ideal bridge rectifier could draw 31.25 nJ and 125 nJ at best from the same weak and strong inputs, respectively.

While these comparisons provide an intuitive perspective on the performances of three different approaches, a practical comparison must consider the losses accompanying the energy transactions in each system. In general, to reduce losses, it is better to limit the use of battery energy for investing. Battery energy in miniaturized systems is ultimately harvested energy that had already incurred some losses when it was transferred into the battery. This means that investing battery energy fundamentally requires more transfers that consume power than the re-investing case. In addition, especially for low-power applications, reducing the number of switches in the energy-transfer path typically raises efficiency as the switches and their driving circuits are the major consumers of power. However, it is challenging to assess these three investing strategies without specific circuits because the losses can vary significantly depending on the specific design parameters. Therefore, SPICE simulations of the single-inductor investing harvester circuits, which are presented in Figures 4.6, 4.10, and 4.12, were performed to compare and evaluate each approach [209]. The simulations used TSMC's 0.35-μm CMOS devices whose channel lengths were 1.5 μm (instead of 0.35 μm), because 15-V devices demand a longer channel length than low-voltage devices in the process. The widths of the switches in each system were designed to use the same total silicon real estate for fairness across the implementations. Body effects of the transistors

were ignored for simplicity, and the control losses of each system were assumed to be the same. The capacitance of the piezoelectric transducer C_{PZ} and the inductance L_H were 20 nF and 100 µH, respectively. Table 4.1 illustrates the parameters of the switches.

Table 4.1. Emulated 15-V CMOS switches.

Re-invest (Figure 4.6) & Combined (Figure 4.12)	S_C	NMOS	W / L R_{ON} C_G	30,000 µm / 1.5 µm 0.78 Ω 51.8 pF
	S_B (D_B)	PMOS	W / L R_{ON} C_G	80,000 µm / 1.5 µm 1.09 Ω 138 pF
Invest (Figure 4.10)	S_C S_{X1} S_{X2}	NMOS	W / L R_{ON} C_G	10,000 µm / 1.5 µm 2.33 Ω 17.3 pF
	S_{B1} S_{B2}	PMOS	W / L R_{ON} C_G	40,000 µm / 1.5 µm 2.17 Ω 69 pF

Figure 4.14 illustrates the charging profiles of the three approaches under weak vibrations that induced 1.25-V open-circuited voltage at the piezoelectric device. Since the harvested energy during a half cycle was insufficient to pre-charge the piezoelectric transducer to the breakdown voltage of the process, the combined investing approach generated more energy than the re-investing technique. Investing battery energy resulted in the middle performance among the three, because it harnessed more energy than the re-invest case, but lost more than the combined approach did. Ideally, as Figure 4.13 predicts, the re-invest, invest, and combined schemes would have harnessed 250 nJ, 625 nJ, and 625 nJ per cycle, respectively, from the weak vibrations. However, the three systems lost the considerable amounts of 18 nJ, 325 nJ, and 224 nJ respectively, during the investing and harvesting energy transfers through the conduction and gate-driving losses of the switches.

The same circuits harvested energy from vibrations that drove 2.5-V open-circuited voltage at the piezoelectric transducer. Figure 4.15 demonstrates the charging profiles of the re-invest and invest approaches only, because the combined approach reduces to the re-investing case if the vibration is strong enough to pre-charge C_{PZ} to the

breakdown voltage. Because it consumed a smaller (i.e., 82 nJ per cycle) amount of conduction and gate-driving loss than the investing system did (i.e., 221 nJ per cycle), the re-invest approach yielded more than the investing approach.

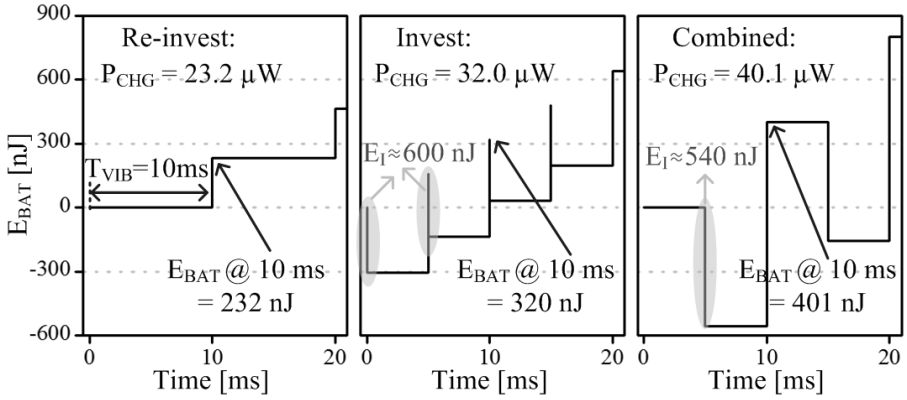

Figure 4.14. Charging profiles of re-investing, investing, and combined investing approaches under weak vibrations (V_{OC} = 1.25 V).

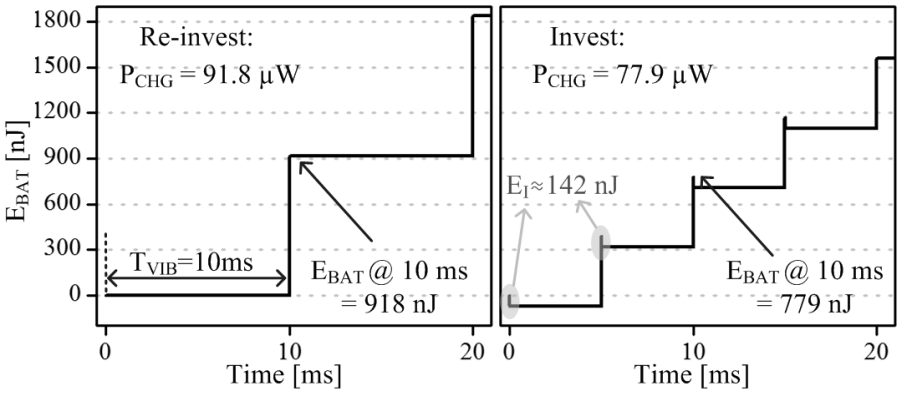

Figure 4.15. Charging profiles of re-investing and investing strategies under strong vibrations (V_{OC} = 2.5V).

4.6. Summary

Energy investment can strengthen the electrical damping force of a transducer to compensate for the weak electromechanical coupling factor and the limited space for movements of tiny piezoelectric devices, and ultimately induce the system to augment the amount of energy harvested. Several investing piezoelectric harvesters in the literature

apply this idea by re-investing the harvested input energy or by investing the battery energy. However, they tend to rely on bridge rectifiers that impose thresholds and extra losses on the system or multiple off-chip inductors and high-voltage batteries that burden the system volume and cost. The three single-inductor energy-investing piezoelectric harvesters proposed in this chapter increase the electrical damping force and the output power by re-investing the input energy, by investing the battery energy, or by investing and re-investing both, while eliminating the limitations of the input energy and output voltage. Although the over-damping of a transducer and the breakdown voltage of circuit elements can limit the investment and the output power, the losses of harvesting circuits often present the major trade-off for energy-investing harvesters. Because every energy transfer through switches generates losses that increase with the amount of energy transferred, an energy-investing harvester must minimize the losses by reducing both the number of energy transactions through switches and the size of energy packets.

CHAPTER 5

ENERGY-INVESTING HARVESTER

A harvester circuit can invest energy into a piezoelectric transducer to strengthen the electrical damping force of the transducer and increase the amount of electrical energy converted from a given vibration. However, electrical circuits always incur energy losses when they transfer energy. Hence, to yield the most amount of energy from investing, the harvester circuit must be as efficient as possible. While the efficiency of a circuit can significantly vary depending on specific implementations and the given technology platform of the circuit, the investigation results in Chapter 4 reveal that the invest and re-invest approach using two power switches offers the highest net-energy gain among three single-inductor energy-investing schemes assuming the same silicon area assigned for the systems. Based on the conclusions of Chapter 4, an energy-investing harvester IC prototype that adopts the invest and re-invest approach was built using 0.35-μm CMOS process. This chapter presents the operation, IC design, and experimental results of the prototype to validate the idea of energy-investing harvester.

5.1. Switched-inductor Power Stage

The proposed harvester uses the switched-inductor circuit in Figure 5.1a to incorporate the investing concept and strengthen the electrical damping force. As the experimental waveforms in Figure 5.1b show, the harvester first waits until the vibration (with i_{PZ}) charges C_{PZ} to its peak voltage $V_{PZ(PK)}^{+}$. The system then invests battery energy from v_{BAT} into inductor L_H by closing switch S_{BAT} across investment time τ_I. Afterwards, S_{BAT} opens and switch S_{PZ} closes to first harvest all the energy in C_{PZ}, which C_{PZ} accrued across the positive half cycle, into L_H during τ_H^{+}. Then, after harvesting C_{PZ}'s energy, S_{PZ} stays engaged to drain the energy in L_H back into C_{PZ} until inductor current i_L nears zero,

pre-charging C_{PZ} to $-V_{PC}$. This investment creates a larger absolute value of v_{PZ} in the negative half than that of the positive half, and thus vibrations will work against a stronger electrical damping force to convert more mechanical energy into the electrical domain than without $-V_{PC}$. At the negative peak $V_{PZ(PK)}^{-}$, the circuit recovers its investment and collects all derived gains in C_{PZ} to charge v_{BAT} by energizing and de-energizing L_H across τ_H^{-} and τ_{CHG} through S_{PZ} and S_{BAT}, respectively.

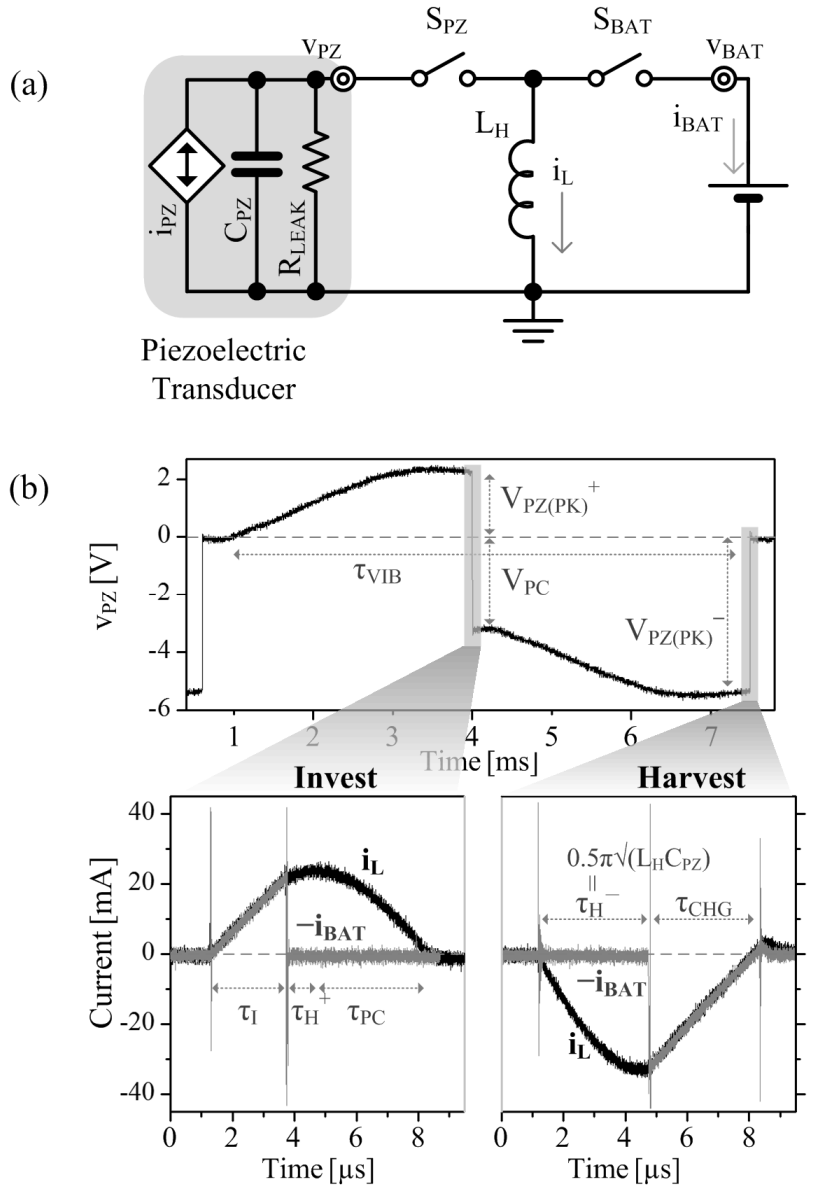

Figure 5.1. (a) Simplified power stage and (b) measured waveforms.

Because the length of each energy transaction through L_H is much shorter than that of half cycles (i.e., about 7 μs of 3.5 ms), the system can invest and harvest with only one inductor. In addition, by combining the energy in C_{PZ} and v_{BAT} with the inductor, the harvester builds a damping voltage that is greater than the open-circuited voltage of C_{PZ}, $V_{PZ(OC)}$, and v_{BAT}. Even if the v_{BAT} amplitude is low, the proposed system can raise the damping force of the transducer by extending investing time τ_I.

The harvester invests energy from v_{BAT} to pre-charge C_{PZ} from $V_{PZ(PK)}^{+}$ to $-V_{PC}$. Hence, v_{BAT} initially loses $E_{I(BAT)}$ as quantified in the following equation:

$$E_{I(BAT)} = 0.5C_{PZ}\left[\left(-V_{PC}\right)^2 - \left(V_{PZ(PK)}^{+}\right)^2\right] + E_{LOSS}^{+}, \tag{5.1}$$

where E_{LOSS}^{+} represents all the losses during the positive cycle operation. Then at the negative peak $V_{PZ(PK)}^{-}$, the system charges v_{BAT} with E_{CHG}

$$E_{CHG} = 0.5C_{PZ}\left(V_{PZ(PK)}^{-}\right)^2 - E_{LOSS}^{-}, \tag{5.2}$$

where E_{LOSS}^{-} is the total losses of the harvester during the negative half. From (5.1) and (5.2), the net energy E_{NET} that v_{BAT} gained is

$$E_{NET} = E_{CHG} - E_{I(BAT)} = 0.5C_{PZ}\left[\left(V_{PZ(PK)}^{-}\right)^2 - V_{PC}^2 + \left(V_{PZ(PK)}^{+}\right)^2\right] - E_{LOSS}^{+} - E_{LOSS}^{-}. \tag{5.3}$$

If the damping effect due to the investment is negligible, the amplitude of $V_{PZ(PK)}^{-}$ is approximately equal to the sum of V_{PC} and $V_{PZ(PK)}^{+}$, as shown in Figure 5.1b. Consequently, E_{NET} can be expressed as

$$E_{NET} = C_{PZ}\left(V_{PZ(PK)}^{+}\right)^2 + C_{PZ}V_{PZ(PK)}^{+}V_{PC} - E_{LOSS}^{+} - E_{LOSS}^{-}. \tag{5.4}$$

5.2. IC Implementation

The harvester proposed in Figure 5.2 integrates power switches and control blocks into a 0.35-μm CMOS IC. Off-chip components includes a piezoelectric transducer whose measured capacitance and leakage resistance are 15 nF and 10 MΩ, respectively, a 330-

μH / 1.6-Ω inductor, a battery or a large capacitor, and a negative-peak tracker consisting of a Schottky-diode D_{SS} and a 36-nF ceramic capacitor C_{SS}. Note that this negative-peak tracker that sets substrate voltage V_{SS} near the negative peak of v_{PZ} can be omitted if a given silicon technology offers isolated-NMOS devices or it can be replaced by a voltage inverter in [210] that biases the negative V_{SS}. However, this simple peak-and-hold circuit allows the system to use more common CMOS-technology platforms where NMOS devices are typically grown from the substrate while demanding no additional control circuits and power.

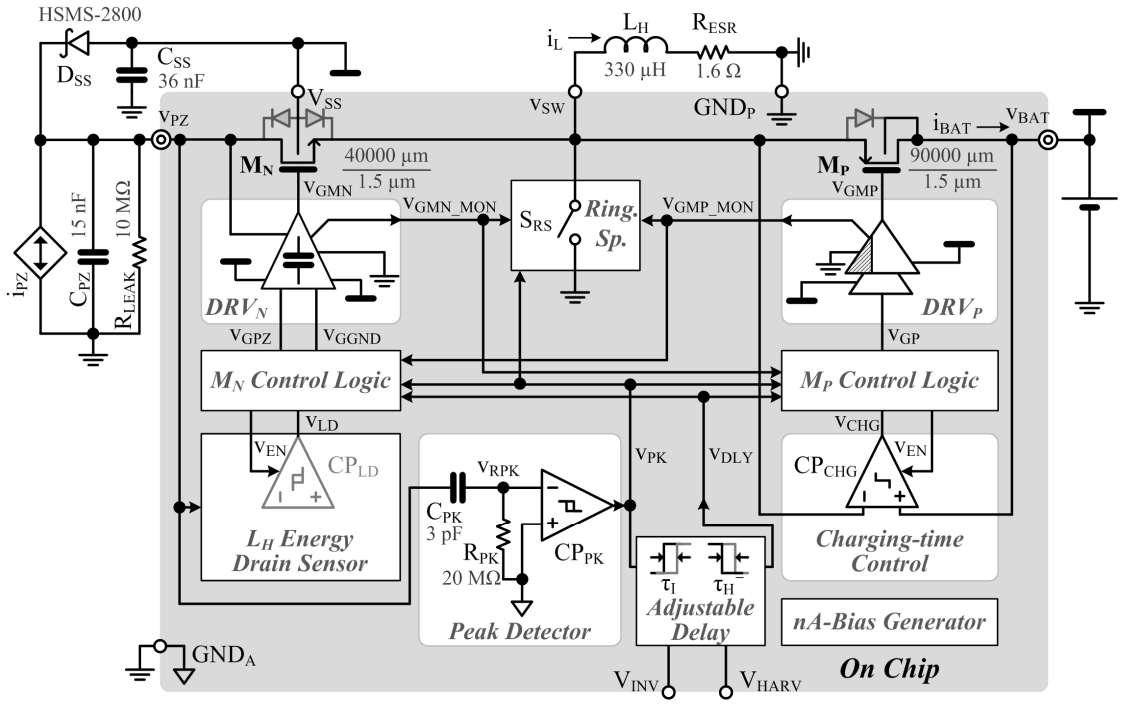

Figure 5.2. Energy-investing switched-inductor piezoelectric harvester.

5.2.1. Power Stage

In Figure 5.2, power switches M_N and M_P are 15-V devices with a minimum channel-length of 1.5 μm that allow large voltage swings at v_{PZ} and switching node v_{SW}. The switching frequency is low, but the peak-current level is relatively high for μW-power

converters. Therefore, the switches are large to reduce the channel resistances of the switches and the conduction losses of the harvester.

The large switch sizes, however, may induce large gate-driving losses if they are driven by conventional inverter-chain gate-drivers using the large rail-to-rail (V_{BAT}+|V_{SS}|) voltage of the harvester. To reduce the gate-driving losses under large rail-to-rail supply voltage, the prototype harvester adopts charge-pump and level-shifting approaches. Figure 5.3 illustrates the simplified schematic and measured waveforms of NMOS driver $DRV_{N,}$ which adopts a charge-pump approach.

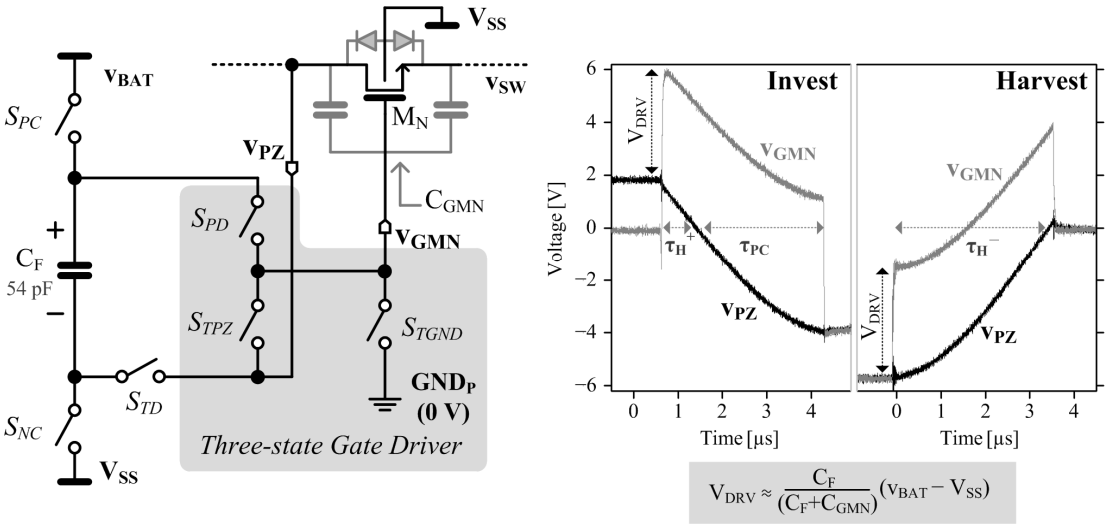

Figure 5.3. M_N's charge-pumped three-state driver DRV_N with measured waveforms.

During a positive-v_{PZ} cycle before M_N engages, DRV_N charges flying capacitor C_F through switches S_{PC} and S_{NC} while keeping M_N disengaged by applying 0 V to gate voltage v_{GMN} through switch S_{TGND}. Then DRV_N turns M_N on by placing the charged C_F across v_{PZ} and v_{GMN} through switches S_{TD} and S_{PD}. Due to charge sharing between C_F and gate capacitance C_{GMN}, overdrive voltage V_{DRV} scales down from (V_{BAT}+|V_{SS}|) by a factor of $C_F/(C_F+C_{GMN})$. While this reduced voltage swings across C_{GMN} allows DRV_N to spend only 8.3 nJ instead of 24.2 nJ, the amount which a conventional rail-to-rail driver would have consumed, the overdrive for M_N can actually be higher than that which

occurs when applying V_{BAT} to v_{GMN}, as the waveforms in Figure 5.3 illustrate. This strong overdrive is, in fact, necessary to lower the channel resistance of M_N, because M_N suffers from a serious body-effect caused by the large source-to-body voltage of M_N. Moreover, V_{DRV} increases with increasing amplitude of V_{SS} to partially cancel the body-effect. In the negative half, DRV_N connects v_{GMN} to v_{PZ} through S_{TPZ} to keep M_N disengaged until the negative peak of v_{PZ}, at which point DRV_N turns M_N on through S_{TD} and S_{PD} to harvest the energy in C_{PZ} into L_H.

Figure 5.4 illustrates the transistor-level schematic of DRV_N. To prevent shoot-through losses in charging and discharging C_F, non-overlapping clock generator commands S_{PC} and S_{NC} to charge C_F if one of the input signals (v_{GGND} and v_{GPZ}) is HIGH, or commands S_{PD} and S_{TD} to discharge C_F otherwise. Moreover, the OR- and AND-gates in front of S_{PD}, S_{TPZ}, and S_{TGND} ensure that no shoot-through current flows between the switches.

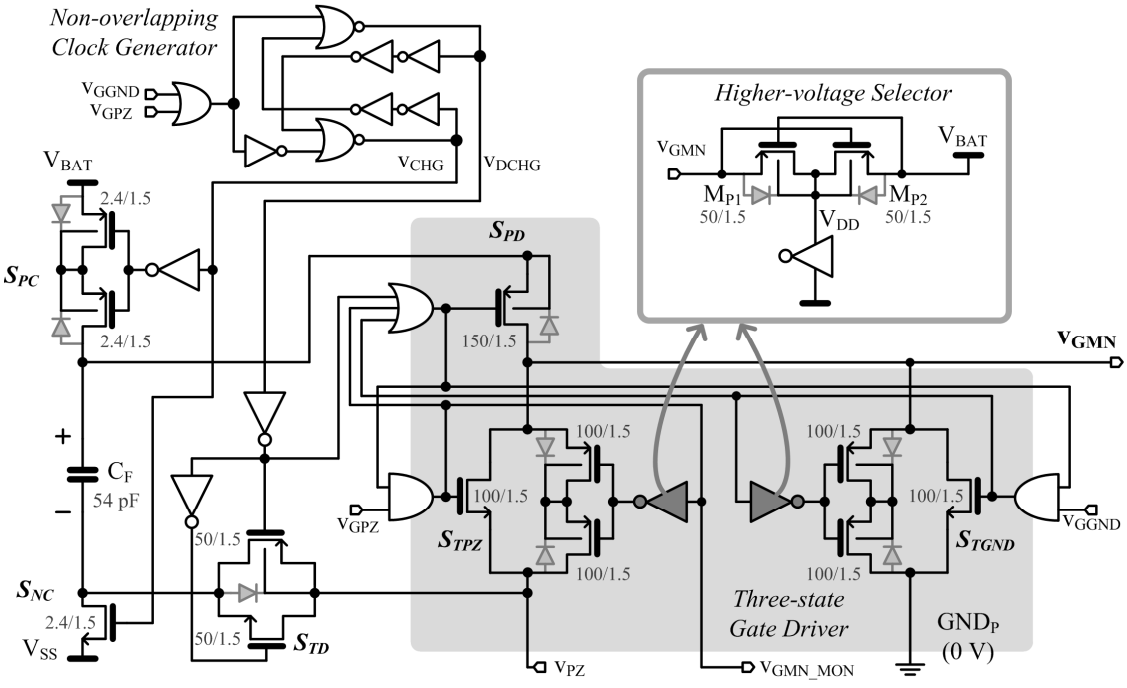

Figure 5.4. Transistor-level schematic of DRV_N (Transistor dimensions are µm/µm, and the unspecified bodies of transistors are tied to their respective supplies).

C_F-charging switches S_{PC} and S_{NC} use PMOS and NMOS as they connect V_{BAT} and V_{SS} to the top and bottom plates of C_F, respectively. Note that back-to-back PMOS transistors block the body-diode conduction path of S_{PC} as its lower terminal is exposed to $v_{GMN,}$ which can rise above and fall below V_{BAT} when S_{PD} is on. Depending on operation phases, v_{GMN} is connected either to the top plate of C_F through S_{PD}; to v_{PZ} through S_{TPZ}; or to 0 V through S_{TGND}. These switches, except for S_{PD}, utilize transmission gates since a single NMOS or PMOS is difficult to turn on under the body-effects and negative-v_{PZ} conditions. Similar to the case with S_{PC}, PMOS transistors in S_{TPZ} and S_{TGND} need to adopt the back-to-back structure as the voltages across the switches change polarities when the switches are off. In addition, because v_{GMN}, which is connected to the source of PMOS devices in S_{TPZ} and S_{TGND}, can go higher than V_{BAT} while S_{TPZ} and S_{TGND} need to be kept off, the cross-coupled M_{P1} and M_{P2} in the inset of Figure 5.4 automatically choose the higher voltage between v_{GMN} and V_{BAT} to set V_{DD} of PMOS drivers, which in turn keep the PMOS devices of S_{TPZ} and S_{TGND} off.

On the other hand, M_P driver DRV_P shown in Figure 5.5 adopts an inverter-chain structure except for the last level-shifting stage and the PMOS/TG inverter, which drive the power switch M_P in Figure 5.2 and M_{PDRV1} in Figure 5.5, respectively. The inverter-chain driver prevents shoot-through current between M_{PDRV1} and M_{PDRV2}. The PMOS-only or PMOS/TG drivers save gate-driving losses by applying 0 V, instead of V_{SS}, to turn on the ensuing large PMOS switch. In addition, by discharging the gate charge in large transistors to ground, not to V_{SS} which is held by C_{SS} (Figure 5.2), the piezoelectric transducer can lose less opportunity costs as it can use less energy to replenish C_{SS} and further increase the damping force under the given vibration and investment. Despite the benefits of these level-shifted stages, they are applicable when one terminal of the PMOS device driven by the level-shifted driver is connected to V_{BAT} as in M_{PDRV1} in Figure 5.5 and M_P in Figure 5.2; otherwise, the overdrive voltage may not be sufficient for the following PMOS.

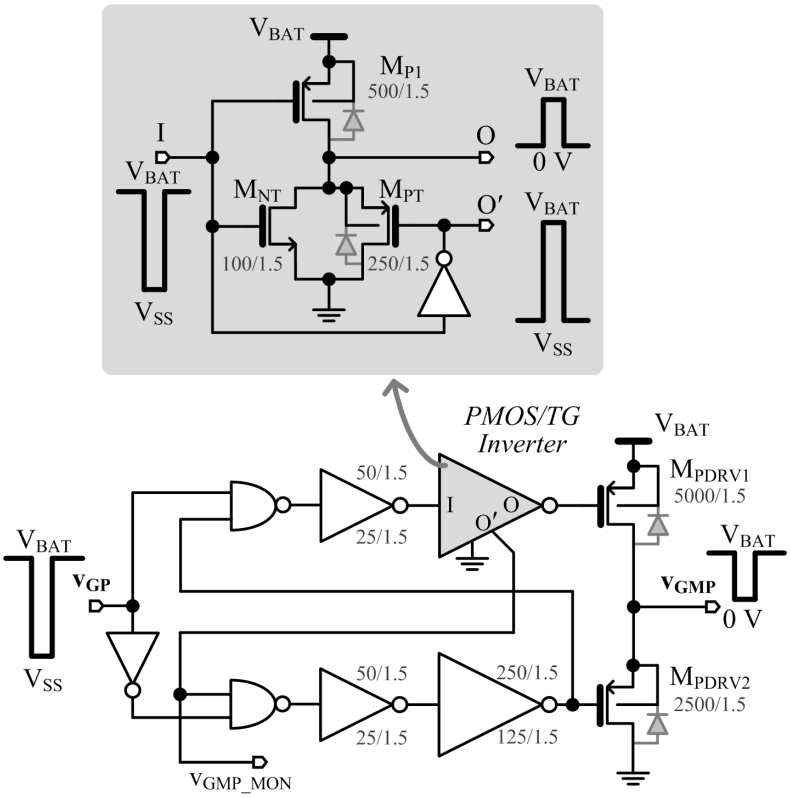

Figure 5.5. M_P's level-shifting driver DRV_P.

When the system turns off both switches, any charge left in parasitic capacitance C_{PAR} at v_{SW} rings with L_H. Figure 5.6 shows the ringing-suppressor that shorts v_{SW} to ground by engaging M_{NRS} and M_{PRS} after the switching operations. On the other hand, as soon as the system detects the peaks of v_{PZ}, the system quickly releases v_{SW} so that the system can use L_H to transfer energy.

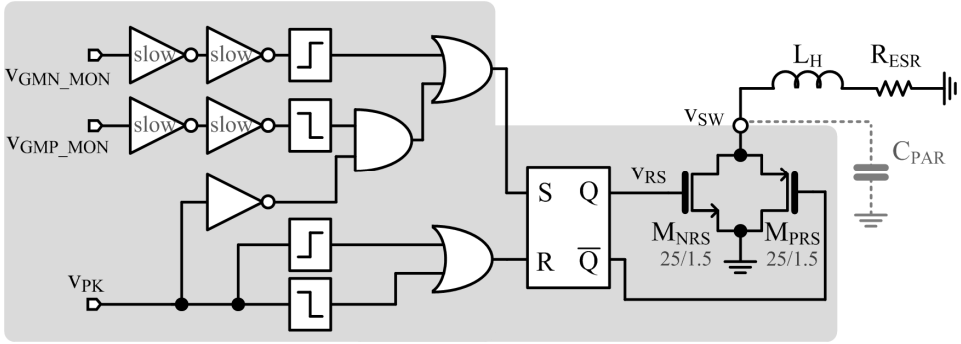

Figure 5.6. Ringing suppressor.

5.2.2. Control Logic

The control logic shown in Figure 5.7 commands DRV_P and DRV_N by interpreting the input signals v_{PK}, v_{DLY}, v_{GMP_MON} and v_{GMN_MON}. When the system detects the positive peak of v_{PZ}, v_{PK} rises HIGH and v_{GP} (Figure 5.7a) falls LOW to turn M_P on. After battery-investment time τ_I, v_{DLY}, and thus v_{GP} transitions HIGH to turn M_P off. Then, after the driver-chain of DRV_P (Figure 5.5) secures a dead-time to prevent a shoot-through current from flowing through the power switches, v_{GMP_MON} transitions LOW to pull v_{GGND} (Figure 5.7b) LOW, which in turn engages power switch M_N and enables L_H-drain sensing comparator CP_{LD}. Next, when CP_{LD} detects the zero-crossing of i_L, v_{LD} rises HIGH to disable CP_{LD} and to set v_{GPZ} HIGH, shutting M_N off to conclude a positive half cycle.

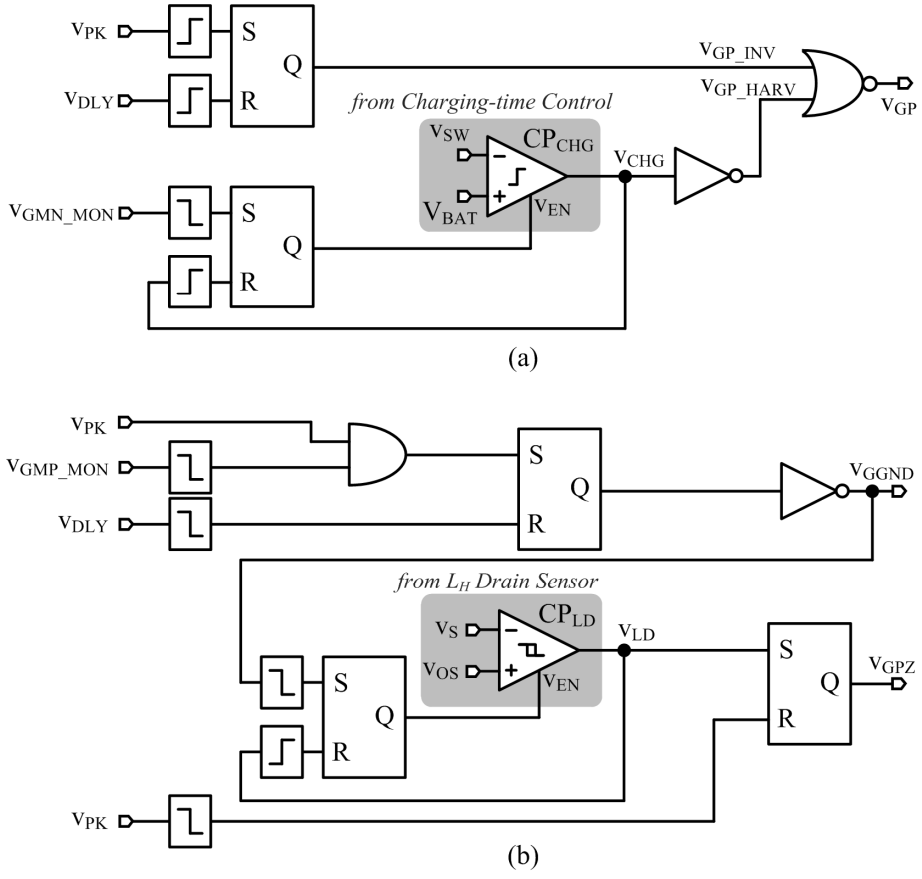

Figure 5.7. Control logic for (a) M_P's DRV_P and (b) M_N's DRV_N.

At the negative peak of v_{PZ}, v_{PK} falls LOW to reset v_{GPZ} (Figure 5.7b) and engage M_N. Note that the charging-time control comparator CP_{CHG} in Figure 5.7a was enabled through v_{GMN_MON} from DRV_N in Figure 5.4 when v_{GPZ} was reset. After a quarter L_HC_{PZ}-resonance periods (τ_H^-) set by the delay block in Figure 5.2, v_{DLY} transitions LOW to drive v_{GGND} HIGH and disengage M_N. Subsequently, when i_L drives switching node v_{SW} above V_{BAT}, CP_{CHG} drives v_{CHG} and v_{GP} LOW to turn M_P on. As L_H fully de-energizes into the battery and v_{SW} falls below V_{BAT}, CP_{CHG} disables itself and shuts M_P off by driving v_{CHG} and v_{GP} HIGH, completing a full harvesting cycle.

5.2.3. Peak Detector

Figure 5.8 illustrates peak-detection comparator $CP_{PK,}$ which consists of twin sub-comparators CP_{PK}^+ and CP_{PK}^-, each of which detect the positive and negative peaks of v_{PZ}, respectively. At first, v_{PK} is LOW and only CP_{PK}^+ is enabled to sense the positive peak of v_{PZ}. When v_{PZ} reaches the peak and starts to fall, the current flowing through capacitor C_{PK} changes its direction and therefore v_{PZ_D}, which is connected to v_I^- of CP_{PK}^+ (Figure 5.8b), falls below 0 V. As a result, M_{P2} in Figure 5.8b steers the tail current into v_{O1}, which then rises to pull v_{O2} down through M_{N3}. The bias current is in the nA-range to save power, but this decision speed is only partially limited by the low bias current because it takes advantage of the common-source amplifier $M_{N3,}$ which can momentarily sink much more current than the bias current. In addition, the positive feedback set by M_{N3} and M_H expedites the voltage transitions at v_{O1}, v_{O2}, and v_O to accelerate the decision speed. After the decision and before CP_{PK}^+ is disabled, M_H sets the hysteresis to prevent potential inadvertent decisions caused by noisy input voltages.

The rising edge of v_{PK} disables CP_{PK}^+ and enables the other sub-comparator CP_{PK}^- to detect the negative peak. The sub-comparators quickly enable the current sources, but hold nodes v_{O1} and v_{O2} for about 100 μs through a de-glitching circuit, because the substrate can be noisy for a while after the switching events. Figure 5.9

shows the de-glitch circuit that generates delay by charging a capacitor with a 3-nA current source. Similar to CP_{PK}^{+}, CP_{PK}^{-} can also exploit the fast decision process under the nA-bias currents by connecting its v_I^{+} to v_{PZ_D}, which rises above 0 V after the negative peak of v_{PZ}. Despite the dynamic v_{PZ} moving across positive and negative voltages, because C_{PK}–R_{PK} has set the input voltages of the sub-comparators near 0 V, the input-common-mode range (ICMR) of CP_{PK} need only include ground. Note that the hysteresis of each sub-comparator is activated only after each sub-comparator makes a decision. Therefore, the hysteresis prevents each sub-comparator from revoking its decision without delaying the peak detection speed.

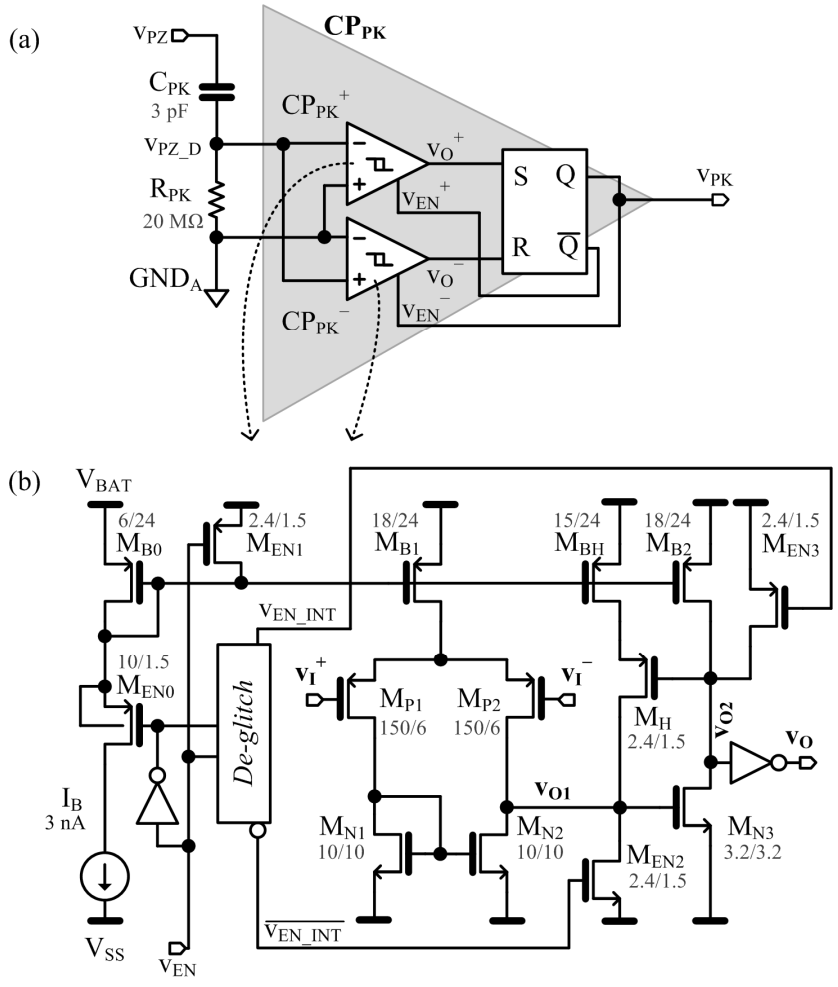

Figure 5.8. (a) Block diagram of a peak detector, and (b) the transistor-level schematic of sub-comparators.

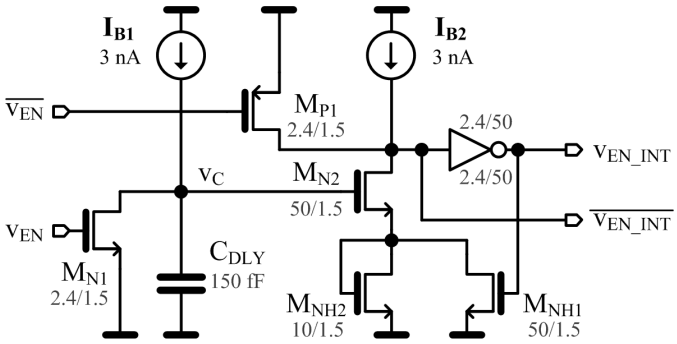

Figure 5.9. De-glitch circuit for CP_{PK}^{+} and CP_{PK}^{-}.

5.2.4. Adjustable Delay Controller

The adjustable delay block in Figure 5.10 controls τ_I and τ_H^- (Figure 5.1b) by allowing a user to adjust V_{INV} or V_{HARV}. When v_{PK} rises from LOW to HIGH, an SR-latch sets v_{EN_INV} to HIGH until the current established by V_{INV} charges C_{RAMP} and triggers the ensuing hysteretic stages to drive v_{DLY} HIGH. Since the hysteretic drivers take much lesser delay than the charging time of C_{RAMP}, the delay between the rising edges of v_{PK} and v_{DLY}, τ_I, can be controlled by V_{INV}. τ_H^--control shares the same analog stages as τ_I except that V_{HARV} sets the charging current of C_{RAMP}.

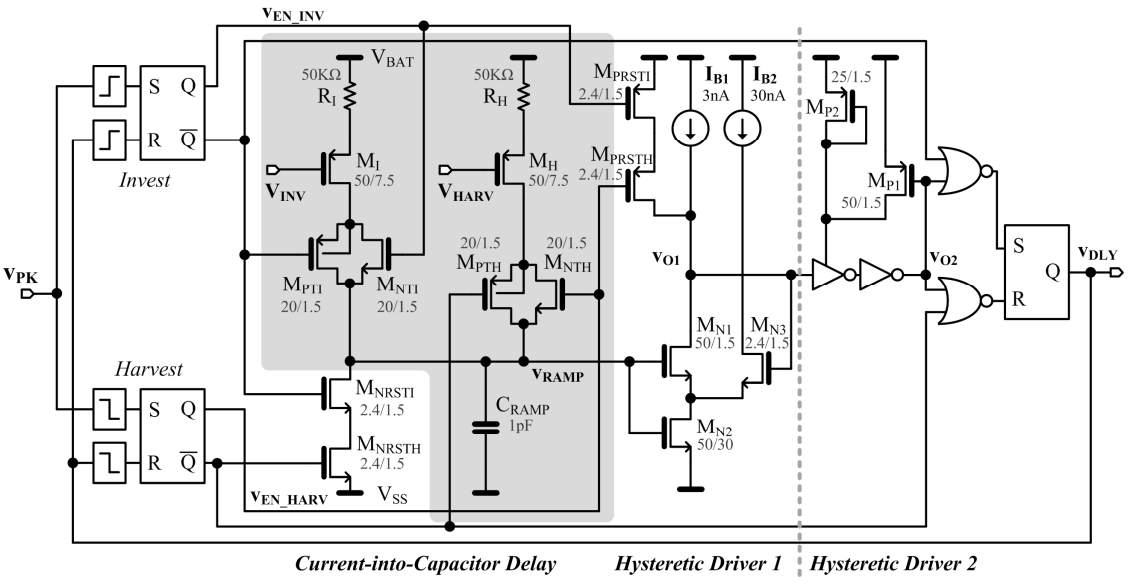

Figure 5.10. Adjustable delay controller.

Because v_{RAMP} rises slowly, the first hysteretic driver uses 3-nA bias current I_{B1} to limit the shoot-through current from V_{BAT} to V_{SS}. When v_{RAMP} increases to a threshold that M_{N1} (whose overdrive voltage is degenerated by the voltage that I_{B2} generates across M_{N2}) starts to sink more current then I_{B1}, v_{O1} begins to roll off and turns M_{N3} off, which subsequently increases the overdrive of M_{N1} to allow M_{N1} to momentarily sink much more than I_{B1}. This positive feedback expedites the falling transition of v_{O1} and prevents the shoot-through current in the ensuing stages.

5.2.5. L_H Energy-drain Sensor

The L_H energy-drain sensor and its experimental waveforms are illustrated in in Figure 5.11. The sensor detects the moment when L_H drains its energy fully into C_{PZ} to open M_N and complete the investment phase. As Figure 5.11b illustrates, when v_{PZ} falls to $-V_{PC}$, this block samples i_L by connecting C_S in parallel to C_{PZ} and then converts the sampled current i_S into a voltage v_S by mirroring i_S across R_S. Because C_S is much smaller than C_{PZ}, this sampling approach virtually does not affect the main energy flow. Moreover, this AC-sampling method, as in the peak-v_{PZ} detector, decouples the dynamic v_{PZ} voltage from comparator CP_{LD} to ease its ICMR requirement.

The system enables CP_{LD} when M_N turns on to conduct i_L and disables CP_{LD} when CP_{LD} senses zero-crossing of i_L in the investing phase. However, comparing v_S to 0 V or a fixed offset may trip the output of CP_{LD}, v_{LD}, later or earlier than the correct moment and therefore induce losses, because, as shown in Figure 5.11c, i_L falls quickly when the pre-charging energy is large but slowly otherwise. Hence, M_{P0}–M_{P2} mirror a small portion of i_S into C_{OS} to build an adaptive offset v_{OS} proportional to the amplitude of i_L to counter different i_L-descending speeds and the delay of CP_{LD}. 1.5 nA from nA Generator in Figure 5.2 also reduces delay by keeping the mirrors from shutting completely.

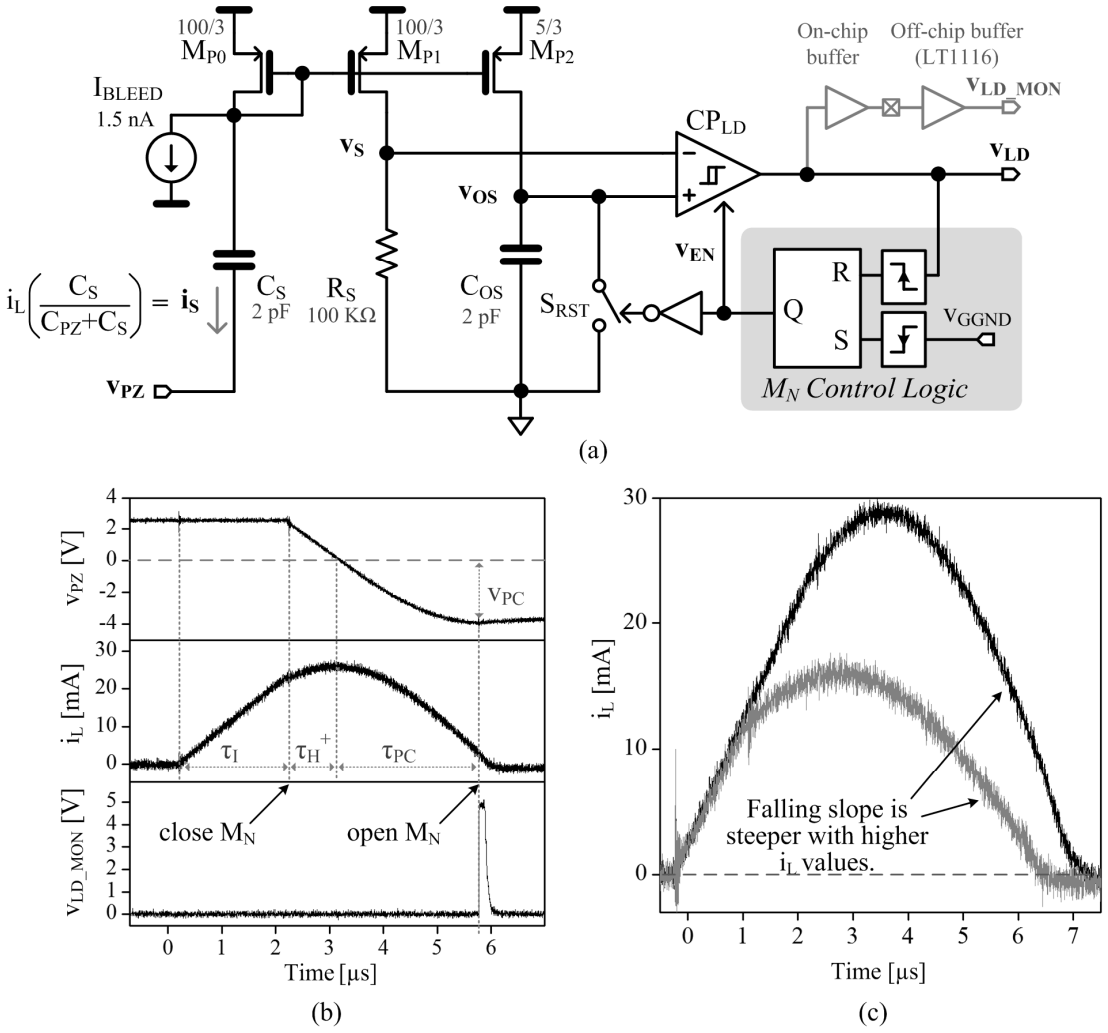

Figure 5.11. (a) L_H's energy-drain sensor and (b) measured waveforms (c) with different pre-charging energy.

The transistor-level schematic of CP_{LD}, which is shown in Figure 5.12, uses the same architecture as CP_{PK}^{+} and CP_{PK}^{-} in Figure 5.8b, but with different bias currents and transistor aspect ratios. Note that the de-glitch circuit shown in Figure 5.12b also adopts a similar delay structure to the de-glitch circuit in Figure 5.9. However, the delay length here should be much shorter; therefore, the current level is higher than those of Figure 5.9. Consequently, the hysteresis is generated by the voltage I_{B2} generates across R_H, instead of diode-connected device in the nA-case in Figure 5.9.

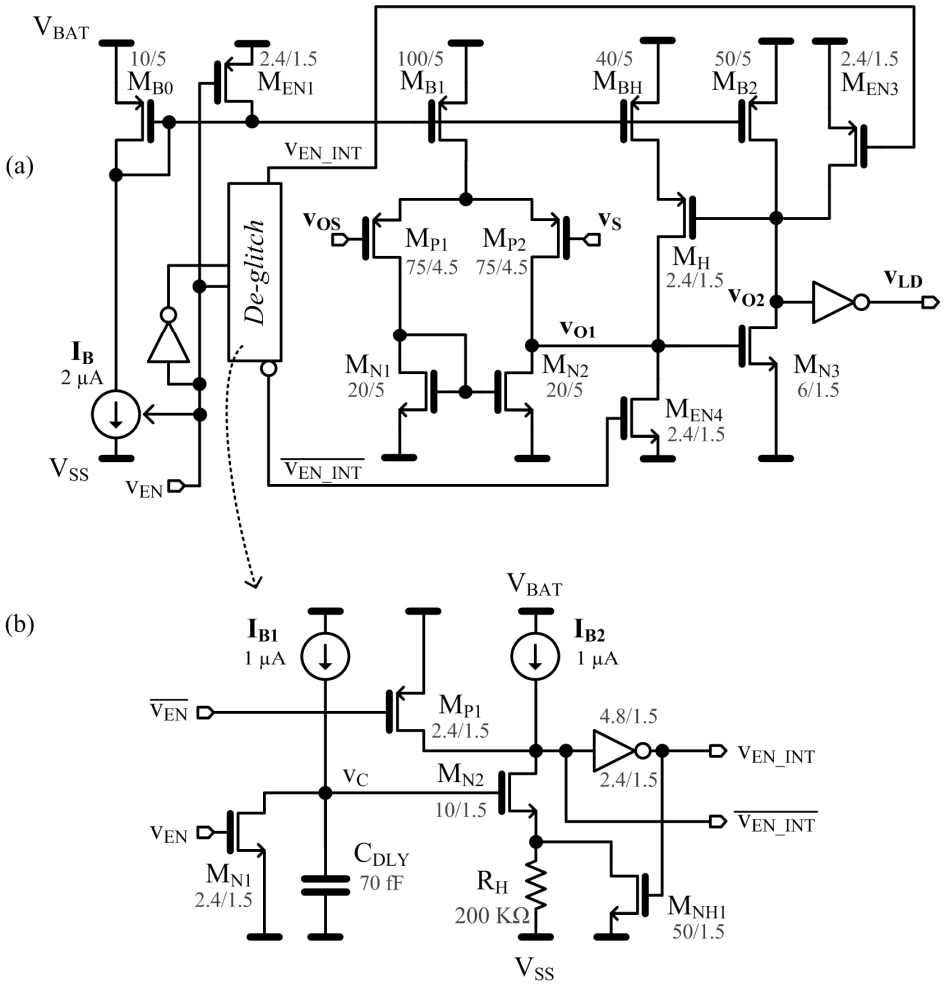

Figure 5.12. (a) Transistor-level schematic of CP_{LD} and (b) de-glitch circuit.

5.2.6. Charging-time Controller

Figure 5.13 shows charging-time comparator CP_{CHG}, which monitors the voltage across M_P to autonomously control M_P as an ideal diode. In the harvesting phase, when M_N turns on and off to finish energizing L_H from C_{PZ}, i_L continues to flow and rapidly charges up parasitic capacitance C_{PAR} at v_{SW}. Hence, CP_{CHG} compares v_{SW} and V_{BAT} to drive v_{CHG} LOW and turn M_P on when v_{SW} surpasses V_{BAT}, and CP_{CHG} does the opposite when v_{SW} falls below V_{BAT}. After the turn-off decision, the control logic disables CP_{CHG} and shuts M_P off, not only to save control power, but also to prevent some possible remaining i_L from operating CP_{CHG} again, which may lead to oscillations and additional

losses. Any remaining i_L will flow into the battery through the body diode of M_P and increase v_{SW} for a short period, as is evidenced by a small voltage glitch at the end of τ_{CHG} in v_{SW} waveform of Figure 5.13. The v_{SW} waveform also illustrates another short body-diode conduction duration (about 48 ns) at the starting of τ_{CHG}, which is the aggregated turning-on propagation delay of CP_{CHG}, control logic, and DRV_P.

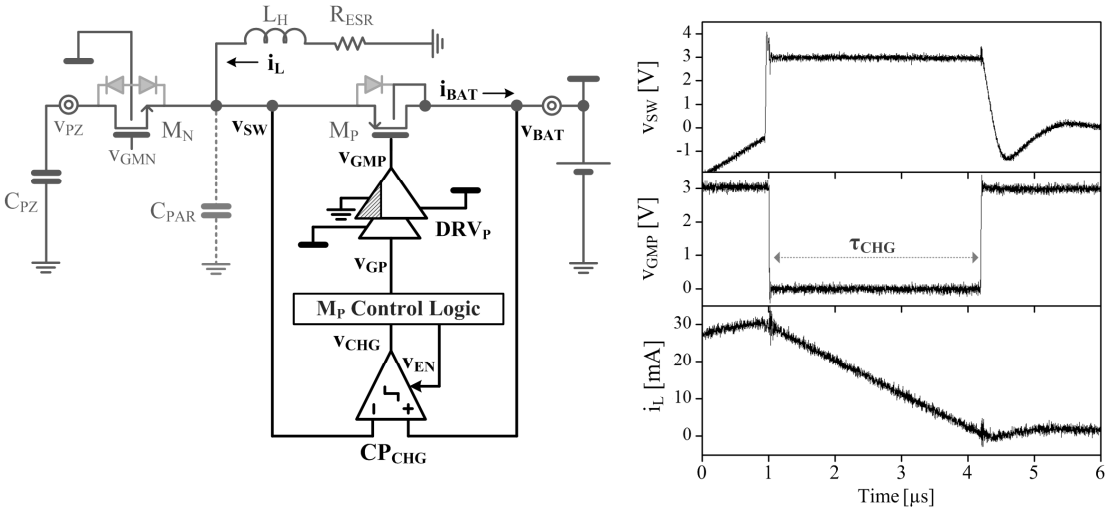

Figure 5.13. Charging-time control with measured waveforms.

Figure 5.14 illustrates the transistor-level schematic of CP_{CHG}. The common-gate input pair M_{P1}–M_{P2} of CP_{CHG} takes advantage of strong overdrive for the turn-on process as i_L charges C_{PAR} very rapidly. However, unlike the fast turn-on decision process, the turn-off decision can be slow because of the small overdrive voltage of the comparator. Hence, CP_{CHG} employs offset current I_{OS} to start the turn-off process when v_{SW} is slightly higher than V_{BAT}. I_{OS} steals the drain current of M_{P1} to raise the trigger voltage of CP_{CHG}, but only after a sufficient delay set by the drain current of M_{P8} and C_{OS}. This delay allows CP_{CHG} to compare the settled down v_{SW} to V_{BAT}. In addition, the diode-connected M_{N11} and M_{N12} clamp v_{O1} so that v_{O1} can descend quickly to turn off M_{N3}, which turns off M_P. The de-glitch circuit in Figure 5.14 is similar to the one in Figure 5.12b, and the output stage is a modified Schmitt-trigger inverter whose current is limited by R_{HYST}.

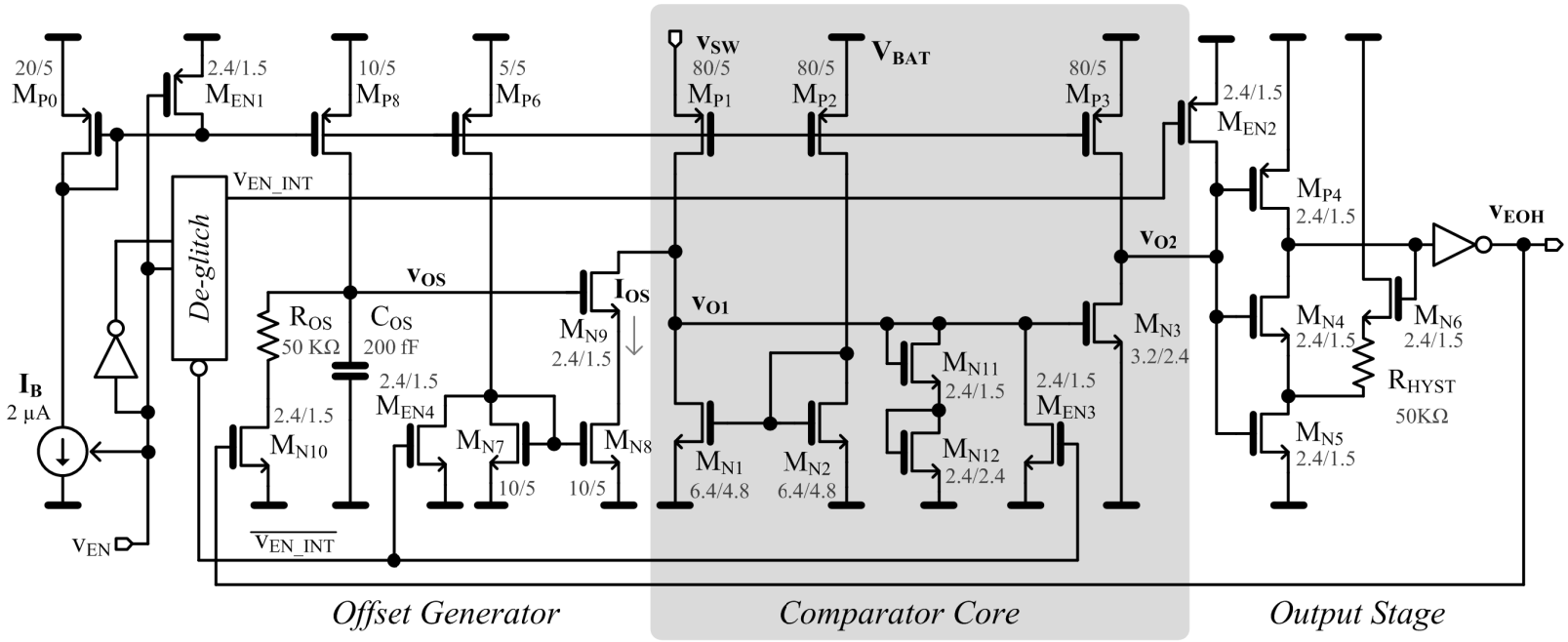

Figure 5.14. Transistor-level schematic of CP_{CHG}.

5.2.7. Nano-ampere Bias-Current Generator

The nA-bias circuit in Figure 5.15 supplies currents for CP_{PK}, the adjustable delay, and the L_H energy-drain sensor. It generates nA-output current without using a large (e.g., 10s of MΩ) on-chip resistor, which would occupy a considerable area of silicon die. This structure, introduced in [211], uses M_{P5} as a CMOS resistor by framing its drain (v_D) and gate (v_G) voltages with M_{P1}-M_{P2} pair and a diode-connected M_{P6}, respectively. The bias core uses high-voltage transistors to cascode the low-voltage transistors that generate matched currents. Because low-voltage transistors adopt thinner gate oxides and higher back-gate (i.e., bulk) doping than high-voltage devices, the matching performance of low-voltage pairs is better than that of high-voltage ones [212].

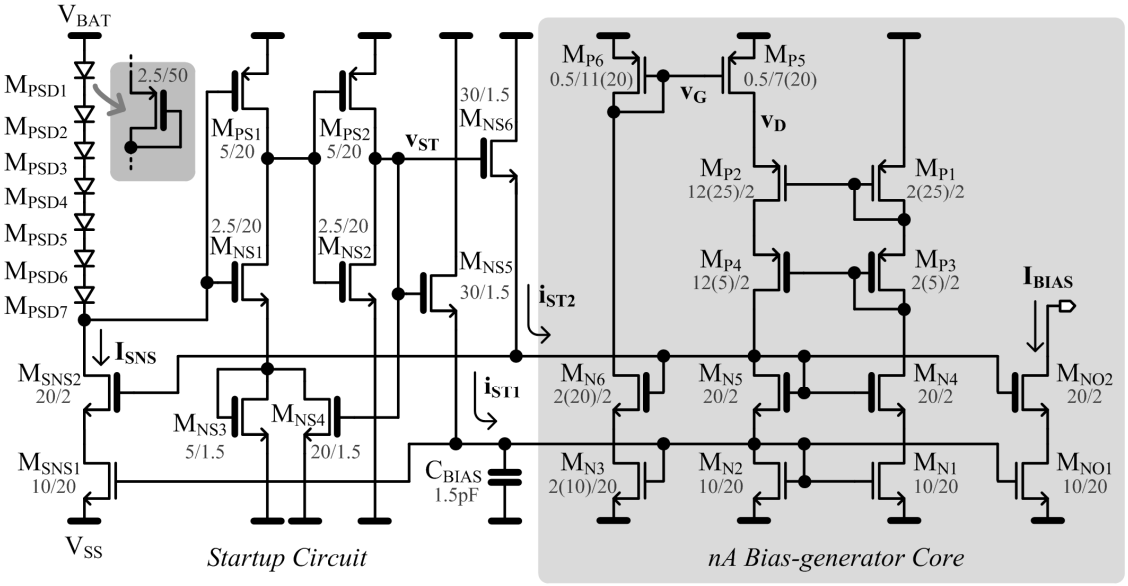

Figure 5.15. Nano-ampere bias-current generator.

To avoid a zero-current state, the startup circuit on the left senses the bias current through M_{SNS1} and pushes startup currents i_{ST1} and i_{ST2} into the bias core if the sampled current i_{SNS} is low enough to pull v_{ST} up to V_{BAT}. After the startup, i_{ST1} and i_{ST2} decrease to 0 A and do not affect the main bias current as v_{ST} falls LOW to V_{SS} when I_{SNS} with diode-connected long-channel PMOS transistors M_{PSD1} to M_{PSD7} pulls the gate voltage of

M_{PS1} and M_{NS1}. The measured output current ranges from 1.2 – 3.6 nA over 2.5 − 12.5 V rail-to-rail voltages at room temperature.

The nA-bias current generator automatically starts as soon as the system connects to battery v_{BAT}. The other circuit blocks initialize their states when this bias circuit is ready for normal operation. Figure 5.16 demonstrates the nA-bias ready signal (v_{NA_RDY}) generator, which the system uses as a power-on-reset signal. When the bias core starts and pulls v_{ST} LOW, this circuit drives v_{NA_RDY} HIGH to V_{BAT} after a long delay set by I_{RDY1} and C_{RDY1}. Similar to the de-glitch circuit shown in Figure 5.9, this circuit establishes a hysteresis using diode-connected transistor M_{NRDY3} as a temporary battery. However, M_{NRDY3} is a low-voltage transistor, which features a lower threshold voltage than high-voltage devices, because at the beginning of system operation, V_{SS} is 0 V and the rail-to-rail voltage may not be sufficient to accommodate several stacked high-voltage devices. The measured waveforms in Figure 5.16 illustrate the operation of the nA-bias ready signal generator at different rising speeds of v_{BAT}.

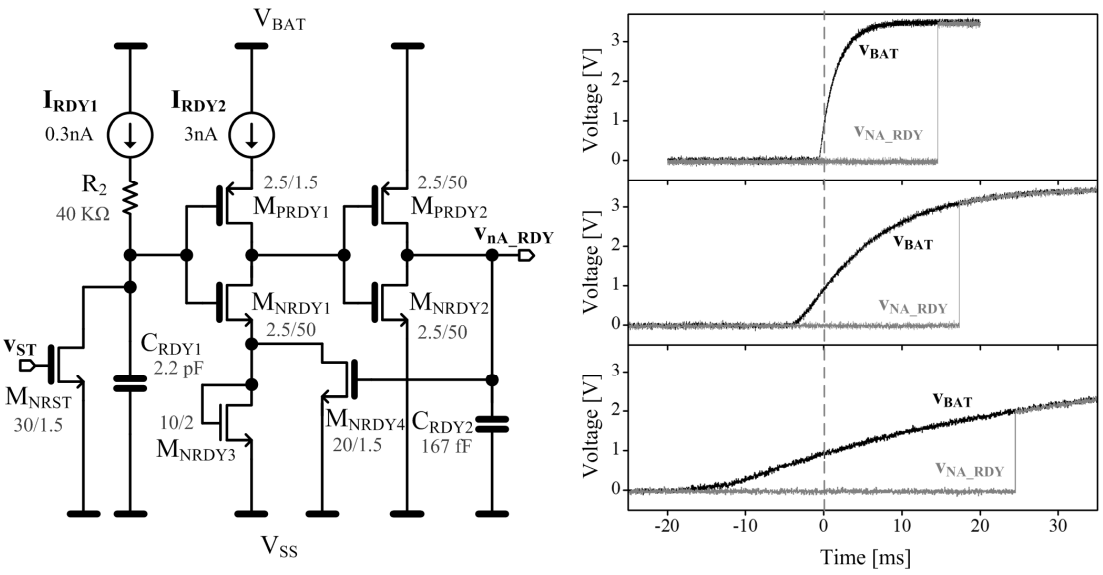

Figure 5.16. nA-bias ready signal generator with measured waveforms.

5.2.8. Local Micro-ampere Bias-current Generator

Figure 5.17 shows another type of current generator that locally biases the fast comparators CP_{LD} and CP_{CHG}. The circuit, modified from [213], starts to generate 2-µA output current when the system drives v_{EN} HIGH to release the gates of M_{P1} and M_{P2} by turning M_{P7} off and to push startup current i_{ST}, set by R_{ST} and M_{P3}, into the main bias circuit. As the core, a proportional-to-absolute-temperature (PTAT) current generator, establishes the current, M_{P6} samples it and turns M_{P4} off to block i_{ST} from the main current loop. The two local µA-current generators for CP_{LD} and CP_{CHG} settle within 1 µs in all measured conditions.

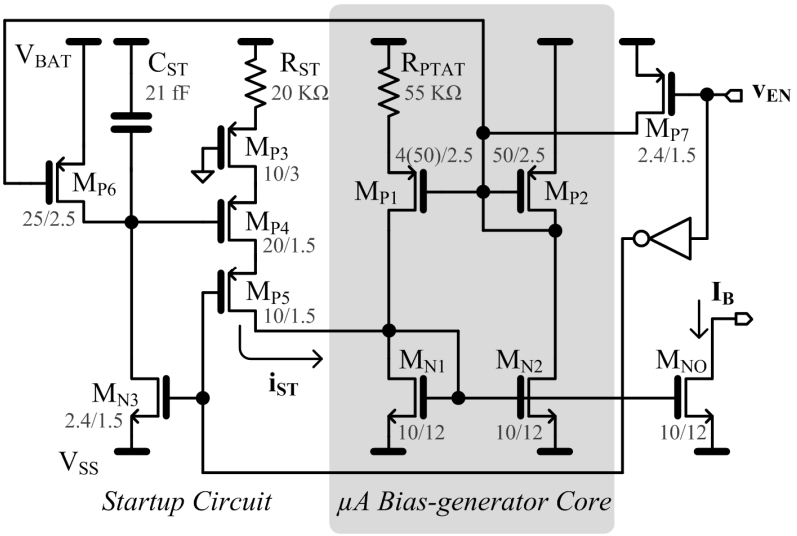

Figure 5.17. Local micro-ampere bias-current generator for CP_{LD} and CP_{CHG}.

5.3. Harvesting Performance

Figure 5.18 shows the die photo of the 1.8 mm × 1.3 mm, 0.35-µm CMOS IC prototype. Power switches M_N and M_P occupy the top corners of the die to shorten the current paths and isolate themselves from the noise-sensitive analog blocks as much as possible. The corner positions also save area for guard rings as two edges of each power transistor face toward the outside of the die and therefore do not need to be surrounded. The other edges, the bottom and side edges, facing toward the inside of the chip, are surrounded by wide

n-well guard rings. DRV_N and DRV_P are positioned near M_N and M_P to minimize the resistance of the signal paths. The 54-nF C_F for DRV_N is a thick poly-poly capacitor, and the 20-MΩ R_{PK} for the peak detector employs an n-well resistor, which exhibits the highest sheet resistance in the given process. Because R_{PK} experiences high-voltage transient responses, field plating is used to prevent parasitic channel generation [212]. Although the whole system shares one substrate, the prototype allocates separate pins for the analog substrate voltage (i.e., V_{SSA}) and the digital/power counterpart (i.e., V_{SSD}) to prevent the crosstalk caused by bond-wire inductances.

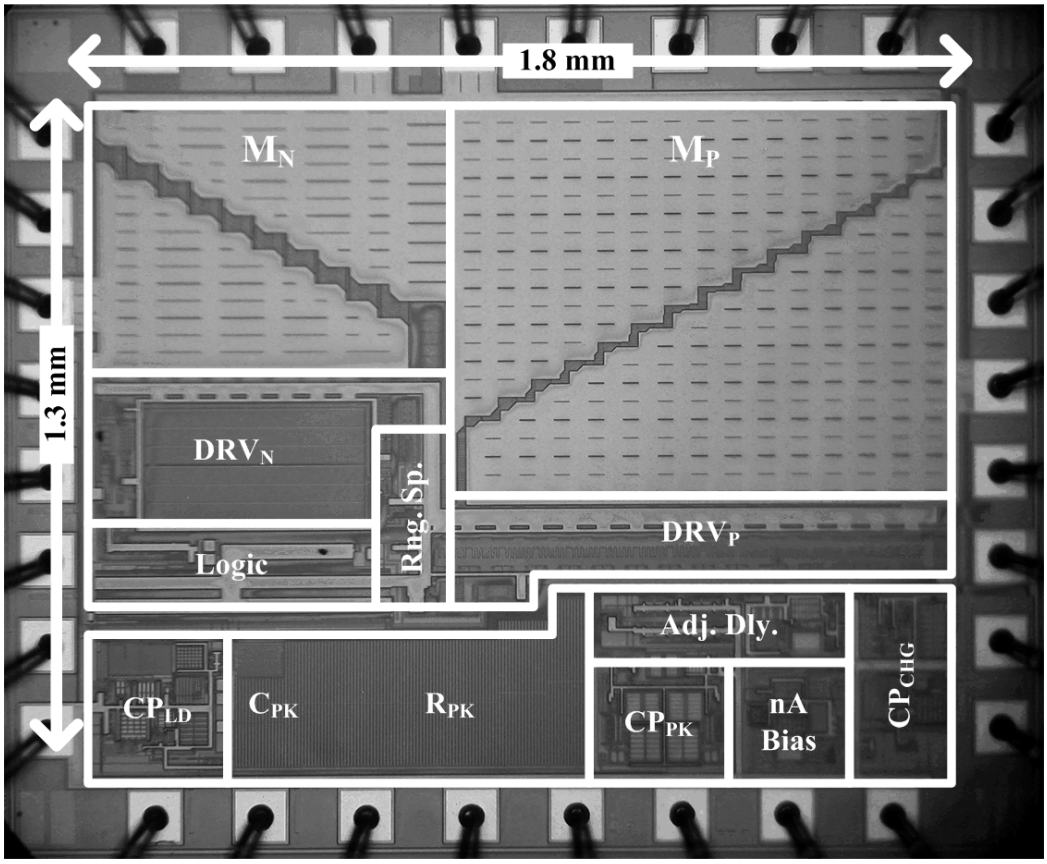

Figure 5.18. Die photograph of the harvester prototype.

The 4.2 cm × 3.3 cm × 0.16 cm printed-circuit board (PCB) shown in Figure 5.19 uses the piezoelectric transducer V22b from Mide Technology, which embeds 25.4 mm × 3.8 mm × 0.25 mm piezoelectric material inside a 2.7-cm cantilever. A plastic bolt fixes

the PCB to a Brüel & Kjær's Mini-shaker 4810. The Schottky diode HSMS-2800 and a 36-nF SMD capacitor are soldered on the bottom layer of the PCB. A slide switch enables and disables the IC for testing purposes, and a displacement sensor LK-G87 (not shown in Figure 5.19) from Keyence Corporation measures the vertical displacements of the transducer.

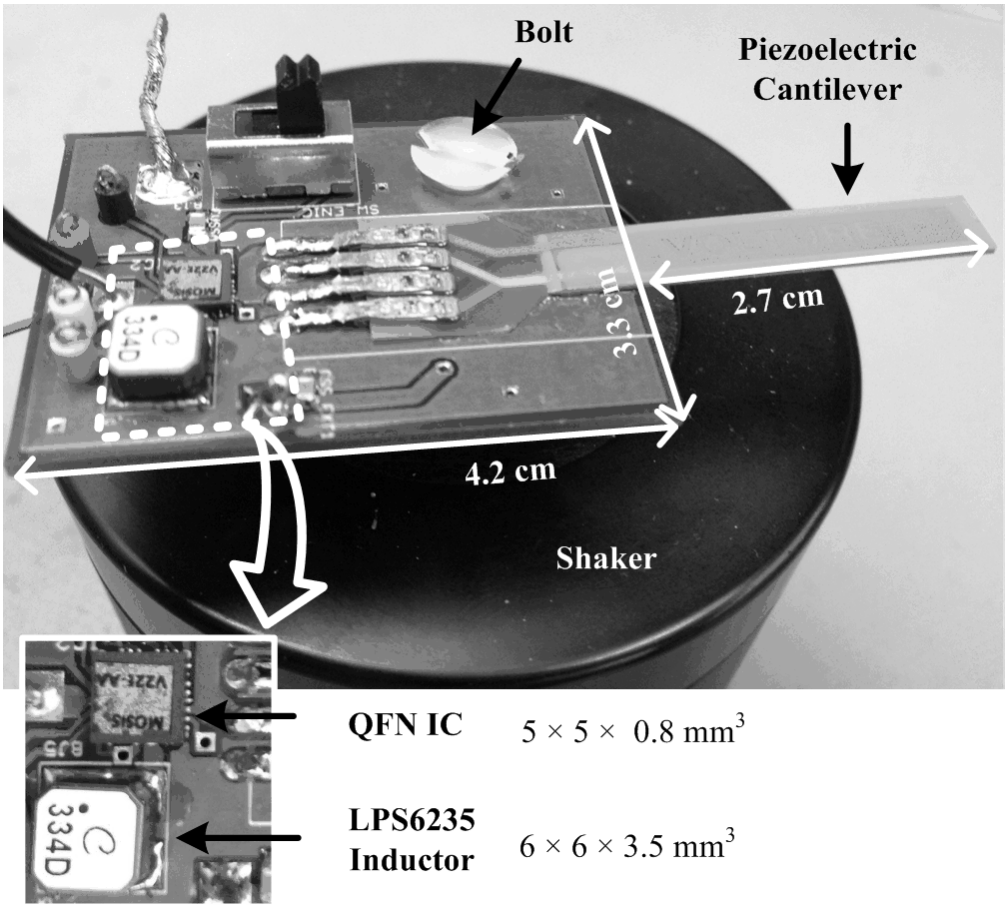

Figure 5.19. Experimental setup photograph of the harvester prototype.

5.3.1. Charging Performance

As Figure 5.20 shows, the prototype charged the 475-nF capacitor at the output (i.e., v_{BAT}) from the vibrations that induced the open-circuited piezoelectric voltage $V_{PZ(OC)}$ of 0.57, 0.68, 0.88, 1.1, 1.5, 1.8 and 2.0 V. The measured acceleration rates at the base of cantilever corresponding to the $V_{PZ(OC)}$ values were 0.06, 0.08, 0.1, 0.13, 0.15, 0.19, and

0.21 m/s^2. Since the harvester invests energy at the positive peak of v_{PZ} and charges v_{BAT} at the negative peak, v_{BAT} waveforms first step down and then step up, resulting in net v_{BAT} increments over the cycles. With τ_I fixed at 1.9 μs, the battery investments are similar for each case shown in Figure 5.20 as the initial drops in v_{BAT} voltage overlap in the graph. However, the amplitudes of the rising steps are larger for stronger vibration inputs. This is because the energy gain from the investment increases with the initial seed energy that the vibration generates and stores in the piezoelectric transducers. Note that from the vibrations that resulted 0.57-V $V_{PZ(OC)}$, the harvester replenished only the amount of energy that the system lost during the energy transfers. However, because the losses decrease with smaller amounts of energy investment, the harvester can derive net energy gains from smaller voltages than the 0.57-V $V_{PZ(OC)}$ case by reducing the amount of battery investment.

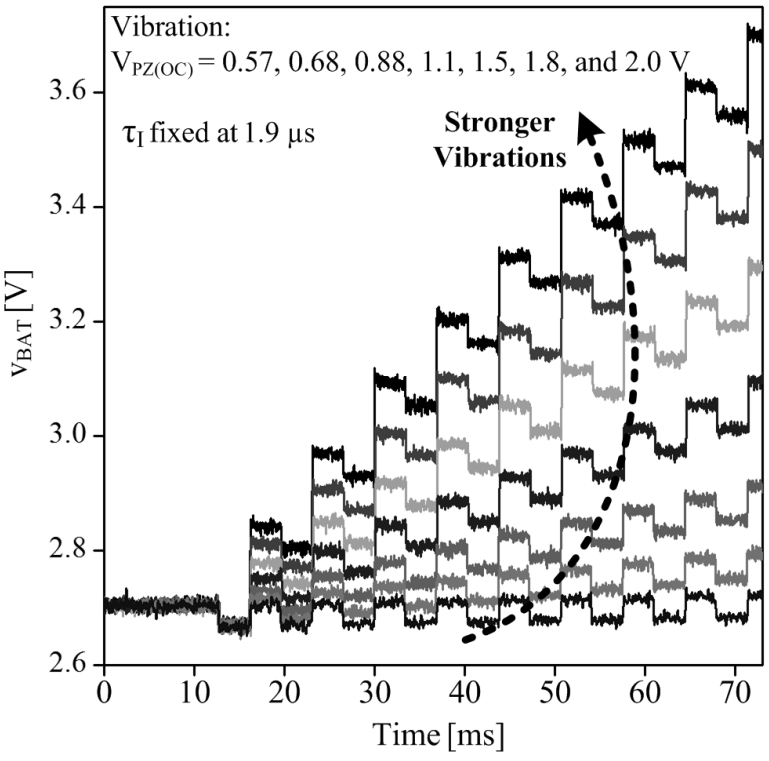

Figure 5.20. 475-nF capacitor charging profiles with various vibrations.

On the other hand, Figure 5.21 shows the charging performance of the harvester at different battery investments. The battery investment increases with longer τ_I's, as the increasing amplitudes of falling v_{BAT} steps reflect. Likewise, the magnitudes of the rising v_{BAT} steps increase with increasing battery investment, but because of losses, the net energy gain does not always rise with increasing battery investments.

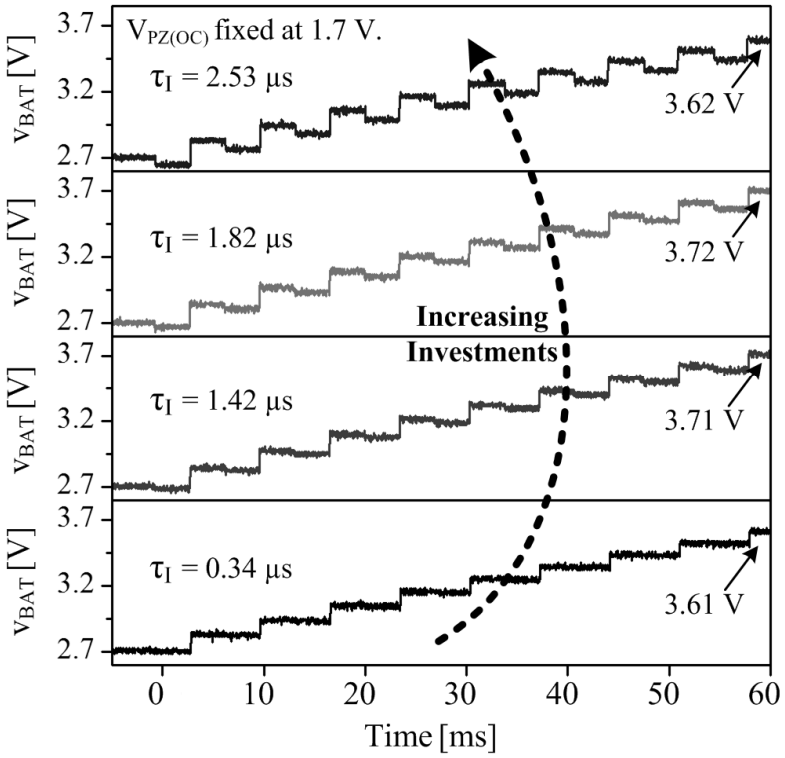

Figure 5.21. 475-nF capacitor charging profiles with various battery investments.

The input (P_{IN}) and net output power (P_O) of the prototype were measured over various vibration strengths and battery investments. Figure 5.22a shows that the harvester drew up to 79-µW P_{IN} from the transducer and delivered 52-µW P_O to the output battery. For comparison, Figure 5.22a also plots the theoretical maximum power $P_{BRG(MAX)}$ of a bridge rectifier assuming lossless elements with perfect maximum power point tracking control. From the same vibrations, the proposed harvester extracted 2.1× – 8.6× more power (P_{IN}) than the ideal bridge rectifier. P_{IN} rose with increasing $E_{I(BAT)}$; however, the

trend was not always the same with P_O. Figure 5.22b demonstrates three representative cases exhibiting different relations between P_O and $E_{I(BAT)}$. With increasing $E_{I(BAT)}$, P_O increased when $V_{PZ(OC)}$ is 2.65 V, but decreased when $V_{PZ(OC)}$ is 0.61 V. In between these two cases, for 1.02-V $V_{PZ(OC)}$, P_O peaked in the middle of the $E_{I(BAT)}$ range.

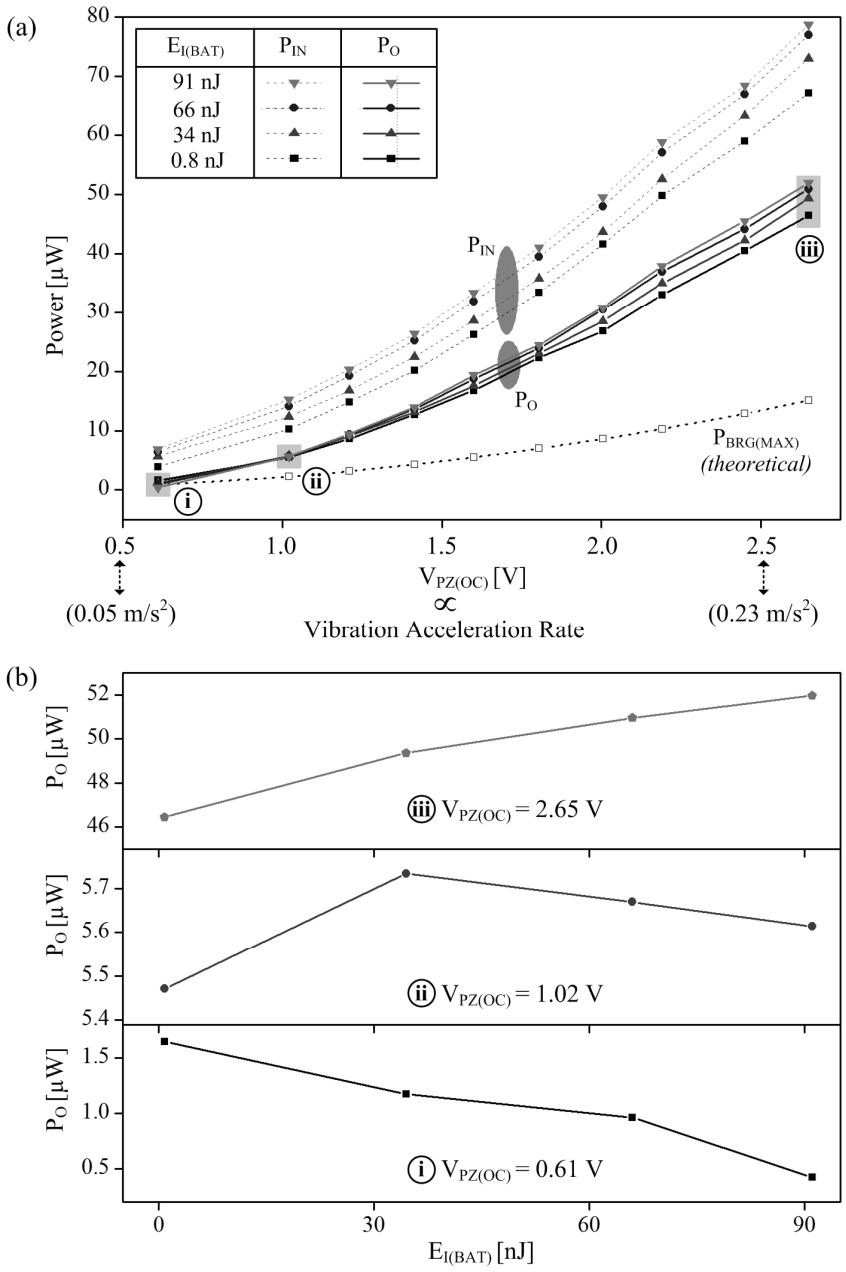

Figure 5.22. Input (P_{IN}) and output (P_O) power over various (a) vibrations and (b) battery investments.

5.3.2. Power-conversion Efficiency

The losses of the circuit increased when the system invested a larger amount of $E_{I(BAT)}$ for a given vibration, and the portion of the investment-induced losses became more noticeable with weak vibration inputs than with strong vibrations. The poor efficiencies at the low P_O range shown in Figure 5.23 corroborate these trends. For relatively strong vibrations, however, the IC efficiency peaked from 66% to 69.2 % with various values of $E_{I(BAT)}$.

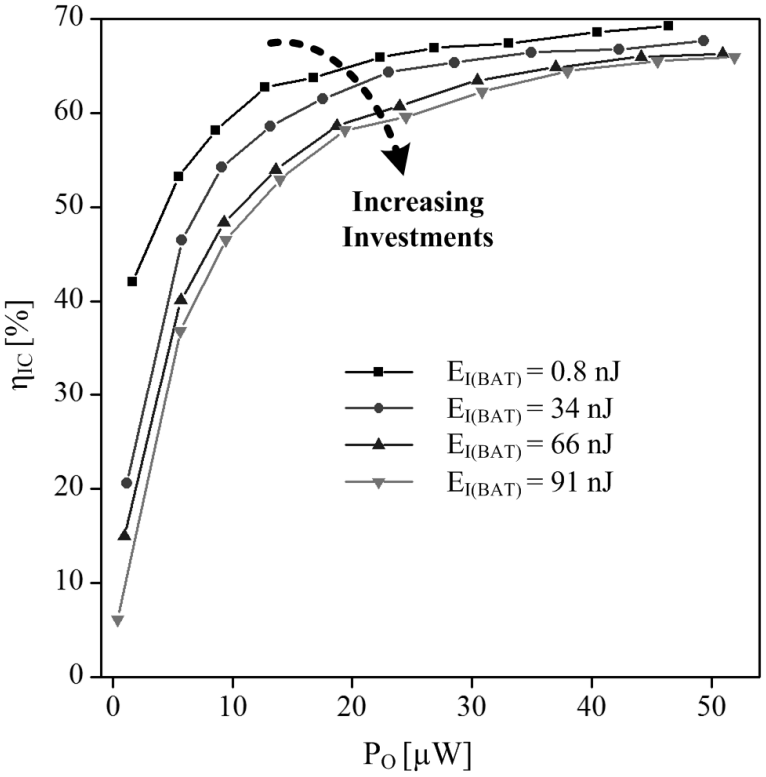

Figure 5.23. Harvester IC efficiency.

Figure 5.24 shows the dissected losses of the system over the measured P_O range. While gate-drive (P_{GD}) and quiescent (P_Q) losses did not vary a lot across P_O, conduction losses (P_{COND}) increased with increasing P_O and dominated the total losses. Despite the large sizes of M_N and M_P, high-voltage devices exhibited low conductivity due to their

thick gate-oxides and low-doping bulk materials. Balancing P_{GD} and P_{COND} at higher P_O levels by designing even larger power switches could have raised the peak efficiency, but the larger P_{GD} raises the threshold of the input vibration strength for a net energy gain. In contrast to P_{COND} and P_{GD}, the constant-operating blocks such as CP_{PK}, adjustable delay and nA-bias generators, or the duty-cycled CP_{LD} and CP_{CHG} consumed a much smaller amount of power ranging 0.28 – 0.51 µW and 45.5 – 116.4 nW, respectively.

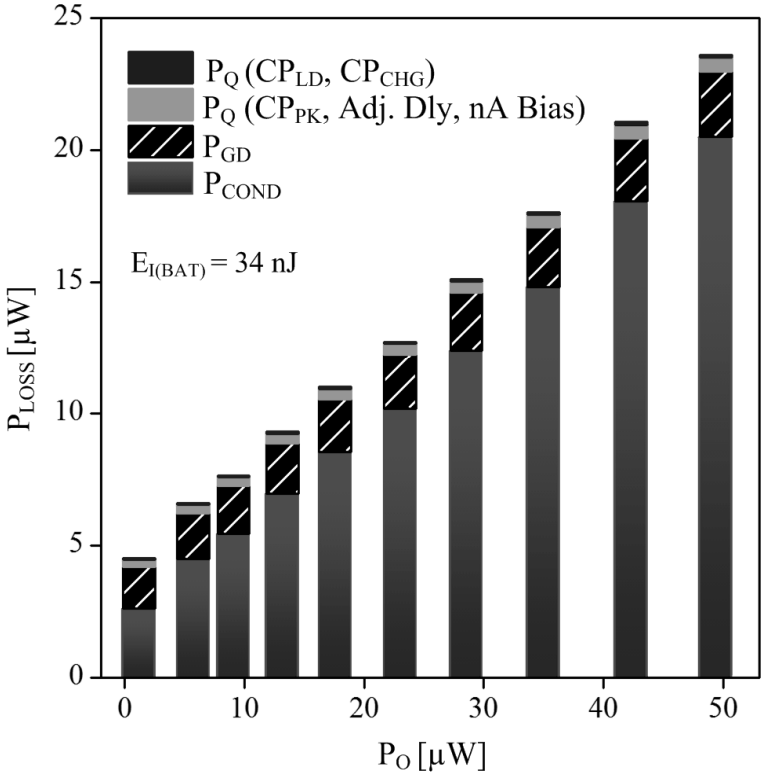

Figure 5.24. Loss breakdown of the harvester prototype.

5.3.3. Harvesting Performance over various vibration frequencies

Piezoelectric transducers generate the highest voltage when vibrations drive the transducer at its resonant frequency. Figure 5.25 shows the harvesting performance of the prototype over various vibration frequencies. P_{IN} and P_O peaked at 53.0 µW and 36.4 µW, respectively, with 143-Hz vibration, and the power levels declined as vibrations

departed from the resonant frequency. From the same vibrations, the prototype induced at least 5.4× higher P_{IN} than the best-possible performance $P_{BRG(MAX)}$ of bridge rectifiers.

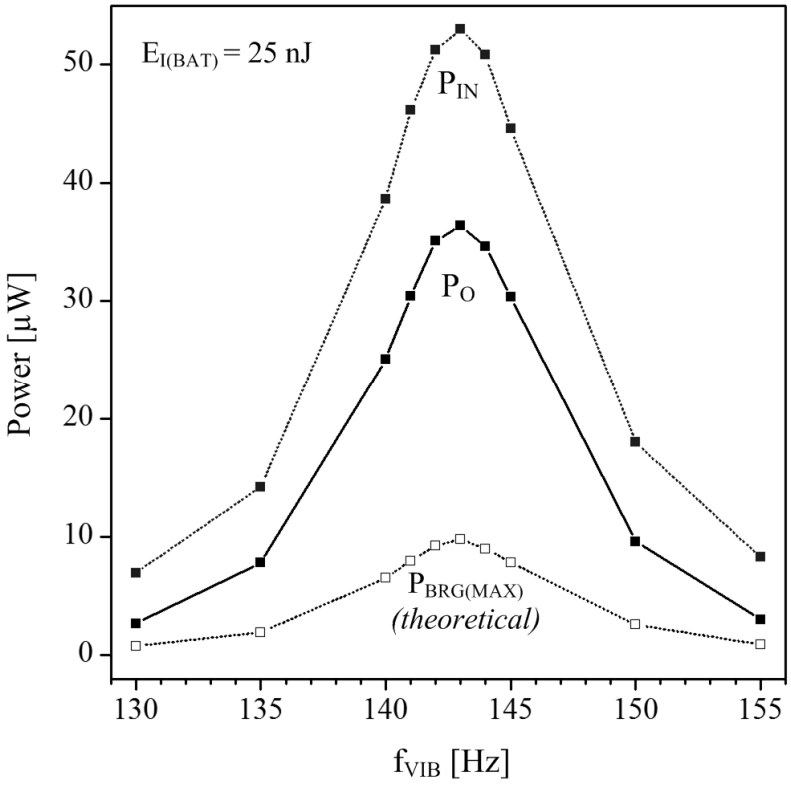

Figure 5.25. Harvesting energy from periodic vibrations at various frequencies.

The prototype also harvested energy from random vibrations, such as impact-induced ones, as it synchronizes its operation to the external vibration every half cycle. Figure 5.26a and b respectively illustrate the seconds- and milliseconds-scale voltage waveforms of the harvester charging 475-nF C_{BAT} under random vibrations generated by finger-tapping motions exerted on the bolt head of the PCB prototype in Figure 5.19. Because the impact-induced v_{PZ} was large at first but decreased rapidly, to prevent over-investments, the prototype re-invested only the energy harvested in C_{PZ} and bypassed the battery investment, which is why the staircase voltage in Figures 5.26a and b only rises.

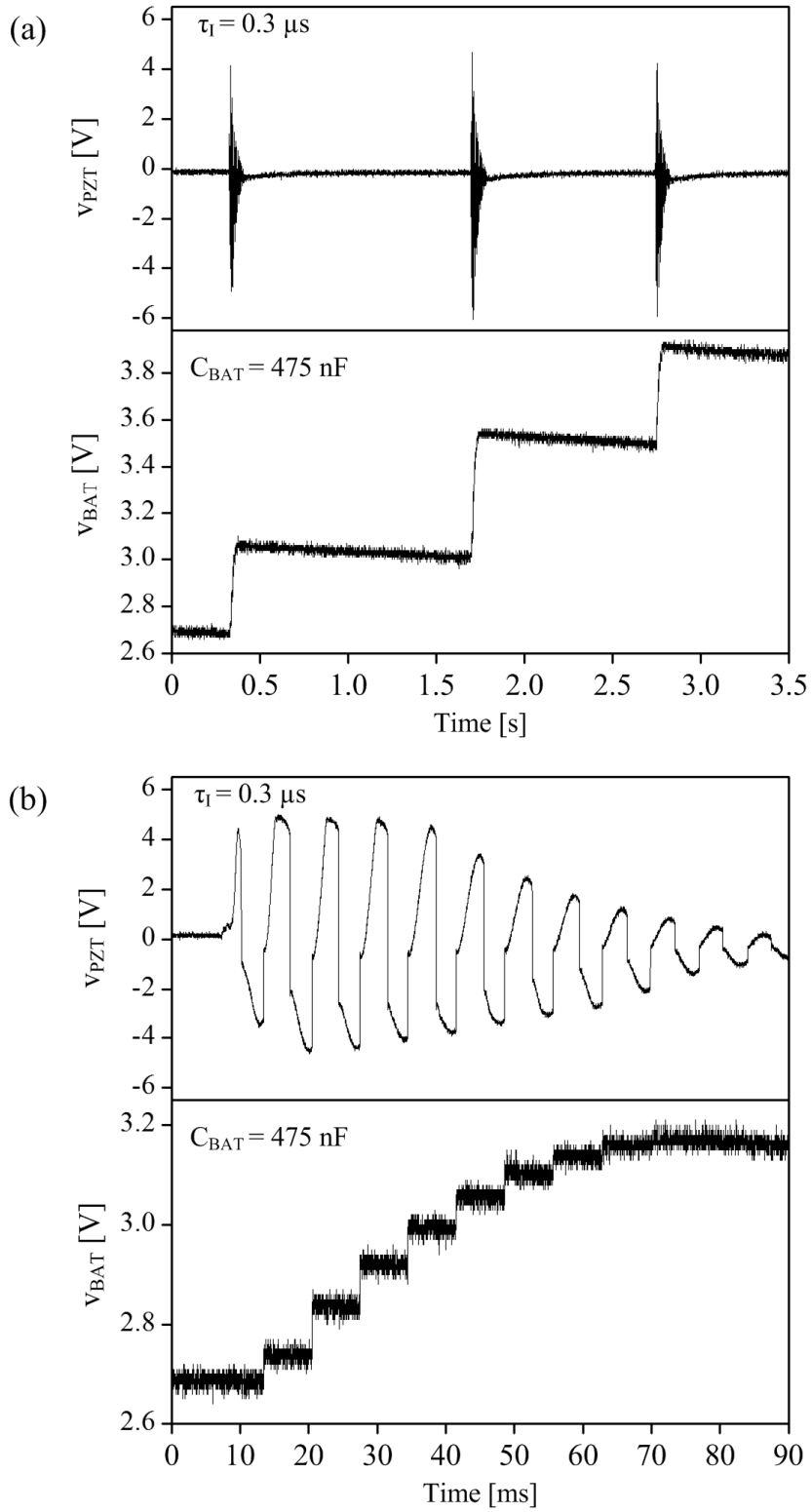

Figure 5.26. Harvesting energy from finger-tapping induced vibrations: (a) seconds-, and (b) milliseconds-scale waveforms.

5.4. Discussion

The experimental results of the prototype confirm that the energy investment in a piezoelectric transducer can increase the harvesting power. In theory, this investing scheme is particularly useful for harvesting energy from the low piezoelectric output voltages that can result from weak vibrations, low piezoelectric-coupling transducers, and the unmatched resonant frequency of transducers, because, as shown in (5.4), the investment can augment the energy gain of harvesting by raising pre-charging voltage V_{PC}. Hence, a harvesting circuit should invest energy into the transducer to increase the damping voltage until it reaches the breakdown voltage limit of a given semiconductor process. However, in reality, the investing scheme can be justified only when the energy gain from the investment surpasses the additional losses associated with the investment. Satisfying this prerequisite can be challenging if the seed energy in piezoelectric voltage Δv_{PZ} is small as the energy gain is proportional to Δv_{PZ} amplitude. This is why P_O in Figure 5.22 decreased with increasing investment for small piezoelectric voltages.

Another potential limiting mechanism for the investing scheme is over-damping of the transducer. When the harvester removes the kinetic energy of a transducer, its displacement, which is proportional to Δv_{PZ}, decreases as a result of harvesting. Figure 5.27 shows the measured displacements at the tip of the piezoelectric cantilever across P_{IN} of the prototype. The vibration strength was constant; however, the displacement decreased as the prototype drew increasing amount of P_{IN} by investing more $E_{I(BAT)}$ into the transducer. Because the decreasing rate of the displacement was small, this prototype was able to produce energy gain from investing. However, if a transducer responds very sensitively to the increased damping force and exhibits rapid displacement attenuation, a harvester may not be able to derive a net energy gain from the investing.

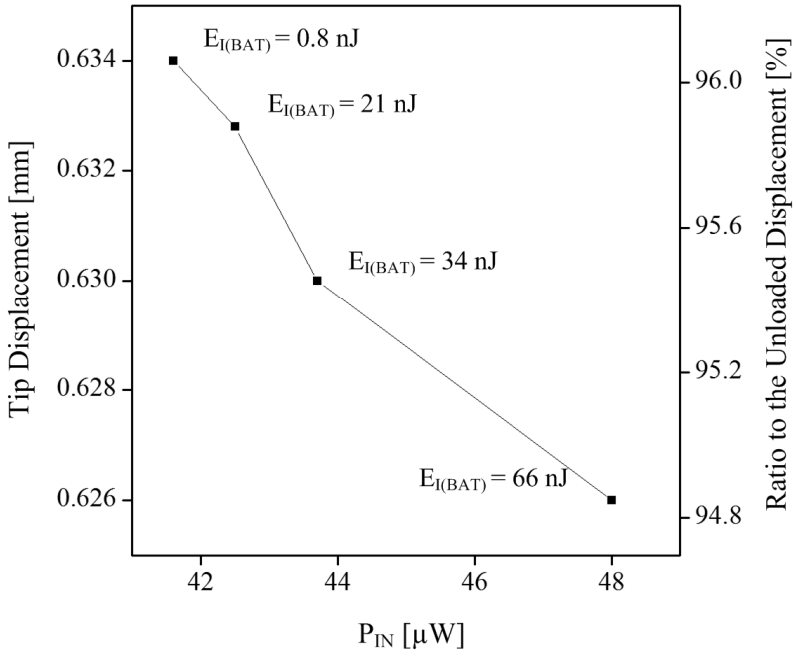

Figure 5.27. Tip displacement variation over the input power of the harvester.

5.5. Summary

The energy-investing piezoelectric harvester harnessed up to 79 μW from a transducer and charged output energy storage with 52 μW. This result proves that the investing harvester can draw 5.3× more energy than the amount of energy an ideal bridge rectifier can maximally draw from the same input vibrations. Moreover, because the switched-inductor converter does not impose a battery-induced input threshold and synchronizes to external vibrations every half cycle, the prototype can harvest energy from random vibrations, which are more prevalent in practical environments than periodic vibrations. However, although the analog control circuits spent less than 1 μW for their operation, the losses in power switches can degenerate the total energy gain of investment if low v_{PZ} inputs provide only small seed energy for the investing-harvester operation. Hence, the proposed single-inductor investing harvester allows a user or a system to adjust the investment to adaptively control the electrical damping force of the piezoelectric

transducer, so that, eventually, the harvester can output the maximum power from ambient vibrations.

CHAPTER 6

CONCLUSIONS

As electronic systems become smaller and smaller, their functionality and lifespan become limited as the available power and energy in the battery of the system decreases. This trade-off between the system dimension and battery capacity becomes a major challenge for micro-scale devices such as wireless micro-sensors and biomedical implants because, in addition to the restricted functionality and short lifetime, replacing or recharging their batteries poses considerable risks and costs. Harvesting ambient energy from light, heat, RF radiations, and vibrations to autonomously replenish the on-board energy storage of miniaturized electronic systems is an attractive alternative to tiny batteries because the energy tanks (i.e., environments) contain a virtually infinite amount of energy.

This research proposes to harvest, among various ambient energy sources, kinetic energy in motion and vibrations as ambient movements are widely available in numerous applications. The primary objective of the investigation is to develop, design, and evaluate CMOS integrated circuits that harvest ambient kinetic energy in periodic and aperiodic vibrations using miniaturized piezoelectric transducers to continually replenish energy-storage devices such as capacitors and rechargeable batteries. Although vibrations in the surrounding environment produce a vast amount of energy over time, tiny transducers can harness only a limited amount of power, especially when the mechanical movements are weak as in the case of many ambient vibrations. Therefore, the harvester circuit must be able to condition the transducer to improve the energy-conversion capability and efficiently transfer energy into electrical storage devices. This chapter summarizes the findings from the investigation by reviewing the challenges of miniaturized piezoelectric energy harvesters and the fundamental contributions of the

conducted research. To conclude this dissertation, it will present important technical limitations and possible future research directions for micro-scale piezoelectric energy harvesting.

6.1. Miniaturized Piezoelectric Harvesters

A piezoelectric transducer generates charges across its top and bottom surfaces when it experiences stress and strain from external vibrations. This piezoelectric effect can be modeled by a motion-dependent current source (i_{PZ}) charging and discharging the inherent capacitance (C_{PZ}) of the piezoelectric device whose voltage is v_{PZ}. Figure 6.1, reproduced from Figure 2.3, illustrates the energy-flow of an open-circuited piezoelectric cantilever across a vibration cycle T_{VIB}.

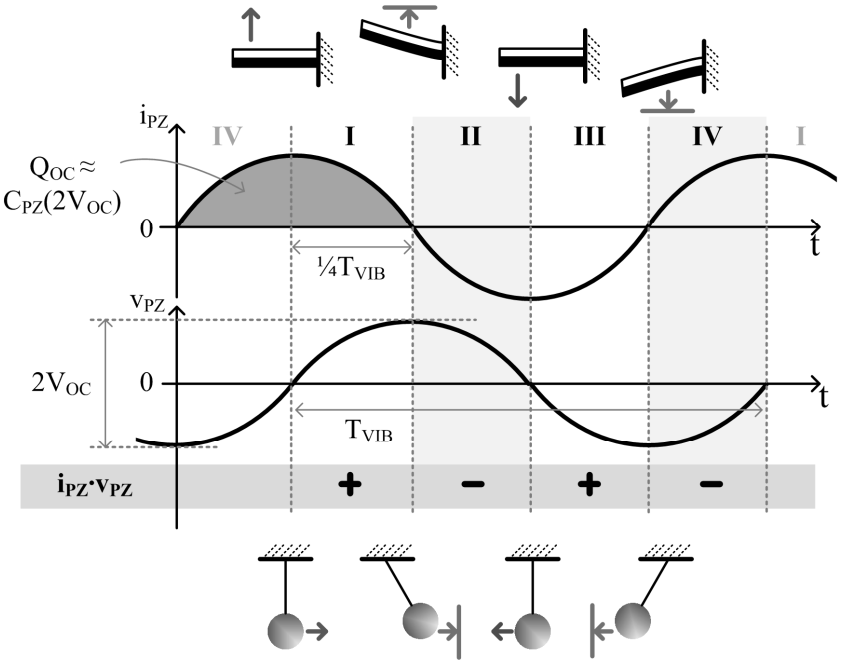

Figure 6.1. Energy-flow of an open-circuited piezoelectric cantilever with a pendulum analogy.

When the cantilever moves upward in Phase I of Figure 6.1, i_{PZ} and v_{PZ} of the transducer are both positive; therefore, the transducer generates net electrical energy, which charges C_{PZ}. Across this Phase I, the electrical damping force caused by v_{PZ} and

the mechanical (elastic) damping force caused by the displacement of the cantilever oppose the external vibration force. At the positive peak of the displacement, v_{PZ} reaches the maximum, but the velocity of the transducer and i_{PZ} cross zero. Hence, at this point, all the kinetic energy of the cantilever is converted into the mechanical potential energy of the cantilever and the electrical potential energy of C_{PZ}.

When the transducer moves downward in Phase II, both the mechanical and electrical potential energy are converted back to kinetic energy as they accelerate the movement of the cantilever. During this process, the electrical energy flows back into the mechanical domain and the transducer discharges C_{PZ} as the product of i_{PZ} and v_{PZ} is negative. At the end of Phase II, the velocity of the cantilever and i_{PZ} peak, and no potential energy exists in the system. The same energy flow occurs during Phase III and IV as in Phase I and II, respectively, resulting in zero electrical energy gain throughout the vibration cycle. Note that this energy flow of a piezoelectric cantilever is analogous to that of a pendulum, which is also presented in Figure 6.1. The well-known moving pendulum system continuously converts mechanical energy between the kinetic energy and the potential energy. The difference between the cases of the piezoelectric transducer and the pendulum is that the potential energy of the piezoelectric transducer consists of both mechanical and electrical components.

To harness the electrical potential energy that piezoelectric transducers generate from external vibrations, bridge rectifiers, as reviewed in Chapter 2, are often employed in harvester systems. Figure 6.2 illustrates i_{PZ} and v_{PZ} of an ideal diode bridge rectifier whose rectified output voltage (V_{RECT}) is regulated at $0.5V_{OC}$, half of the open-circuited voltage of a piezoelectric transducer. To emulate this ideal condition as close as possible, state-of-the-art bridge rectifiers employ switches, instead of diodes, and adaptive output voltage regulation control circuits. Assuming an ideal (i.e., lossless circuits) condition, the maximum output energy that an ideal bridge rectifier can draw from a piezoelectric transducer for a given vibration cycle is $C_{PZ}V_{OC}^2$ as derived in (2.3) and (2.7).

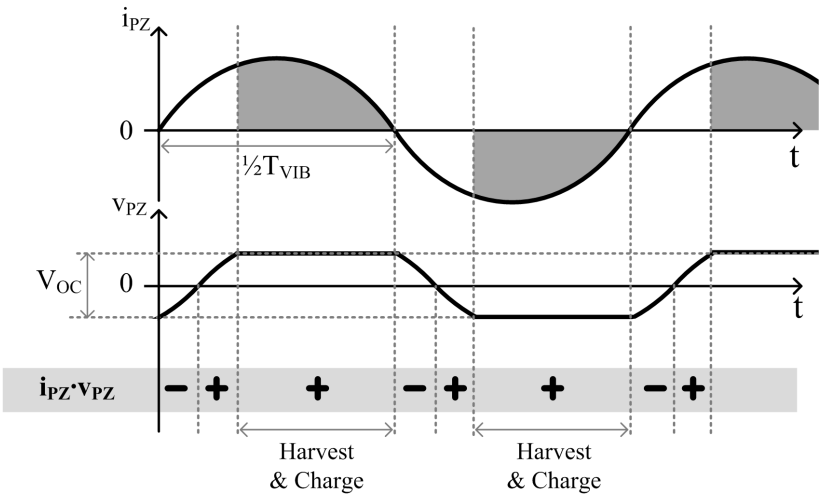

Figure 6.2. Operation of a piezoelectric harvester using an ideal diode bridge rectifier.

The bridge rectifier approaches are simple and matured, and therefore widely adopted in many piezoelectric energy harvesting systems. The reported output power of the bridge rectifiers often rise above several milliwatts, as shown in [155]–[156], when the bridge rectifiers harvest energy from centimeter-scale piezoelectric devices driven by strong vibrations whose frequency is matched to the resonant frequency of the transducer. However, the bridge rectifiers will face difficulties harvesting energy from micro-scale piezoelectric transducers, which typically are implemented using MEMS technology.

The output voltage of micro-scale piezoelectric transducers is generally low, because the displacements of the devices are limited by much smaller system dimensions and stiffer materials than those of larger piezoelectric transducers. Some state-of-the-art MEMS piezoelectric transducers exhibit relatively high voltages above 1 V in the open-circuited condition [151]–[153], but usually the stimulating vibration strengths and frequencies are stronger and higher than those of ambient vibrations, respectively. The low output voltage of a piezoelectric transducer forces the bridge rectifiers to regulate their output voltage below the low open-circuited piezoelectric voltage so that the energy can overcome the inherent voltage threshold of the bridge rectifier and flow through the rectifier. Nevertheless, even if the voltage threshold problem is resolved, because the

rectified output voltage is small, the electrical damping force of the transducer is weak, and therefore the amount of energy the transducer converts from vibrations is low. Hence, achieving net energy gain with bridge rectifiers can be challenging in practical circuits as the amount of input energy to the harvester circuit is small to begin with.

6.2. Research Contributions

6.2.1. Main Contributions

To fundamentally increase the output power of a miniaturized piezoelectric energy harvester, the harvesting circuit should strengthen the electrical damping force of a transducer. The bridge-free harvester circuit presented in Chapter 3 increases the electrical damping force by extracting all the energy C_{PZ} accumulates across a half vibration cycle ($\frac{1}{2}T_{VIB}$) and by resetting v_{PZ} to 0 V every half cycle so that the amplitude of the transducer voltage can rise to $2V_{OC}$. Figure 6.3 illustrates i_{PZ} and v_{PZ} of the bridge-free switched-inductor harvester circuit proposed in Chapter 3.

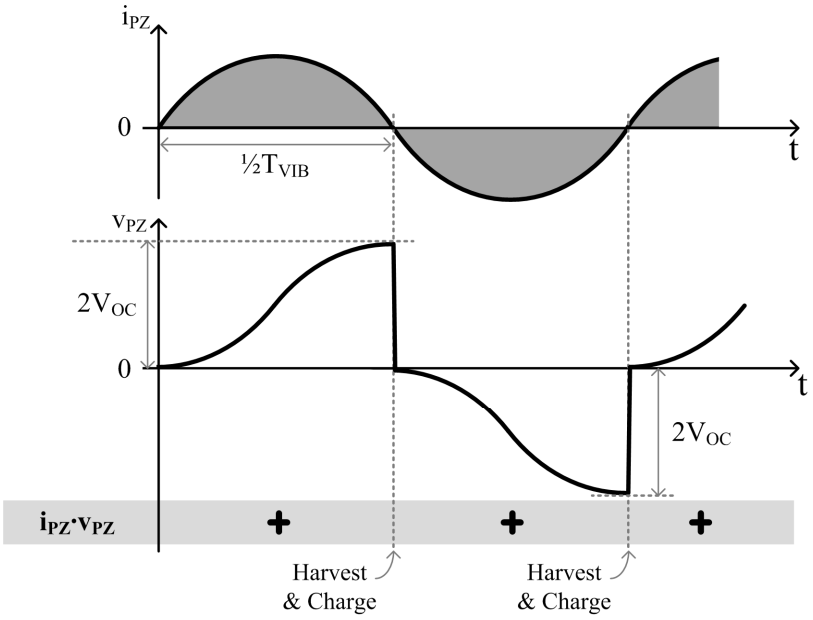

Figure 6.3. Operation of the bridge-free switched-inductor piezoelectric harvester.

Because the electrical damping force is proportional to the piezoelectric voltage, the electrical damping force of this harvester is stronger than those with the open-circuited condition in Figure 6.1 and the bridge rectifiers in Figure 6.2. However, the strengthened electrical damping force opposes the external vibration and decreases the displacement of the transducer. Hence, if, for instance, the strengthened electrical damping force reduces the displacement of the transducer to result in peak voltage of V_{OC}, instead of $2V_{OC}$, then the amount of energy that the switched-inductor harvester collects will be $C_{PZ}V_{OC}^2$, which is the same amount of output energy as in ideal bridge rectifiers. However, the displacements of typical small-scale piezoelectric transducers are dominantly set by external vibrations since the electrical damping force of a small transducer is much weaker than the external mechanical force. The experimental results presented in Chapters 3 and 5 corroborate the negligible effect of electrical damping force. Therefore, despite the increased electrical damping force, the amplitude of v_{PZ} rises approximately up to $2V_{OC}$ every half cycle. By harvesting the energy in C_{PZ} at $2V_{OC}$ twice a cycle, the bridge-free switched-inductor harvester theoretically harnesses $4C_{PZ}V_{OC}^2$ of energy per cycle.

The stronger electrical damping voltage allows the harvester to glean more energy from a vibrating piezoelectric transducer. Accordingly, the operation of the same circuit in Figure 3.3 can be modified to further increase the electrical damping force. Figure 6.4 illustrates the modified operation of the switched-inductor harvester. At the positive peak of v_{PZ}, the system harvests the energy C_{PZ} stored across the positive half of a vibration cycle into an inductor. However, instead of depositing the inductor energy to an output battery, the system invests the energy back to the transducer so that the transducer can exhibit strengthened electrical damping force during the negative half cycle. Because the circuit invests the harvested energy back into the transducer, the term “re-invest” was introduced in Chapter 4 to represent this operation. In fact, the switched-inductor converter in Chapter 3 (Figure 3.3) can be simplified to the circuit in Figure 4.6 if it is

desired that the harvester re-invests all the energy that C_{PZ} accrued across the positive half cycle. As a result of re-investing, the negative peak of v_{PZ} reaches $-4V_{OC}$, and the re-investing harvester can harness $8C_{PZ}V_{OC}^2$ of energy per cycle.

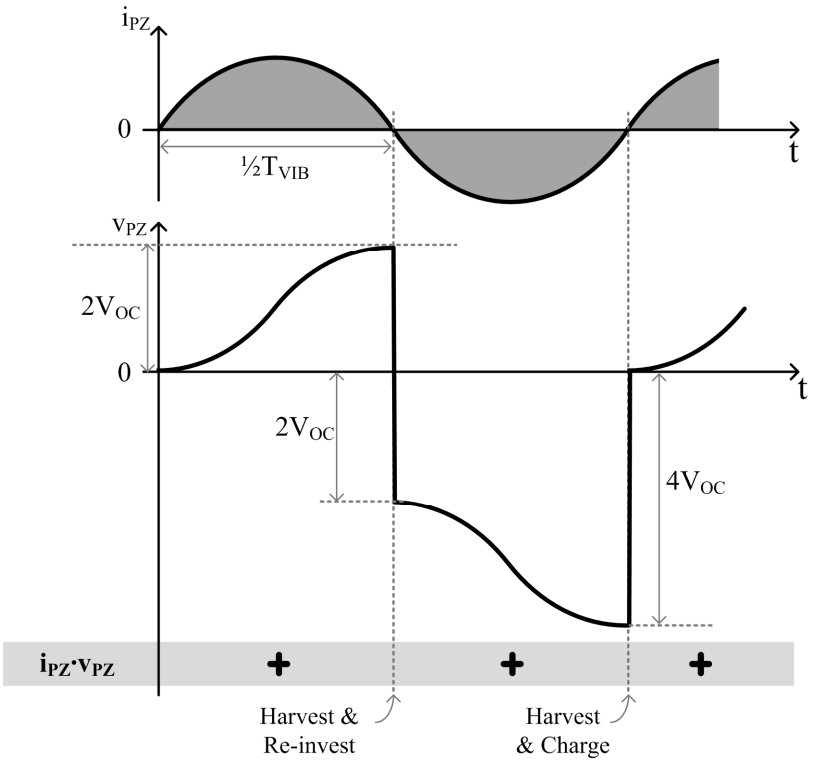

Figure 6.4. Operation of the re-investing piezoelectric harvester.

The electrical damping force can be further increased by investing battery energy into the piezoelectric transducer. Figure 6.5 shows the operation of the battery-energy investing harvester introduced in Chapter 4. The single-inductor switching converter in Figure 4.10 pre-charges the transducer to $+V_{PC}$ and $-V_{PC}$ at the beginning of the positive and negative half cycles, respectively. Because of this pre-charging, the amplitude of v_{PZ} peaks at $2V_{OC}+V_{PC}$ for both the positive and negative cycles; therefore, the theoretical energy gain across a cycle is $4C_{PZ}V_{OC}^2+4C_{PZ}V_{OC}V_{PC}$. This gain increases if the harvester raises the magnitude of V_{PC} by augmenting the amount of battery energy investments until the amplitude of the v_{PZ} swing reaches the breakdown voltage of the system.

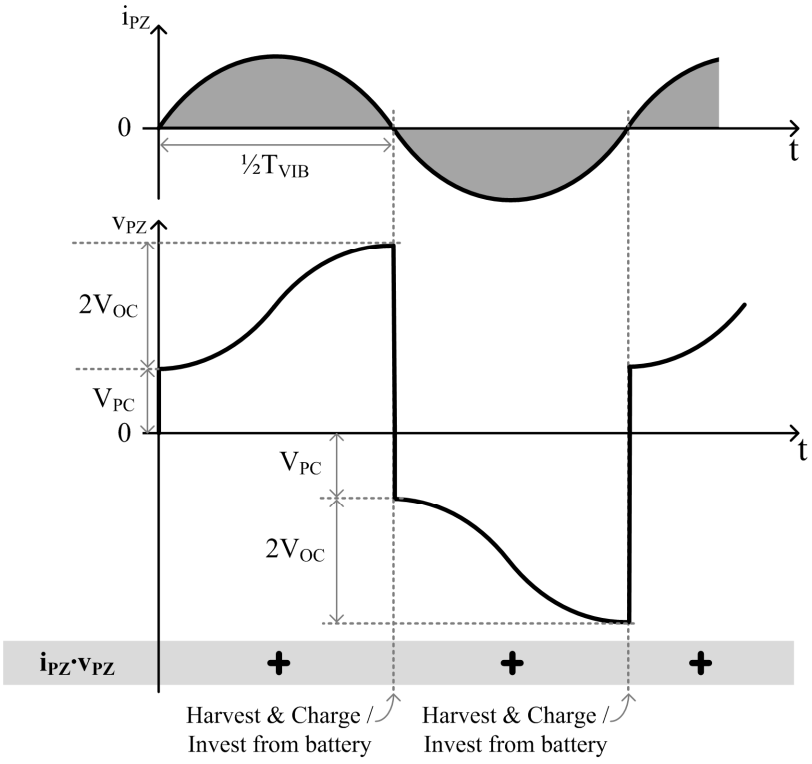

Figure 6.5. Operation of the battery-energy investing piezoelectric harvester.

Switched-inductor converters employed in the proposed harvesters are simple, yet offer versatile approaches to condition v_{PZ} and increase the electrical damping force. In theory switched-inductor circuits are efficient at delivering energy between two capacitive energy storage devices such as capacitors and batteries because the inductor not only transfers energy but also buffers the voltage difference of two capacitive sources so that the switches can exhibit low voltage drops across them. However, in reality, the system loses power when energy flows through the parasitic resistances of switches and the inductor and when the system charges and discharges the parasitic capacitances of switches.

While the losses can differ considerably depending on the specific implementations and the technology used, in general, the re-investing approach is more efficient than the battery-energy investing approach. This is because the battery energy in

miniaturized harvesters is ultimately harvested energy that had already incurred some losses when it was transferred into the battery. In addition, the circuit for the re-investing harvester employs fewer switches and ones that are switched less frequently than does the battery-energy investing harvester, resulting in lower conduction and gate-driving losses. However, the re-investing approach cannot invest more energy than the amount it harvested in advance. This means the electrical damping of the piezoelectric transducer is still limited by the strength of the external vibrations. Hence, a hybrid-energy investing harvester circuit that re-invests the harvested energy and invests the battery energy is proposed in Figure 4.12 and prototyped to experimentally validate the performance, as detailed in Chapter 5. Figure 6.6 demonstrates the operation of the hybrid-energy investing harvester.

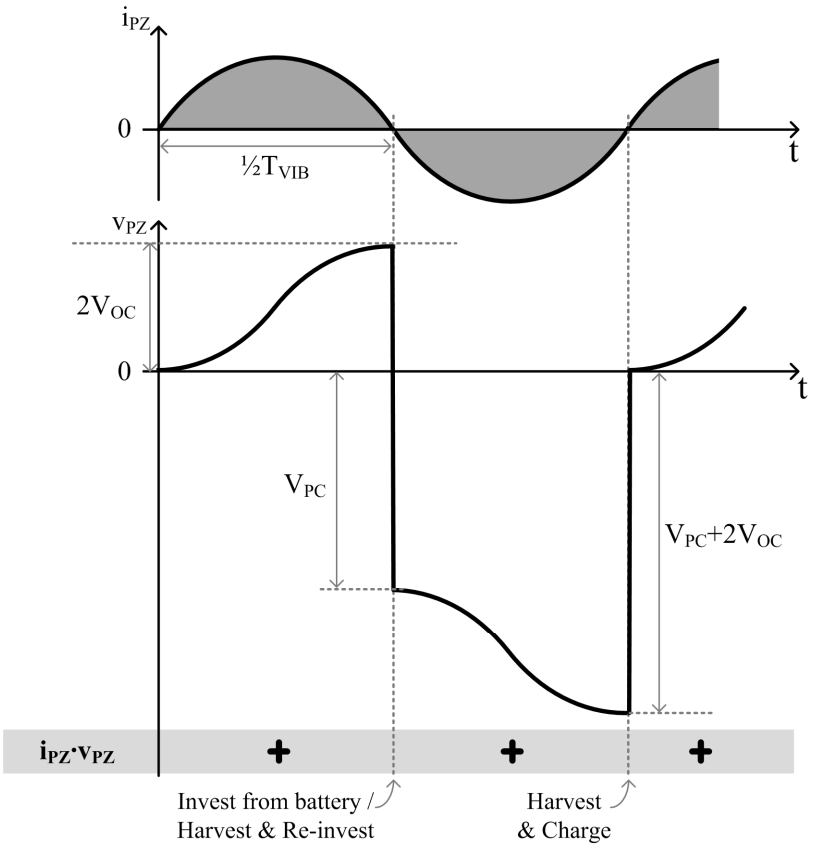

Figure 6.6. Operation of the hybrid-energy investing piezoelectric harvester.

At the positive peak of v_{PZ}, the harvester pre-charges C_{PZ} to $-V_{PC}$ by investing battery energy and re-investing the harvested energy across the positive half cycle. Because of the increased electrical damping voltage, the transducer converts more electrical energy during the negative half cycle than without the investment. Ultimately, the theoretical net energy gain that results from subtracting the battery-energy investment is $4C_{PZ}V_{OC}^2+2C_{PZ}V_{OC}V_{PC}$. As in the battery-energy investing case, the amplitude of V_{PC}, and therefore the energy gain, can be increased by augmenting the battery investment.

Table 6.1 summarizes the developed piezoelectric harvesters and their theoretical energy gain. Note that the gain of the hybrid-energy investing harvester appears to be smaller than that of the battery-energy investing harvester by $2C_{PZ}V_{OC}V_{PC}$. However, as discussed in Chapter 4, because the amplitude of V_{PC} in the hybrid-energy investing case can be twice as large as that of the battery-energy investing approach under the same breakdown voltage limits, the theoretical energy gains of the two are the same.

Table 6.1. Theoretical energy gain of piezoelectric harvesters.

Harvesting Circuit	Theoretical Energy Gain / Cycle	Discussed Chapter
Bridge Rectifier	$C_{PZ}V_{OC}^2$ (maximum)	Chapter 2
Bridge-free Switched-inductor Harvester	$4C_{PZ}V_{OC}^2$	Chapter 3
Re-investing Harvester	$8C_{PZ}V_{OC}^2$	Chapter 4
Battery-energy Investing Harvester	$4C_{PZ}V_{OC}^2 + 4C_{PZ}V_{OC}V_{PC}$	Chapter 4
Hybrid-energy Investing Harvester	$4C_{PZ}V_{OC}^2 + 2C_{PZ}V_{OC}V_{PC}$	Chapter 4, 5

6.2.2. Other Contributions

In addition to these switched-inductor piezoelectric energy-harvesting power-stages, efficient gate-drivers and low-energy analog and digital control circuits were developed throughout the investigation. Because the harvester interfaces with positive and negative voltages that can exhibit relatively large dynamic ranges, the gate-driving circuits used

various architectures such as v_{PZ}-referenced drivers, charge-pumps, and level-shifters. The analog and digital control circuits detected the external vibrations and synchronized the harvester operation so that the system could harness energy from periodic and aperiodic vibration inputs without complex control loops. The trade-off between the energy consumption and the speed was a common challenge of every control block. However, the slow vibrations allowed the slow control circuits that used only nA-currents to detect the peak voltages of the piezoelectric transducer. In addition, the quick electrical-energy transactions through the inductor enabled the system to use fast control circuits that operated for only a negligible fraction of the total vibration period and consumed very low energy. The result of these contributions of the circuit led the harvester to increase the electrical damping force of the transducer and ultimately increased the output power while minimizing the losses that occurred in the circuit.

6.2.3. Published Contributions

The research has produced several publications in peer-reviewed journals and conferences. Four journal papers and seven conference papers have been published. One patent application has been submitted and is currently undergoing review. Finally, one journal paper will be submitted in 2013. The following list presents the publication records.

Journals

[1] D. Kwon and G.A. Rincón-Mora, "Single-inductor–multiple-output switching DC–DC converters," *IEEE Trans. Circuits Syst.–II: Express Briefs*, vol. 56, no. 8, pp. 614–618, Aug. 2009.

[2] D. Kwon and G.A. Rincón-Mora, "A 2-µm BiCMOS rectifier-free AC–DC piezoelectric energy harvester-charger IC," *IEEE Trans. Biomed. Circuits Syst.*, vol. 4, no. 6, pp. 400–409, Dec. 2010.

[3] D. Kwon, G.A. Rincón-Mora, and E.O. Torres, "Harvesting ambient kinetic energy with switched-inductor converters," *IEEE Trans. Circuits Syst.–I: Regular Papers*, vol. 58, no. 7, pp. 1551–1560, July 2011.

[4] R.D. Prabha, D. Kwon, O. Lazaro, K.D. Peterson, and G.A. Rincón-Mora, "Increasing electrical damping in energy-harnessing transducers," *IEEE Trans. Circuits Syst.–II: Express Briefs*, vol. 58, no. 12, pp. 787–791, Dec. 2011.

[5] D. Kwon and G.A. Rincón-Mora, "A single-inductor energy-investing piezoelectric harvester," Scheduled to submit to *IEEE J. Solid-State Circuits*, 2013.

Conferences

[1] D. Kwon and G.A. Rincón-Mora, "A rectifier-free piezoelectric energy harvester circuit," in *Proc. IEEE Int. Symp. Circuits Syst. (ISCAS)*, pp. 1085–1088, May 2009. (2nd Place Award for 2009 SAIC-Georgia Tech Best Paper Contest)

[2] D. Kwon and G.A. Rincón-Mora, "Operation-based signal-flow AC analysis of switching DC-DC converters in CCM and DCM," in *Proc. IEEE Int. Midwest Symp. Circuits Syst. (MWSCAS)*, pp. 957–960, Aug. 2009.

[3] D. Kwon and G.A. Rincón-Mora, "A single-inductor AC–DC piezoelectric energy-harvester/battery-charger IC converting ±(0.35 to 1.2 V) to (2.7 to 4.5 V)," in *IEEE Int. Solid-State Circuits Conf. (ISSCC) Dig. Tech. Papers*, pp. 494–495, Feb. 2010.

[4] D. Kwon, G.A. Rincón-Mora, and E.O. Torres, "Harvesting kinetic energy with switched-inductor DC–DC converters," in *Proc. IEEE Int. Symp. Circuits Syst. (ISCAS)*, pp. 281–284, May 2010.

[5] S. Kim, G.A. Rincón-Mora, and D. Kwon, "Extracting the frequency response of switching DC–DC converters in CCM and DCM from time-domain simulations," in *Proc. IEEE Int. SoC Design Conf. (ISOCC)*, pp. 385–388, Nov. 2011.

[6] D. Kwon and G.A. Rincón-Mora, "Energy-investment schemes for increasing output power in piezoelectric harvesters," in *Proc. IEEE Int. Midwest Symp. Circuits Syst. (MWSCAS)*, pp. 1084–1087, Aug. 2012.

[7] D. Kwon and G.A. Rincón-Mora, "A single-inductor 0.35-µm CMOS energy-investing piezoelectric harvester," in *IEEE Int. Solid-State Circuits Conf. (ISSCC) Dig. Tech. Papers*, pp. 24–25, Feb. 2013.

Patent

[1] D. Kwon and G.A. Rincón-Mora, "Rectifier-free piezoelectric energy harvester and battery charger," US 8,368,290 B2, Feb. 2013.

6.3. Technological Limitations and Future Research Directions

Piezoelectric energy harvesting for micro-scale applications is a relatively new research area. Although a few low-power energy-harvesting systems have been released as commercial products, the dimensions of the reported systems do not readily conform to the requirements of micro-scale applications such as wireless micro-sensors and biomedical implants. Many subjects for micro-scale piezoelectric energy harvesting are in the research stage, and various challenges in terms of cost, integration, and power level need to be overcome for the technology to mature.

Similar to harvester systems, harvesting circuits that bridge piezoelectric transducers and batteries are also a relatively new topic for circuit researchers. Previously, since many harvesters had adopted bridge rectifier approaches, the research efforts for harvesting circuits focused on improving the bridge rectifiers and their conditioning circuits. However, as demonstrated in this research, switched-inductor converters provide more effective and more suitable conditioning approaches for piezoelectric transducers than can bridge rectifiers. The result of improved conditioning schemes is the strengthened electrical damping force of the transducer, which ultimately leads to the increased output power of the harvester. Still, important technological challenges that were found throughout the investigation require significant research efforts and innovations to ultimately implement a micro-scale piezoelectric energy harvester.

6.3.1. High-voltage Transistors in Low-energy Circuits

The piezoelectric energy harvesters developed in this research increase output power by boosting the electrical damping force of a piezoelectric transducer. Because the damping force increases with the higher voltage at the transducer terminals, the CMOS IC prototype described in Chapter 5 used 15-V CMOS transistors to handle higher voltage than typical low-voltage CMOS devices can withstand. However, the high voltage operation that allowed the increased energy gains has critical trade-offs in terms of cost, performance, and power loss.

High-voltage devices increase the manufacturing cost since they increase the number of masks, fabrication steps, and silicon areas. Moreover, high-voltage transistors employing thick gate-oxides and low-doping back-gate materials exhibit various unfavorable characteristics such as higher threshold voltage, higher channel resistance, lower Early voltage, lower transconductance (i.e., g_m), worse matching performance, and larger areas than low-voltage counterparts in the same process. One alternative that would partially mitigate the drawbacks of high-voltage devices is to generate a low-voltage supply inside the system so that control circuit blocks can use low-voltage transistors. However, unlike other electronic applications, micro-scale and microwatt energy harvesters typically have extremely tight energy budgets for their control circuits because the input energy to the system can be very small and unpredictable.

The use of high-voltage transistors in analog and digital control circuits may lead to various performance degradations such as poor matching and slow speed, yet these limited performances can be compensated by circuit techniques such as cascoding low-voltage transistors with high-voltage devices and clamping voltage ranges for low voltage transistors, or by allocating more spaces and bias currents within a justifiable margin. Unfortunately, the increased conduction losses of the power switches, which are caused by high threshold voltages and channel resistances, are difficult to circumvent as long as the system needs high-voltage operation.

For example, a threshold voltage of a high-voltage NMOS transistor is 1.2 V, while that of a low-voltage NMOS transistor is 0.6 V in the same semiconductor process. The channel resistance of the high-voltage transistor is about 4 times larger than that of low-voltage devices when the same aspect ratios (not the area) and the same overdrive voltages (not the gate-to-source or source-to-gate voltages) are assumed for both devices. Enlarging switch sizes and raising gate-driving voltages can reduce the conduction losses of these high-voltage power transistors, but these methods accompany the increased gate-driving losses, which in turn raise the net-energy threshold of the harvester operation. Some fabrication processes offer stepped-gate high-voltage transistors that allows thinner gate-oxide at the source side of the transistor to achieve lower channel resistance. However, these devices are asymmetric, which means that driving the gates and biasing the bodies of the switches may become another design challenges that demand innovations and risks.

6.3.2. Optimal Energy Investment

Although switched-inductor converters can offer the energy-transfer efficiency of near-100 % for high-power (e.g., above several watts) applications, the peak efficiencies tend to decrease for microwatt power applications. Generally, the limitation of efficiency in microwatt power systems occurs because of gate-drive and quiescent control losses that do not automatically scale down with the load power. While this trend was observed in very low-power ranges of the harvester prototypes developed throughout the investigation, the conduction losses of power switches limited the peak energy-transfer efficiencies of the harvesters. The non-ideal efficiencies are critical limitations especially for energy-investing harvesters because the losses generated from energy transfers degenerate the gain of investment, and they can even surpass the amount of energy gain and invalidate the act of investing.

The energy-investing harvester prototype presented in Chapter 5 can be used as an example to illustrate the adverse effects of non-ideal efficiencies. The harvester pre-charges a piezoelectric transducer at the positive peak of vibrations by investing both battery energy $E_{I(BAT)}$ and the harvested energy across the positive half cycle E_{IN}^{+}. If the energy-transfer efficiency for the investing operation is defined as η_{INV}, the following equation describes the energy flow of the investing operation.

$$E_{PC} = \eta_{INV}\left(E_{I(BAT)} + E_{IN}^{+}\right) , \tag{6.1}$$

where E_{PC} represents the amount of energy with which the harvester pre-charges the transducer. Then, during the negative half cycle, the vibration works against the increased damping force to produce E_{IN}^{-}, and at the negative peak, the circuit harvests all the energy in the transducer to charge the output battery by the following amount:

$$E_{CHG} = \eta_{HARV}\left(E_{PC} + E_{IN}^{-}\right) , \tag{6.2}$$

where η_{HARV} is the energy-transfer efficiency for the harvesting and charging operation. Hence, the net energy gain E_{NET} of the battery is

$$\begin{aligned} E_{NET} &= E_{CHG} - E_{I(BAT)} \\ &= \eta_{INV}\eta_{HARV}E_{IN}^{+} + \eta_{HARV}E_{IN}^{-} + \left(\eta_{INV}\eta_{HARV} - 1\right)E_{I(BAT)} . \end{aligned} \tag{6.3}$$

Because η_{INV} and η_{HARV}[1] are smaller than 1 in practical circuits, the third term in the second line of (6.3) is negative, which represents the losses of non-ideal energy-transfer efficiencies. If the efficiencies are close to 1, the net energy gain will increase with larger $E_{I(BAT)}$ since the effect of losses will be small and E_{IN}^{-} rises with an increasing amount of investment that strengthens the electrical damping force. On the other hand, if the efficiencies are considerably lower than 1, the losses that increase with large $E_{I(BAT)}$

[1] Note that these efficiencies η_{INV} and η_{HARV} are not the same as the total energy-conversion efficiency used in Chapter 5, which is defined by the ratio of E_{NET} to the sum of E_{IN}^{+} and E_{IN}^{-}.

can significantly degrade the energy gain. Figure 6.7 illustrates the relationships of the net energy gain and the battery-investment at various efficiencies.

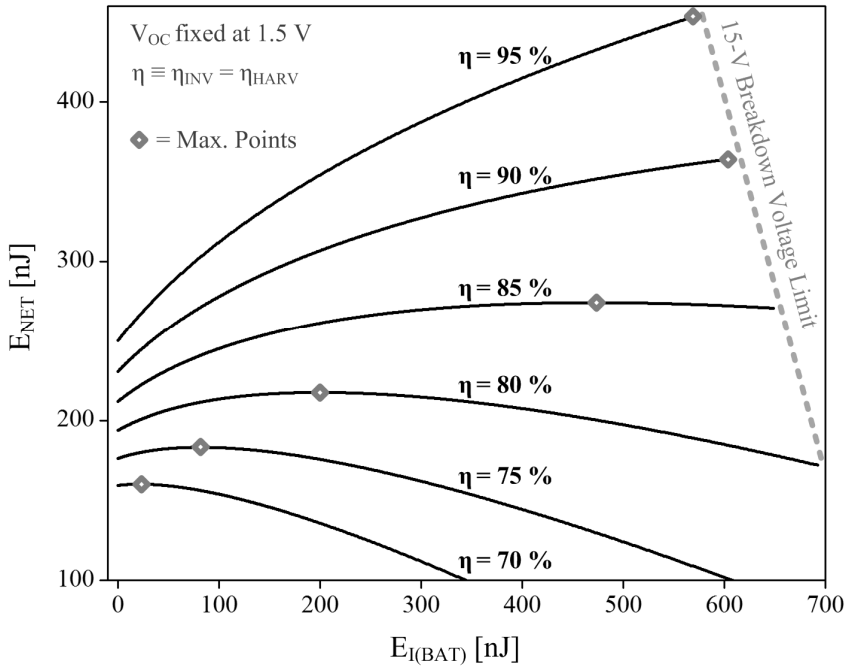

Figure 6.7. Calculated net energy gain over battery-energy investments for various efficiencies.

For the sake of simplicity, η_{INV} and η_{HARV} in Figure 6.7 are assumed to be the same and defined as η. The vibration strength is fixed to generate 1.5-V of open-circuited voltage of a piezoelectric transducer. For all the presented trajectories in Figure 6.7, at first, E_{NET} increases with increasing $E_{I(BAT)}$. However, when η is 70 %, E_{NET} peaks at relatively low $E_{I(BAT)}$ and decreases after that point. As η changes from 70 % to 95 %, the E_{NET} curves ascend, and the peak of each E_{NET} occurs at higher $E_{I(BAT)}$, except in the case with 95 % efficiency, which is limited by the 15-V breakdown voltage of the given process. The breakdown occurs when the peak-to-peak piezoelectric voltage reaches 15 V. For low efficiencies, the piezoelectric voltage cannot reach the breakdown point because of losses. As a matter of fact, for η lower than 90 %, the maximum net energy

gain is limited by the efficiency of the circuit, not by the breakdown voltage of the system.

Because of the increased electrical damping force from the investment, even when η_{INV} and η_{HARV} are 70 %, the net energy gain is considerably greater than the maximum output energy of ideal bridge rectifiers, which in this case can harness a maximum of 33.75 nJ per cycle. However, efficiency is important because, depending on the efficiency of the circuit, the gain of the investing harvester can vary more than 400 % even if the input vibration and the energy investment are the same.

Equation (6.3) also conveys that the investment from a battery, $E_{I(BAT)}$, can potentially lead the investing harvesters to exhibit a negative net energy gain. If the efficiencies are poor and the vibration is too weak to result in only a small E_{IN}^{+} and E_{IN}^{-}, too much $E_{I(BAT)}$ can induce more losses than the system harvests. Figure 6.8 demonstrates this potential problem of negative E_{NET}.

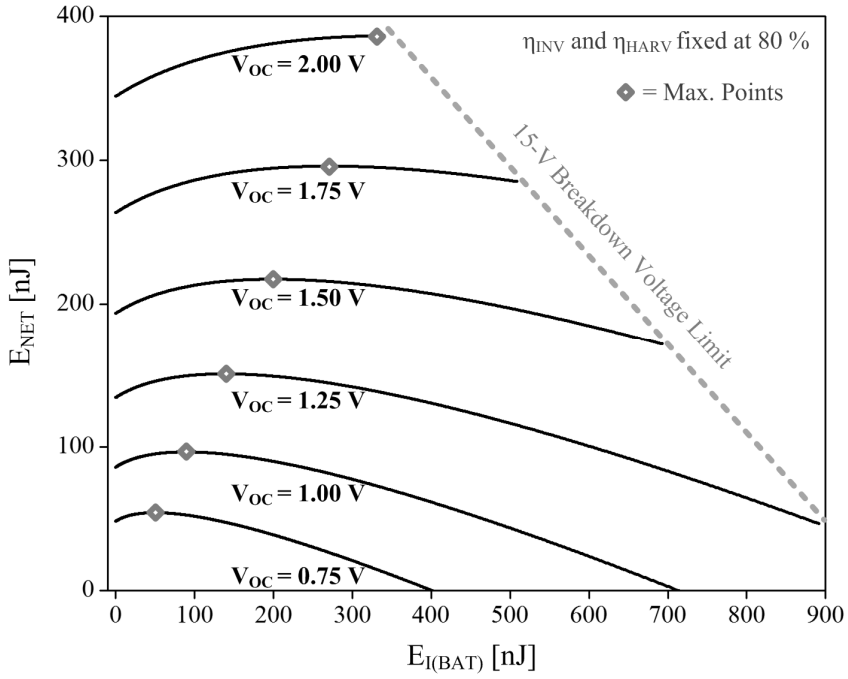

Figure 6.8. Calculated net energy gain over battery-energy investments for various vibration strengths.

With a fixed energy-transfer efficiency of 80 %, when the vibrations induce lower open-circuit voltages such as 0.75 V and 1 V, E_{NET} peaks at lower $E_{I(BAT)}$ values and decreases with steeper slope along the increasing $E_{I(BAT)}$. This is because the gain of E_{IN}^- caused by the increased $E_{I(BAT)}$ is small if the seed energy generated by the piezoelectric transducer from weak vibrations is small. If the vibration is strong and the resulting piezoelectric voltage is large, E_{IN}^- increases at a higher rate with increasing $E_{I(BAT)}$, causing E_{NET} to rise quickly and fall slowly before and after the optimal $E_{I(BAT)}$ point that maximizes E_{NET}.

The results shown in Figures 6.7 and 6.8 occur because the system invests battery energy in practical (i.e., lossy) circuits. If the efficiencies are high so that the product of η_{INV} and η_{HARV} is close to 1, then increasing the amount of battery-energy investment into the transducer will monotonically raise the net energy gain until the voltage reaches the breakdown voltage limit of the system. In this case, to achieve the optimal energy investment, the energy-investing harvester circuit can increase the amount of battery-energy investment until the voltage amplitude reaches the breakdown limit.

On the other hand, if the battery-energy investment is zero, the potential risk of exhibiting negative energy gain is eliminated regardless of energy-transfer efficiencies. The hybrid-energy investing harvester without battery-energy investment is reduced to become re-investing harvester. The electrical damping force and the energy gain can be lower than when the battery-energy strengthened the electrical damping force. Nonetheless, the fact that the system operates with only what it harvested from the input guarantees positive energy gain as long as the control and driver circuits consume lesser energy than the harvested amount. The harvester circuit still needs to monitor the voltage amplitude to limit the re-investing amount to prevent the breakdown of the system.

In reality, optimal energy investing will require more functionalities than just regulating the piezoelectric voltage lower than the breakdown limit. The efficiency cannot be 100 %, and the opportunity cost of bypassing the battery-energy investment

can be too high for the micro-scale applications where every nJ is precious. However, the optimal investment strategy is not obvious because the amount of optimal energy investment changes with the energy-transfer efficiencies and the input vibrations strengths. Furthermore, the efficiencies changes with the amount of energy transferred through the circuit, as shown in Figure 5.23. In addition, even though the movements of the piezoelectric transducer tested with implemented prototypes did not change much with the investing and harvesting energy, if the piezoelectric transducer sensitively responds to the electrical loading, the optimal investment scheme should take that into consideration.

Taking all these factors into consideration separately may increase the complexity and power consumption of an optimal investing scheme. Hence, one alternative is to adopt a Hill-climbing optimization approach, which finds the maximum output power point by sequentially increasing or decreasing the amount of investment until the output power peaks. However, this approach may not be optimal for impact-induced or random vibration harvesting because, as was discussed in Chapter 2, the Hill-climbing approach requires several vibration cycles to find the optimal investment value.

6.3.3. Zero-energy Startup

The piezoelectric energy harvesters proposed in this research are active harvesters that require initial energy to start their operations. Because the harvesters monitor the piezoelectric voltage input and control the switches to synchronize their operation and increase the electrical damping force of the transducer, they are not able to trigger the harvesting operation if there is no energy for the active control blocks to begin with. Fortunately, since the control circuits demand quiescent current lower than 100 nA, if the harvester is within a system that employs a battery for energy storage, it will be able to restart the harvesting even if it was inactive for a long period of time. However, if the battery is virtually depleted or if the system uses a capacitor as its energy storage, the

harvester must be capable of starting up without initial energy because the relatively low capacity of capacitors cannot guarantee the existence of energy over a long duration.

This zero-energy startup is also a critical problem for other kinetic-energy harvesters such as electrostatic- and electromagnetic-energy harvesters. Electrostatic-energy harvesters demand pre-charging energy to establish the electrical damping force of the transducer. Therefore, the system should possess initial energy for investing in addition to the energy for control circuits. Small-scale electromagnetic energy transducers generate even lower voltage than piezoelectric transducers. Hence electromagnetic energy harvesters often utilize transformers [85] or piezoelectric transducers [214] for startup. Moreover, light- and heat-energy harvesters also consider the zero-energy startup as a main challenge as the micro-scale solar cells and thermo-piles produce very low-input voltages.

One approach to starting piezoelectric energy harvesting without initial energy is to employ passive circuits for the startup. For instance, diode-bridge rectifiers can transfer piezoelectric energy to the output without using existing battery energy as long as the vibration is strong enough to raise the input voltage above the threshold voltage of diode-bridge rectifiers. The inherent threshold voltage of bridge rectifiers can be relatively low for a zero-energy startup as the output voltage of the rectifier is presumably low. The diodes dissipate power during the energy transfer, but the power dissipated is deducted from the input energy. Therefore, the output capacitor can accumulate net energy from the input without any need for initial energy. However, because the input threshold increases with the output voltage increase, the bridge rectifier will not be able to harvest input energy after some point unless either the input vibration becomes stronger or the output voltage is lowered by another circuit that drains the charge of the output capacitor.

Switch-bridge rectifiers using low-threshold transistors to implement low-headroom comparators and power switches can also start the harvesting process using

input energy [175]–[176]. If the comparator can function and power switches can be turned on and off with lower voltage amplitudes than that of diode-voltage drops in diode-bridge rectifiers, the switch-bridge rectifiers can start up from lower input voltage than that of diode-bridge rectifiers.

A harvester system can combine passive and active harvesting circuits to enable zero-energy startup through the passive approach while taking advantage of the increased electrical damping force and low-input threshold of active approaches. Figure 6.9 shows a possible modification of the energy-investing harvester prototype introduced in Chapter 5 that enables zero-energy startup. The modified harvester employs a Schottky-diode D_{ST} as the passive energy-harvesting path, and the other system remains the same as presented in Figure 5.2.

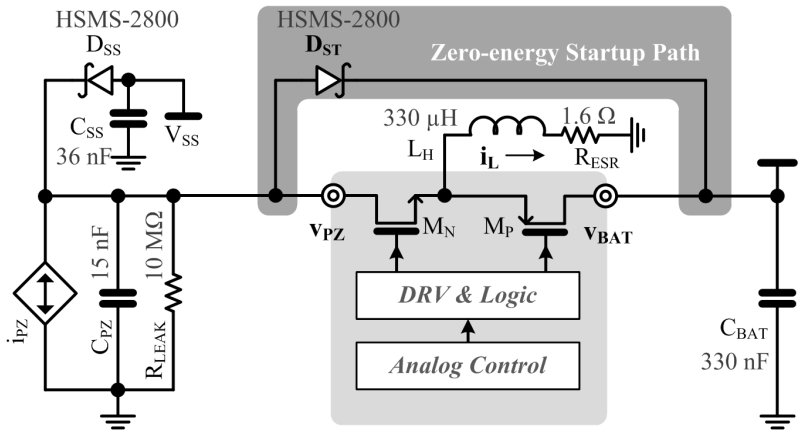

Figure 6.9. A modified energy-investing harvester for zero-energy startup.

Initially, capacitors C_{SS} and C_{BAT} are depleted, and the system energy is zero. When vibrations charge C_{PZ} with i_{PZ}, D_{ST} and D_{SS} channel some portions of i_{PZ} into C_{BAT} and C_{SS} across the positive and negative vibration cycles, respectively. Consequently, the amplitude of v_{BAT} and V_{SS} rise, and when the headroom set by v_{BAT} and V_{SS} becomes sufficient for the analog control circuits and drivers to function, the switched-inductor circuit will start harvesting the piezoelectric energy. Even after the main active harvesting circuit starts operating, D_{ST} will transfer energy to v_{BAT} if input voltage v_{PZ} rises above

v_{BAT}. However, the amplitude of v_{BAT} will eventually surpass that of v_{PZ} as the switched-inductor circuit will deposit charge into v_{BAT} regardless of the magnitude of v_{PZ}. In other words, as the active harvesting circuit starts, the system can harness energy from low-v_{PZ} inputs with increased electrical damping force. Figure 6.10 shows the simulation results of the modified energy-investing harvester. The vibration was fixed to generate the open-circuit voltage of 1.27 V, and v_{BAT} was clamped by a diode and a 3.5-V voltage source. The transistor-level circuits in Chapter 5 were used without any modifications, and the battery-energy investing was bypassed for this simulation.

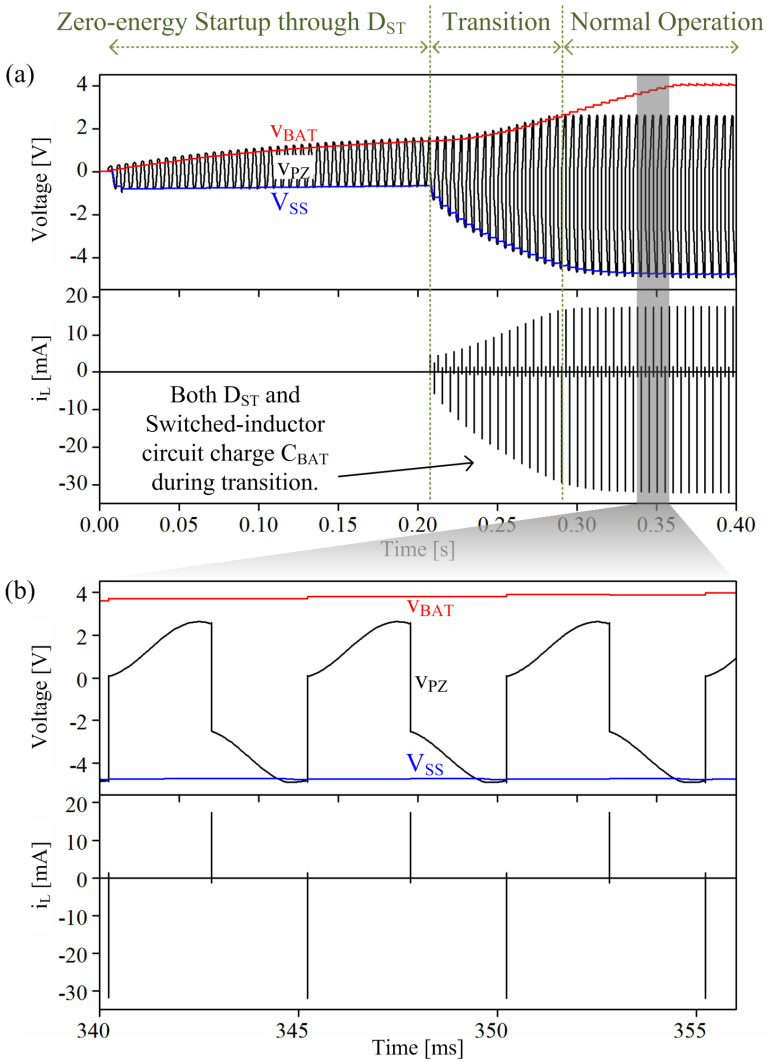

Figure 6.10. Zero-energy startup operation of the modified energy-investing harvester: (a) seconds- and (b) milliseconds-scale waveforms.

During the zero-energy startup phase, v_{BAT} increases slowly due to large C_{BAT} in contrast to V_{SS}, which quickly settles to its temporary steady-state value. When the switched-inductor converter begins its operation, the circuit stretches the envelope of v_{PZ} in both positive and negative directions to a new steady state. Because of the increased electrical damping force of the active harvester, v_{BAT} increases faster than it does during the zero-energy startup phase. When v_{BAT} rises above the positive peak of v_{PZ}, the system reaches the normal operation condition of the active harvester circuit where only the switched-inductor circuit harvests energy from the piezoelectric transducer input.

A more general approach of combining passive and active harvester circuits to enable zero-energy startup is shown in Figure 6.11. The system consists of parallel passive and active harvesting circuits. The two paths share the same input terminal, but the outputs are separated into two capacitors, $C_{PASSIVE}$ and C_{ACTIVE}.

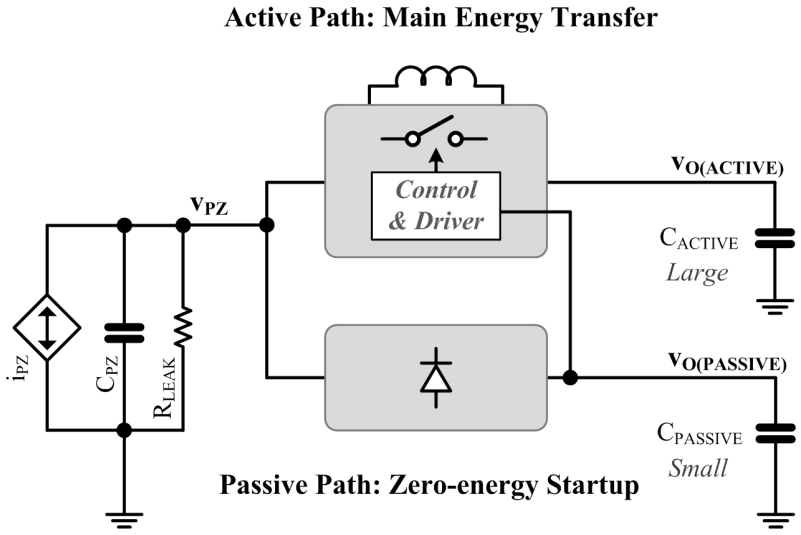

Figure 6.11. A generalized zero-energy startup approach for active harvester circuits.

When vibrations generate charges across C_{PZ}, the passive rectifier channels some portion of the produced charge to $C_{PASSIVE}$ and increases its voltage $v_{O(PASSIVE)}$. As soon as $v_{O(PASSIVE)}$ rises high enough to secure the headroom and energy for the control and driver circuits of active path, the system can engage the active energy-harvesting path and

charge its output capacitor C_{ACTIVE}. The passive rectifier in parallel to the main harvesting path may load the piezoelectric voltage and lower the electrical damping forces; however, the loading effect can be reduced if $C_{PASSIVE}$ is smaller than that of input, C_{PZ}. Eliminating any possible loading effect can be accomplished by disconnecting the passive path after the zero-energy startup phase, but to control the status of the passive harvester and the supply of the active harvester, the system needs additional circuits that consume power.

These approaches allow the active energy harvesters to start from a zero-energy state by adding the passive harvesting path in parallel to the main harvesting path. On the other hand, by making use of the parasitic body-diodes of the power switches, active harvesters using switched-inductor converters can also collect input energy without demanding control power from an energy storage device [215]–[218]. This can be a more compact solution compared to a system adopting parallel passive circuits. However, if the output capacitor for the startup and normal operation are the same and its capacitance is large, considerable amount of time and energy may be required before the system starts active harvesting because of the low efficiency of body-diode-based rectifiers.

6.3.4. Bandwidth of Micro-scale Transducers

Mechanical impedance of piezoelectric transducers consists of effective stiffness k, lumped mass m, and mechanical damping d of the material. Each mechanical impedance can be modeled by electrical counterparts such as capacitance $C_{1/k}$, inductance L_m, and resistance R_d, as shown in Figure 2.2. An AC voltage source can represent the external vibrations, whose acceleration rate and frequency determine the amplitude and frequency of the AC voltage, respectively. Accordingly, the displacement and the velocity of the transducer movement are reflected as the voltage across the equivalent capacitor $C_{1/k}$ and the current flowing through the $C_{1/k}$-L_m-R_d circuit, respectively. Therefore, analogous to

the electrical current in an RLC-circuit, the movements of the transducer exhibit frequency dependence based on the mechanical properties of the transducer.

If the frequency of the external vibration is matched to the resonant frequency of the piezoelectric transducer, the mechanical impedance is minimized and the velocity of the transducer is maximized. Consequently, the displacement and the output voltage of the piezoelectric transducer will peak for a given mechanical vibration. However, if the external vibration frequency deviates outside of the vicinity of the transducer's resonant frequency, the movement and the induced voltage decrease rapidly. The attenuated response means poor mechanical-to-electrical energy conversion performance. This is the reason for the bell-shaped power curve of Figure 5.25. Since energy-investing harvesters increase the electrical damping voltage even if the natural (i.e., open-circuited) piezoelectric voltage is small, the investing harvester can improve the energy-conversion performance of the piezoelectric transducer driven by out-of-resonance vibrations. However, as reviewed in Chapter 6.3.2, the small seed voltage of the piezoelectric transducer reduces the gain of the energy investment.

The bandwidth of the transducer is analogous to the bandwidth of the RLC-circuit. A transducer can feature wide bandwidth by increasing mechanical damping but at the expense of increased losses (or reduced conversion gain). If the mechanical resistance is very small, the conversion gain will be greatly increased, but the bandwidth will be narrow. This frequency selectivity is a critical problem for kinetic-energy harvesters because, in general, ambient vibrations are neither constant frequency nor periodic. Moreover, as the dimensions of transducers shrink and as stiff materials are used to support the micro-scale structure, the resonant frequency tends to rise much higher than what ambient surroundings can usually provide. Therefore, to overcome the bandwidth limitation of the transducer, researchers are currently studying various approaches, such as wideband transducers [219], multiple resonant frequency transducers

[220], and tunable resonant frequency system including the transducer and interface circuits [221]–[223].

On the other hand, some research groups are exploring harvester systems that attempt to harvest impact-induced vibrations, or more generally, random vibrations, which are more prevalent in the surroundings compared to periodic vibrations. The mechanical impedance of the transducer also affects the response of a piezoelectric transducer from an impact input. Similar to the impulse response in an electrical RLC circuit, the impact-induced movement is filtered by the mechanical impedance. Thus, after the impact, the transducer vibrates around its resonant frequency and the movement attenuates quickly if the mechanical resistance is large. The reported investigations such as [190], [219], and [224] focus on implementing the optimized mechanical structures to harvest energy from impact-induced vibration harvesting. However, the electrical interface circuits customized for these transducers are not easily found in the literature.

6.3.5. Integrated Micro-scale Harvesters

Ultimately, the presented research envisions a micro-scale piezoelectric energy harvesting system that includes a micro-scale (presumably MEMS) transducer and micro-battery in addition to the harvesting circuits. Unfortunately, the current research could not find an adequate way to incorporate MEMS piezoelectric transducers or micro-batteries because of limited expertise and resources in the respective areas. Hence, the implemented harvesters operated with centimeter-scale off-the-shelf piezoelectric transducers which are driven by very weak stimuli to emulate the low-voltage output of MEMS piezoelectric transducers. For the output storage devices, SMD-ceramic, SMD-tantalum, electrolytic capacitors and small Li-ion coin cells were utilized as an alternative to micro-batteries.

The MEMS piezoelectric transducers will produce charges across their surfaces through a piezoelectric effect as their centimeter-scale counterparts do. However, the

electrical and mechanical features such as breakdown voltage, electromechanical coupling, and capacitance can be very different. Similarly, even though the micro-batteries store electrical charge and energy like the conventional capacitors and Li-Ion batteries, their electrical characteristics such as capacity, over- and under-voltage limits, and cycle-life will differ from their macro-scale counterparts. These practical differences of micro-scale transducers and micro-batteries, which are summarized in Table 6.2, will potentially present important challenges for future piezoelectric harvester circuits.

Table 6.2. Challenges for a harvester circuit interfacing MEMS transducer and micro-battery.

MEMS Piezoelectric Transducer	Micro-battery
Breakdown Voltage	Capacity
Electromechanical Coupling Coefficient	Over- and Under-voltage Protection
Capacitance	Leakage
Resonant Frequency	Equivalent-series Resistance
Durability	Charging and Recharging Cycle Life

6.4. Summary

A piezoelectric transducer produces electrical charges across its surface in response to external mechanical stimulations. The charges induce an electrostatic force that can either dampen or accelerate the movement of the transducer. The kinetic energy in external vibrations is converted into the electrical domain when the electrostatic force dampens the movement. Because the electrical damping forces of tiny piezoelectric transducers in ambient vibrations are weak, the converted electrical energy is small. The presented research generated several switched-inductor circuits that strengthen the electrical damping force of the transducer to increase the output power of a harvester. The switched-inductor circuits not only eliminated the bridge rectifiers and their drawbacks, but also allowed various energy-investing strategies to improve the harvesting

performance. Low-energy analog control circuits and switch drivers synchronized the harvester operation to external vibrations to harness energy from periodic and aperiodic mechanical inputs. Experimental validations of the prototypes not only confirmed the proposed harvesting operations, but also revealed important technological limitations, which can lead to interesting future research opportunities.

REFERENCES

[1] I.F. Akyildiz, W. Su, Y. Sankarasubramaniam, and E. Cayirci, "Wireless sensor networks: a survey," *Computer Networks*, vol. 38, pp. 393–422, 2002.

[2] R.J.M. Vullers, R. van Schaijk, H.J. Visser, J. Penders, and C. Van Hoof, "Energy harvesting for autonomous wireless sensor networks," *IEEE Solid-State Circuits Magazine*, vol. 2, issue 2, pp. 29–38, 2010.

[3] J. Marek, "MEMS for automotive and consumer electronics," in *IEEE Int. Solid-State Circuits Conf. (ISSCC) Dig. Tech. Papers*, pp. 9–17, Feb. 2010.

[4] J. Yoo, L. Yan, S. Lee, Y. Kim, and H.-J. Yoo, "A 5.2 mW self-configured wearable body sensor network controller and a 12 μW wirelessly powered sensor for a continuous health monitoring system," *IEEE J. Solid-State Circuits*, vol. 45, no. 1, pp. 178–188, Jan. 2010.

[5] R.F. Yazicioglu, P. Merken, R. Puers, and C. Van Hoof, "A 60 μW 60 nV/√Hz readout front-end for portable biopotential acquisition systems," *IEEE J. Solid-State Circuits*, vol. 42, no. 5, pp. 1100–1110, May. 2007.

[6] L.S.Y. Wong, S. Hossain, A. Ta, J. Edvinsson, D.H. Rivas, and H. Nääs, "A very low-power CMOS mixed-signal IC for implantable pacemaker applications," *IEEE J. Solid-State Circuits*, vol. 39, no. 12, pp. 2446–2456, Dec. 2004.

[7] S. Smith, T.B. Tang, J.G. Terry, J.T.M. Stevenson, B.W. Flynn, H.M. Reekie, A.F. Murray, A.M. Gundlach, D. Renshaw, B. Dhillon, A. Ohtori, Y. Inoue, and A.J. Walton, "Development of a miniaturised drug delivery system with wireless power transfer and communication," *IET Nanobiotechnol.,* vol. 1, no. 5, pp. 80–86, 2007.

[8] A.C. Richards Grayson, I.S. Choi, B.M. Tyler, P.P. Wang, H. Brem, M.J. Cima, and R. Langer, "Multi-pulse drug delivery from a resorbable polymeric microchip device," *Nature Materials*, vol. 2, pp. 767–772, Nov. 2003.

[9] D.A. La Van, T. McGuire, and R. Langer, "Small-scale systems for *in vivo* drug delivery," *Nature Biotechnology*, vol. 21, no. 10, pp. 1184–1191, Oct. 2003.

[10] A.C. Richards Grayson, R.S. Shawgo, A.M. Johnson, N.T. Flynn, Y. Li, M.J. Cima, and R. Langer, "A BioMEMS review: MEMS technology for physiologically integrated devices," *Proceedings of the IEEE*, vol. 92, no. 1, pp. 6–21, Jan. 2004.

[11] M. Flatscher, M. Dielacher, T. Herndl, T. Lentsch, R. Matischek, J. Prainsack, W. Pribyl, H. Theuss, and W. Weber, "A robust wireless sensor node for in-tire-pressure monitoring," in *IEEE Int. Solid-State Circuits Conf. (ISSCC) Dig. Tech. Papers*, pp. 286–287, Feb. 2009.

[12] M. Flatscher, M. Dielacher, T. Herndl, T. Lentsch, R. Matischek, J. Prainsack, W. Pribyl, H. Theuss, and W. Weber, "A bulk acoustic wave (BAW) based transceiver for an in-tire-pressure monitoring sensor node," *IEEE J. Solid-State Circuits*, vol. 45, no. 1, pp. 167–177, Jan. 2010.

[13] M. Löhndorf, T. Kvisterøy, E. Westby, and E. Halvorsen, "Evaluation of energy harvesting concepts for tire pressure monitoring systems," in *Proc. PowerMEMS 2007*, pp. 331–334, 2007.

[14] J. Yan, R.J. Wood, S. Avadhanula, M. Sitti, and R.S. Fearing, "Towards flapping wing control for a micromechanical flying insect," in *Proc. IEEE Int. Conf. Robotics and Automation*, pp. 3901–3908, May 2001.

[15] R. Sahai, S. Avadhanula, R. Groff, E. Steltz, R. Wood, R.S. Fearing, "Towards a 3g crawling robot through the integration of microrobot technologies," in *Proc. IEEE Int. Conf. Robotics and Automation*, pp. 296–302, May 2006.

[16] D.C. Daly, P.P. Mercier, M. Bhardwaj, A.L. Stone, Z.N. Aldworth, T.L. Daniel, J. Voldman, J.G. Hildebrand, and A.P. Chandrakasan, "A pulsed UWB receiver SoC for insect motion control," *IEEE J. Solid-State Circuits*, vol. 45, no. 1, pp. 153–166, Jan. 2010.

[17] S. Lee, L. Yan, T. Roh, S. Hong, H.-J. Yoo, "A 75 μW real-time scalable network controller and a 25 μW ExG sensor IC for compact sleep-monitoring applications," in *IEEE Int. Solid-State Circuits Conf. (ISSCC) Dig. Tech. Papers*, pp. 36–37, Feb. 2011.

[18] K.A. Cook-Chennault, N. Thambi, and A.M. Sastry, "Powering MEMS portable devices– a review of non-regenerative and regenerative power supply systems with special emphasis on piezoelectric harvesting systems," *Smart Mater. Struct.*, vol. 17, no. 4, p. 043001 (33 pp.), Aug. 2008.

[19] D. Linden and T.B. Reddy, *Handbook of Batteries-3rd Ed.*, New York, NY: McGraw-Hill, 2001.

[20] M.H. Miles, "Recent advances in lithium battery technology," in *IEEE GaAs Digest*, pp. 219–222, 2001.

[21] J.B. Bates, N.J. Dudney, B. Neudecker, A. Ueda, C.D. Evans, "Thin-film lithium and lithium-ion batteries," *Solid State Ionics*, vol. 135, pp. 33–45, 2000.

[22] R.P. Raffaelle, J.D. Harris, D. Hehemann, D. Scheiman, G. Rybicki, and A.F. Hepp, "A facile route to thin-film solid state lithium microelectronic batteries," *J. Power Sources*, vol. 89, pp. 52–55, 2000.

[23] J. Peirs, D. Reynaerts, and F. Verplaetsen, "A microturbine for electric power generation," *Sensors and Actuators A*, vol. 113, pp. 86–93, 2004.

[24] C.M. Spadaccini, A. Mehra, J. Lee, X. Zhang, S. Lukachko, and I.A. Waitz, "High power density silicon combustion systems for micro gas turbine engines," *J. Engineering for Gas Turbines and Power*, vol. 125, pp. 709–719, July 2003.

[25] R. Khanna, "MEMS fabrication perspectives from the MIT Microengine project," *Surface and Coatings Technology*, vol. 163–164, pp. 273–280, 2003.

[26] S. Whalen, M. Thompson, D. Bahr, C. Richards, and R. Richards, "Design, fabrication and testing of the P^3 micro heat engine," *Sensors and Actuators A*, vol. 104, pp. 290–298, 2003.

[27] L. Carrette, K.A. Friedrich, and U. Stimming, "Fuel cells: principles, types, fuels, and applications," *CHEMPHYSCHEM*, vol. 1, pp. 162–193, 2000.

[28] C.K. Dyer, "Fuel cells for portable applications," *J. Power Sources*, vol. 106, pp. 31–34, 2002.

[29] H.L. Maynard and J.P. Meyers, "Miniature fuel cells for portable power: Design considerations and challenges," *J. Vac. Sci. Technol. B*, vol. 20, no. 4, pp. 1287–1297, Jul/Aug 2002.

[30] R. O'Hayre, D. Braithwaite, W. Hermann, S.-J. Lee, T. Fabian, S.-W. Cha, Y. Saito, and F.B. Prinz, "Development of portable fuel cell arrays with printed-circuit technology," *J. Power Sources*, vol. 124, pp. 459–472, 2003.

[31] M.M. Mench, H.M. Chance, and C.Y. Wang, "Direct dimethyl ether polymer electrolyte fuel cells for portable applications," *J. Electrochemical Society*, vol. 151, no. 1, pp. A144–A150, 2004.

[32] C.W. Moore, J. Li, and P.A. Kohl, "Microfabricated fuel cells with thin-film silicon dioxide proton exchange membranes," *J. Electrochemical Society*, vol. 152, no. 8, pp. A1606–A1612, 2005.

[33] W.Y. Sim, G.Y. Kim, and S.S. Yang, "Fabrication of micro power source (MPS) using a micro direct methanol fuel cell (μDMFC) for the medical application," in *Proc. IEEE Int. Conf. MEMS*, pp. 341–344, 2001.

[34] Y. Kenarangui, S. Wang, and B. Fahimi, "On the impact of fuel cell system response on power electronics converter design," *in Proc. IEEE Vehicle Power and Propulsion Conf.,* pp. 1–6, 2006.

[35] M. Chen and G.A. Rincón-Mora, "A compact electrical model for microscale fuel cells capable of predicting runtime and I–V polarization performance," *IEEE Trans. Energy Conversion*, vol. 23, no. 3, pp. 842–850, 2008.

[36] M. Chen, J.P. Vogt and G.A. Rincón-Mora, "Design methodology of a hybrid micro-scale fuel cell-thin-film lithium ion source," in *Proc. IEEE Int. Midwest Symp. Circuits Syst. (MWSCAS)*, pp. 674–677, Aug. 2007.

[37] W. Sun, N.P. Kherani, K.D. Hirschman, L.L. Gadeken, P.M. Fauchet, "A three-dimensional porous silicon p-n diode for betavoltaics and photovoltaics," *Adv. Mater.*, vol. 17, pp. 1230–1233, 2005.

[38] M. Paulson, "Nano-nuclear batteries," http://tahan.com/charlie/nanosociety/course 201/nanos/MPnuke.pdf (Accessed Oct. 4, 2012).

[39] H. Guo and A. Lal, "Nanopower betavoltaic microbatteries," in *Proc. IEEE Int. Conf. Solid State Sensors, Actuators, and Microsystems*, pp. 36–39, 2003.

[40] H. Li and A. Lal, "Self-reciprocating radioisotope-powered cantilever," *J. Appl. Phys.*, vol. 92, no. 2, pp. 1122–1126, July 2002.

[41] A. Lal, R.M.B.Y. León, H. Guo, H. Li, S. Santanam, R. Yao, J. Blanchard, D. Henderson, "A nuclear microbattery for MEMS devices," http://homepages.cae.wisc.edu/~blanchar/res/iconebattery.pdf (Accessed Oct. 4, 2012).

[42] A. Lal and J. Blanchard, "The daintiest dynamos," *IEEE Spectrum*, vol. 41, no. 9, pp. 36–41, Sept. 2004.

[43] M.V.S. Chandrashekhar, C.I. Thomas, and M.G. Spencer, "Betavoltaic cell," *US 7,663,288 B2*, Feb. 2010.

[44] S. Roundy, P.K. Wright, and J. Rabaey, "A study of low level vibrations as a power source for wireless sensor nodes," *Comput. Commun.*, vol. 26, pp. 1131–1144, 2003.

[45] S.P. Beeby, M.J. Tudor, and N.M. White, "Energy harvesting vibration sources for Microsystems applications," *Meas. Sci. Technol.*, vol. 17, pp. R175–R195, 2006.

[46] P.D. Mitcheson, E.M. Yeatman, G.K. Rao, A.S. Holmes, and T.C. Green, "Energy harvesting from human and machine motion for wireless electronic devices," *Proceedings of the IEEE*, vol. 96, no. 9, pp. 1457–1486, Sept. 2008.

[47] N.E. duToit, B.L. Wardle, and S.-G. Kim, "Design considerations for MEMS-scale piezoelectric mechanical vibration energy harvesters," *Integrated Ferroelectronics*, v. 71, pp. 121–160, 2005.

[48] J.A. Paradiso and T. Starner, "Energy scavenging for mobile and wireless electronics," *IEEE Pervasive Comput*, vol. 4, no. 1, pp. 18–27, 2005.

[49] R.J.M Vullers, R. van Schaijk, I. Doms, C. Van Hoof, and R. Mertens, "Micropower energy harvesting," *Solid-State Electronics*, vol. 53, pp. 684–693, 2009.

[50] R.W. Miles, K.M Hynes, and I. Forbes, "Photovoltaic solar cells: An overview of state-of-the-art cell development and environmental issues," *Progress in Crystal Growth and Characterization of Materials*, vol. 51, pp. 1–42, 2005.

[51] B.A. Warneke, M.D. Scott, B.S. Leibowitz, L. Zhou, C.L. Bellew, J.A. Chediak, J.M. Kahn, B.B. Boser, and K.S.J. Pister, "An autonomous 16 mm^3 solar-powered node for distributed wireless sensor networks," in *Proc. IEEE Sensors*, vol. 2, pp. 1510–1515, 2002.

[52] D.M. Bennett, R. Selfridge, P. Humble, and J.N Harb, "Hybrid power systems for autonomous MEMS," in *Proc. of SPIE*, vol. 4334, pp. 354–362, 2001.

[53] H. Shao, C.-Y. Tsui, and W.-H. Ki, "The design of a micro power management system for applications using photovoltaic cells with the maximum output power control," *IEEE Trans. Very Large Scale Integration (VLSI) Systems*, vol. 17, no. 8, pp. 1138–1142, Aug. 2009.

[54] N.J. Guilar, T.J. Kleeburg, A. Chen, D.R. Yankelevich, and R. Amirtharajah, "Integrated solar energy harvesting and storage," *IEEE Trans. Very Large Scale Integration (VLSI) Systems*, vol. 17, no. 5, pp. 627–637, May 2009.

[55] M. Ferri, D. Pinna, E. Dallago, and P. Malcovati, "Integrated micro-solar cell structures for harvesting supplied microsystems in 0.35-µm CMOS technology," in *Proc. IEEE Sensors*, pp. 542–545, 2009.

[56] J. Lu, A.Y. Kovalgin, K.H.M. van der Werf, R.E.I. Schropp, and J. Schmitz, "Integration of solar cells on top of CMOS chips Part I: a-Si solar cells," *IEEE Trans. Electron Devices*, vol. 58, no. 7, pp. 2014–2021, July 2011.

[57] J. Lu, W. Liu, A.Y. Kovalgin, Y. Sun, and J. Schmitz, "Integration of solar cells on top of CMOS chips Part II: CIGS solar cells," *IEEE Trans. Electron Devices*, vol. 58, no. 8, pp. 2620–2627, Aug. 2011.

[58] J.B. Lee, Z. Chen, M.G. Allen, A. Rohatgi, and R. Arya, "A miniaturized high-voltage solar cell array as an electrostatic MEMS power supply," *J. Micromechanical Systems*, vol. 4, no. 3, pp. 102–108, Sept. 1995.

[59] A.R. Lingley, B.P. Otis, T.T. Shen, and B.A. Parviz, "A contact lens with integrated micro solar cells," *Microsyst. Technol.*, vol. 18, pp. 453–458, 2012.

[60] J. Merten, J.M. Asensi, C. Voz, A.V. Shah, R. Platz, and J. Andreu, "Improved equivalent circuit and analytical model for amorphous silicon solar cells and modules," *IEEE Trans. Electron Devices*, vol. 45, no. 2, pp. 423–429, Feb. 1998.

[61] T. Esram and P.L. Chapman, "Comparison of photovoltaic array maximum power point tracking techniques," *IEEE Trans. Energy Conversion*, vol. 22, no. 2, pp. 439–449, June 2007.

[62] K. Kobayashi, H. Matsuo, and Y. Sekine, "An excellent operating point tracker of the solar-cell power supply system," *IEEE Trans. Industrial Electronics*, vol. 53, no. 2, pp. 495–499, Apr. 2006.

[63] R. Enne, M. Nikolic, and H. Zimmermann, "A maximum power-point tracker without digital signal processing in 0.35µm CMOS for automotive applications," in *IEEE Int. Solid-State Circuits Conf. (ISSCC) Dig. Tech. Papers*, pp. 102–103, Feb. 2012.

[64] Y. Qui, C. Van Liempd, B.O. het Veld, P.G. Blanken, and C. Van Hoof, "5µW-to-10mW input power range inductive boost converter for indoor photovoltaic energy harvesting with integrated maximum power point tracking," in *IEEE Int. Solid-State Circuits Conf. (ISSCC) Dig. Tech. Papers*, pp. 118–119, Feb. 2011.

[65] G. Spiazzi, S. Buso, P. Mattavelli, and P. Tenti, "Low complexity MPPT techniques for PV module converters," in *Proc. IEEE Int. Power Electronics Conf.*, pp. 2074–2081, 2010.

[66] E.M. Yeatman, "Energy harvesting – small scale energy production from ambient sources," in *Proc. of SPIE*, vol. 7288, pp. 728802-1–7, 2009.

[67] F.J. DiSalvo, "Thermoelectric cooling and power generation," *Science*, vol. 285, pp. 703–706, July 1999.

[68] R. Venkatasubramanian, E. Siivola, T. Colpitts, and B. O'Quinn, "Thin-film thermoelectric devices with high room-temperature figures of merit," *Nature*, vol. 413, pp. 597–602, 2001.

[69] M. Chen, S.-S. Lu, and B. Liao, "On the figure of merit of thermoelectric generators," *J. of Energy Resources Technology*, vol. 127, pp. 37–41, March 2005.

[70] G.J. Snyder and E.S. Toberer, "Complex thermoelectric materials," *Nature Materials*, vol. 7, pp. 105–114, Feb. 2008.

[71] H. Lhermet, C. Condemine, M. Plissonnier, R. Salot, P. Audebert, and M. Rosset, "Efficient power management circuit: from thermal energy harvesting to above-IC microbattery energy storage," *IEEE J. Solid- State Circuits*, vol. 43, no. 1, pp. 246-255, Jan. 2008.

[72] E.J. Carlson, K. Strunz, and B.P. Otis, "A 20 mV input boost converter with efficient digital control for thermoelectric energy harvesting," *IEEE J. Solid-State Circuits*, vol. 45, no. 4, pp. 741–750, Apr. 2010.

[73] Y.K. Ramadass and A.P. Chandrakasan, "A battery-less thermoelectric energy harvesting interface circuit with 35 mV startup voltage," *IEEE J. Solid-State Circuits*, vol. 46, no. 1, pp. 333–341, Jan. 2011.

[74] J.-P. Im, S.-W. Wang, K.-H. Lee, Y.-J. Woo, Y.-S. Yuk, T.-H. Kong, S.-W. Hong, S.-T. Ryu, and G.-H. Cho, "A 40mV Transformer-reuse self-startup boost converter with MPPT control for thermoelectric energy harvesting," in *IEEE Int. Solid-State Circuits Conf. (ISSCC) Dig. Tech. Papers*, pp. 104–105, Feb. 2012.

[75] K. Kadirvel, Y. Ramadass, U. Lyles, J. Carpenter, V. Ivanov, V. McNeil, A. Chandrakasan, and B. Lum-Shue-Chan, "A 330nA energy-harvesting charger with battery management for solar and thermoelectric energy harvesting," in *IEEE Int. Solid-State Circuits Conf. (ISSCC) Dig. Tech. Papers*, pp. 106–107, Feb. 2012.

[76] Tellurex, Z-Max® G1-1.0-127-1.27 datasheet, 2007.

[77] Tellurex, G1-34-0315 Thermoelectric module specifications.

[78] Nextreme, eTEG™ HV37 Power Generator datasheet, DTB0018 rev. 1.0.

[79] Micropelt, MPG-D651, MPG-D751 datasheet, 0025DSPG6&70210v1e.

[80] R. Venkatasubramanian, C. Watkins, D. Stokes, J. Posthill, and C. Caylor, "Energy harvesting for electronics with thermoelectric devices using nanoscale materials," in *Proc. IEEE Int. Electron Devices Meeting*, pp. 367–370, 2007.

[81] M. Strasser, R. Aigner, C. Lauterbach, T.F. Sturm, M. Franosch, and G. Wachutka, "Micromachined CMOS thermoelectric generators as on-chip power supply," *Sensors and Actuators A*, vol. 114, pp. 362–370, 2004.

[82] M. Strasser, R. Aigner, M. Franosch, and G. Wachutka, "Miniaturized thermoelectric generators based on poly-Si and poly-SiGe surface micromachining," *Sensors and Actuators A*, vol. 97-98, pp. 535–542, 2002.

[83] M.P. Flynn, B.H.G. Rhew, J. Jeong, and J.A. Fredenburg, "Ultra low power microsystems using RF energy scavenging ," in *Proc. IEEE Int. Electron Devices Meeting*, pp. 10.3.1–10.3.4, 2011.

[84] H. Nishimoto, Y. Kawahara, and T. Asami, "Prototype implementation of ambient RF energy harvesting wireless sensor networks," in *Proc. IEEE Sensors*, pp. 1282–1287, 2010.

[85] R. Moghe, Y. Yang, F. Lambert, and D. Divan, "Design of a low cost self powered "stick-on" current and temperature wireless sensor for utility assets," in *Proc. IEEE Energy Conversion Congress and Exposition (ECCE)*, pp. 4453–4460, 2010.

[86] R. Moghe, Y. Yang, F. Lambert, and D. Divan, "A scoping study of electric and magnetic field energy harvesting for wireless sensor networks in power system applications," in *Proc. IEEE Energy Conversion Congress and Exposition (ECCE)*, pp. 3550–3557, 2009.

[87] S.A. Bhalerao, A.V. Chaudhary, R.B. Deshmukh, and R.M. Patrikar, "Powering wireless sensor nodes using ambient RF energy," in *Proc. IEEE Int. Conf. Systems, Man, and Cybernetics*, pp. 2695–2700, 2006.

[88] A. Nimo, D. Grgić, and L.M. Reindl, "Ambient electromagnetic wireless energy harvesting using multiband planar antenna," in *Proc. IEEE Int. Multi-Conf. Systems, Signals, and Devices*, pp. 1–6, 2012.

[89] M. Hata, "Empirical formula for propagation loss in land-mobile radio service," *IEEE Trans. Veh. Technol.*, vol. VT-29, no. 3, pp. 317–325, Aug. 1980.

[90] E.D. Mantiply, K.R. Pohl, S.W. Poppell, and J.A. Murphy, "Summary of measured radiofrequency electric and magnetic fields (10KHz to 30GHz) in the general and work environment," *Bioelectromagnetics*, vol. 18, no. 8, pp. 563–577, 1997.

[91] H.J. Visser, A.C.F. Reniers, and J.A.C. Theeuwes, "Ambient RF energy scavenging: GSM and WLAN power density measurements," in *Proc. European Microwave Conf.*, pp. 721–724, 2008.

[92] D. Bouchouicha, M. Latrach, F. Dupont, and L. Ventura, "An experimental evaluation of surrounding RF energy harvesting devices," in *Proc. European Microwave Conf.*, pp. 1381–1384, 2010.

[93] T. Le, K. Mayaram, and T. Fiez, "Efficient far-field radio frequency energy harvesting for passively powered sensor networks," *IEEE J. Solid-State Circuits*, vol. 43, no. 5, pp. 1287–1302, May 2008.

[94] T. Salter, K. Choi, M. Peckerar, G. Metze, and N. Goldsman, "RF energy scavenging system utilising switched capacitor DC-DC converter," *Electronic Letters*, vol. 45, no. 7, pp. 374–376, Mar. 2009.

[95] P. Nintanavongsa, U. Muncuk, D.R. Lewis, and K.R. Chowdhury, "Design optimization and implementation for RF energy harvesting circuits," IEEE *J. Emerging and Selected Topics in Circuits and Systems* , vol. 2, no. 1, pp. 24–33, Mar. 2012.

[96] H. Reinisch, S. Gruber, H. Unterassinger, M. Wiessflecker, G. Hofer, W. Pribyl, and G. Holweg, "An electro-magnetic energy harvesting system with 190 nW idle mode power consumption for a BAW based wireless sensor node," *IEEE J. Solid-State Circuits*, vol. 46, no. 7, pp. 1728–1741, July 2011.

[97] G. Papotto, F. Carrara, and G. Palmisano, "A 90-nm CMOS threshold-compensated RF energy harvester," *IEEE J. Solid-State Circuits*, vol. 46, no. 9, pp. 1985–1997, Sept. 2011.

[98] T. Paing, E. Falkenstein, R. Zane, and Z. Popovic, "Custom IC for ultra-low power RF energy harvesting," in *Proc. IEEE Applied Power Electronics Conf. and Expo. (APEC)*, pp. 1239–1245, 2009.

[99] A. Dolgov, R. Zane, and Z. Popovic, "Power management system for online low power RF energy harvesting optimization," *IEEE Trans. Circuits and Syst.–I: Regular Papers*, vol. 57, no. 7, pp. 1802–1811, July 2010.

[100] T. Paing, J. Shin, R. Zane, and Z. Popovic, "Resistor emulation approach to low-power RF energy harvesting," *IEEE Trans. Power Electronics*, vol. 23, no. 3, pp. 1494–1501, May 2008.

[101] M. Keck, “A new approach of a piezoelectric vibration-based power generator to supply next generation tire sensor systems,” in *Proc. IEEE Sensors*, pp. 1299–1302, 2007.

[102] P. Niu, P. Chapman, R. Riemer, and X. Zhang, “Evaluation of motions and actuation methods for biomechanical energy harvesting,” in *Proc. IEEE Power Electronics Specialists Conf.*, pp. 2100–2106, 2004.

[103] T. von Büren, P.D. Mitcheson, T.C. Green, A.S. Holmes, and G. Tröster, “Optimization of inertial micropower generators for human walking motion,” *IEEE Sensors Journal*, vol. 6, no. 1, pp. 28–38, Feb. 2006.

[104] V. Blasko, “Power conditions and control of a regenerative brake,” in *Proc. IEEE Industry Applications Conf.*, pp. 1504–1510, 1998.

[105] S. Roundy, P.K. Wright, and J.M. Rabaey, *Energy Scavenging for Wireless Sensor Networks with Special Focus on Vibrations*, 1st ed., Boston, MA: Kluwer Academic Publishers, 2004.

[106] S. Meninger, J.O. Mur-Miranda, R. Amirtharajah, A.P. Chandarakasan, and J.H. Lang, “Vibration-to-electric energy conversion,” *IEEE Trans. VLSI Syst.*, vol. 9, no. 1, pp. 64–76, Feb. 2001.

[107] M.E. Kiziroglou, C. He, and E.M. Yeatman, “Rolling rod electrostatic microgenerator,” *IEEE. Trans. Ind. Electron.*, vol. 56, no. 4, pp. 1101–1108, Apr. 2009.

[108] M.E. Kiziroglou, C. He, and E.M. Yeatman, “Flexible substrate electrostatic energy harvester,” *Electron. Lett.*, vol. 46, no. 2, pp. 166–167, Jan. 2010.

[109] M. Miyazaki, H. Tanaka, C. Ono, T. Nagano, N. Ohkubo, T. Kawahara, and K. Yano, “Electric-energy generation using variable-capacitive resonator for power-free LSI: efficiency analysis and fundamental experiment,” in *Proc. Int. Symp. Low Power Electron. Design*, pp. 193–198, Aug. 2004.

[110] Y. Chiu and V.F.G. Tseng, “A capacitive vibration-to-electricity energy converter with integrated mechanical switches,” *J. Micromech. Microeng.*, vol. 18, no. 10, pp. 1–8, Oct. 2008.

[111] B.C. Yen, J.H. Lang, "A variable-capacitance vibration-to-electric energy harvester," *IEEE Trans. Circuits Syst. I: Regular Papers*, vol. 53, no. 2, pp. 288–295, Feb. 2006.

[112] E.O. Torres and G.A. Rincón-Mora, "Electrostatic energy-harvesting and battery-charging CMOS system prototype," *IEEE Trans. Circuits Syst. I: Regular Papers*, vol. 56, no. 9, pp. 1938–1948, Sept. 2009.

[113] E.O. Torres and G.A. Rincón-Mora, "A 0.7μm BiCMOS electrostatic energy-harvesting system IC," *IEEE J. Solid-State Circuits*, vol. 45, no. 2, pp. 483–496, Feb. 2010.

[114] E.O. Torres and G.A. Rincón-Mora, "Self-tuning electrostatic energy-harvester," *IEEE Trans. Circuits Syst. II: Express Briefs*, vol. 57, no. 10, pp. 808–812, Oct. 2010.

[115] P.D. Mitcheson, P. Miao, B.H. Stark, E.M. Yeatman, A.S. Holmes, and T.C. Green, " MEMS electrostatic micropower generator for low frequency operation," *Sensors and Actuators A (Physical)*, vol. 115, pp. 523–529, Sept. 2004.

[116] P. Miao, P.D. Mitcheson, A.S. Holmes, E.M. Yeatman, T.C. Green, and B.H. Stark, "MEMS inertial power generators for biomedical applications," Microsyst. Technol., vol. 12, no. 10–11, pp. 1079–1083, Sept. 2006.

[117] G. Despesse, J.J. Chaillout, T. Jager, F. Cardot, and A. Hoogerwerf, "Innovative structure for mechanical energy scavenging," in *Proc. Int. Conf. Solid-State Sensors, Actuators and Microsystems,* pp. 895–898, 2007.

[118] M. Hayakawa, "Electronic wristwatch with generator," U.S. Patent 5,001,685, Mar. 1991.

[119] R. Amirtharajah and A.P. Chandrakasan, "Self-powered signal processing using vibration-based power generation," *IEEE J. Solid-State Circuits*, vol. 33, no. 5, pp. 687–695, May 1998.

[120] C. Shearwood and R.B. Yates, "Development of an electromagnetic micro-generator," *Electron. Lett.*, vol. 33, no. 22, pp. 1883–1884, Oct. 1997.

[121] M. El-hami, P. Glynne-Jones, N.M. White, M. Hill, S. Beeby, E. James, A.D. Brown, and J.N. Ross, "Design and fabrication of a new vibration-based electromechanical power generator," *Sensors and Actuators A (Physical)*, vol. 92, pp. 335–342, Aug. 2001.

[122] P. Glynne-Jones, M.J. Tudor, S.P. Beeby, and N.M. White, "An electromagnetic, vibration-powered generator for intelligent sensor systems," *Sensors and Actuators A (Physical)*, vol. 110, pp. 344–349, Feb. 2004.

[123] D.P. Arnold, "Review of microscale magnetic power generation," *IEEE Trans. Magn.*, vol., 43, pp. 3940–3951, Nov. 2007.

[124] E.P. James, M.J. Tudor, S.P. Beeby, N.R. Harris, P. Glynne-Jones, J.N. Ross, and N.M. White, "An investigation of self-powered systems for condition monitoring applications," *Sensors and Actuators A (Physical)*, vol. 110, pp. 171–176, Feb. 2004.

[125] S.P. Beeby, R.N. Torah, M.J. Tudor, P. Glynne-Jones, T. O'Donnell, C.R. Saha, and S. Roy, "A micro electromagnetic generator for vibration energy harvesting," *J. Micromech. Microeng.*, vol. 17, no. 7, pp. 1257–1265, July 2007.

[126] F. Khan, F. Sassani, and B. Stoeber, "Copper foil-type vibration-based electromagnetic energy harvester," *J. Micromech. Microeng.*, vol. 20, pp. 125006-1–10, Nov. 2010.

[127] S.D. Senturia, *Microsystem Design,* 1st ed., Boston, MA: Kluwer Academic Publishers, 2001.

[128] M.J. Madou, *Fundamentals of Microfabrication*, 1st ed., Boca Raton, FL: CRC Press, 1998.

[129] H.A.C. Tilmans, "Equivalent circuit representation of electromechanical transducers: I. Lumped-parameter systems," *J. Micromech. Microeng.*, vol. 6, pp. 157–176, 1996.

[130] H.A.C. Tilmans, "Equivalent circuit representation of electromechanical transducers: II. Distributed-parameter systems," *J. Micromech. Microeng.*, vol. 7, pp. 285–309, 1997.

[131] S. Priya and D.J. Inman, *Energy Harvesting Technologies*, New York, NY: Springer Science+Business Media, LLC 2009.

[132] L. Steinke, Hegnach, Wurttemberg, and W. Wiest, "Piezoelectric igniter for gaseous fuels or the like," U.S. Patent 3 457 461, July 22, 1969.

[133] R.P. Ried, E.S. Kim, D.M. Hong, and R.S. Muller, "Piezoelectric microphone with on-chip CMOS circuits," *IEEE J. Microelectromech. Syst.*, vol. 2, no. 3, pp. 111–120, Sept. 1993.

[134] B. Orten, "Piezoelectric vibration sensor," U.S. Patent 7 368 855, May 6, 2008.

[135] J. Kymissis, C. Kendall, J. Paradiso, and N. Gershenfeld, "Parasitic power harvesting in shoes," in *Proc. IEEE Int. Symp. Wearable Computers*, Oct. 1998.

[136] N.S. Shenck and J.A. Paradiso, "Energy scavenging with shoe-mounted piezoelectrics," *IEEE Micro*, vol. 21, no. 3, pp. 30–42, May-June 2001.

[137] M. Umeda, K. Nakamura, and S. Ueha, "Energy storage characteristics of a piezo-generator using impact induced vibration," *Jpn. J. Appl. Phys.*, vol. 36, no. 5B, pp. 3146–3151, May 1997.

[138] N.G. Elvin, N. Lajnef, and A.A. Elvin, "Feasibility of structural monitoring with vibration powered sensors," *Smart Mater. Struct.*, vol. 15, pp. 977–986, 2006.

[139] N.M. White, P. Glynne-Jones, and S.P. Beeby, "A novel thick-film piezoelectric micro-generator," *Smart Mater. Struct.*, vol. 10, pp. 850–852, 2001.

[140] P. Glynn-Jones, S.P. Beeby, and N.M. White, "Towards a piezoelectric vibration-powered microgenerator," *IEE Proc.-Sci. Meas. Technol.*, vol. 148, no. 2, pp. 68–72, Mar. 2001.

[141] H.-B. Fang, J.-Q. Liu, Z.-Y. Xu, L. Dong, L. Wang, D. Chen, B.-C. Cai, and Y. Liu, "Fabrication and performance of MEMS-based piezoelectric power generator for vibration energy harvesting," *Microelectronics Journal*, vol. 37, pp. 1280–1284, 2006.

[142] M. Marzencki, Y. Ammar, and S. Basrour, "Integrated power harvesting system including a MEMS generator and a power management circuit," in *Proc. IEEE Int. Solid-State Sensors, Actuators, and Microsystems Conf.*, pp. 887–890, June 2007.

[143] M. Marzencki, Y. Ammar, and S. Basrour, "Integrated power harvesting system including a MEMS generator and a power management circuit," *Sensors and Actuators A: Physical,* vol. 145-146, no. 1-2, pp. 363–370, July/Aug. 2008.

[144] B.-S. Lee, S.-C Lin, and W.-J. Wu, "Comparison of the piezoelectric MEMS generators with interdigital electrodes and laminated electrodes," in *Proc. SPIE-The International Society for Optical Engineering*, pp. 69331B-1–69331B-8, Mar. 2008.

[145] M. Renaud, K. Karakaya, T. Sterken, P. Fiorini, C. Van Hoof, and R. Puers, "Fabrication, modelling and characterization of MEMS piezoelectric vibration harvesters," *Sensors and Actuators A: Physical*, vol. 145–146, pp. 380–386, July-Aug. 2008.

[146] Y.B. Jeon, R. Sood, J.-h. Jeong, and S.-G. Kim, "MEMS power generator with transverse mode thin film PZT," *Sensors and Actuators A: Physical*, vol. 122, pp. 16–22, Feb. 2005.

[147] P.D. Mitcheson, E.K. Reilly, T. Toh, P.K. Wright, and E.M. Yeatman, "Performance limits of the three MEMS inertial energy generator transduction types," *J. Micromech. Microeng.*, vol. 17, no. 9, pp. S211–S216, 2007.

[148] H.A. Sodano, D.J. Inman, and G. Park, "A review of power harvesting from vibration using piezoelectric materials," *The Shock and Vibration Digest*, vol. 36, no. 3, pp. 197–205, May 2004.

[149] H. Kim and S. Priya, "Piezoelectric microgenerator – current status, challenges, and applications," in *Proc. IEEE Int. Symp. Application of Ferroelectrics*, pp. 1–2, Feb. 2008.

[150] R. Elfrink, T.M. Kamel, M. Goedbloed, S. Matova, D. Hohlfeld, Y. van Andel, and R. van Schaijk, "Vibration energy harvesting with aluminum nitride-based piezoelectric devices," *J. Micromech. Microeng.*, vol. 19, pp. 094005-1–8, 2009.

[151] R. Elfrink, V. Pop, D. Hohlfeld, T.M. Kamel, S. Matova, C. de Nooijer, M. Jambunathan, M. Goedbloed, L. Caballero, M. Renaud, J. Penders and R. van Schaijk, "First autonomous wireless sensor node powered by a vacuum-packaged

piezoelectric MEMS energy harvester," in *Proc. IEEE Int. Electron Devices Meeting*, pp. 22.5.1–4, 2009.

[152] E.E. Aktakka, R.L. Peterson, and K. Najafi, "A CMOS-compatible piezoelectric vibration energy scavenger based on the integration of bulk PZT films on silicon," in *Proc. IEEE Int. Electron Devices Meeting*, pp. 31.5.1–4, 2010.

[153] E.E. Aktakka, R.L. Peterson, and K. Najafi, "A self-supplied inertial piezoelectric energy harvester with power-management IC," in *IEEE Int. Solid-State Circuits Conf. (ISSCC) Dig. Tech. Papers*, pp. 120–121, Feb. 2011.

[154] E.O. Torres, M. Chen, H.P. Forghani-zadeh, V. Gupta, N. Keskar, L.A. Milner, H.-I. Pan, and G.A. Rincon-Mora, "SiP integration of intelligent, adaptive, self-sustaining power management solutions for portable applications," in *Proc. IEEE Int. Symp. of Circuits and Systems,* pp. 5311–5314, 2006.

[155] G.K. Ottman, H.F. Hofmann, A.C. Bhatt, and G.A. Lesieutre, "Adaptive piezoelectric energy harvesting circuit for wireless remote power supply," *IEEE Trans. Power Electronics*, vol. 17, no. 5, pp. 669–676, Sept. 2002.

[156] G.K. Ottman, H.F. Hofmann, and G.A. Lesieutre, "Optimized piezoelectric energy harvesting circuit using step-down converter in discontinuous conduction mode," *IEEE Trans. Power Electronics*, vol. 18, no. 2, pp. 696–703, Mar. 2003.

[157] L. Chao, C.-Y. Tsui, and W.-H. Ki, "A batteryless vibration-based energy harvesting system for ultra low power ubiquitous applications," in *Proc. IEEE Int. Symp. of Circuits and Systems,* pp. 1349–1352, 2007.

[158] L. Chao, C.-Y. Tsui, and W.-H. Ki, "Vibration energy scavenging system with maximum power tracking for micropower applications," *IEEE Trans. Very Large Scale Integration (VLSI) Systems*, vol. 19, no. 11, pp. 2109–2119, Nov. 2011.

[159] Y. Sun, N.H. Hieu, C.-J. Jeong, and S.-G. Lee, "An integrated high-performance active rectifier for piezoelectric vibration energy harvesting system," *IEEE Trans. Power Electronics*, vol. 27, no. 2, pp. 623–627, Feb. 2012.

[160] T.T. Le, J. Han, A. von Jouanne, K. Mayaram, and T.S. Fiez, "Piezoelectric micro-power generation interface circuits," *IEEE J. Solid-State Circuits*, vol. 41, no. 6, pp. 1411–1420, June 2006.

[161] E. Dallago, D. Miatton, G. Venchi, V. Bottarel, G. Frattini, G. Ricotti, and M. Schipani, "Active autonomous AC-DC converter for piezoelectric energy scavenging systems," in *Proc. IEEE Custom Integrated Circuits Conf.*, pp. 555–558, 2008.

[162] D. Marinkovic, A. Frey, I. Kuehne, and G. Scholl, "A new rectifier and trigger circuit for a piezoelectric microgenerator," *Procedia Chemistry*, vol. 1, pp. 1447–1450, 2009.

[163] S. Cheng, Y. Jin, Y. Rao, and D.P. Arnold, "An active voltage doubling AC/DC converter for low-voltage energy harvesting applications," *IEEE Trans. Power Electronics*, vol. 26, no. 8, pp. 2258–2265, Aug. 2011.

[164] N.J. Guilar, R. Amirtharajah, and P.J. Hurst, "A full-wave rectifier with integrated peak selection for multiple electrode piezoelectric energy harvesters," *IEEE J. Solid-State Circuits*, vol. 44, no. 1, pp. 240–246, Jan. 2009.

[165] A. Tabesh and L.G. Fréchette, "A low-power stand-alone adaptive circuit for harvesting energy from a piezoelectric micropower generator," *IEEE Trans. Industrial Electronics*, vol. 57, no. 3, pp. 840–849, Mar. 2010.

[166] S. Sankaran and K.O. Kenneth, "Schottky barrier diodes for millimeter wave detection in a foundry CMOS process," *IEEE Electron Device Letters*, vol. 26, no. 7, pp. 492–494, July 2005.

[167] P. Li and R. Bashirullah, "A wireless power interface for rechargeable battery operated medical implants," *IEEE Trans. Circuits and Systems–II: Express Briefs,* vol. 54, no. 10, pp. 912–916, Oct. 2007.

[168] T. Umeda, H. Yoshida, S. Sekine, Y. Fujita, T. Suzuki, and S. Otaka, "A 950MHz rectifier circuit for sensor networks with 10m-distance," in *IEEE Int. Solid-State Circuits Conf. (ISSCC) Dig. Tech. Papers*, pp. 256–257, Feb. 2005.

[169] T. Umeda, H. Yoshida, S. Sekine, Y. Fujita, T. Suzuki, and S. Otaka, "A 950-MHz rectifier circuit for sensor network tags with 10-m distance," ," *IEEE J. Solid-State Circuits*, vol. 41, no. 1, pp. 35–41, Jan. 2006.

[170] H. Nakamoto, D. Yamazaki, T. Yamamoto, H. Kurata, S. Yamada, K. Mukaida, T. Ninomiya, T. Ohkawa, S. Masui, and K. Gotoh, "A passive UHF RFID tag LSI with 36.6% efficiency CMOS-only rectifier and current-mode demodulator in

0.35μm FeRAM technology," in *IEEE Int. Solid-State Circuits Conf. (ISSCC) Dig. Tech. Papers*, pp. 1201–1202, Feb. 2006.

[171] C. Peters, J. Handwerker, F. Henrici, M. Ortmanns, and Y. Manoli, "Experimental results on power efficient single-poly floating gate rectifiers," in *Proc. IEEE Int. Symp. Circuits and Systems (ISCAS)*, pp. 1097–1100, 2009.

[172] Y.-H. Lam, W.-H. Ki, and C.-Y. Tsui, "Integrated low-loss CMOS active rectifier for wirelessly powered devices," *IEEE Trans. Circuits Syst. II: Express Briefs*, vol. 53, no. 12, pp. 1378–1382, Dec. 2006.

[173] S. Guo and H. Lee, "An efficiency-enhanced CMOS rectifier with unbalanced-biased comparators for transcutaneous-powered high-current implants," *IEEE J. Solid-State Circuits*, vol. 44, no. 6, pp. 1796–1804, June 2009.

[174] H.-M. Lee and M. Ghovanloo, "An adaptive reconfigurable active voltage doubler/rectifier for extended-range inductive power transmission," in *IEEE Int. Solid-State Circuits Conf. (ISSCC) Dig. Tech. Papers*, pp. 286–287, Feb. 2012.

[175] C. Peters, M. Ortmanns, and Y. Manoli, "Fully CMOS integrated active rectifier without voltage drop," in *Proc. IEEE Midwest Symp. Circuits and Systems (MWSCAS)*, pp. 185–188, 2008.

[176] Y. Rao and D.P. Arnold, "An input-powered vibrational energy harvesting interface circuit with zero standby power," *IEEE Trans. Power Electronics*, vol. 26, no. 12, pp. 3524–3533, Dec. 2011.

[177] H. Lee and S.-R. Ryu, "An efficiency-enhanced DCM buck regulator with improved switching timing of power transistors," *IEEE Trans. Circuits Syst. II: Express Briefs*, vol. 57, no. 3, pp. 238–242, Mar. 2010.

[178] T.Y. Man, P.K.T. Mok, and M.J. Chan, "A 0.9-V input discontinuous-conduction-mode boost converter with CMOS-control rectifier," *IEEE J. Solid-State Circuits*, vol. 43, no. 9, pp. 2036–2046, Sept. 2008.

[179] J.L. Wardlaw, A.İ. Karşılayan, "Self-powered rectifier for energy harvesting applications," *IEEE J. Emerging and Selected Topics in Circuits Syst.*, vol. 1, no. 3, pp. 308–320, Sept. 2011.

[180] S. Masui, E. Ishii, T. Iwawaki, Y. Sugawara, and K. Sawada, "A 13.56MHz CMOS RF identification transponder integrated circuit with a dedicated CPU," in *IEEE Int. Solid-State Circuits Conf. (ISSCC) Dig. Tech. Papers*, pp. 162–163, Feb. 1999.

[181] M. Ghovanloo and K. Najafi, "Fully integrated wideband high-current rectifiers for inductively powered devices," *IEEE J. Solid-State Circuits*, vol. 39, no. 11, pp. 1976–1984, Nov. 2004.

[182] D. Kwon and G.A. Rincón-Mora, "A single-inductor AC–DC piezoelectric energy-harvester/battery-charger IC converting ±(0.35 to 1.2 V) to (2.7 to 4.5 V)," in *IEEE Int. Solid-State Circuits Conf. (ISSCC) Dig. Tech. Papers*, pp. 494–495, Feb. 2010.

[183] D. Kwon and G.A. Rincón-Mora, "A 2-μm BiCMOS rectifier-free AC–DC piezoelectric energy harvester-charger IC," *IEEE Trans. Biomed. Circuits Syst.*, vol. 4, no. 6, pp. 400–409, Dec. 2010.

[184] D. Kwon, G.A. Rincón-Mora, and E.O. Torres, "Harvesting ambient kinetic energy with switched-inductor converters," *IEEE Trans. Circuits Syst.–I: Regular Papers*, vol. 58, no. 7, pp. 1551–1560, July 2011.

[185] D. Kwon and G.A. Rincón-Mora, "A rectifier-free piezoelectric energy harvester circuit," in *Proc. IEEE Int. Symp. Circuits Syst. (ISCAS)*, pp. 1085–1088, May 2009.

[186] D. Kwon, G.A. Rincón-Mora, and E.O. Torres, "Harvesting kinetic energy with switched-inductor DC–DC converters," in *Proc. IEEE Int. Symp. Circuits Syst. (ISCAS)*, pp. 281–284, May 2010.

[187] J. Li, E. Murphy, J. Winnick, and P.A. Kohl, "The effects of pulse charging on cycling characteristics of commercial lithium-ion batteries," *J. Power Sources*, vol. 102, pp. 302–309, 2001.

[188] Z. Jiang, and R.A. Dougal, "Synergetic control of power converters for pulse current charging of advanced batteries from a fuel cell power source," *IEEE Trans. Power Electronics*, vol. 19, no. 4, pp. 1140–1150, July 2004.

[189] L.-R. Chen, "A design of an optimal battery pulse charge system by frequency-varied technique," *IEEE Trans. Industrial Electronics*, vol. 54, no. 1, pp. 398–405, Feb. 2007.

[190] F. Cottone, H. Vocca, and L. Gammaitoni, "Nonlinear energy harvesting," *Phys. Rev. Lett.*, vol. 102, pp. 080601-1 – 080601-4, Feb. 2009.

[191] P.D. Mitcheson, T.C. Green, E.M. Yeatman, and A.S. Holmes, "Architectures for vibration-driven micropower generators," *J. Microelectromechanical Systems,* vol. 13, no. 3, pp. 429–440, June 2004.

[192] D. Galayko and P. Basset, "A general analytical tool for the design of vibration energy harvesters (VEHs) based on the mechanical impedance concept," *IEEE Trans. Circuits and Systems—I: Regular Papers,* vol. 58, no. 2, pp. 299–311. Feb. 2011.

[193] G.A. Lesieutre, G.K. Ottman, and H.F. Hofmann, "Damping as a result of piezoelectric energy harvesting," *J. Sound and Vibration*, vol. 269, pp. 991–1001, 2004.

[194] J. Dicken, P.D. Mitcheson, I. Stoianov, and E.M. Yeatman, "Increased power output from piezoelectric energy harvesters by pre-biasing," in *Proc. PowerMEMS*, pp. 75–78, Dec. 2009.

[195] D. Guyomar, A. Badel, E. Lefeuvre, and C. Richard, "Toward energy harvesting using active material and conversion improvement by nonlinear processing," *IEEE Trans. Ultrasonics, Ferroelectronics, and Frequency Control*, vol. 52, no. 4, pp. 584–595, Apr. 2005.

[196] A. Badel, D. Guyomar, E. Lefeuvre, and C. Richard, "Piezoelectric energy harvesting using a synchronized switch technique," *J. Intelligent Material Systems and Structures*, vol. 17, pp. 831–839, Aug./Sept. 2006.

[197] E. Lefeuvre, A. Badel, C. Richard, L. Petit, and D. Guyomar, "A comparison between several vibration-powered piezoelectric generators for standalone systems," *Sensors Actuators A,* vol. 126, pp. 405–416, 2006.

[198] A. Badel, A. Benayad, E. Lefeuvre, L. Lebrun, C. Richard, and D. Guyomar, "Single crystals and nonlinear process for outstanding vibration-powered electrical generators," *IEEE Trans. Ultrasonics, Ferroelectronics, and Frequency Control*, vol. 53, no. 4, pp. 673–684, Apr. 2006.

[199] D. Guyomar, G. Sebald, S. Pruvost, and M. Lallart, “Energy harvesting from ambient vibrations and heat,” *J. Intelligent Material Systems and Structures*, vol. 20, pp. 609–624, Mar. 2009.

[200] D. Guyomar and M. Lallart, “Energy conversion improvement in ferroelectrics: application to energy harvesting and self-powered systems,” in *Proc. IEEE Int. Ultrasonics Symp.*, 2009.

[201] M. Lallart, L. Garbuio, C. Richard, and D. Guyomar, “Low-cost capacitor voltage inverter for outstanding performance in piezoelectric energy harvesting,” *IEEE Trans. Ultrasonics, Ferroelectronics, and Frequency Control*, vol. 57, no. 2, pp. 281–291, Feb. 2010.

[202] D. Guyomar, Y. Jayet, L. Petit, E. Lefeuvre, T. Monnier, C. Richard, and M. Lallart, “Synchronized switch harvesting applied to selfpowered smart systems: Piezoactive microgenerators for autonomous wireless transmitters,” *Sensors and Actuators A*, vol. 138, pp. 151–160, 2007.

[203] M. Lallart and D. Guyomar, “An optimized self-powered switching circuit for non-linear energy harvesting with low voltage output,” *Smart Mater. Struct.*, vol. 17, pp. 1–8, 2008.

[204] M. Lallart, L. Garbuio, L. Petit, C. Richard, and D. Guyomar, “Double synchronized switch harvesting (DSSH): a new energy harvesting scheme for efficient energy extraction,” *IEEE Trans. Ultrasonics, Ferroelectronics, and Frequency Control*, vol. 55, no. 10, pp. 2119–2130, Oct. 2008.

[205] L. Garbuio, M. Lallart, D. Guyomar, C. Richard, and D. Audigier, “Mechanical energy harvester with ultralow threshold rectification based on SSHI nonlinear technique,” *IEEE Trans. Ind. Electronics*, vol. 56, no. 4, pp. 1048–1056, Apr. 2009.

[206] M. Lallart and D. Guyomar, “Piezoelectric conversion and energy harvesting enhancement by initial energy injection,” *Appl. Phys. Lett.*, vol. 97, pp. 014104-1–014104-3, 2010.

[207] Y. Liu, G. Tian, Y. Wang, J. Lin, Q. Zhang, and H.F. Hofmann, “Active piezoelectric energy harvesting: General principle and experimental demonstration,” *J. Intelligent Material Systems and Structures*, vol. 20, pp. 575–585, Mar. 2009.

[208] C. Luo, "Active energy harvesting for piezoelectric dynamic systems," Ph.D. dissertation, College of Engineering, Penn. State Univ., 2010.

[209] D. Kwon and G.A. Rincón-Mora, "Energy-investment schemes for increasing output power in piezoelectric harvesters," in *Proc. IEEE Int. Midwest Symp. Circuits Syst. (MWSCAS)*, pp. 1084–1087, Aug. 2012.

[210] Y.K. Ramadass and A.P. Chandrakasan, "An efficient piezoelectric energy harvesting interface circuit using a bias-flip rectifier and shared inductor," *IEEE J. Solid-State Circuits*, vol. 45, no. 1, pp. 189–204, Jan. 2010.

[211] H.J. Oguey and D. Aebischer, "CMOS current reference without resistance," *IEEE J. Solid-State Circuits*, vol. 32, no. 7, pp. 1132–1135, July 1997.

[212] A. Hastings, *The Art of Analog Layout*, 2st ed., Upper Saddle River, NJ: Prentice Hall, 2005.

[213] Q.A. Khan, S.K. Wadhwa, and K. Misri, "Low power startup circuits for voltage and current reference with zero steady state current," in *Proc. Int. Symp. Low Power Electron. Design (ISLPED)*, pp. 184–1888, 2003.

[214] R. Dayal and L. Parsa, "Hybrid start-up strategy for low voltage electromagnetic energy harvesting systems," in *Proc. IEEE Applied Power Electronics Conf. Expo. (APEC)*, vol. 38, pp. 675–680, 2012.

[215] S. Xu, K.D.T. Ngo, T. Nishida, G.-B. Chung, and A. Sharma, "Low frequency pulsed resonant converter for energy harvesting," *IEEE Trans. Power Electronics*, vol. 22, no. 1, pp. 63–68, Jan. 2007.

[216] E. Dallago, D. Miatton, G. Venchi, V. Bottarel, G. Frattini, G. Ricotti, and M. Schipani, "Electronic interface for piezoelectric energy scavenging system," in *Proc. European Solid-State Circuits Conf. (ESSCIRC)*, pp. 402–405, 2008.

[217] T. Hehn, D. Maurath, F. Hagedorn, D. Marinkovic, I. Kuehne, A. Frey, and Y. Manoli, "A fully autonomous pulsed synchronous charge extractor for high-voltage piezoelectric harvesters," in *Proc. IEEE European Solid-State Circuits Conf. (ESSCIRC)*, pp. 371–374. 2011.

[218] I.M. Darmayuda, Y. Gao, M.T. Tan, S.-J. Cheng, Y. Zheng, M. Je, and C.-H. Heng, "A self-powered power conditioning IC for piezoelectric energy harvesting from short-duration vibrations," *IEEE Trans. Circuits and Systems–II: Express Briefs,* vol. 59, no. 9, pp. 578–582, Sept. 2012.

[219] A. Hajati and S.-G. Kim, "Ultra-wide bandwidth piezoelectric energy harvesting," *Appl. Phys. Lett*., vol. 99, pp. 083105-1–3, 2011.

[220] M. Ferrari, V. Ferrari, M. Guizzetti, D. Marioli, and A. Taroni, "Piezoelectric multifrequency energy converter for power harvesting in autonomous microsystems," *Sensors and Actuators A*, vol. 142, pp. 329–335, 2008.

[221] M. Lallart, S.R. Anton, and D.J. Inman, "Frequency self-tuning scheme for broadband vibration energy harvesting," *J. Intelligent Material Systems and Structures*, vol. 21, pp. 897–906, June 2010.

[222] M. Wischke, M. Masur, F. Goldschmidtboeing and P. Woias, "Electromagnetic vibration harvester with piezoelectrically tunable resonance frequency," *J. Micromech. Microeng*, vol. 20, p. 035025 (7pp), 2010.

[223] P.D. Mitcheson, T.T. Toh, K.H. Wong, S.G. Burrow, and A.S. Holmes, "Tuning the resonant frequency and damping of an electromagnetic energy harvester using power electronics," *IEEE Trans. Circuits and Systems–II: Express Briefs,* vol. 58, no. 12, pp. 792–796, Dec. 2011.

[224] E. Halvorsen, "Energy harvesters driven by broadband random vibrations," *J. Microelectromech. Syst.*, vol. 17, no. 5, pp. 1061–1071, Oct. 2008.

VITA

DONGWON KWON

Dongwon Kwon received his Bachelor of Science (B.S.) degree from Seoul National University, Korea, in 2003 and Master of Science (M.S.) degree from the Georgia Institute of Technology, Atlanta, GA in 2008. He joined the Georgia Tech Analog, Power, and Energy IC Lab in 2007, where he has pursued his Ph.D. degree since.

From 2003 to 2006, he worked as a Research Engineer at Hantel Inc., Kyunggi, Korea, developing MP3 players. In 2010, he designed switching power converter integrated circuits (ICs) as a Design Intern at Linear Technology Corporation, Milpitas, CA, where he is currently working as a Design Engineer. His research interests include piezoelectric energy harvesting circuits, switching-mode power ICs, and ultra-low-power analog IC design.